

***Design and fabrication  
concepts for nanolasers***

Lewis Kastein

PhD Thesis

School of Physics and Astronomy  
Cardiff University

September 2015

## Declaration

This work has not been submitted in substance for any other degree or award at this or any other university or place of learning, nor is being submitted concurrently in candidature for any degree or other award.

Signed ..... (candidate) Date .....

### STATEMENT 1

This thesis is being submitted in partial fulfilment of the requirements for the degree of PhD.

Signed ..... (candidate) Date .....

### STATEMENT 2

This thesis is the result of my own independent work/investigation, except where otherwise stated. Other sources are acknowledged by explicit references. The views expressed are my own.

Signed ..... (candidate) Date .....

### STATEMENT 3

I hereby give consent for my thesis, if accepted, to be available for photocopying and for inter-library loan, and for the title and summary to be made available to outside organisations.

Signed ..... (candidate) Date .....

## **Publications and Conferences**

2015 Conference. "IEEE Photonics Conference 2015", Reston, Virginia, USA, presentation on "Design and fabrication towards plasmonic and nanopillar lasers."

2015 Conference. "Semiconductor and Integrated Optoelectronic conference 2015", Cardiff University, Cardiff, UK, 2015, presentation on "Design and fabrication of quantum dot composite nanopillar-polymer lasers".

2014 Conference: "Semiconductor and Integrated Optoelectronic conference 2014", Cardiff University, Cardiff, UK, 2014, presentation on "'Anodic Oxide Suitability for Plasmonic Nanolasers".

2013 Conference: "Semiconductor and Integrated Optoelectronic conference 2013", Cardiff University, Cardiff, UK, 2013, presentation on progress in the "Fabrication of nanolaser devices".

2012 Conference: "The Celebration of the 50th Anniversary of the Diode Laser", University of Warwick, Coventry, UK, 2012, presentation on "Nanolaser Design and Fabrication".

## Abstract

This thesis investigated the design and fabrication of three nanodevices, a hybrid-plasmonic device, an InP composite pillar-polymer device, and a GaN composite pillar-polymer device.

The hybrid plasmonic device consists of a gain material separated from a metal stripe layer by a dielectric layer. The optical mode within the gain material becomes bound to the metal region and hybridises with surface plasmon oscillations, resulting in Ohmic absorption losses. The dielectric gap is used to reduce Ohmic absorption losses. A Fabry-Perot cavity can be formed by reflections from the edges of the metal stripe. Aspects of the device were investigated, including its fabrication, the importance of the alignment of smaller structures to larger structures, and contact metallisation. A more detailed study was carried out on the fabrication of two aspects of the device, the semiconductor slab thickness and dielectric gap thickness.

For this device a TM emitting 633nm laser structure was designed to provide gain, the characteristics of the grown wafer were confirmed using edge photovoltage spectroscopy, showing that the electron to light hole transition was at a lower energy than the electron to heavy hole transition, and existed at a wavelength of 633nm. A strong dependence of loss with the semiconductor slab thickness and dielectric gap thickness was calculated. A single nanometer change in the dielectric gap thickness can alter the mode cut-off by a semiconductor slab thickness of up to 100nm, and can change the mode loss up to  $600\text{cm}^{-1}$ . In addition, the mode is pulled towards the metal/dielectric region, resulting in a small optical confinement factor in the central quantum well region, and a low modal gain that can not compensate losses. A high energy density was modelled within the dielectric layer, and the mode was found to be bound to the metal region, which may be useful for some applications. Fabrication of a nanosquare device with electrical injection was investigated, the importance of alignment procedures were noted and metallisation was explored. The specific contact resistivity of the contacts was found to be in the order of, or better than, similar fabricated contacts, found to be  $3 \times 10^{-3} \text{ ohms.cm}^2$  and  $4 \times 10^{-6} \text{ ohms.cm}^2$  for the p and n type contacts respectively. However, the small injection mesa suffered from heating and resulted in contact metal delamination. An alternative injection method using current apertures was presented, and fabrication of aspects of the design were explored.



The dielectric layer was fabricated through the anodisation of GaAs. Growth over large area samples showed a good thickness control, in the order of 1nm per 0.0018 mA cm<sup>-2</sup>. The Ga-oxide to As-oxide ratio was found to be close to 3:4, which, as is further discussed in chapter 4, has been shown to have good electrical and thermal stability. Growth conditions were optimised in order to obtain a conformal oxide with low roughness and peak to trough topography. At a selected starting current a low roughness in the order of 0.06 nm, close to the roughness of the unoxidised GaAs surface, was obtained. A change in peak to trough topography from the GaAs surface of 0.7 nm was obtained for thin oxides. The ability to selectively oxidise small features using a resist mask, aligned to larger structures, was highlighted. The barrier height of a 3nm layer of the oxide was determined to be in the order of 0.87eV. The semiconductor slab thickness and current aperture was determined through the steam oxidation of AlGaAs. Calibration of the constructed apparatus showed the ability to repeatedly fabricate small current apertures, and determined that the oxidation was a reaction rate rather than a diffusion rate limited process. A controlled oxidation rate of approximately 0.06  $\mu\text{m}/\text{min}$  at 360°C is achievable. The activation energy of the oxidation process was found to be 1.79 eV.

The InP pillar device consists of an etched array of pillars with a quantum dot active region, terminated at both ends by distributed Bragg reflectors, embedded in a Benzocyclobutene (BCB) waveguiding polymer with a lower air gap. A viable design for a composite pillar-polymer nanolaser was investigated and fabricated. This included the development of InP ICP etching and the novel and new use of polymer materials in a waveguide. The absorption and gain of the nanopillar structure were not successfully measured due to a lack of light coupling into the active region when optically pumped. This was likely a result of the unintentional annealing of the nickel etch mask which resists chemical removal, blocking pump light from reaching the active region. However, the absorption and internal optical mode loss of a ridge of an equivalent width was measured, and a dependency of absorption with pump power was noted. The internal optical mode loss for the 10 $\mu\text{m}$  ridge structure was found to be  $7.5 \pm 2.5 \text{ cm}^{-1}$ , measured using the variable stripe length method. To allow characterisation of the pillars using this optically pumped technique further work must see the development of an inductive coupled plasma (ICP) etch mask that is able to better preserve the semiconductor surface, such as an oxide-nickel bilayer etch mask.

The GaN composite pillar-polymer device utilised the same waveguide configuration as the InP device. A GaN nanopillar array was embedded in a BCB polymer with a lower air gap to act as an optical waveguide. The internal optical mode loss of the nanopillar array without a polymer waveguide was determined to be  $\alpha_i = 4 \pm 4 \text{ cm}^{-1}$ . This was determined using the shifting excitation spot method. A slight redshift in peak wavelength of 20 meV was observed for the polymer sample, attributed to a lower confinement factor of each individual pillar. Additional optical emission at long wavelengths was detected from the composite nanopillar-polymer waveguide which was not detected for the structure without a waveguide, and did not emanate from the polymer itself. The emission may be attributed to emission from doping atoms or the lower unetched 2D GaN layer. Modelling showed that the polymer waveguide is able to more strongly guide a broader and longer range of wavelengths, whilst the non-polymer structure shows indications that long wavelengths are not guided. The increased absorption at the peak wavelength for the polymer waveguide indicates an increased optical confinement factor across the composite polymer quantum well layer, the magnitude suggests that a 2nd order mode is guided within the polymer waveguide that is not guided with the non-polymer waveguide.

## Summary of Thesis

In this work the miniaturisation of laser devices was investigated. Design and fabrication concepts of three nanoscale devices were explored: These were a hybrid-plasmonic device, an InP composite pillar-polymer device, and a GaN composite pillar-polymer device.

The hybrid plasmonic device consisted of a gain material separated from a metal stripe layer by a dielectric gap. The optical mode within the gain material becomes bound to the metal region and hybridises with surface plasmon oscillations. The hybrid-plasmonic structure was fabricated. A more detailed study was carried out on the fabrication of two aspects of the device which were found to be important to the reduction of Ohmic losses (experienced by the optical mode), these are the semiconductor slab thickness and dielectric gap.

The InP pillar device consisted of an etched array of pillars with a quantum dot active region. The pillar arrays were terminated at both ends by distributed Bragg reflectors for optical feedback. The architecture was embedded in a novel BCB waveguide with a lower air gap. A viable design for a composite pillar-polymer nanolaser was explored and InP pillar and polymer waveguide fabrication techniques were developed. The GaN composite pillar-polymer device utilised the same waveguide configuration as the InP device. It exhibited an enhanced ability to guide long wavelength emission.

## Acknowledgements

I would like to thank my supervisors Peter Smowton and Phil Buckle for their guidance throughout this work. I would also like to thank Peter Blood for interesting postgraduate discussions.

For my initial introduction into semiconductor fabrication I thank Angela Sobiesierski and Karen Barnett. I would like to thank Stella Elliot for her assistance with EPVS characterisation and computing, Rob Tucker for his knowledge of electronics, Samuel Shutts for his assistance with ICP etching, and Robert Thomas for his assistance in device characterisation. In particular I thank Sam and Rob for their discussions, support and humour. Their wide knowledge, expertise and enthusiasm were invaluable.

I thank my family, friends, and colleagues in Scouting. I would like to thank the Beavers and Cubs who have provided inspiration and smiles throughout this process.

# Contents

<b>Chapter 1. Introduction.....</b>	<b>1</b>
1.1. Thesis rationale.....	1
1.2. Thesis structure.....	2
Chapter References.....	2
<b>Chapter 2. Background Theory.....</b>	<b>3</b>
2.1. Introduction.....	3
2.2. The laser diode.....	3
2.2.1 Light amplification.....	3
2.2.2 Optical feedback.....	7
2.3. Nanolasers and plasmonics.....	9
2.3.1 Laser size reduction.....	9
2.3.2 Small-Cavity quantum electrodynamics.....	11
2.3.3 Plasmonics.....	15
2.4. Anodic oxidation.....	22
2.4.1 Electrolyte solution.....	24
2.4.2 Oxide density and composition.....	25
2.4.3 Pulsed voltage mode.....	27
2.5. Steam oxidation.....	28
2.6 Distributed Bragg Reflectors.....	31
Chapter References.....	32
<b>Chapter 3. Experimental Techniques.....</b>	<b>35</b>

3.1. Introduction.....	35
3.2. GaAs-Oxide Growth and Characterisation.....	35
3.2.1. Anodic oxidation.....	35
3.2.2. Atomic force microscopy.....	37
3.2.3. Spectroscopic ellipsometry.....	40
3.2.4. Metallisation transmission line measurements.....	41
3.2.5. Current-voltage-temperature diode measurements.....	44
3.3. Buried AlGaAs-Oxide Growth and Characterisation.....	49
3.3.1. Steam Oxidation.....	49
3.3.2. Oxide extent measurement.....	51
3.4. Device Characterisation Techniques.....	53
3.4.1. Edge photovoltage spectroscopy (EPVS).....	53
3.4.2. Shifting excitation spot (SES).....	55
3.4.3. Variable stripe length measurements (VSL).....	57
3.5. Summary.....	60
Chapter References.....	60
<b>Chapter 4. Hybrid Plasmonic Device.....</b>	<b>63</b>
4.1. Introduction.....	63
4.2. Device Design.....	63
4.2.1. Wafer Design.....	64
4.2.2. Dielectric gap and semiconductor material requirements and constraints.....	70

4.3. Device Fabrication.....	79
4.3.1. Nanosquare electrical injection.....	79
4.3.2. Alignment procedures.....	81
4.3.3. Current-voltage measurements and contact metallisation.....	86
4.3.4. Current apertures.....	91
4.4. Dielectric gap via anodisation of GaAs.....	93
4.4.1. Thickness control and composition.....	93
4.4.2. Roughness and topography.....	95
4.4.3. Selective area growth/patterning and chemical resistance.....	99
4.4.4. Diode electrical characteristics.....	101
4.5. Semiconductor slab thickness via AlGaAs steam oxidation.....	110
4.6. Summary.....	114
Chapter References.....	116
<b>Chapter 5. InP Pillar Device.....</b>	<b>119</b>
5.1. Introduction.....	119
5.2. Device Design.....	119
5.2.1. Epitaxial structure.....	120
5.2.2. Wavelength tuning.....	121
5.2.3. Waveguide design.....	122
5.2.4. Distributed Bragg reflectors.....	124
5.2.5. Nanopillar array.....	125
5.2.6. Device length.....	126

5.3. Device Fabrication.....	127
5.3.1. Electron beam lithography.....	127
5.3.2. ICP etching.....	129
5.3.3. Polymer waveguide fabrication.....	137
5.4. Results.....	142
5.4.1. Gain and absorption measurements.....	142
5.5. Summary.....	148
Chapter References.....	148
<b>Chapter 6. GaN Pillar Device.....</b>	<b>149</b>
6.1. Introduction.....	149
6.2. Device Design.....	149
6.3. Device Fabrication.....	150
6.4. Results.....	151
6.5. Summary.....	160
Chapter References.....	161
<b>Conclusions.....</b>	<b>162</b>
<b>Appendix: Shifting excitation spot apparatus.....</b>	<b>165</b>



# Chapter 1. Introduction

## 1.1. Thesis rationale

Advancements in technology and computing are achievable by the miniaturisation and dense integration of photonic components in devices and electronic circuits (Fang, Y 2015) (Sorger, V.J 2012). Nanolasers have the potential to close the gap between the size of silicon based microelectronics and compound semiconductor based optoelectronic devices. The current discrepancy in size of these components is a result of the difference in operating wavelength of photonics compared to electronics. The de Broglie wavelength of a free electron with an energy of 2eV is 700 times smaller than the wavelength of a photon of equivalent energy. The use of plasmonics in which the photonic wavelength is reduced through hybridisation with free surface electrons is one attempt to close this size gap. The reduction in the size of lasers introduces novel physics which can be advantageous for a number of applications, including high speed low power optical interconnects, biomedical devices and sensors.

This piece of work primarily investigates the fabrication and physics of plasmonic and nanopillar devices. Plasmonic nanolasers are arguably one of the most promising candidates for reduced dimensionality lasers, however, they exhibit an inherent optical loss that may be too large to be fully compensated. This together with the practicality of approaches to fabricate nanolaser are investigated in this work. Composite nanopillar-polymer lasers have to my knowledge not been widely imagined, investigated or fabricated. Although the nanopillars in this work are not fabricated on silicon substrates the architecture is designed with the associated problems of integration in-mind. The direct growth of III-V material on silicon substrates is paramount to full on-chip integration of optical and electrical components, this is due both to the maturity of silicon electronics and the high quality oxide that can be grown on silicon necessary for many electronic components. The small footprint of III-V nanopillars when grown directly on silicon substrates may lessen the operational impact of strain dislocations (caused by atomic lattice mismatch between the materials). In addition, the composite pillar/polymer design envisioned in this work has potential to be developed into an on-chip sensor.

The design, fabrication and characterisation of nanolasers introduces novel physics and technological challenges, both of which motivate this project.

## **1.2. Thesis structure**

The basic laser theory required for the understanding of this work is presented in chapter 2. The approach taken to achieve the miniaturisation of laser devices is justified within this section. Additional theory regarding aspects of the device and its fabrication are included in this chapter. Chapter 3 provides details of the experimental techniques of anodic and steam oxidation, as well as device characterisation techniques for the fabricated structures. Chapters 4, 5 and 6 explore the Hybrid-plasmonic, InP pillar and GaN pillar devices respectively. Included in each chapter are design details, fabrication steps and characterisation results. A summary of the conclusions of this work can be found in chapter 7.

## **Chapter References**

Fang, Y.; Sun, M. (2015). "Nanoplasmonic waveguides: towards applications in integrated nanophotonic circuits." *Light Sci Appl* **4**: e294.

Sorger, V.J.; Ma, R.; Zhang, X. (2012). "Toward integrated plasmonic circuits. ." *MRS Bulletin*, **37**: pp 728-738.

# Chapter 2. Background Theory

## 2.1. Introduction

This chapter provides a brief summary of the underpinning theory regarding the operation of laser devices and goes on to provide justification for the steps taken in order to reduce their dimensionality. Furthermore this section includes required theory for aspects of fabrication (anodic and steam oxidation).

## 2.2. The laser diode

A laser diode has three basic components, a gain medium, in which light amplification can take place through carrier population inversion, a resonant cavity, which provides optical feedback for stimulated emission (whilst allowing some of the light to escape as useful output), and a means to pump the material to produce a population inversion for laser action to take place.

### 2.2.1 Light amplification

The coherent amplification of light in a gain medium can be quantified by the optical gain coefficient. The magnitude of the gain coefficient is controlled by the occupation probabilities of the upper and lower electron states within the material. The optical gain coefficient is defined as the fractional increase in the energy of the optical mode with propagation distance, as given in equation 2.1 (Blood, P. 2015).

$$G = \frac{1}{\Delta L} \frac{\Delta E}{E} \quad (2.1)$$

Where  $\Delta L$  is the propagation distance,  $E$  is the energy in the whole optical mode, and (for a quantum confined structure)  $\Delta E$  is the increase in energy in the gain providing region (quantum dot or quantum well epitaxial layers). The increase in energy is provided by the difference in upward and downward photon transitions.

A semiconductor gain medium contains bands of electronic energy levels due to the periodic potential of the crystal lattice. The highest electron occupied states (in thermal equilibrium without excitation) form the valence band, whilst the next highest unoccupied states form the conduction band.

Four main electronic transitions between the valence and conduction bands can be described, as illustrated in figure 2.1 (Coldren, L. 1995). Three of the transitions are radiative processes, whilst one is non-radiative. The processes are spontaneous emission ( $R_{sp}$ ), in which non-coherent photons are emitted (through electron perturbation with vacuum photons), stimulated absorption ( $R_{12}$ ), where an electron is raised to the conduction band, stimulated emission ( $R_{21}$ ), in which the emitted photon has the same phase and polarisation as the stimulating photon, and nonradiative recombination ( $R_{nr}$ ).

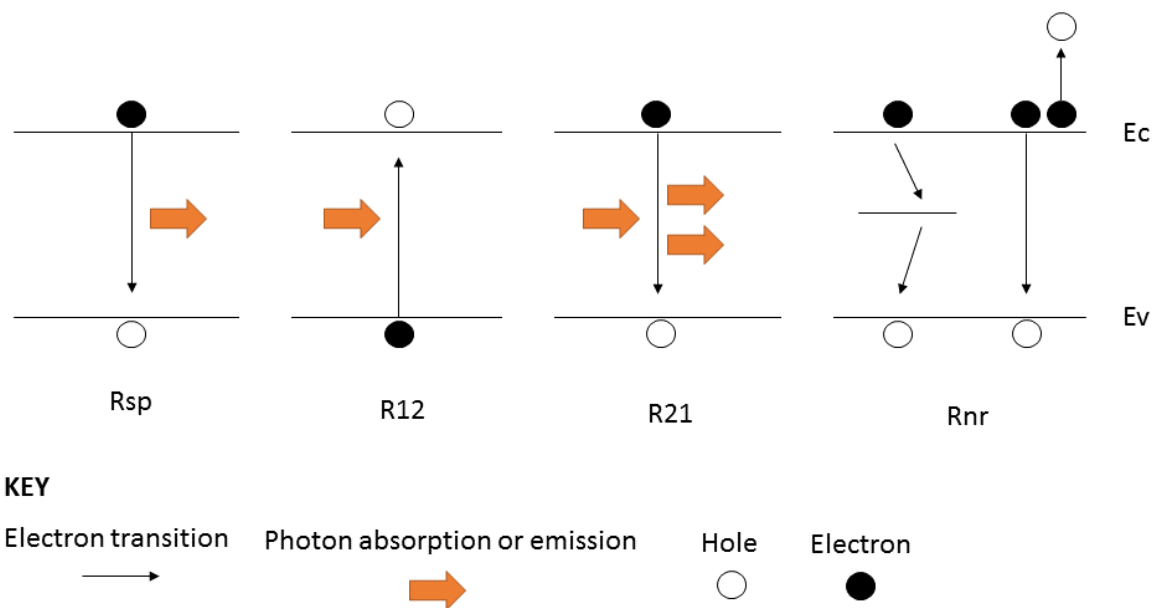


**Figure 2.1: Illustration of electronic transitions between conduction and valence bands**

Stimulated emission is necessary for laser action. Once electrons are excited into the conduction band (leaving an empty state, a hole, in the valence band), they may be perturbed by an incoming photon, and return to the valence band via a process of radiative electron-hole recombination. The emitted photon has an energy equivalent to the separation of the conduction and valence band states, and has the same phase and polarisation as the perturbing photon, resulting in coherent light.

Population inversion can be achieved by either electrically injecting electrons directly into the conduction band of a p-n structure, or optically pumping a gain material. Optical pumping relies on the absorption of a photon to raise an electron to the conduction band. This requires a pump wavelength that is shorter than the emission wavelength of the

semiconductor material, whilst not being so small that the pump photons are absorbed by other (cladding) layers that exist in a double heterostructure laser diode design.

The conditions for laser action require that the net downward transition rate of electrons must exceed the net upward transition rate of electrons. To meet this requirement a population inversion of electrons must be sustained. For a given  $k$  value the probability of an electron occupying a state in the conduction band (energy level  $E_2$ ) must be greater than the probability of an electron occupying a state in the valence band (energy level  $E_1$ ).

The probability of occupation of a state is governed by Fermi statistics, where the Fermi energy ( $E_f$ ) is determined by the total number of electrons in the system. The Fermi energy describes the point at which the electron occupation probability is 0.5. In thermal equilibrium the Fermi function for the electron occupation probability is given by equation 2.2.

$$f(E) = \frac{1}{1 + \exp\left[\frac{(E - E_f)}{k_B T}\right]} \quad (2.2)$$

For an intrinsic semiconductor in thermal equilibrium states below the Fermi energy are mostly occupied, whilst states above it are mostly empty. Few conduction band electrons exist in this case because the Fermi energy is near the middle of the band gap, which is much larger than  $k_B T$ .

However, due to the lack of thermal equilibrium when carriers are injected, separate Fermi energies (quasi-Fermi energies) are assigned to the conduction and valence bands. The probability of an electron occupying the conduction band ( $f_2$ ) and valence band ( $f_1$ ) are shown in equations 2.3 and 2.4 respectively.

$$f_2 = \frac{1}{1 + \exp\left[\frac{(E_2 - E_{f2})}{k_B T}\right]} \quad (2.3)$$

$$f_1 = \frac{1}{1 + \exp\left[\frac{(E_1 - E_{f1})}{k_B T}\right]} \quad (2.4)$$

The quasi Fermi energy of electrons in the conduction band is increased relative to the thermal equilibrium Fermi energy due to an increased number of electrons in the

conduction band, whilst the quasi Fermi energy of electrons in the valence band is decreased due to the extraction of electrons. The separation of the conduction and valence band quasi Fermi energies indicates the degree of population inversion, the greater the quasi Fermi level separation the greater the difference between the electron populations (of the conduction band minus the valence band), and the greater the gain. Under electrical injection the quasi Fermi level separation is related to the external forward bias applied to the p-n junction of a laser diode.

The condition for population inversion is derived from considering the photon rate equations for the downward and upward transition of electrons, shown in equations 2.5 and 2.6 respectively. Where  $C$  is a rate constant,  $N_A$  is the number of atoms, and  $N_p$  is the number of photons in the system. The net rate at which photons are added to the mode is given by equation 2.7.

$$\frac{dN_p}{dt} = C \cdot N_A \cdot N_p \cdot f_2 \cdot (1 - f_1) \quad (2.5)$$

$$\frac{dN_p}{dt} = C \cdot N_A \cdot N_p \cdot f_1 \cdot (1 - f_2) \quad (2.6)$$

$$\left[ \frac{dN_p}{dt} \right]^{net} = C \cdot N_A \cdot N_p \cdot (f_2 - f_1) \quad (2.7)$$

Using equation 2.7, the energy added per unit distance to the mode can be written in the form of equation 2.8, where  $v_E$  is the photon energy velocity and  $h\nu$  is the photon energy.

$$\frac{dE}{dL} = \left[ \frac{dN_p}{dt} \right]^{net} \cdot h\nu \cdot \frac{1}{v_E} \quad (2.8)$$

Using equation 2.1, 2.7 and 2.8 the gain can be written in the form of equation 2.9.

$$G = \frac{CN_A}{v_E} [f_2 - f_1] \quad (2.9)$$

It is evident that the electron occupation probability of the upper conduction band must be greater than that of the lower valence band in order to achieve gain. Using equations 2.3 and 2.4 this observation leads to the Bernard and Duraffourg condition, given in equation 2.10 and 2.11. It is additionally evident that a slower photon energy velocity can result in an increased gain, which is further discussed in this work.

$$E_{f2} - E_{f1} > E_2 - E_1 \quad (2.10)$$

$$\Delta E_f > h\nu \quad (2.11)$$

The condition states that for population inversion (gain) the quasi Fermi energy separation between the conduction and valence bands must be greater than the bandgap of the semiconductor, and hence greater than the energy of the photon emitted. When the photon energy is equal to the quasi Fermi energy separation the material is said to be “transparent”, the upward and downward transition rates between a pair of states in the conduction and valence bands are equal, there is no net absorption or gain. The transparency point depends upon the quasi Fermi energy separation. At photon energies above the quasi Fermi energy separation, net absorption occurs, whilst at photon energies below the quasi Fermi energy separation, net gain occurs.

As more carriers are injected or pumped into the conduction band the quasi Fermi level separation continues to increase, with a corresponding increase in net modal gain, until the onset of laser action. The point at which this occurs is referred to as the current threshold. When the Fermi energy separation is large enough, sufficient gain can be provided to match losses. Additional electrons injected recombine in the process of stimulated emission, this increases the photon density and stimulated emission rate, which then increases the probability of recombination, decreasing the number of electrons in the conduction band (relaxation oscillations). At the onset of lasing the Fermi levels of the conduction and valence band are said to be pinned as a result of this.

### 2.2.2 Optical feedback

Optical feedback in a resonant laser cavity is provided by light reflected at the interface between materials with a suitable refractive index contrast. A schema of a laser cavity is shown in figure 2.2.

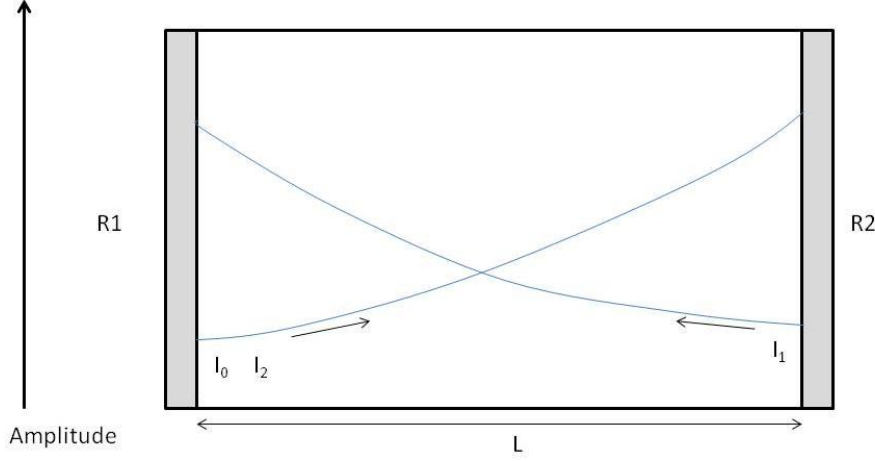


**Figure 2.2:** Schema of a laser cavity used in the derivation of the threshold material gain for the laser round-trip condition.

The threshold material gain that satisfies the round-trip condition for a laser cavity is derived below. The light intensity leaving mirror  $R_2$ , where  $R_2$  is the intensity reflectivity coefficient of the mirror, is derived by considering the change to the initial light intensity  $I_0$ . The light with intensity  $I_0$  is exponentially amplified by the gain material within the cavity over the cavity length  $L$ , but also suffers absorption losses, attributed to the internal optical mode loss  $\alpha_i$ . The material gain coefficient is denoted  $g$ . A confinement factor  $\Gamma$  is also included to account for the proportion of the optical mode within the cavity over-lapping the amplifying gain region. The modal gain is given by the product of the material gain and the confinement factor. Upon reflection with mirror  $R_2$  the amplitude of the light decreases, resulting in light with intensity designated  $I_1$ , given in equation 2.12.

$$I_1 = I_0 e^{(\Gamma g - \alpha_i)L} R_2 \quad (2.12)$$

A second reflection, this time at mirror  $R_1$ , sees light propagating with an intensity  $I_2$ , given in equation 2.13.

$$I_2 = I_1 e^{(\Gamma g - \alpha_i)L} R_1 = I_0 e^{2(\Gamma g - \alpha_i)L} R_1 R_2 \quad (2.13)$$

To form the round-trip lasing condition the gain must match the loss, requiring the intensity of light  $I_2$  to match the intensity of light  $I_0$ , resulting in equations 2.14 and 2.15.

$$I_2 = I_0 \quad (2.14)$$

$$1 = e^{2(\Gamma g - \alpha_i)L} R_1 R_2 \quad (2.15)$$



This results in the round trip threshold gain condition given in equation 2.16. The value of the material gain that satisfies the lasing condition is called the threshold gain, denoted  $g_{th}$ .

$$g_{th} = \left[ \frac{1}{2L} \ln \left( \frac{1}{R_1 R_2} \right) + \alpha_i \right] \frac{1}{\Gamma} \quad (2.16)$$

The threshold gain condition can also be derived through considering the electric field rather than the light intensity (in order to derive the phase condition). In this case a complex propagation constant is used, giving rise to the phase condition in equation 2.17.

$$2\beta L = \pm 2m\pi \quad (2.17)$$

Where  $m$  is an integer and  $\beta$  is the propagation constant given by equation 2.18 The wavevector is given in equation 2.19.

$$\beta = n_{eff} k \quad (2.18)$$

$$k = \frac{2\pi}{\lambda} \quad (2.19)$$

This leads to an expression for the cavity length, given by equation 2.20.

$$L = \left( \frac{\lambda}{2n_{eff}} \right) m \quad (2.20)$$

## 2.3. Nanolasers and plasmonics

### 2.3.1 Laser size reduction

A Laser can be called a nanolaser when its' dimensions are in the order of or below its free space operating wavelength (in at least one, but more often two dimensions). The effective modal volume of a traditional Fabry-Perot laser cannot be smaller than the diffraction limit, given by equation 2.21 (Hill, M. 2007). The limit describes the minimum standing wave condition for the cavity in all three spatial dimensions.

$$V_{eff} > \left[ \frac{\lambda}{2n_{eff}} \right]^3 \quad (2.21)$$

Where  $\lambda$  is the free space wavelength and  $n_{eff}$  is the effective refractive index of the semiconductor material. The use of plasmonic components can, however, lead to a reduction in this allowed modal volume. This condition, together with the length of gain

material required to allow laser action (round-trip gain condition, equation 2.16), places size limits on a traditional laser device. The minimum allowed cavity length occurs when  $m$  is unity in equation 2.20, forming the half wavelength length-limit, given in equation 2.22 (Ning, C.Z. 2010).

$$L_1 = \lambda/2n_{eff} \quad (2.22)$$

$L_1$  can be reduced by using a high effective refractive index, such as that which exists near the surface-plasmon-polariton (SPP) resonance of plasmonic devices. The second length-limit, given in equation 2.23, derives from the round-trip gain condition, equation 2.16.

$$L_2 = \frac{1}{2(\Gamma g_{th} - \alpha_i)} \left[ \ln \left( \frac{1}{R_1 R_2} \right) \right] \quad (2.23)$$

This length limit can be reduced by maximising the material gain, the confinement factor and the mirror reflectivities, and further reduced by minimising optical losses. The ability to engineer the optical confinement factor (and losses) by altering the device geometry has led to a surge of different device architectures for nanoalasers (Oulton, R.F. 2008) (Ma, R. 2013). Although geometrical considerations for confinement and losses can lead to size reduction, further reductions can be made by using new gain materials and, in the case of plasmonics, could one day be reduced through the engineering of lossless metals (Khurgin, J.B. 2015). The extent to which plasmonic losses can be compensated for by gain and changes in geometry (semiconductor slab thickness and dielectric layer thickness) are explored in this work.

The use of metallic components for plasmonic devices can allow the size reduction of the cavity beyond the diffraction limit of light. The free surface electrons of a metal can hybridise with photons forming a quasi-particle called a plasmon. The electrons give additional momentum to the photons, reducing the wavelength of the resultant hybrid particle. Higher surface plasmon frequencies result in higher confinement of the mode. In addition the energy velocity of the mode can be reduced, resulting in a higher gain, as further discussed in section 2.3.3.

### 2.3.2 Small-Cavity quantum electrodynamics

A small modal volume can result in a strong confinement of the electromagnetic field. A strong confinement (lower loss) can lead to a high cavity quality factor,  $Q$ , as defined in equation 2.24. The quality factor is a figure of merit for a cavity which takes into account the cavities spectral width. A smaller spectral width is synonymous with a longer photon lifetime and lower photon decay rate (cavity loss rate). The longer a photon of a given energy survives within the cavity, the smaller the spread of frequencies stimulated within it.

$$Q = \omega/\Delta\omega \quad (2.24)$$

Where  $\omega$  is the angular frequency of the resonant mode and  $\Delta\omega$  is the spectral width of the resonant mode, dependent on the photon loss rate in the cavity.

Furthermore, the altered cavity quantum electrodynamics of a small cavity can lead to an enhanced spontaneous emission rate (Fox, M. 2006). This enhancement is known as the Purcell effect. Spontaneous emission is triggered by zero-point fluctuations of the electromagnetic field (vacuum field). The vacuum field is a randomly fluctuating electric field that is present everywhere. The magnitude of the vacuum field energy of a cavity can be calculated for a given mode volume.

The vacuum field energy is larger for smaller cavities. As the mode volume decreases for a constant photon number, the energy density of the cavity increases, increasing the magnitude of the vacuum field energy, which increases the atom-cavity coupling rate. The atom-cavity coupling rate is a measure of how emitters interact with light fields (for stimulated emission) or vacuum fields (for spontaneous emission). The interaction energy between the atom and cavity vacuum field is given by the electric dipole interaction for the transition. The coupling is determined by the dipole moment, the angular frequency and the modal volume (Fox, M. 2006). The weak coupling regime occurs when the coupling rate is smaller than the loss rate, in which photons are lost from the cavity faster than the characteristic interaction between the atom and the cavity. A high  $Q$  cavity is required for the strong coupling regime.

The magnitude of the vacuum field energy and zero point energy can be derived from considering the quantum harmonic oscillator model using Schrödinger's time independent

wave equation for a photon. One can consider the analogy of an oscillating mass on a spring, illustrated in figure 2.3, to find the potential for the harmonic oscillator.

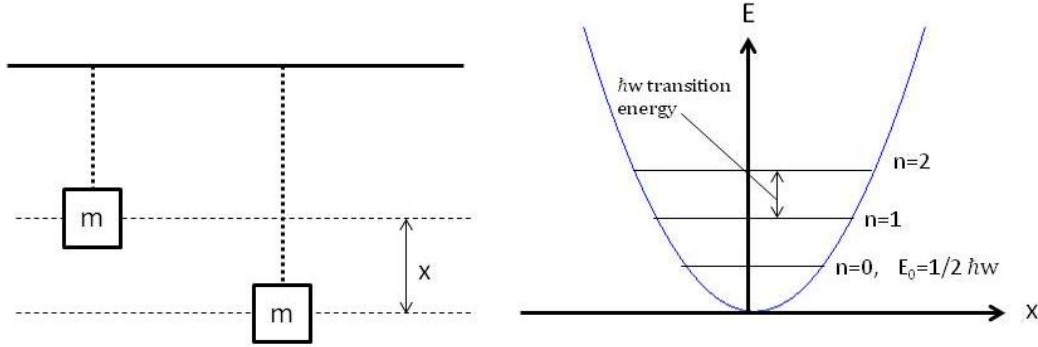


**Figure 2.3:** Left: An illustration of a mass ( $m$ ) suspended on the end of a spring (vertical dotted line) before and after extension in the vertical direction by a distance  $x$ . Right: A schema showing the first few allowed energy states in the quantum harmonic oscillator model, where  $E_n = \left(n + \frac{1}{2}\right) \hbar \omega$ ,  $n = 0, 1, 2 \dots$

The form of the potential for the harmonic oscillator is found from considering Hooke's Law for an oscillating mass on a spring. Hooke's Law for the system is given in equation 2.25.

$$m \frac{d^2 x}{dt^2} = -kx \quad (2.25)$$

Where  $m$  is the mass of the object,  $x$  is the displacement of the object and  $k$  is the spring constant. The right hand side of the equation is equivalent to the force,  $F$ . Using a sinusoidal solution, shown in equation 2.26, the spring constant takes on the form of equation 2.27. It follows that the potential energy is given by equation 2.28.

$$x = x_0 \sin(\omega t) \quad (2.26)$$

$$k = m\omega^2 \quad (2.27)$$

$$V(x) = \int_0^x F dx = \frac{1}{2} kx^2 = \frac{1}{2} m\omega^2 x^2 \quad (2.28)$$

The time independent Schrödinger wave equation for a photon is given in equation 2.29, where the first term represents the kinetic energy, the second term represents the potential energy, and the third term is the total energy.

$$\frac{-\hbar^2}{2m} \frac{d^2 \Psi(x)}{dx^2} + \frac{1}{2} m\omega^2 x^2 \Psi(x) = E \Psi(x) \quad (2.29)$$

The solution for the ground state of the above equation ( $n=0$ ), is given in equation 2.30, where  $C$  is a normalising coefficient and  $\alpha$  is determined below. For solutions higher than the ground state,  $n \geq 1$ ,  $C$  is a function of  $x$ , in which case one must perform normalisation using a Hermite polynomial of order  $n$ .

$$\Psi(x) = C e^{-\alpha \frac{x^2}{2}} \quad (2.30)$$

Using the solution for the ground state, and equating the coefficients of  $x$  in the Schrödinger time independent wave equation, the value of  $\alpha$  can be determined, shown in equation 2.31, leading to the ground state energy, known as the zero point energy, shown in equation 2.32. The full form of the allowed energy states is given in equation 2.33.

$$\alpha = \frac{mw}{\hbar} \quad (2.31)$$

$$E_0 = \frac{\hbar w}{2} \quad (2.32)$$

$$E_n = \left(n + \frac{1}{2}\right) \hbar w, \text{ for } n = 0, 1, 2 \dots \quad (2.33)$$

The vacuum field energy is found by considering the time averaged electromagnetic energy contributions of the electric and magnetic fields in a mode volume,  $V$ , and equating it to the zero point energy per mode. This is shown in equation 2.34. The vacuum field energy is therefore inversely proportional to the mode volume, shown in equation 2.35.

$$2 \int \frac{1}{2} \epsilon_0 E_{vac}^2 dV = \frac{\hbar w}{2} \quad (2.34)$$

$$E_{vac} = \left(\frac{\hbar w}{2 \epsilon_0 V}\right)^{\frac{1}{2}} \quad (2.35)$$

The transition rate for spontaneous emission is given by Fermi's golden rule, which uses the theory of dipole emission. For a large (free-space) cavity the transition rate is dependent upon the density of states for photon modes in free space and the transition matrix element. The transition matrix element is dependent on the electric dipole interaction with the vacuum electric field averaged over all possible orientations of the atomic dipole with respect to the field. A single-mode cavity and free-space clearly have different density of states for photon modes and vacuum field magnitudes.

Fermi's Golden Rule is given in equation 2.36.

$$W = \frac{2\pi}{\hbar^2} |M_{12}|^2 g(w) \quad (2.36)$$

Where  $W$  is the spontaneous emission rate in the cavity,  $M_{12}$  is the electric dipole for the vacuum field interaction and  $g(w)$  is the free space density of photonic states (DOS).

For a volume in  $k$ -space,  $V$ , where  $V=L^3$  the density of photonic states can be calculated. Using equations 2.37 and 2.38, the  $k$ -space wave vector takes the form of equation 2.39 in three dimensions (3D).

$$K = \frac{2\pi}{\lambda} \quad (2.37)$$

$$\lambda = \frac{L}{n} \quad (2.38)$$

$$K_{x,y,z} = \frac{2\pi}{L} (n_x, n_y, n_z) \quad (2.39)$$

The 3D DOS can be derived by considering the number of states within a volume  $k$  to  $k+dk$ , and dividing by the effective volume per  $k$  state, shown in equation 2.40.

$$g(k)^{3D} dk = \frac{4\pi k^2 dk}{\left(\frac{2\pi}{L}\right)^3} = \frac{V k^2}{2\pi^2} dk \quad (2.40)$$

Inserting equation 2.40 into equation 2.36 and taking into consideration that the electric dipole in free space is proportional to the vacuum field energy and therefore inversely proportional to volume, it is clear that the spontaneous emission rate in free space is independent of volume.

However, in the case of a single mode cavity where only one resonant mode exists, the DOS becomes unity, and can be described by a Lorentzian function that is independent of volume. In this case the spontaneous emission rate is inversely proportional to volume.

The Purcell factor,  $F_P$ , given in equation 2.41, is the ratio of the transition rate for spontaneous emission in the cavity,  $W_{cav}$ , compared to the transition rate for spontaneous emission in free-space  $W_{free}$ .

$$F_P = \frac{3Q\left(\frac{\lambda}{n}\right)^3}{4\pi^2 V} \quad (2.41)$$

Purcell factors greater than unity indicate that spontaneous emission is enhanced by the cavity. Enhancement on resonance is related to the large density of states at the cavity mode frequency. The implication of a high Purcell factor is that one can operate with higher losses compared to a conventional laser. A Purcell factor of 6 has previously been obtained for metal-dielectric-semiconductor nanowire structures (Oulton, R.F. 2012).

Furthermore, due to their small size, nanolasers have very few allowed modes, this means that a larger proportion of spontaneous emission is funnelled into the useful (lasing) cavity mode compared to larger devices with many modes. The fraction of spontaneous emission that is funnelled into the useful cavity mode is called the  $\beta$  value, defined in equation 2.42. In nanolasers this value can be close to unity (requiring the Purcell Factor to be much larger than unity), whilst in larger lasers this value can be 100,000 times smaller (Hachair, X. 2011). A high  $\beta$  value can result in a low current threshold.

$$\beta = W_{cav}/(W_{free} + W_{cav}) = F_P/(1 + F_P) \quad (2.42)$$

The slope of a light-current curve for a laser is partly dependent on the efficiency of the spontaneous emission being channelled into the lasing mode. As a device dynamically changes between spontaneous and stimulated emission (at the current threshold for laser action) the slope of the light-current curve becomes steeper due to an increased efficiency. For a  $\beta=1$  laser only one photon needs to be emitted for it to go into the useful mode to trigger stimulated emission, resulting in a light-current curve with no clear change in slope as the device dynamically changes from spontaneous to stimulated emission, the efficiency is already at a maximum. This has given rise to the misleading term “thresholdless” lasers. However, in these lasers there is still a dynamic transition between spontaneous and stimulated emission (Hachair, Braive et al. 2011). Below threshold the dynamics are governed by a slower spontaneous emission rate, and above threshold they are governed by a faster stimulated emission rate.

### 2.3.3 Plasmonics

Plasmonics allows the reduction of the wavelength of light beyond the diffraction limit, allowing the miniaturisation of laser devices and the generation of intense optical fields. Light-matter interactions are strongly enhanced because the plasmonic wavelength is closer

to that of the atomic electronic wavefunction of solids, useful for sensing applications. This section describes plasmonics at a planar metal-dielectric interface, as shown in figure 2.4.

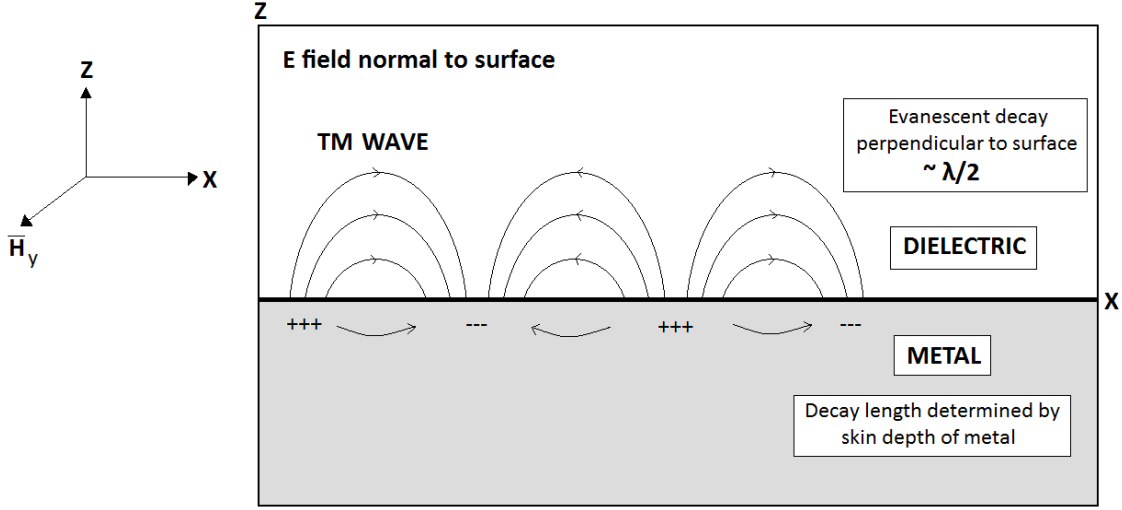


**Figure 1.4: Schema of a metal-dielectric interface. The electric field normal to the surface creates the charge disturbance.**

Plasma oscillations are longitudinal oscillations of electron density in a conducting media. A metal consists of a neutral plasma of negative electrons and positive nuclei. When an electric field is applied across the metal the electrons move to oppose the field, resulting in a polarised sample. The positive atomic nuclei impose a restoring force to the electrons, which over-shoot their original position, resulting in plasma oscillations.

The plasma frequency of a bulk metal can be derived from an equation of motion, equation 2.43, where an electric field  $E$  opposes the displacement of electrons.

$$F = m_0 a = -qE \quad (2.43)$$

Where  $m_0$  is the electron mass and  $q$  is the electron charge, hereafter denoted  $e$ . Using Gauss law, equation 2.44, the electric field can be written for the displacement of a volume of electrons in one direction, over a distance  $U$ .

$$\int E \cdot ds = \frac{1}{\epsilon_0} \sum q = \frac{NeU}{\epsilon_0} \quad (2.44)$$



Where  $N$  is the electron density per unit volume and  $U$  is the displacement of electrons in one direction. Inserting the expression for the electric field into equation 2.43, one can derive the expression given in equation 2.46.

$$\frac{-eNeU}{\epsilon_0} = m_0 \frac{d^2U}{dt^2} \quad (2.45)$$

$$\frac{d^2U}{dt^2} + \left[ \frac{Ne^2}{\epsilon_0 m_0} \right] U = 0 \quad (2.46)$$

The above equation has the form of a simple harmonic oscillator, where the bulk plasma frequency,  $w_p$ , is given in equation 2.47 (in radians).

$$w_p = \left[ \frac{Ne^2}{\epsilon_0 m_0} \right]^{1/2} \quad (2.47)$$

The surface plasma frequency (SP),  $w_{sp}$ , further takes into consideration the structure geometry. A schema of a planar metal-dielectric interface, studied in this work, is shown in figure 2.5.



**Figure 2.5: Cross-section of planar metal-dielectric interface. Layers extend in the x-y plane, with a layer thickness in the z direction.**

The surface plasma frequency for the planar metal-dielectric interface is given in equation 2.48.

$$w_{sp} = \frac{w_p}{\sqrt{\varepsilon_M + \varepsilon_D}} \quad (2.48)$$

Where  $\varepsilon_M$  is the background permittivity of the metal and  $\varepsilon_D$  is the background permittivity of the dielectric. The real component of the metal permittivity is negative.

The surface plasma frequency for the structure is a solution to the Laplace equation, equation 2.49, where  $\phi$  is the electric potential.

$$\nabla^2 \phi = 0 \quad (2.49)$$

The surface plasma frequency is derived by considering a wave travelling at the interface of the materials. The wave is wavelike in the  $x$  direction and exponentially decaying in the  $Z$  direction. The wave functions are shown in equation 2.50 and 2.51, where the boundaries are referenced to figure 2.5.

$$Z > 0, \phi(Z) = A_M e^{(i\beta x - k_M z)} \quad (2.50)$$

$$Z < 0, \phi(Z) = A_D e^{(i\beta x - k_D z)} \quad (2.51)$$

Where  $\beta$  is a propagation constant and  $A_M$  and  $A_D$  are amplitude coefficients for the metal and dielectric. For continuity of tangential and normal components of dielectric displacement the solution requires that  $k_M = k_D = \beta$ , and continuity of  $\phi$  and  $\varepsilon d\phi/dz$ , as well as  $A_M = A_D$  and  $\varepsilon_M(w) + \varepsilon_D = 0$ . It can be shown that  $w_{sp}$  is the frequency that is satisfied when the free electron dielectric function is put into the dispersion relation for the interface, which is given in equation 2.52.

$$\beta = k_0 \sqrt{\frac{\varepsilon_M \varepsilon_D}{\varepsilon_M + \varepsilon_D}} \quad (2.52)$$

Using equation 2.47, and an electron density for silver of  $5.86 \times 10^{28} \text{ m}^{-3}$ , the bulk plasmon wavelength can be shown to be  $\lambda_p = 138 \text{ nm}$ . For a planar GaAs-oxide to silver interface, used in this work, the surface plasmon wavelength is in the order of  $80 \text{ nm}$ .

Below the surface plasma frequency the coupling strength between electrons and photons is weak. Confinement relies on capacitive optical energy storage effects in which the electric field is confined by the surface charge generated by SPs as they propagate. This uses only surface electrons within the Thomas-Fermi screening distance of the interface. Near the SP

frequency electrons up to the skin-depth of the metal contribute to the momentum of the light, resulting in a larger increase in momentum than possible with capacitive confinement alone (Oulton 2012).

It can be further noted that in this geometry there are six possible electromagnetic components from the Helmholtz wave equation, Transverse Magnetic (TM) components:  $E_x$ ,  $E_z$ ,  $H_y$  and Transverse Electric (TE) components:  $H_x$ ,  $H_z$ ,  $E_y$ . If the EM wave were to be generated far from the interface, for example, in certain gain-material/dielectric/metal configurations, the wave can become unbound from the interface and couple to these possible components. This is further discussed in section 4.2.2.

Only TM solutions are applicable when considering a bound plasmonic wave at the interface. If TE solutions are considered when attempting to find interface modes, continuity of  $E_y$  and  $H_x$  at the interface leads to the condition given in equation 2.53.

$$A_M(k_M + k_D) = 0 \quad (2.53)$$

However, as  $Re[k_1] > 0$  and  $Re[k_2] > 0$  this is only satisfied if  $A_M = 0$ , since  $A_M = A_D = 0$  no TE surface modes can exist.

Management of the optical loss of the structure is of critical importance. The Drude model can be used to describe the loss caused by the metal as a result of electron scattering. Considering the configuration shown in figure 2.5 it is clear that the absorption coefficient of the SPs is partly dependent on the permittivity of the dielectric material. SPs propagate with a lower loss when the planar metal shares an interface with a material of lower permittivity. The SP propagation distance at an air-metal interface can be 40 times larger than that of a semiconductor-metal interface (Oulton 2012). The use of a dielectric gap and a semiconductor gain material to respectively reduce and compensate for the propagation loss is a subject of this work.

The use of a dielectric layer in-between the semiconductor gain material and metal has the advantage of providing additional confinement by utilising the capacitively coupled surface charge confinement mechanism. The surface charge on the metal and polarised semiconductor create a strongly localised field in the dielectric region through capacitive coupling. The resultant hybrid mode has a strong confinement but with reduced loss.

The negative real component of the complex permittivity of the metal is accompanied by an energy dissipating (absorbing) imaginary part causing lossy propagation. This energy dissipation limits the effective propagation length to the  $\mu\text{m}$ -mm range highlighting the need for optical gain. Silver has traditionally been used as a plasmonic metal due to its low loss in the infra-red wavelength range compared to other metals, but also exhibits comparably low loss in the visible range (Maziar, P.N, 2007).

Plasmonics also holds the potential benefit of an increased modal gain due to a reduced average optical energy velocity near metal surfaces. This has previously been referred to as “slow light” (Li, D.B. 2009) (Li, D.B. 2010) (Ning, C.Z. 2010). Slow light is a result of a lower energy velocity within the optical mode as a result of a larger group refractive index. Traditionally the optical power confinement factor has been defined as the ratio of the optical power in the gain region to the total optical power of the mode. The confinement factor acts as a conversion factor between material and modal gain and traditionally can not exceed unity. In plasmonic devices the average energy velocity is reduced due to the interaction with the negative imaginary permittivity of the metal, allowing confinement factors larger than unity and modal gains larger than material gain.

As described elsewhere (Ning, C.Z. 2010) the confinement factor can be derived from considering the energy flux within regions of a structure using Poyntings theorem. This can be done using a structure that has a gain medium (active region) and waveguide. The equation for Poyntings theorem is given in equation 2.54, where  $S$  is the energy flux and  $E$  and  $H$  are the electric and magnetic field vectors respectively.

$$S = E \times H \quad (2.54)$$

The energy flux within the active region can be found from considering the relation given in equation 2.55.

$$\oint S \cdot dS = - \int J \cdot E \, dV = - \int \sigma E \cdot E \, dV \quad (2.55)$$

$$\sigma = -\epsilon_0 c n_b G_{material} \quad (2.56)$$

Where  $J$  is the current density and  $\sigma$  is the conductivity given by equation 2.56, noting that  $n_b$  is the background index of refraction and  $G_{material}$  is the material gain.

The energy flux within the waveguide is proportional to the relation given in equation 2.57.

$$\oint S \cdot dS \propto E X H^* + E^* X H \quad (2.57)$$

The modal gain is proportional to the ratio of the energy flux in the active region and the energy flux within the full waveguide. Using the same co-ordinate system as figure 2.5, the wave in the structure is propagating in the  $x$  direction with transverse guiding in the  $y$ - $z$  plane. The modal gain is therefore proportional to equation 2.58.

$$G_{\text{modal}} \propto \frac{\iint dydz \sigma E^2}{\iint dydz (EXH^* + E^*XH)} \quad (2.58)$$

Using the expression for the conductivity in equation 2.56, and the relationships shown in equations 2.59 to 2.62, an expression for the confinement factor can be found.

$$G_{\text{modal}} = \Gamma G_{\text{material}} \quad (2.59)$$

$$S = [EXH^* + E^*XH] = v_E [\omega_E + \omega_H] \quad (2.60)$$

$$v_{ph} = \frac{c}{n_b} \quad (2.61)$$

$$v_E = \frac{c}{n_g} \quad (2.62)$$

Note that  $\omega_E$  and  $\omega_H$  are the stored energy in the electric and magnetic fields respectively,  $n_b$  is the background index of refractive and  $n_g$  is the group index of refraction. The resulting expression for the confinement factor, equation 2.63, is proportional to the ratio of the phase velocity  $v_{ph}$  in the active region and the energy velocity  $v_E$  of the waveguide.

$$\Gamma = \frac{v_{ph}}{v_E} (\Gamma_0) \quad (2.63)$$

Where  $\Gamma_0$  is the traditional definition of the confinement factor, which is the ratio of the energy in the active region to the energy in the waveguide.  $\Gamma_0$  is always smaller than unity. The prefactor, the ratio of phase and energy velocities, is responsible for confinement factors larger than unity. For a purely dielectric waveguide the energy and group velocities are equal, however, for structures with a large group index and reduced energy velocity the confinement factor  $\Gamma$  can be greater than unity. This is true in structures with strong guiding and high index contrasts. This can result in a modal gain larger than the material gain. A

slow mode experiences more gain per unit length than a plane wave travelling in the uniform medium. The resulting decrease in threshold holds true in both time and space evolution of the mode. However, when considering time evolution it is instead described by a decrease in loss per unit time experienced by the slow mode.

## 2.4. Anodic Oxidation

Anodic oxidation is a suitable method of growing close to atomically flat oxides. Anodic oxidation was first developed in 1963 (Revesz, A.G. 1963), but little progress was made in achieving a low conductivity oxide until 1973 (Logan, R.A, et al 1973). Work continued into the late 1990s in order to improve the grown oxide. Although the use of anodic oxides of GaAs for laser devices are a proven technology, its suitability for use as a thin film in a hybrid-plasmonic architecture has, to the best of my knowledge, not previously been tested. The miniaturisation of devices puts new constraints on various components of devices and the techniques used to fabricate them.

Anodic oxidation has a number of advantages over commonly used oxide deposition techniques such as thermal/e-beam evaporation, sputtering and chemical vapour deposition (CVD). These methods can result in porous films with poor adhesion (Hasegawa, H. 1976). Thermally deposited films often have large grain sizes resulting in thickness variations of a few nanometres, and the methods have a poor thickness controllability, with thickness variations in the order of 5-10 nm measured experimentally. Under correct growth conditions anodic oxides have the potential to be smooth and conformal, with a consistent and controllable thickness. Anodic oxides have been shown to have a higher specific charge transfer resistance compared to thermal and plasma formed oxides (Schmuki, P. 1996), and can out-perform CVD deposited silicon dioxide when used in oxide isolated 50 $\mu$ m stripe lasers (Grove, M.J. 1994). A further technique developed in this work also allows for oxide alignment to other structures using photolithographic or e-beam alignment protocols when working on the nanoscale. Other techniques such as local oxidation using microelectrodes or AFM tips (Chien-Huang, T. 2007) are less efficient at the alignment procedure.

A high control of the oxide thickness is possible in the electrochemical reaction of anodic oxidation because the reaction rate can be precisely controlled by the amount of charge

according to Faraday's law of electrolysis. Equation 2.64 uses Faradays law to quantify oxide growth (Kaneshiro, C. 1975).

$$T = \left(\frac{I}{F}\right) \left(\frac{M}{x}\right) \left(\frac{1}{\rho A}\right) t \quad (2.64)$$

Where  $T$  is oxide thickness,  $I$  is applied current,  $F$  is faradays constant,  $M$  is the molecular weight of GaAs,  $x$  is the number of holes required to oxidise one molecule of GaAs,  $\rho$  is the density of the oxide,  $A$  is the cross-sectional area of the oxide, and  $t$  is the time of oxidation. Equation 2.64 can be re-arranged in order to determine the oxide density using experimental results of oxide thickness and oxidation time. It is commonly accepted that six holes are needed to oxidise one GaAs atom (Kaneshiro, C. 1975). The chemical reaction produces oxides of Ga and As is shown in equation 2.65.



The quality of the oxide and resultant thickness is further dependent upon the make-up of the electrolytic solution, oxide dissolution rate and the bias applied. For etching using an electrical bias the redox potential of the oxidising species, which must overlap with the valence band of the semiconductor (and is dependent upon the PH of the electrolyte), is less critical as the applied electrical bias becomes the dominant method of electron extraction from the valence band. A schema of the GaAs p-n sample in contact with the electrolyte solution can be seen in figure 2.6. The top of the p layer is highly doped in order to ensure a high hole density. When the sample is driven under reverse bias the band bending at the p-electrolyte interface reduces allowing for hole accumulation at the interface which encourages the formation of oxides. Negative oxygen ions in the electrolyte are attracted to the interface forming new compounds when they combine with the "dangling bonds" (holes) at the interface.

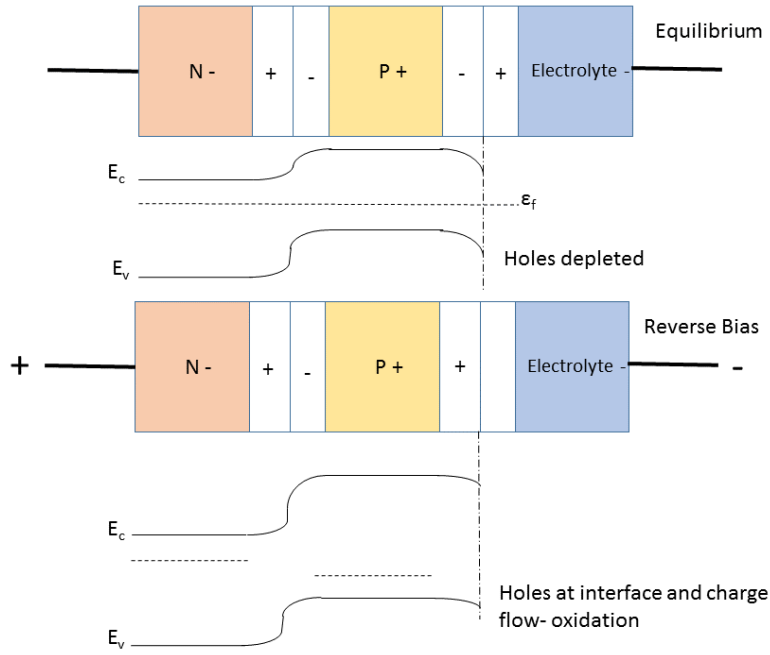


Figure 2.6: schematic band diagram of GaAs p-n sample connected to electrolyte at equilibrium and in reverse bias.  $E_c$  and  $E_v$  are the conduction and valence bands respectively.

#### 2.4.1 Electrolyte Solution

An acid, aqueous solution (AAS), such as those using  $H_2O_2$  was not chosen for this process. The  $H_2O_2$  process lacks stability against small amounts of impurities, resulting in oxidation becoming etching, and is fairly sensitive to the pH of the electrolytic solution (Hasegawa, H. 1975). The grown oxide is not very resilient and is unable to withstand deposition of metals. The acid, glycol, water (AGW) solution has a lower sensitivity to impurities and pH of the solution. The AGW process is more stable, reliable and reproducible. The grown oxide is able to withstand metal deposition and has small leakage currents in the order of  $10^{-11}$  to  $10^{-9}$  A/cm<sup>2</sup> without any annealing, compared to  $10^{-5}$  to  $10^{-6}$  A/cm<sup>2</sup> for AAS processes (Hasegawa, H. 1975). Further to this, interface properties can be improved by annealing in an inert gas atmosphere, reducing charge trap density by a factor up to 15 (Hasegawa, H. 1976). A large reduction in charge trap density with annealing is not seen for deposited oxides, supporting the use of anodic oxidation for low defect interfaces needed for plasmonics.

The glycol in the solution stabilises the oxidation process by striking a balance between growth and simultaneous dissolution of the oxide during formation. This ensures a uniform and dense film. The oxide is less soluble in glycol compared to water, reducing the



dissolution rate, and has a high purity. The use of only water as in the AAS process can result in pit formations in the oxide due to impurities, requires stricter pH controls and is more irreproducible. A small amount of water is used in the AGW process. It acts as the basic anodic oxidant of GaAs. Negative oxygen ions from the water molecules form at the semiconductor-electrolyte interface creating oxide-compounds when combined with positive Ga and As ions. The acid, tartaric acid in this case, is necessary to establish suitable ionic conduction in the electrolyte. The acid is chosen to avoid destructive dissolution. The resultant oxide density is partly dependent upon the choice of acid as it dictates the amount of GaAs consumed for a given thickness of oxide. Tartaric acid results in a consumption of GaAs and formation of oxide with a thickness ratio of approximately 3:4 (Hasegawa, H. 1975).

#### **2.4.2 Oxide density and composition**

The oxidation of GaAs produces Ga-oxides ( $\text{Ga}_2\text{O}_3$ ) and As-oxides ( $\text{As}_2\text{O}_3$ ). The formation of  $\text{Ga}_2\text{O}_3$  and  $\text{As}_2\text{O}_3$  occur simultaneously, and are controlled by the Ga-ion flux and As-ion flux from the GaAs sample. The As-ions have a higher mobility than Ga-ions so form an  $\text{As}_2\text{O}_3$  layer above the  $\text{Ga}_2\text{O}_3$  layer, as sketched in figure 2.7. The chemical composition, uniformity, speed of growth, density and ultimately chemical solubility of the formed oxide depends on the mode of growth. Experimental controls were put in place to obtain the desired mode of growth.

The Ga-ion flux and As-ion flux may either be diffusion controlled or field controlled. The control mechanism is determined by the initial ion flux at the semiconductor-electrolyte interface. A high initial ion flux will result in a diffusion controlled process due to a low ion concentration at the interface. A low initial flux will result in a field controlled process due to the build up of a high ion concentration at the interface. This results in the formation of an initial dense oxide layer due to the high ion concentrations present, which then further supports field controlled oxide formation. The ion transfer rate in the latter case is controlled by the applied potential as ions move along the established field.

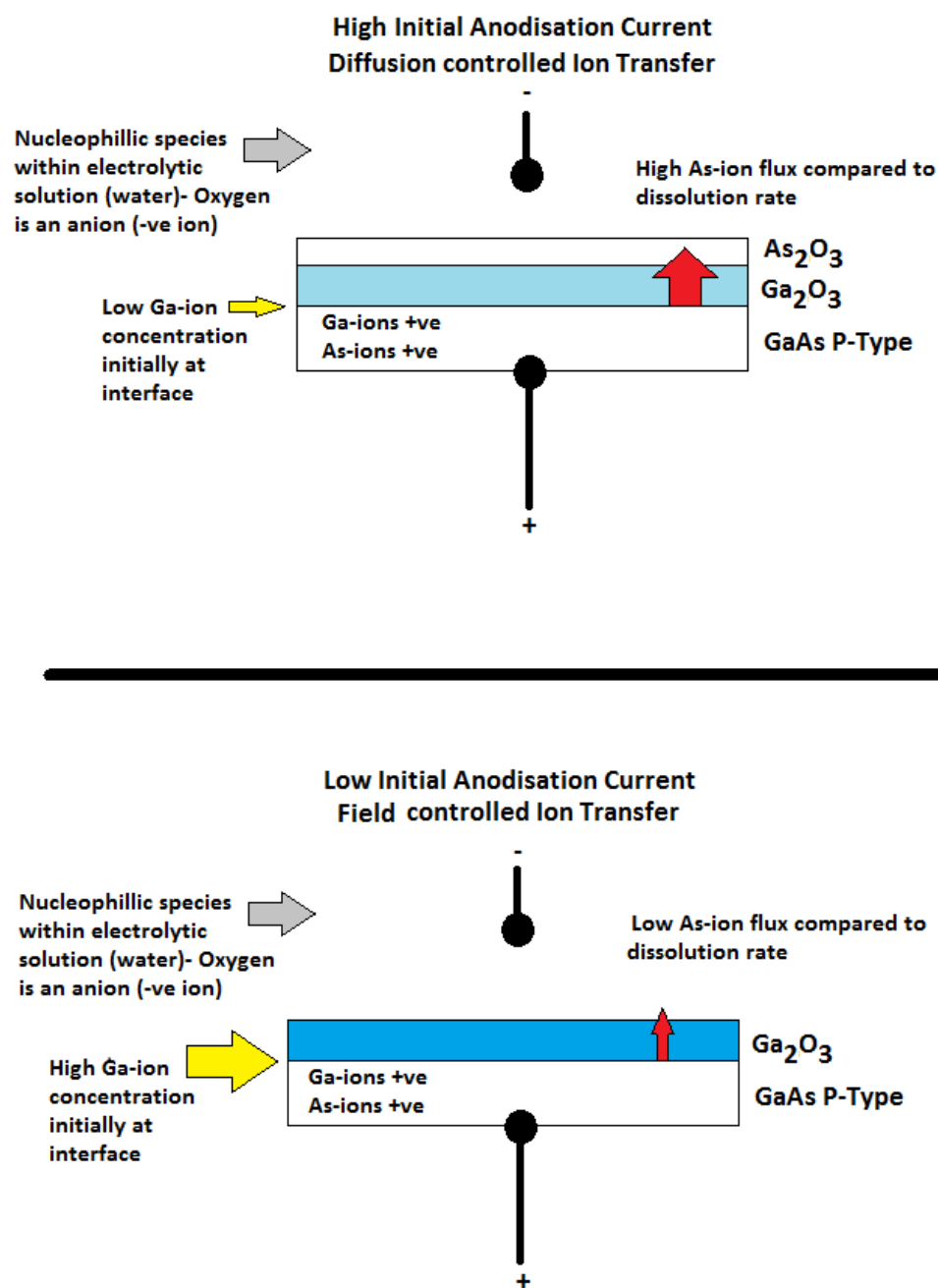


Figure 2.7: Diffusion and field controlled anodic oxidation modes of growth.

The low ion concentration at the interface for the diffusion controlled process results in the formation of a low quality and low density  $\text{Ga}_2\text{O}_3$  layer. In addition to this the upper more highly water-soluble  $\text{As}_2\text{O}_3$  layer remains, making it less useful for practical applications. This layer remains if the As-ion flux is higher than the  $\text{As}_2\text{O}_3$  dissolution rate. This growth/etch balance is sometimes referred to as the active-passive transition of the oxide. If the process is field controlled a dense almost non-water soluble  $\text{Ga}_2\text{O}_3$  layer is formed (Schmuki, P.

1996), with a much higher (40 times higher) specific charge transfer resistance than could otherwise be obtained. The  $\text{As}_2\text{O}_3$  may not remain, dependent on the active-passive transition.

The reduction of the initial ion flux rate is therefore important. The As-ion flux rate must be reduced so that it better matches the dissolution rate of the  $\text{As}_2\text{O}_3$  layer. The Ga-ion flux rate must be reduced to allow a high ion concentration at the interface for the growth of a dense  $\text{Ga}_2\text{O}_3$  layer. The growth of a dense  $\text{Ga}_2\text{O}_3$  film will itself help to reduce the As-ion flux rate.

The ion flux throughout the layers is dependent on the charge transfer resistance of the layers, a layer with a high charge transfer resistance must be formed at the initial stages of passivation. This can be achieved if either a resistive precursor layer is formed due to the chemistry of the electrolyte (under which the lower oxide will grow), or if a low initial anodisation current is used. This is a particular reason for including a potentiometer in the experimental set-up, to allow for a low initial anodisation current. A pulsed voltage supply is also used to ensure  $\text{As}_2\text{O}_3$  dissolution. The dissolution that takes place in the off pulse removes the As-oxide and also removes the less dense  $\text{Ga}_2\text{O}_3$  products. This allows for a denser more uniform  $\text{Ga}_2\text{O}_3$  layer to form.

### **2.4.3 Pulsed voltage mode**

The use of a pulsed voltage source for anodic oxidation produces uniform oxides about ten times faster than constant voltage source (Grove, M.J. 1994). It also allows for a method of real time electrical monitoring of the oxide. In the constant voltage case the high current leads to non-uniform electric fields particularly around edges of samples, causing non-uniform growth. In the pulsed case the non-uniform fields are suppressed even at high currents allowing uniform growth (Grove, M.J. 1994). It has been shown experimentally that for high currents, as the pulse-width is increased (for a fixed repetition rate) the non-uniformity of the oxide increases. The oxide near the edges become thicker. As stated above the use of a pulsed voltage source also allows for etching of the oxide in the off-pulse, which is necessary for the growth of a dense  $\text{Ga}_2\text{O}_3$  layer.

## 2.5 Steam Oxidation Theory

Steam oxidation was investigated as a fabrication technique for the hybrid-plasmonic device. Buried oxidised AlGaAs layers are used for vertical confinement of the optical mode within the hybrid-plasmonic device, and for the formation of a current aperture when under electrical injection. Attempts to electrically inject the hybrid-plasmonic device using very small contact pads were made, resulting in the metal over-heating and burning out, necessitating the use of current apertures.

Further details of the experimental technique of wet steam oxidation can be found in section 3.3.1. Wet oxidation at high temperatures is well understood, the chemistry of the oxidation of AlGaAs at high temperatures can be seen in equation 2.66, showing the formation of  $\text{Al}_2\text{O}_3$  (Asby, C.I.H. 1997).



At high temperatures further reactions occur due to the increased availability of atomic ionised hydrogen, resulting in the dissolution of the  $\text{As}_2\text{O}_3$  compounds, which if remained would increase the volume of the buried layer, causing delamination. The As by-products from the dissolution are removed in the carrier gas used in the experimental technique. The buried layers suffer shrinkage due to the dissolution of material, which can affect the strain of layers surrounding it. The choice of layer thickness and aluminium composition can reduce this strain.

The oxidation rate of AlGaAs can be precisely controlled, and depends on a number of factors, both in the conditions of oxidation and the oxidisable layers themselves. For control and repeatability of lateral oxidation depth the conditions of oxidation and the layers themselves were designed to maintain a reaction rather than a diffusion limited process.

A diffusion rate limited reaction is dependent upon the supply of oxidising species to the oxidation front within the sample, and the removal of etch products. The diffusion and removal of products takes longer with an increasing oxidation depth, resulting in a parabolic dependence on oxidation depth with time. Reaction rate limited processes however do not change with depth of oxidation, but do exponentially increase with temperature (Michell.

G.J. 2010). At very high temperatures with high reaction rates, oxidising species are unable to be supplied to the oxidising front fast enough, which can result in a diffusion limited process. Very high temperatures are avoided for this reason.

The dependence of oxidation rate with temperature, and for different aluminium concentrations  $x$ , in 84 nm thick  $\text{Al}_x\text{Ga}_{1-x}\text{As}$  layers, can be seen in figure 2.8 a. Higher aluminium containing layers oxidise significantly faster than lower aluminium containing layers. The rate also depends on the layer thickness. The rate dependency can be seen in figure 2.8 b for isolated layers. The decrease of oxidation with decreasing layer thickness at a turn-on point is attributed to the increased curvature of the oxidation front within thinner layers which affects the activation energy of the oxidation process (Michell. G.J. 2010) (Naone, R.L. 1997). Although the layers designed in this work are not isolated layers, a precaution was taken to design  $x=0.98$  layers with thicknesses close to the linear regime, at 40 nm. There exists a trade-off between the use of thin high aluminium containing layers and the use of thicker high aluminium containing layers for a constant and higher oxidation rate. To mitigate this compromise thin high aluminium containing layers can be placed next to thicker low aluminium containing layers, which can lessen the curvature front of the thin layers. High aluminium percentage containing layers placed near lower percentage layers act as a feed layer of oxidation species by vertical cross-diffusion, increasing the oxidation rate of the lower layer in proportion to its proximity to the higher layer (Naone, R.L. 1997). For this reason a thicker 1000 nm  $x=0.8$  layer was placed in direct contact with the 40 nm  $x=0.98$  feed layer in the device design.

An inert gas, nitrogen, was used as the carrier gas to ensure control, and to maximise the oxidation rate. In larger than trace amounts molecular oxygen,  $\text{O}_2$ , can result in the reduction of the oxidation rate due to a rapid consumption of atomic hydrogen (Asby, C.I. H. 1997), which is required for oxidation to occur. Figure 2.8 c shows the oxidation extent against time for different carrier gases. The carrier gas was set to 3l/min flow and bubbler temperature to 90°C to ensure a high oxidation rate in a regime of saturation, as shown in figure 2.8 d. This ensures that small fluctuations in carrier gas flow have little effect on the oxidation rate.

The buried AlGaAs layers, once oxidised, can exhibit a high resistivity suitable for current apertures and a low refractive index suitable for optical confinement, reported to be in the region of 1.6 (at 633 nm) (Sfigakis, F. 2000) depending on composition. Both of these qualities are required for application in the hybrid-plasmonic device.

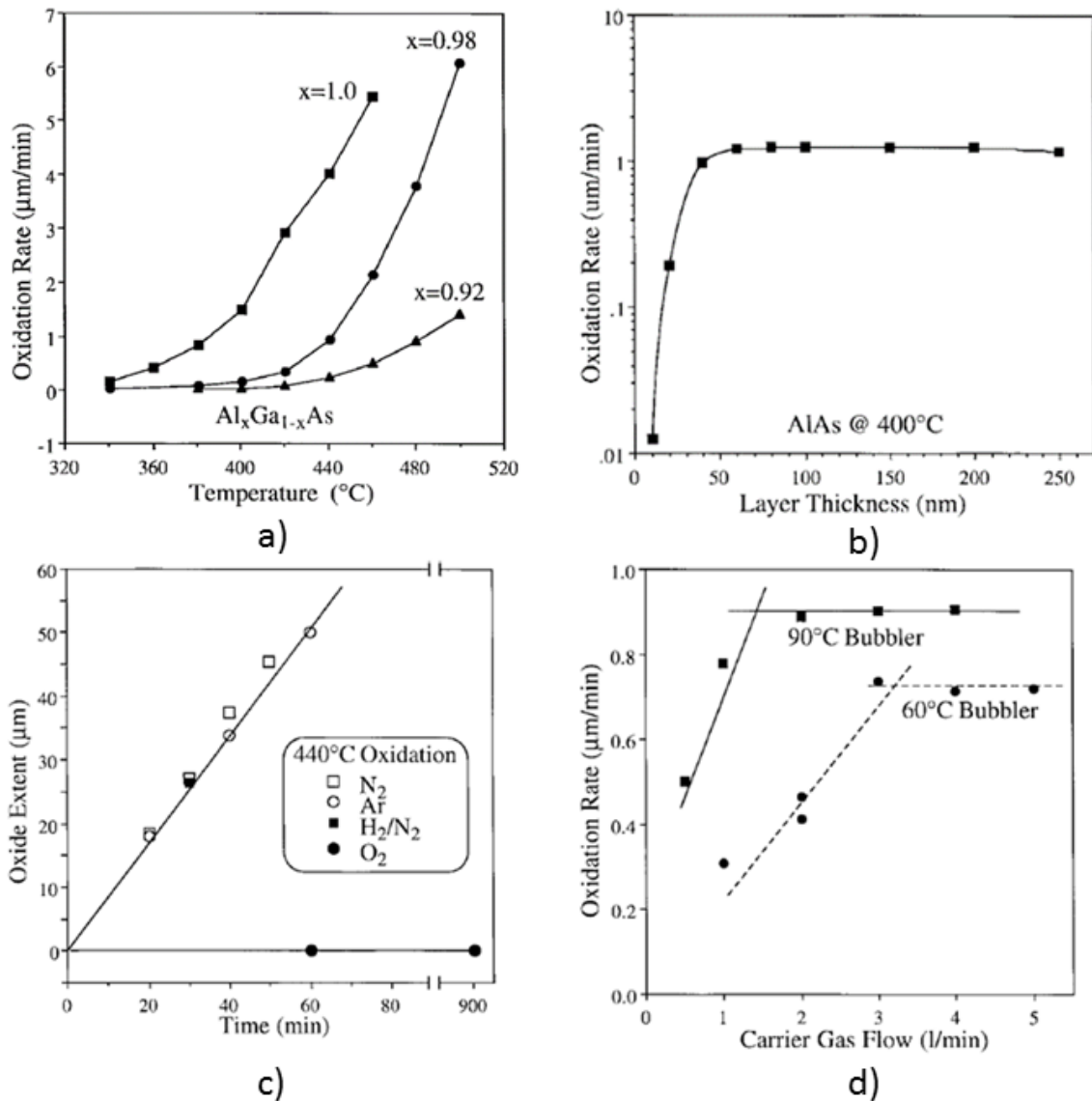


Figure 2.8: Data for 84 nm  $\text{Al}_x\text{Ga}_{1-x}\text{As}$  layers produced by Choquette et al (Choquette, K.D. 1997). a: Oxidation rate as a function of temperature for various aluminium concentrations,  $x$ . b: Oxidation rate dependence on layer thickness at  $400^\circ\text{C}$  for an  $x=0.98$  layer. c: Oxide extent dependence on carrier gas with time for an  $x=0.98$  layer. d: Oxidation rate dependence on carrier gas flow at different bubbler temperatures for an  $x=0.98$  layer.

## 2.6 Distributed Bragg Reflectors

This section briefly describes the theoretical principle behind distributed Bragg reflectors (DBRs). The structures designed and fabricated are further described in section 5.2.4. A DBR, sometimes referred to as a one dimensional photonic crystal, is made up of multiple layers with a periodically alternating refractive index. The reflection of light at each interface can be described using Bragg's law, illustrated in figure 2.9. The reflections at each interface must be in phase and constructively interfere to obey the Bragg condition, given in equation 2.67.

$$2d\sin\theta = mn\lambda \quad (2.67)$$

Where  $d$  is the layer thickness,  $\theta$  is the angle of incidence,  $n$  is the refractive index,  $\lambda$  is the wavelength and  $m$  is the order of the wavelength.

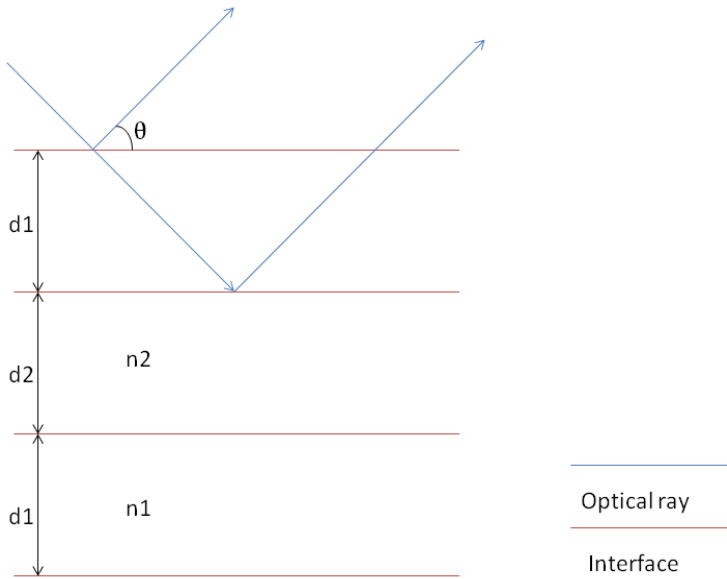


**Figure 2.9:** Schema showing the reflections at the interfaces of a multi-layer DBR structure, with layer refractive indices  $n_1$  and  $n_2$ , layer thicknesses  $d_1$  and  $d_2$ , and incident light hitting the surface at an angle  $\theta$ .

A computer simulation was written in order to aid in the design of a DBR with suitable dimensions. The model utilises the quarter wave stack condition. Partial reflection takes place at each interface across  $N$  pairs of layers, where the alternating layers have refractive indices of  $n_1$  and  $n_2$  and thicknesses of  $d_1$  and  $d_2$  respectively. The optical path length through each layer is matched to the quarter wave condition, given in equation 2.68.

$$n_1 d_1 = n_2 d_2 = \frac{\lambda}{4} \quad (2.68)$$

The width of the reflectivity spectrum is termed the stop-band. The width of the stop-band is determined by the ratio of the refractive index of each layer,  $n_1/n_2$ , a larger ratio results in a broader stop-band, and therefore a high reflectivity over a broader range of wavelengths. The peak magnitude of the stop-band is determined by the number of layer pairs,  $N$ . The field reflectivity is calculated through the Fresnel equations, and is given in equation 2.69.

$$\hat{r} = \frac{n_2 - n_1}{n_2 + n_1} = \sqrt{R} \quad (2.69)$$

The model was written in Matlab code using a Transfer Matrix Method which solves the electric and magnetic fields at the boundaries. It was observed that after four periods (layer pairs) the incremental increase in reflectivity begins to saturate, negating the benefit of additional periods. It was observed that an increase in the order of the wavelength,  $m$ , shown in equation 2.70, decreases the stop-band width and the maximum reflectivity.

$$n_1 d_1 = \frac{\lambda}{4} m \quad (2.70)$$

However, higher orders are often used in order to make fabrication more practical, in which structures of thickness  $d$ , given in equation 2.71, must be patterned and etched.

$$d = \frac{m\lambda}{4n} \quad (2.71)$$

## Chapter References

Asby, C.I.H.; Sullivan, J.P.; Choquette, K.D.; Geib K.M.; Hou H.Q. (1997). "Wet oxidation of AlGaAs: the role of hydrogen", *Journal of Applied Physics*, 82.

Baba, T. (2004). "Observation of fast spontaneous emission decay in GaInAsP photonic crystal point defect nanocavity at room temperature." *Applied Physics Letters* 85(18): 3989-3991.

Blood, P. (2015). *Quantum confined laser devices*, Clarendon Press Oxford.



Chien-Huang, T. (2007). "Tip-induced local anodic oxidation on p-GaAs surface with non-contact atomic force microscopy," *Applied Surface Science*, no. 254: 1357-1362

Choquette, K.D.; Geib, K.M.; Ashby, C.I.; Twesten, R.D.; Blum, O.; Hou.H.Q.; Follstaedt, D.M.; Hammons, B.E.; Mathes, D. Hull, R. (1997). "Advances in selective wet oxidation of AlGaAs alloys." *Journal of Selected Topics in Quantum Electronics*, 3 (3).

Coldren, L. (1995). *Diode Lasers and Photonic Integrated Circuits*, Wiley-Interscience

Fox, M. (2006). *Quantum Optics: An introduction*, Oxford University Press.

Grove, M.J. (1994). "Pulsed anodic oxides for IIIV semiconductor device fabrication," *Applied Physics Letters* 76: 587.

Hachair, X. (2011). "Identification of the stimulated-emission threshold in high-beta nanoscale lasers through phase-space reconstruction." *Physical Review A* 83(5): 053836.

Hasegawa, H.; Forward, K.E.; Hartnagel, H. (1975). "Improved method of anodic oxidation of GaAs," *Electronics Letters* , 11 (3): 53-54

Hasegawa, H.; Hideki. (1976). "Anodic Native Oxidation of GaAs by AGW process," *Bulletin of the faculty of engineering, Hokkaido University* (79): 79-88.

Hill, M. T. (2007). "Lasing in metallic-coated nanocavities." *Nat Photon* 1(10): 589-594.

Kaneshiro, C.; Sato, T.; Hasegawa,H. (1975). "Electrochemical etching of Indium phosphide surfaces studied by voltammetry and scanned probe microscopy", *Japanese journal of applied physics*, 38-2B, 1147.

Khurgin, J. B. (2015). "How to deal with the loss in plasmonics and metamaterials." *Nat Nano* 10(1): 2-6.

Li, D. B.; Ning, C.Z. (2009). "Giant modal gain, amplified surface plasmon-polariton propagation, and slowing down of energy velocity in a metal-semiconductor-metal structure." *Physical Review B* 80(15): 153304.

Li, D. B.; Ning, C.Z. (2010). Novel features of the confinement factor in a plasmonic waveguide. *Photonics Society Winter Topicals Meeting Series (WTM)*, 2010 IEEE.

- Li, D. B.; Ning, C.Z. (2010). "Peculiar features of confinement factors in a metal-semiconductor waveguide." *Applied Physics Letters* 96(18): 181109.
- Logan, R.A; Schwarz, B; Sundberg, W.J. (1973). *Electrochem Soc* 120: 1385
- Ma, R.M. (2013). "Plasmon lasers: coherent light source at molecular scales." *Laser & Photonics Reviews* 7(1): 1-21.
- Maziar, P.N. (2007). "Active and passive plasmonic devices", PhD thesis. UC San Diego.
- Michell, G.J. (2010). "Characterisation and advanced applications of the steam oxidation of AlGaAs", PhD Thesis, Cardiff University.
- Naone, R.L.; Coldren, L.A. (1997). "Surface energy model for the thickness dependence of the lateral oxidation of AlAs." *Journal of Applied Physics*, 82.
- Naone, R.L.; Hegblom, E.R.; Thibeault, B.J.; Coldren, L. (1997) "Oxidation of AlGaAs layers for tapered apertures in vertical cavity lasers." *Electronics Letters*, 33.
- Ning, C. Z. (2010). "Semiconductor nanolasers." *physica status solidi (b)* 247(4): 774-788.
- Oulton, R. F. (2012). "Surface plasmon lasers: sources of nanoscopic light." *Materials Today* 15(1–2): 26-34.
- Oulton, R. F. (2008). "Confinement and propagation characteristics of subwavelength plasmonic modes." *New Journal of Physics* 10(10): 105018.
- Revesz, A.G.; Zaininger, K.H, J. (1963). *American Ceramis Soc.* 118: 606
- Schmuki, P.; Buchanan, M.; Mason, B. F.; Sproule, G. I.; Graham, M. J. (1996). "Thickness measurements of thin anodic oxides on GaAs using atomic force microscopy, profilometry, and secondary ion mass spectrometry." *Applied Physics Letters*, 68: 2675-2677
- Sfigakis, F.; Paddon, P. (2000). "Near-infrared refractive index of thick, laterally oxidised AlGaAs cladding layers." *Journal of Lightwave Technology*, 18 (2).

# Chapter 3. Experimental Techniques

## 3.1. Introduction

This chapter describes the experimental techniques and methods used in the growth and characterisation of the grown oxide of GaAs, the buried AlGaAs, and varied device characterisation techniques. These include the shifting excitation spot experiment and the variable stripe length experiment.

## 3.2. GaAs-Oxide Growth and Characterisation

This section describes the experimental techniques used in the growth and characterisation of GaAs-oxide. Apparatus were designed and constructed in order to grow GaAs-oxide using an electrochemical process of anodisation. Spectroscopic ellipsometry and atomic force microscopy were used to characterise the thickness and topography of the grown films. Transmission line measurements were performed on electrical contacts. Metal-oxide-semiconductor-metal structures were fabricated in order to study the electrical properties of the grown oxide via current-voltage-temperature measurements.

### 3.2.1 Anodic Oxidation

The theory relating to the growth of GaAs-oxide using an electrochemical process of anodisation can be found in section 2.4. The oxide was grown in a pulsed voltage mode using an acid-glycol-water electrolytic solution (Hasegawa, H. 1975) (Grove, M.J. 1994). A schema of the constructed apparatus can be seen in figure 3.1.

The anodic oxide was grown on the p doped GaAs contact layer of pn heterostructure laser material. Prior to growth native oxide was removed using a solution of deionised (DI) water: ammonia at a ratio of 20:1.

The samples were held by vacuum suction within an electrochemical cell. The p doped GaAs side of the sample (anode electrode) was held in contact with the electrolytic solution via the formation of a liquid meniscus. The electrolytic solution consisted of deionised (DI) water: glycol at a ratio of 1:2, with tartaric acid dissolved to a molarity of 0.02 mol/L. A platinum wire was submerged within the electrolytic solution to act as a cathode electrode.

A constant voltage supply was converted into a pulsed voltage supply by using an in-house switching circuit, triggered by a signal generator. The switching circuit was made by Mr Rob Tucker, Cardiff University, using a metal-oxide-semiconductor field effect transistor (MOSFET). The oxides were grown at a pulse frequency of 50 Hz with a pulse width of 1000  $\mu$ s, a potentiometer was used to aid the control of the starting anodisation current for reasons detailed in section 2.4.

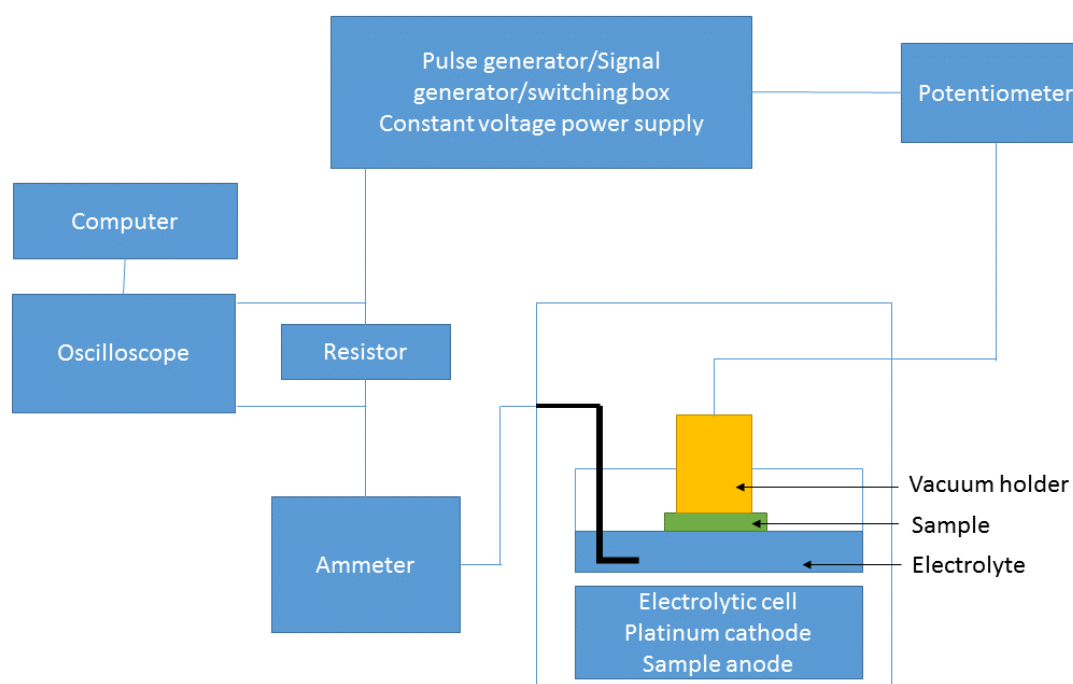


**Figure 3.1: Schema of constructed anodic oxidation apparatus.**

The sample was driven under reverse bias to form a high hole density at the p-GaAs-electrolyte interface. This enabled Ga and As ions at the interface to lose electrons, producing positive Ga and As ions with associated dangling bonds. Nucleophilic species in the electrolyte (in the form of negative oxygen ions) combined with the dangling bonds to create a new chemical compound of Ga and As oxides.

Real-time measurement of the growth of the oxides was made by monitoring the change in the current pulse after the circuit load. The current pulse was measured across a resistor using a probe and oscilloscope, connected to a computer using Tektronix “open-choice” software. The current pulse decreased as a result of the increasing oxide resistance with oxide thickness. Figure 3.2 shows the voltage switching pulse in orange, and the measured current pulse in blue. Capacitance associated with the MOSFET switching circuit caused a

slow rise in the leading edge of the switching pulse, however, this had no observable detriment to the current pulse.

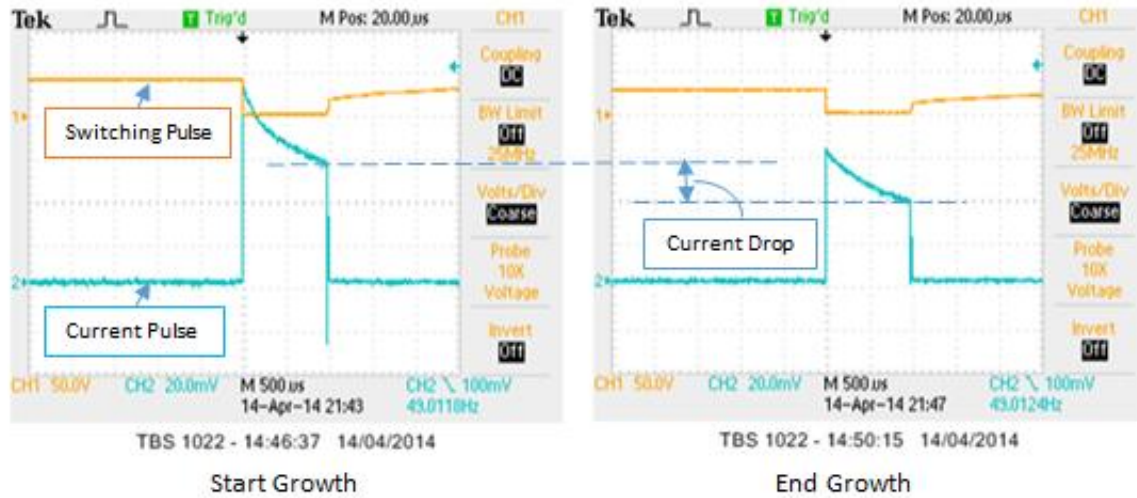


Figure 3.2: Decrease in amplitude of current pulse (blue) after oxidation, used for real time monitoring of oxide growth. Images processed using Tektronix open-choice software.

### 3.2.2 Atomic Force Microscopy

An Atomic Force Microscope (AFM), Veeco Multimode IIIa model (Veeco, 1996) was used to determine the surface roughness and topography of the Anodic Oxide. A schema of a typical AFM set-up can be seen in figure 3.3.

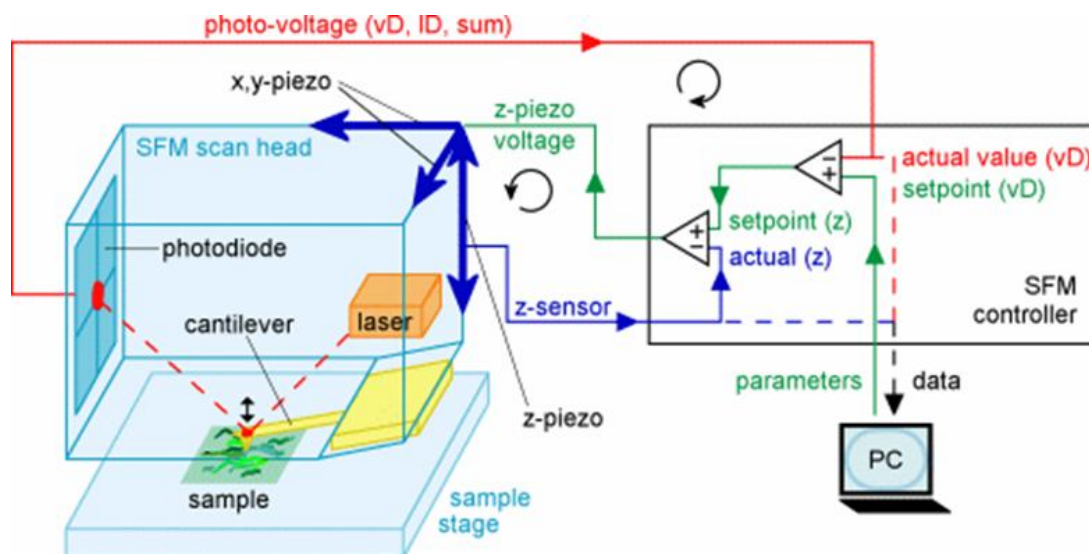
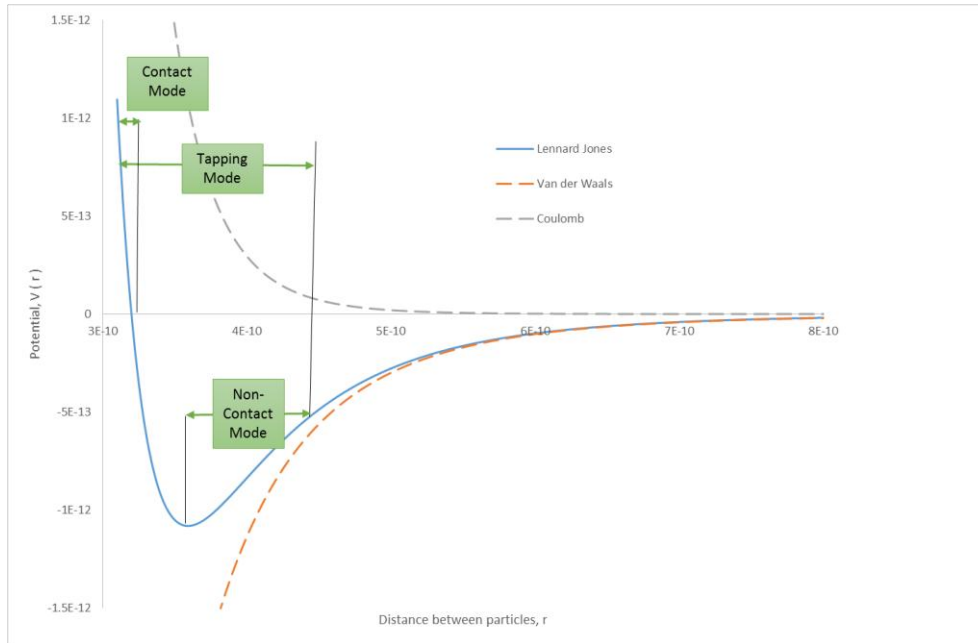


Figure 3.3: Schema of typical AFM apparatus (Kas, J.A. 2015).

An AFM has numerous modes of operation, including contact mode, non-contact mode and tapping mode. Tapping mode was used to maintain good resolution whilst avoiding the surface damage that can be produced using contact mode

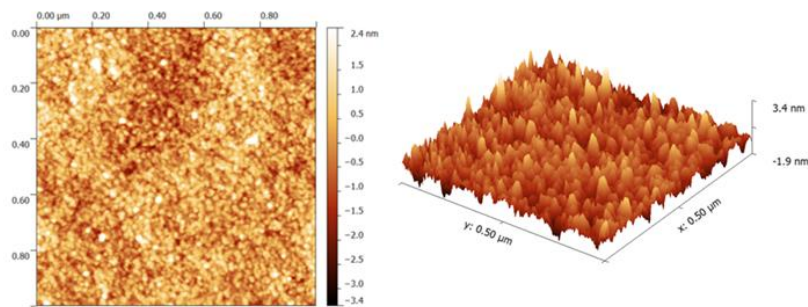
The samples were placed on a piezoelectric x,y,z stage. A cantilever, set to oscillate close to its resonance frequency, was placed above its surface. The sample was brought close to the cantilever to allow the cantilever tip to touch the surface of the sample at the far extent of its oscillation. The cantilever was rastered across the set scan area. As the topography of the sample surface changes so do the atomic forces acting upon the cantilever, altering its oscillation amplitude. The change in oscillation of the cantilever is detected by a laser beam reflected from the back of the cantilever, which is detected by a split-photodetector. The difference in the signal falling on the sections of the photodetector is used as feedback. The voltage applied to the piezoelectric in the vertical z direction is changed accordingly to maintain a constant oscillation frequency. The change in voltage applied is used as a measure of the topography of the underlying surface.

The resolution that can be obtained is dependent on both the mode of operation and the limitations of the cantilever-laser system. The mode of operation affects the atomic forces acting upon the cantilever affecting the resolution that can be achieved. The Lennard-Jones potential, shown in figure 3.4 with arbitrary units, is a combination of the two dominating forces acting upon the cantilever, namely the attractive van der Waals force and repulsive Coulomb force (Kas, J.A. 2015). An increased height resolution can be achieved where the potential slope is steeper, this is because the cantilever will bend under a larger force with a smaller change in tip-sample distance. The cantilever-laser system also affects the resolution achievable. The smallest displacement a split-photodiode can detect is generally in the order of 10 angstroms (Howland, R. 1998), however, the ratio of the path length between the cantilever and detector and the length of the cantilever itself causes a mechanical amplification, allowing for sub-angstrom resolution in height displacement. The lateral resolution, routinely in the order of 50 angstroms, is dependent on both the minimum radius of the cantilever tip and the step size when rastering. The interaction area between the tip and sample is a fraction of the tip radius, allowing for resolution smaller than the tip radius.



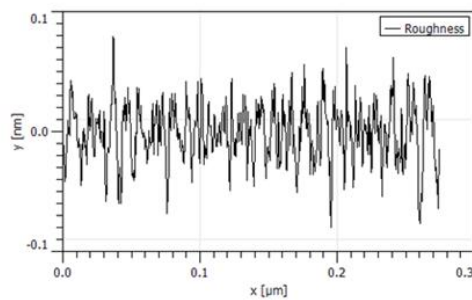
**Figure 3.4:** AFM modes of operation indicated using an example of a Lennard-Jones potential curve in arbitrary units.

Gwyddion open-source software was used to plot the recorded AFM data, and to analyse the surface roughness and topography of the grown oxides. A scan example can be seen in figure 3.5.



AFM scan image of 6.9nm thick anodic oxide

Three dimensional view of AFM scan image



Roughness profile using Gwyddion software

**Figure 3.5:** AFM data processed using Gwyddion software for a 6.9nm thick anodic oxide.

### 3.2.3 Spectroscopic Ellipsometry

A J.A. Woollam spectroscopic ellipsometer was used to determine the thin film thickness of the anodic oxide layers. Laser light of a known polarisation was directed onto the sample. In a multi-layered structure the light is reflected and refracted at each interface, interfering under a process of superposition, with a resultant change in polarisation. The polarisation, measured using a rotating polariser and detector, is dependent upon the thickness and optical constants of the layers, a schema of the polarisation change can be seen in figure 3.6. Polarisation change is measured as an amplitude ratio ( $\psi$ ) of the input to the collected light intensity and their difference in phase ( $\Delta$ ). Sub monolayer thickness resolution is achievable due to the sensitivity of the change in the phase of the light (Woollam, J.A. 2015).

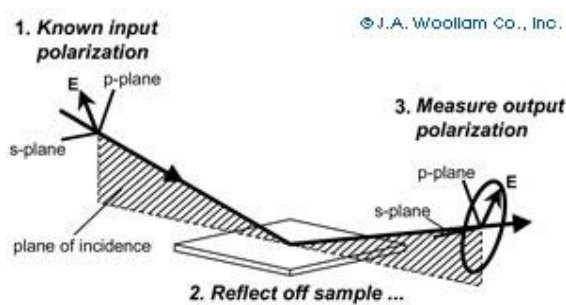


**Figure 3.6:** Schema showing the change in the polarisation of light after reflection from a surface. The polarisation change is used as a measure in spectroscopic ellipsometry (Woollam, J.A. 2015).

The J.A. Woollam complete-ease software allows the user to build a model of the multi-layered structure with estimates of the thicknesses and optical constants of each layer. Simulation software calculates the predicted response of incident light using Fresnel equations at each interface. Regression analysis is used to vary unknown parameters to improve the fit between experimental and calculated data. Oscillator theory is used within the software for absorbing layers.

An example of a fit achieved using the Cody-Lorentz model, which includes terms to describe bandgap energy, can be seen in figure 3.7. The figure shows data for an anodic oxide, grown on a multi-layered structure, with a fitted oxide thickness of 183nm. This was consistent with a surface profilometer depth measurement of 180nm +/- 5nm.



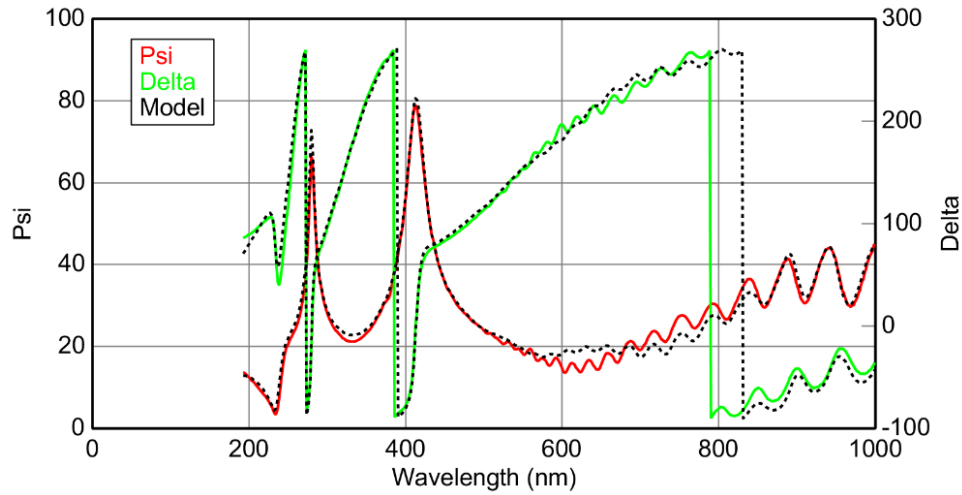


**Figure 3.7:** Fit of simulated and experimental SE data for anodic oxide grown on a laser structure. Psi is the amplitude ratio of the input to the collected light intensity and Delta is their difference in phase.

### 3.2.4. Metallisation transmission line measurements

The metallisation of the fabricated nanosquare devices were tested in order to determine if the contacts were Ohmic or Schottky, and to determine the specific contact resistivity of the contacts. Transmission line measurements (TLM) were used to measure resistances using a Keithley current source and a probe station in order to determine the specific contact resistivity of the metal contacts.

Test structures were fabricated consisting of annealed metal contacts on the semiconductor surface, patterned with varying spacing,  $L(n)$ , and a fixed width  $W$ , perpendicular to the direction of current flow. A schema of the test structures can be seen in figure 3.8.

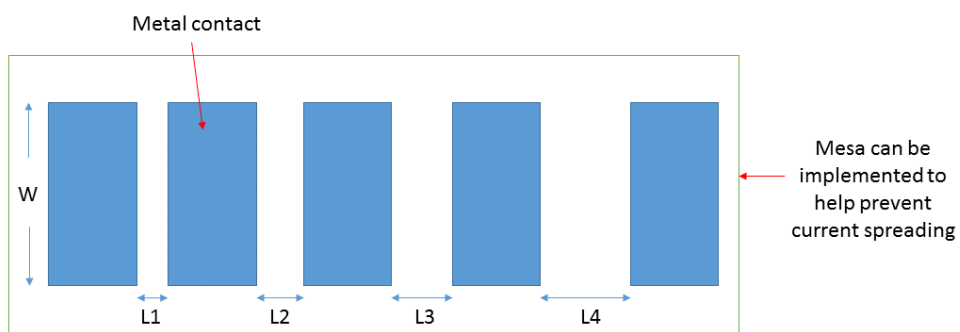


**Figure 3.8:** Schema of TLM structures, not to scale.

A constant current was set between two pads, and the voltage dropped between them was measured. A four probe TLM measurement was used instead of a two probe measurement.

For two probe measurements each probe acts as a current and a voltage probe. The total resistance measured would in this case be the sum of the resistance associated with the probes and the contact of the probes to the metal, and the resistance of the metal semiconductor contact and the semiconductor itself. These resistances associated with the measurement are schematically shown in figure 3.9. In a two probe measurement finding the metal semiconductor contact resistance independent of the probe resistance is not possible with great accuracy. For a four probe measurement the voltage is measured with two additional probes, whilst the current path is identical to that of the two probe measurement. The voltage measuring probes still contain probe resistance ( $R_p$ ) and probe to metal resistance ( $R_{p-m}$ ), but carry a very small current due to the high input impedance (10 M $\Omega$ ) of the Keithley, so the voltage drops across the  $R_p$  and  $R_{p-m}$  are very small and can be neglected (which is not the case for two probe measurement). The measured voltage is just that of the metal-semiconductor junction and the semiconductor, therefore eliminating parasitic voltage drops.

The four point TLM method takes into account the probe resistance,  $R_p$ , the contact resistance of the probe to the metal contact,  $R_{p-m}$ , the metal to semiconductor resistance,  $R_{m-s}$ , and the semiconductor sheet resistance,  $R_s$ .

The semiconductor sheet resistance is contained within the expression for the semiconductor resistance  $R_{semi}$  (equation 3.1) and can be understood by taking a slab of semiconductor material with length  $L$ , width  $W$ , thickness  $t$  and resistivity  $\rho$ . Considering the resistance between two ends of the slab, and taking a cross-section area of this slab ( $tW$ ), it is possible to see that  $L/W$  has no units, meaning  $\rho/t$  has units of ohms, although by itself is not the resistance. This ratio is therefore given units of ohms/square, and is named the sheet resistance,  $R_s$ .

$$R_{semi} = \frac{\rho}{t} \frac{L}{W} = R_s \frac{L}{W} \quad (3.1)$$

According to the equivalent circuit model, the total resistance  $R_T$  as a function of length between the pads  $L(n)$ , can be written in the form of equation 3.2.

$$R_T(L(n)) = 2R_{m-s} + R_s \frac{L(n)}{W} = \frac{V}{I} \quad (3.2)$$

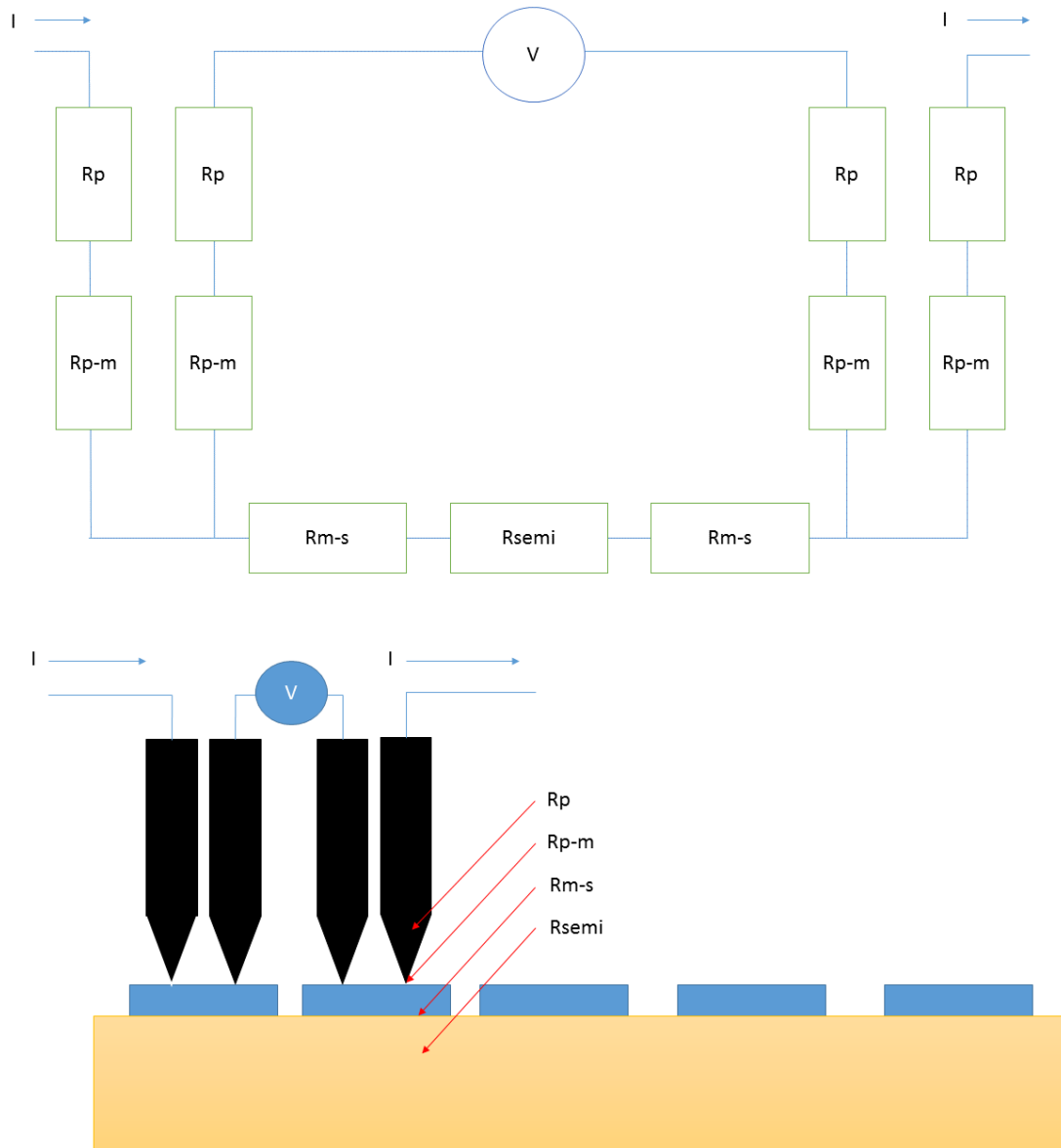


**Figure 3.9: Top: Schema circuit of resistances associated with TLM measurements. Bottom: Schema drawing of cross-section of TLM device showing source of resistance.  $R_p$  is the probe resistance,  $R_{p-m}$  is the probe to metal resistance,  $R_{m-s}$  is the metal to semiconductor resistance and  $R_{semi}$  is the semiconductor resistance.**

$R_T(L(n))$  can be plotted against  $L(n)$ . The series resistance of the semiconductor can be found from the slope of the linear plot. The metal-semiconductor contact resistance can be calculated from the y-intercept.

There is a transfer length  $L_T$  within which the current transfers from the metal to the semiconductor. This can be found when  $R_T$  is zero, where the value on the x axis is  $2L_T$  by interpolation. The metal-semiconductor resistance is given by equation 3.3

$$R_{m-s} = \frac{\rho}{t} \frac{L_T}{W} = R_s \frac{L_T}{W} \quad (3.3)$$

Equation 3.4 is formed from inserting equation 3.3 into equation 3.2.

$$R_T(L(n)) = \frac{R_s}{W} (2L_T + L) \quad (3.4)$$

From equation 3.2, setting  $L=0$ , equation 3.5 can be formed, and the specific contact resistivity is given by equation 3.6 (Schroder, D.K. 2006).

$$R(L = 0) = 2R_{m-s} = 2R_s \frac{L_T}{W} \quad (3.5)$$

$$\rho_{m-s} = R_{m-s} W L_T = R_s L_T^2 \quad (3.6)$$

### 3.2.5. Current-voltage-temperature diode measurements

Metal-insulator-semiconductor-metal (MISM) structures were fabricated in order to perform current-voltage measurements across the grown anodic oxide as a function of temperature.

Anodic oxide was grown in pads of various dimensions and thicknesses. Exposed surface metal in contact with the electrolyte during the electrolytic growth procedure can result in a variation of oxide thickness across the sample due to current leakage paths. Figure 3.10 is an optical microscope image of a sample with a variation of oxide thickness across its surface. For this particular sample bottom metal contact pads were deposited before oxide growth and then coated in resist to prevent current leakage paths, however, uncoated transmission line measurement (TLM) pads out of shot to the left hand side of the image were also present. The variation in thickness of the oxides is apparent by the colour change due to thin film interference. This was calibrated using a height profilometer and spectroscopic ellipsometry. The thicknesses can be very roughly estimated from the colours. From right to left the oxide thickness decreases approximately from 130nm (light blue) to 100nm (royal blue) to 80nm (dark violet) to 50nm (brown) (Hasegawa, H. 1976).

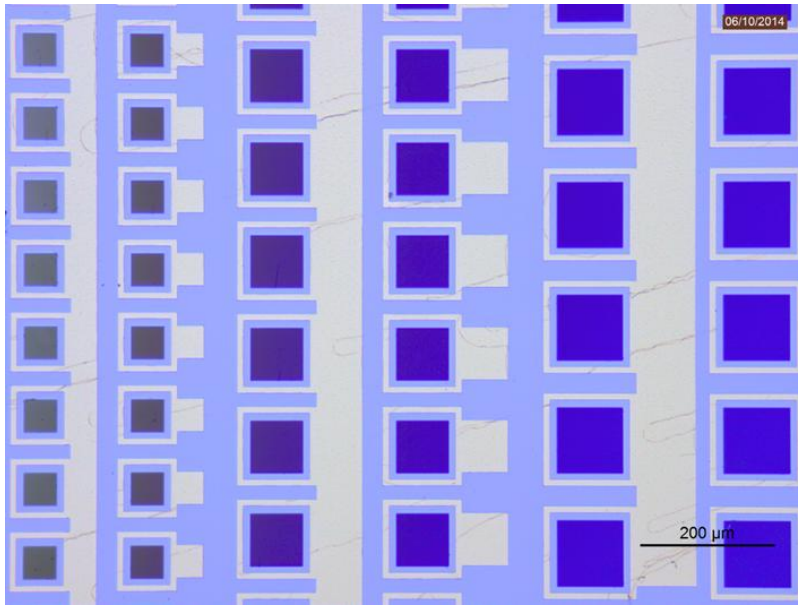


**Figure 3.10:** Oxide thickness variation was observed across the sample as a result of a current leakage path resulting from exposed metal. The thickness change is indicated by colour variation using an optical microscope.

To prevent the potential for oxide variation across the sample due to metal induced current leakage paths the anodic oxide was grown prior to any metal deposition. This also allowed for the simultaneous annealing of the oxide and bottom metal contact pad at 385°C for 45 minutes. A photoresist mask was used to selectively oxidise the required areas. Oxides of various thicknesses imaged after the anneal process can be seen in figure 3.11.

Top contacts were patterned using e-beam lithography. This was done to preserve the thickness of the grown oxide, which dissolves at a rate of 1 nm/sec when using most photolithographic developers. The anodic oxide is untouched by Isobutyl Methyl Ketone (IBMK), the developer used for the electron sensitive resist, Poly methyl methacrylate (PMMA). An example of a fabricated structure with top contacts can be seen in figure 3.12.

The fabricated structures were characterised by measuring current-voltage curves as a function of temperature (IVT). The samples were securely mounted into ceramic microchip packages using vacuum grease. Top and bottom contacts were connected to terminals on the packages using a heated wire-bonder. They were connected using 30 μm diameter gold wire. The packages were connected to a wired circuit board within a closed loop helium recycling Cryomech cryostat. Individual diode connections were made accessible by an external BNC enabled terminal box connected to the circuit board. A four point IV

measurement to the terminal box accounts for resistance associated with the external leads and connectors. The temperature was controlled using a commercial Mercury iTc temperature controller, and the current-voltage sweeps were automated through an Agilent E5270B precision mainframe using control software.

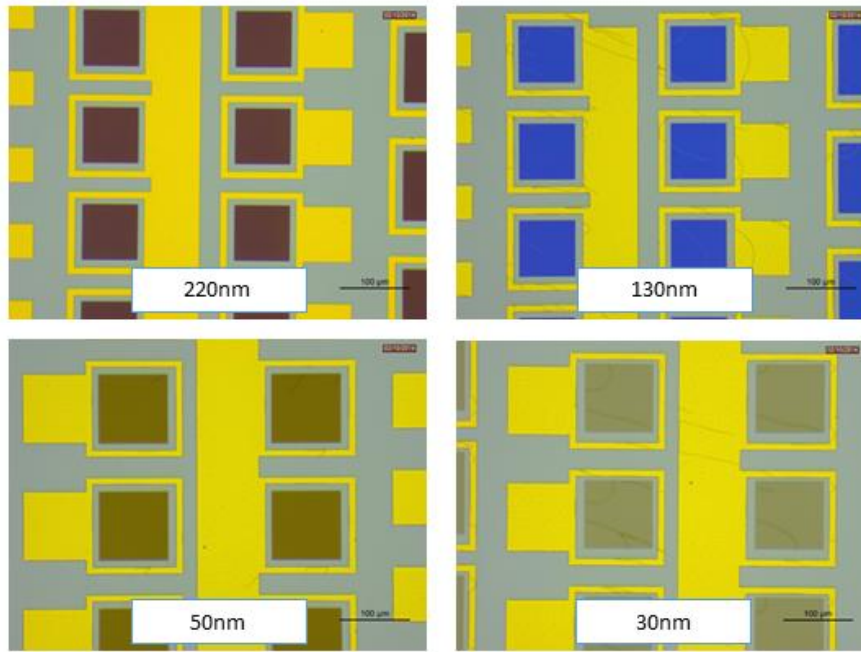


**Figure 3.11: Optical microscope image of annealed anodic oxides of various thicknesses/colours with post-deposited lower metal contacts.**

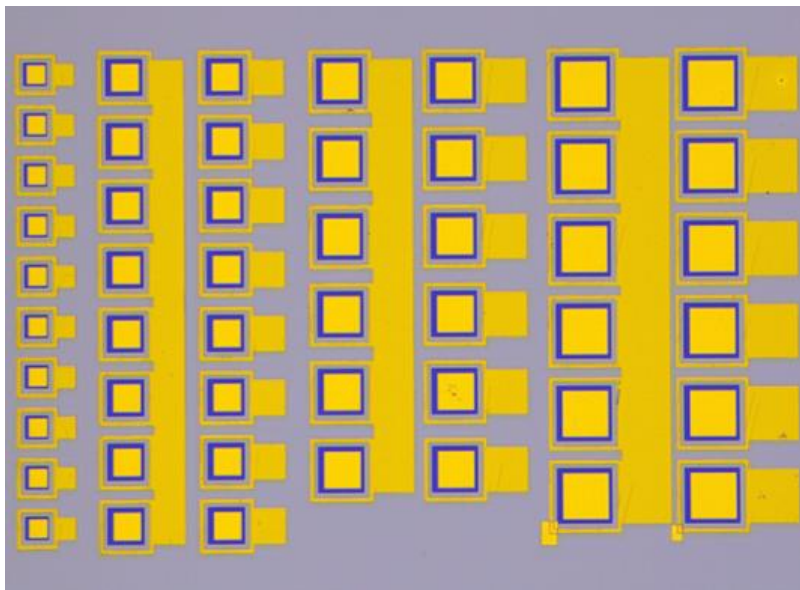


**Figure 3.12: MISM structures with top and bottom contact pads. Zn/Au p-type contacts were used.**

A method to determine the barrier height and Richardson constant of a dielectric in a metal-dielectric-semiconductor diode configuration is described using thermionic emission theory. The Richardson constant is a material dependent parameter and is a coefficient in calculating the thermionic emission current density. The method is extended to determine the mean barrier height of an inhomogeneous distribution of barrier heights that deviates from ideal thermionic emission theory. This analysis technique is widely used (Tataroglu, A. 2013).

In this technique a voltage is applied across the diode and the current is measured. In the following equations the voltage,  $V$ , given in equation 3.7, is the adjusted applied voltage to take into account the series resistance of the contact wires that are not accounted for by the four point measurement to the terminal box. This is done by taking the gradient of the linear part of the current-voltage ( $I$ - $V$ ) curve where series resistance,  $R_s$ , dominates.

$$V = V_{applied} - IR_s \quad (3.7)$$

The  $I$ - $V$  characteristics of a structure exhibiting ideal diode behaviour can be described by equation 3.8.

$$I = I_o \left[ \exp\left(\frac{qV}{kT}\right) - 1 \right] \quad (3.8)$$

where  $I_o$  is the reverse saturation current,  $T$  is the temperature in Kelvin,  $k$  is the Boltzmann constant and  $q$  is the electronic charge. An ideality factor  $n$  is included in equation 3.9 to account for any deviation from ideal diode behaviour.

$$I = I_o \left[ \exp\left(\frac{qV}{nkT}\right) - 1 \right] \quad (3.9)$$

The reverse saturation current can be extracted from the intercept of the plot of  $\ln(I)$  against  $V$ , whilst the ideality factor can be extracted from the slope. The reverse saturation current and the ideality factor are given by equation 3.10 and 3.11.

$$I_o = AA * T^2 \exp\left(\frac{-q\Phi_b}{kT}\right) \quad (3.10)$$

$$n = \frac{q}{kT} \left[ \frac{dV}{d(\ln I)} \right] \quad (3.11)$$

where  $A$  is the effective diode area,  $A^*$  is the effective Richardson constant, and  $\Phi_b$  is the zero bias barrier height. From manipulating equation 3.10 into the form of equation 3.12,  $A^*$  can be found from the intercept of a plot of  $\ln(I_o/T^2)$  against  $q/kT$ .  $\Phi_b$  can be found from the slope, and can be calculated using equation 3.13.

$$\ln\left(\frac{I_o}{T^2}\right) = \ln(AA^*) - \frac{q\Phi_b}{kT} \quad (3.12)$$

$$\Phi_b = \frac{kT}{q} \ln\left(\frac{AA^*T^2}{I}\right) \quad (3.13)$$

For large non ideality factors, often arising due to other conduction mechanisms or barrier inhomogeneities, it is necessary to apply an analysis that assumes an inhomogeneous barrier height at the metal-dielectric-semiconductor interface. A Gaussian distribution of barrier heights is assumed with a mean value of barrier heights  $\overline{\Phi_b}$ , and standard deviation  $\delta_s$ . The normalised distribution function giving the probability of the barrier height is given by equation 3.14.

$$P(\Phi_b) = \frac{1}{\delta_s\sqrt{2\pi}} \exp\left[-\frac{(\Phi_b - \overline{\Phi_b})^2}{2\delta_s^2}\right] \quad (3.14)$$

The total current density through the barrier is given by equation 3.15, where factors for the current at a given bias and barrier height, and the normalised distribution function giving the probability of the barrier height are included.

$$I(V) = \int_{-\infty}^{+\infty} I(\Phi_b, V) P(\Phi_b) d\Phi_b \quad (3.15)$$

Inputting equations 3.9 and 3.14 into the equation 3.15 a reverse saturation current in the same form as equation 3.10, but with an apparent barrier height, can be written, where the apparent barrier height is in the form of equation 3.16.

$$\Phi_{ap} = \overline{\Phi_b} - \frac{q\delta_s^2}{2kT} \quad (3.16)$$

The mean value of the barrier height and standard deviation can be found from a plot of the apparent barrier height against  $q/2kT$ , the values can be extracted from the intercept and slope respectively. Replacing  $\Phi_b$  in equation 3.10 with  $\Phi_{ap}$  the modified Richardson equation can be obtained, given by equation 3.17.



$$\ln\left(\frac{I_0}{T^2}\right) - \left(\frac{q^2\delta_s^2}{2k^2T^2}\right) = \ln(AA^*) - \frac{q\Phi_b}{kT} \quad (3.17)$$

From the above equation the mean barrier height and Richardson constant can be determined from the slope and intercept respectively.

### 3.3 Buried AlGaAs-Oxide Growth and Characterisation

This section describes the experimental techniques used in the oxidation and characterisation of buried AlGaAs layers. Apparatus were designed and constructed for this purpose. Oxidised AlGaAs layers are used for vertical confinement of the optical mode within the hybrid-plasmonic device, and for the formation of a current aperture when under electrical injection.

#### 3.3.1 Steam Oxidation

The theory relating to the steam oxidation of AlGaAs can be found in section 2.5. Wet oxidation at elevated temperatures is an effective technique for the controlled oxidation of high aluminium containing buried AlGaAs layers (Dallesasse, J.M. 1990). This technique is commonly used for edge emitting and vertical cavity laser diodes (Choquette, K.D. 1995). A schema of the constructed apparatus used for this purpose can be seen in figure 3.13. The apparatus were based on designs from previous work (Michell, G.J 2010) but with a number of improvements.

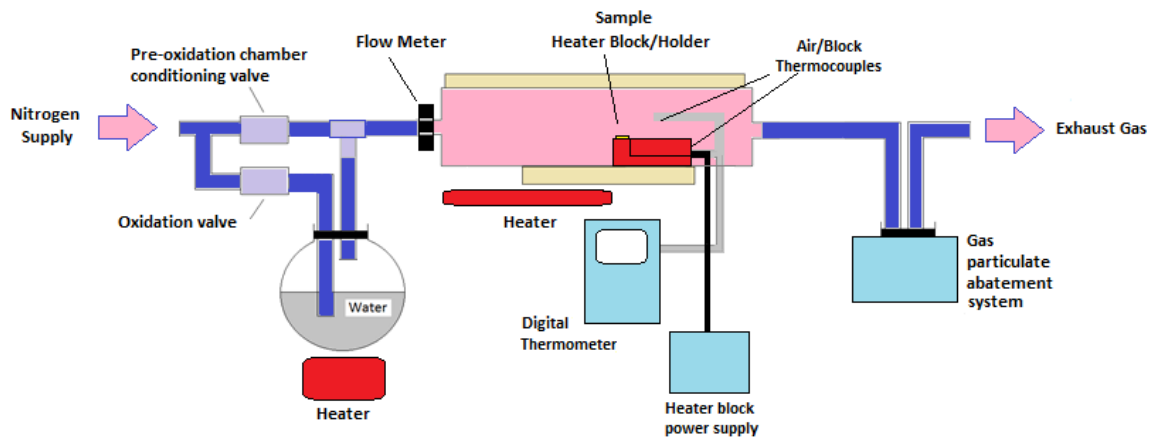


Figure 3.13: Schema of constructed steam oxidation apparatus

Pressurised nitrogen carrier gas was passed through a glass diffuser into a bubbler containing water that was heated to boiling point. The rate of flow of gas was measured using a flow meter. The glass diffuser was used to maximise the surface area of the nitrogen bubbles, allowing more steam to be carried into the main chamber within the carrier gas. The main chamber, shaped to promote laminar gas flow, was kept at an elevated temperature to prevent water condensation. The sample was placed on a sample holder in contact with a heating block, the temperature was monitored using an in-contact thermocouple as well as a nearby thermocouple to measure the temperature of the surrounding gas environment. A calibrated fluke thermometer was used to read-out the temperature. The wet carrier gas passed over the sample causing selective oxidation. The exhaust gas was passed through a gas particulate abatement system in the form of a glycol trap. A valve system was used to control the on-set of oxidation in order to more accurately time the oxidation procedure. The sample was allowed to reach its required temperature under a nitrogen environment before the carrier gas was passed through the heated water to begin oxidation.

The apparatus included a number of design improvements to previous work (Michell, G.J 2010). This included a smoother and more consistent gas flow, needed for repeatability and precision, and a higher temperature operation, needed to increase the oxidation rate for lower aluminium percentage containing layers. The gas flow was improved by altering the design of the configuration of gas lines in the system to reduce areas of steam condensation and water accumulation. In addition pressurised-gas-grade tubing was used throughout with stainless steel barbed connections where appropriate to reduce flow fluctuations. Stainless steel valves and plastic push-fittings were also used to avoid rusting and contamination of the gas. The sample housing section of the main chamber was blown by SGS (scientific glass services) using boronsilicate glass, allowing for safe operation up to at least 500°C. The sample housing section was formed with an open-cone end to make a tight seal with the main chamber. Thermocouples with high temperature sheaths, ceramic connectors and a calibrated fluke digital thermometer were purchased for high temperature monitoring. A metal sample holder was made to ensure the sample was in good thermal contact with the heater block.

The temperature of the sample and the duration of oxidation were varied. The timescale of oxidation was chosen through experimental calibration, details of which can be seen in section 4.5. A regime in which the oxidation rate plateaus and is constant was chosen by setting the gas flow to 3l/min with the bubbler set to 90°C (Choquette, K.D. 1997). Under these conditions the oxidation is reaction rate limited rather than diffusion limited. The main chamber was kept at 350°C to prevent condensation.

### 3.3.2 Oxide extent measurement

Mesa structures were fabricated in order to measure the extent of oxidation of the buried AlGaAs layers as a function of time and sample temperature. The mesa structures were fabricated using a variety of wet etches developed for the material structure. Wet etching results in a sloping mesa side-wall profile. Wet etching was used to replicate the side-wall profile of the hybrid-plasmonic devices which is the intended device for this technique. Structures of similar dimensions to the hybrid-plasmonic device were used.

The mesas were deeply etched to expose the lower AlGaAs layers. A table of the layer structure can be found in figure 4.2, section 4.2.1 After oxidation the structures were cleaved and imaged using a scanning electron microscope (SEM), e-line Raith. The oxidised sections are imaged as darker areas as a result of the lower conduction of the material which alters the scattering of the secondary electrons emitted from the sample atoms. An example of a wet etched mesa before and after oxidation can be seen in figure 3.14.

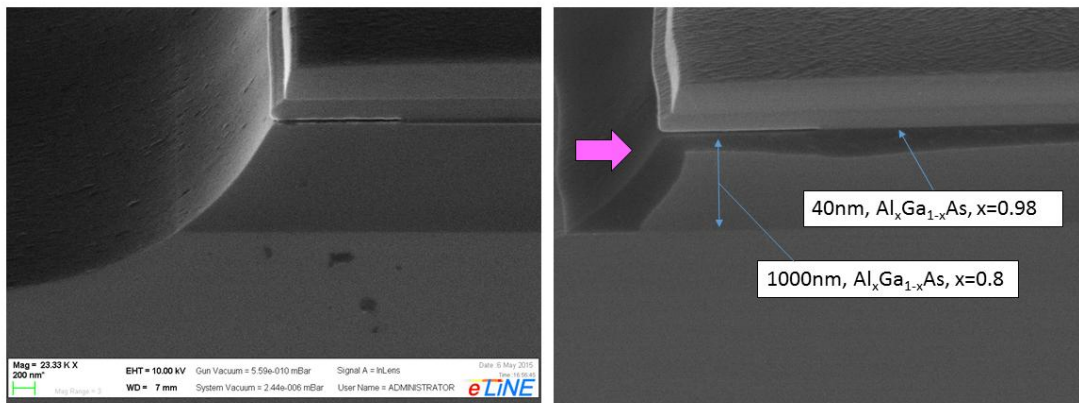


**Figure 3.14: (left) Cleaved facet of wet etched mesa edge. (right) Cleaved facet of oxidised mesa edge. The purple arrow shows the direction of oxidation. SEM images, e-line Raith.**

The lateral oxidation rate was measured from the edge of the mesa and averaged over many samples, an example of which can be seen in figure 3.15.

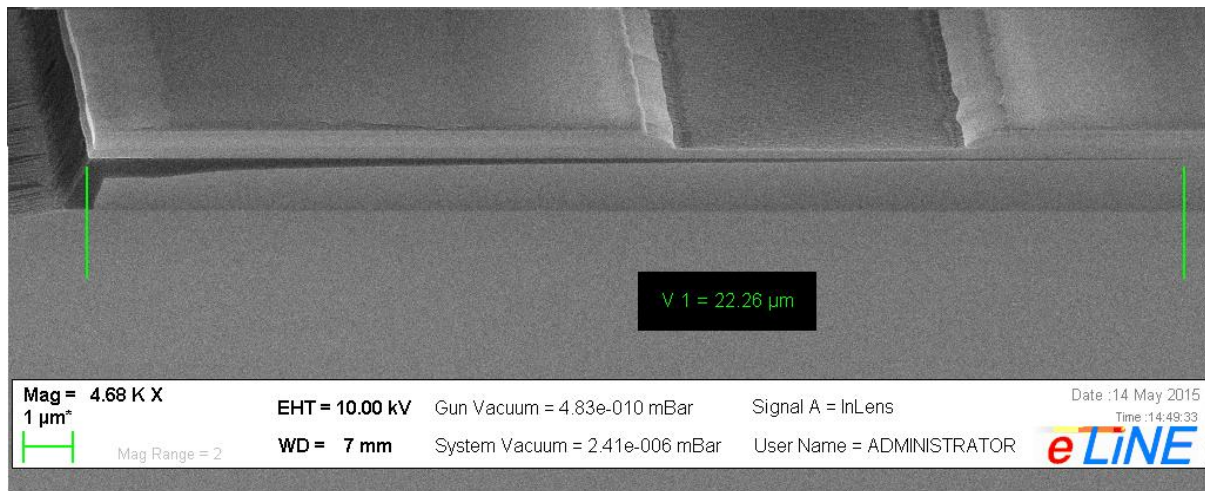


**Figure 3.15: Oxide extent measurement. Cleaved facet of oxidised mesa edge. Sample was oxidised at 430°C for 10 minutes. SEM image, e-line Raith.**

Controlled lateral oxidation was used to fabricate structures to be used as current apertures, the extent of oxidation was measured using the same method, an example of which can be seen in figure 3.16.



**Figure 3.16: Current aperture measurement. The current aperture is measured with respect to the oxidation of the Al<sub>x</sub>Ga<sub>1-x</sub>As x=0.98 layer. SEM image, e-line Raith.**

### 3.4. Device Characterisation Techniques

This section describes the experimental techniques used in the characterisation of semiconductor material and devices. Existing experimental set-ups were used for edge photovoltage spectroscopy (EPVS) measurements and gain stripe length measurements. EPVS measurements were performed by Stella Elliott, Cardiff University. The shifting excitation spot apparatus was constructed in order to obtain absorption spectra for GaN material at its associated wavelength.

#### 3.4.1 Edge photovoltage spectroscopy (EPVS)

Edge photovoltage spectroscopy (EPVS) measurements were used to determine the transition energies within the grown hybrid-plasmonic material, which was compared to the calculated transition energies of the designed material.

EPVS measurements were performed using a pre-existing experimental set-up, first constructed by Paul Mogensen (Mogensen, P. 1997), Cardiff University, with a number of later adaptations (Mexis, M. 2009) (Elliott, S.N. 2010). A schema of the set-up can be seen in figure 3.17.

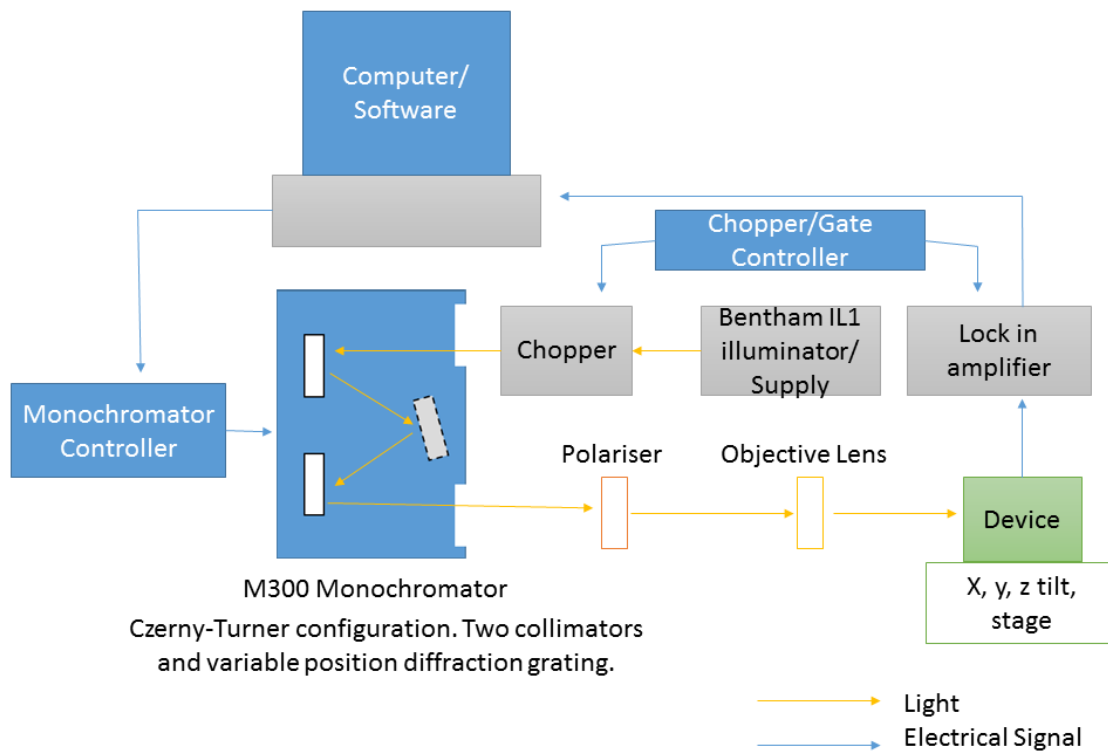


**Figure 3.17: Schema of Edge photovoltage spectroscopy (EPVS) measurement set-up**

The hybrid-plasmonic semiconductor wafer was processed into 50  $\mu\text{m}$  oxide isolated stripe laser devices. These were mounted onto transistor headers with electrical connections to the n and p sides of the device. The end facet of the device was illuminated with light of different wavelengths in order to measure the induced photovoltage across a spectrum of wavelengths. This was done in order to determine the transition energies within the material. The end facet was illuminated instead of illuminating the device from above to avoid the need for the fabrication of a top window in the top metal contact, and to allow a more reliable measurement of both the TE and TM energy transitions. When illuminated from above the electric vector of the illuminating light can not directly excite the TM mode.

A Bentham IL1 illuminator containing a halogen light source was used to produce a continuous white light wavelength spectrum of light, with an inbuilt quartz condenser lens to match the light shape to the monochromator input slit and optics. The input light was pulsed using a mechanical optical chopper to reduce heating of the device, and to improve the signal to noise ratio of the resultant measured photovoltage of the device by integrating and amplifying the signal over each pulse using a precision lock-in amplifier, which was gated to the chopper controller. A M300 monochromator with a Czerny-Turner configuration was used to select out and vary the wavelength of the light incident on the device facet. The monochromator uses a collimator to focus the chopped light at infinity, which is directed onto a diffraction grating to spread the white light into its various wavelength components. The light is then directed onto a second collimator, which reflects light towards the output slit of the monochromator. Wavelength components exiting the output slit are selected by varying the position of the diffraction grating to alter the reflected path with respect to the slit. The light was then passed through a polariser to select TM or TE polarisation, and an objective lens to focus the light onto the facet of the device. The device was mounted on a x,y,z, tilt translation stage for alignment. The induced photovoltage was measured via connections to the transistor header on which the device was mounted, using a precision lock in amplifier, with an output feed to computer controlled software for plotting the results.

### 3.4.2 Shifting Excitation Spot (SES)

The shifting excitation spot (SES) experiment is a technique that can be used to measure the passive optical mode loss of a semiconductor waveguide (Mogensen, P.C. et al 1997). This technique was used to measure the absorption of the GaN device structures.

The SES method uses Beer-Lamberts law of optical attenuation, a form of which is given in equation 3.18.

$$I = I_0 e^{-(A + \alpha_i)L} \quad (3.18)$$

where  $I$  is the axially collected light intensity of spontaneous emission from the device under test,  $L$  is the distance travelled by the light in the unpumped material,  $I_0$  is the intensity at  $L=0$ , and  $A + \alpha_i$  is the absorption and internal optical mode loss of the material respectively.

A diode laser was used to optically pump the GaN material. The pump spot was directed onto the surface of the sample perpendicular to the epitaxial layers (Z direction of figure 3.18). Emitted light from the guided mode was collected from the edge of the sample. The pump spot was progressively translated away from the edge of the sample, from which the emitted light was collected.

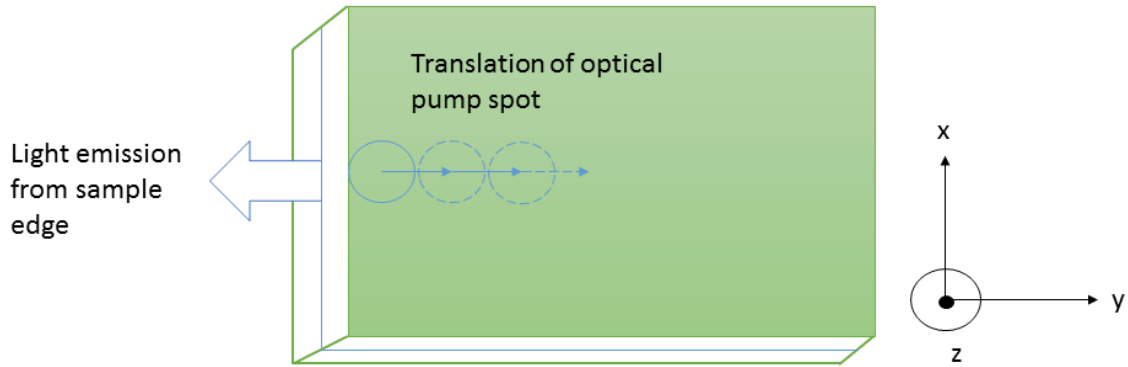


**Figure 3.18: Optical pumping and emitted light collection orientation for SES experiment.**

The optically excited light was attenuated as a function of distance as it propagated through unpumped regions of the waveguide. The length of the unpumped region that the light propagated through was varied by linearly translating the pump laser spot away from the facet/edge of the device using a mirror on a linear translation stage. The absorption was extracted using equation 3.18. The natural logarithm of the light intensity (in arbitrary

units) was plotted against the distance travelled by the light in the unpumped region. The gradient of the linear plot provided the absorption coefficients.

The 450 nm emitting GaN devices were pumped with a 405 nm laser diode. A schema of the set-up can be seen in figure 3.19.

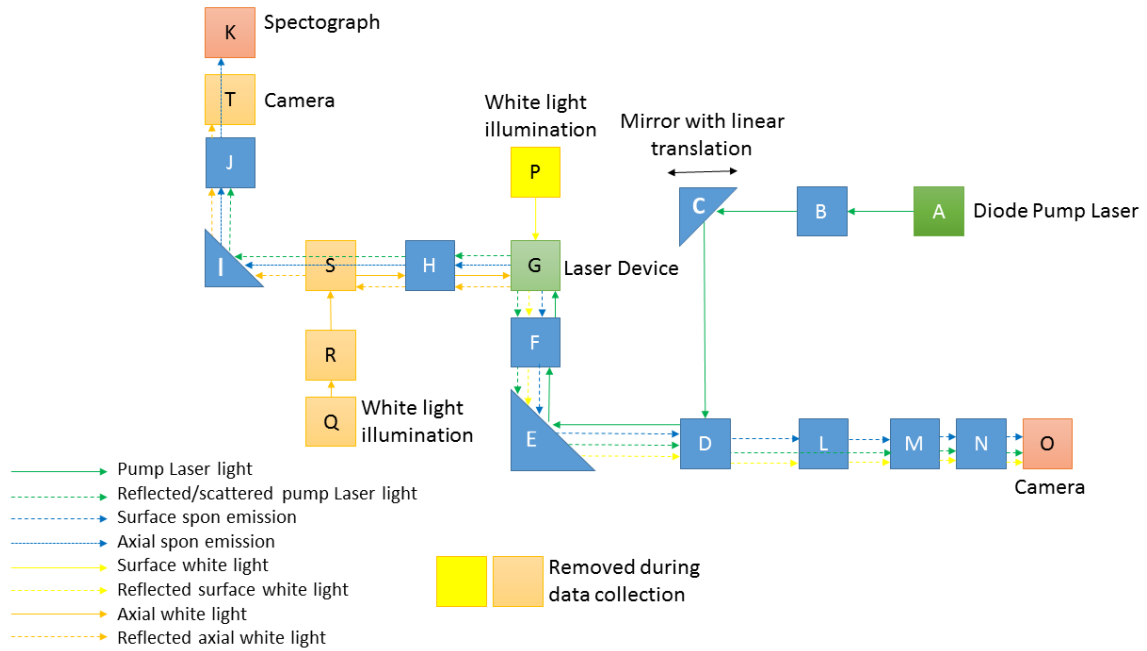


**Figure 3.19: Schema of constructed experimental set-up for the shifting excitation spot (SES) experiment, details of all components can be found in the appendix. A-G are used for optical pumping. G-K are used for emitted light collection. L-O are used for alignment and positioning.**

The various components of the experiment are labelled in figure 3.19. This set-up was required to perform the shifting excitation spot experiment. The optical set-up consisted of a number of “optical arms”. The “optical pumping arm” is labelled A-G, where A is the diode pump laser and G is the laser device sample being optically pumped. The laser device was pumped on its top surface, parallel to the direction of semiconductor layer growth. This arm included a mirror with linear translation in order to move the pump spot along the top surface of the device that was being pumped. The “emitted light collection arm” is labelled G-K, where G is the laser device (emitting light), and K is a spectrograph. The “alignment and positioning arm” uses reflected light, which reaches components L-O, where O is a camera. The camera is used to image the size of both the pump laser spot and the spontaneous emission spot on the top surface of the device. In order to visualise the pump spot position



relative to the sample surface a white light source was used, labelled P. In addition, in order to visualise the facet of the laser device sample another white light source, labelled Q, is used. This is imaged using another camera labelled T, which was also used to image the nearfield of the emitted light from the device. Optical posts with holes at the same height were used when aligning the optical components. Further details concerning the components labelled in figure 3.19 can be found listed in the appendix.

### 3.4.3. Variable stripe length measurements (VSL)

The gain and absorption of the InP device structures were obtained using the optically pumped variable stripe length technique. A number of different techniques to determine optical gain have historically been used including the Hakki-Paoli technique (Hakki, B.W. Paoli, T.L. 1975) in which longitudinal modes in the stimulated emission are used, the Henry technique (Henry, C.H. Logan, R.A. Merritt, F.R. 1980) in which the spontaneous emission is used, and the variable stripe length method in which the amplified spontaneous emission is used (Oster, A. Erbert, G. Wenzel, H. 1997). The variable stripe length method can be performed using either electrical injection with segmented contacts or with optical pumping. Both methods show good agreement between gain and emission spectra at the same inversion (Thomas, R. Smowton, P.M. Blood, P. 2015). The optically pumped technique has the advantage that electrical contacts do not have to be fabricated, which for some material systems can be problematic.

The material was pumped by a length of laser pump light *S1S2* with uniform intensity. A schema of the pump length configuration is shown in figure 3.20, the stripe length was reduced in length, and section length *S2* was pumped. The pump stripe was then translated to pump section length *S1*. Sections *S1* and *S2* were of equal length. This was assured by fabricating etched rulers as guides on the sample surface to ensure precision when changing the length of the pump stripe length. The emitted light was collected from the edge of the sample. The exponential increase of the emitted light with stripe length is used to determine the material gain, using sections *S1S2* and *S1*, whilst the decrease in the emitted light with translation of the stripe length away from the edge was used to measure absorption, using sections *S1* and *S2*.

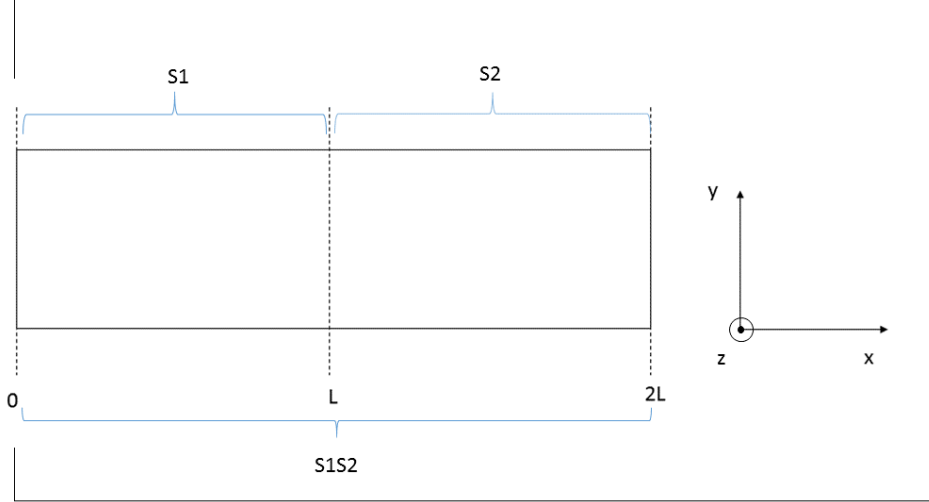


**Figure 3.20:** Schema of the top view of a semiconductor sample. The epitaxial layers are grown in the  $z$  direction. Position 0 indicates the cleaved edge of the sample from which light emission is collected. Lengths  $0-L$  and  $0-2L$  indicate lengths of the material through which light propagates. Labels  $S1$ ,  $S2$  and  $S1S2$  indicate the length of material optically pumped from the surface of the sample in the  $x$ - $y$  plane.

The optically pumped stripe length method produces light intensity spectra. The equations used to calculate the net gain and absorption from the light intensity spectra are derived below.

The one dimensional optical amplifier model can be used to describe the gain. From this the intensity of the paraxial amplified spontaneous emission as a function of pumped stripe length can be found (Thomas, R. Smowton, P.M. Blood, P. 2015). The net gain is derived by considering the light intensity measured from position 0 of figure 3.20 when length  $S1$  and then length  $S1S2$  are optically pumped from the surface of the sample. The intensity measured when length  $S1$  is pumped is given in equation 3.19 and 3.20.

$$I(S1) = CI_{spont} \int_0^L e^{(G-\alpha_i)x} dx \quad (3.19)$$

$$I(S1) = CI_{spont} [e^{(G-\alpha_i)L} - 1] \cdot \frac{1}{G-\alpha_i} \quad (3.20)$$

In the equation  $C$  is a collection efficiency factor that accounts for the spectrograph responsivity and optical collection geometry,  $I_{spont}$  is the spontaneous emission rate per unit area per unit energy,  $G$  is gain and  $\alpha_i$  is the internal optical mode loss. The light intensity when section length  $S1S2$  is pumped is shown in equation 3.21.

$$I(S1S2) = CI_{spon} [e^{(G-\alpha_i)2L} - 1] \cdot \frac{1}{G-\alpha_i} \quad (3.21)$$

The ratio of these intensities allows the net modal gain to be calculated, as shown in equation 3.22 and 3.23 (Thomson, J.D. Summers, H.D. 1999), resulting in a gain spectrum.

$$\frac{I(S1S2)}{I(S1)} = \frac{e^{(G-\alpha_i)2L}-1}{e^{(G-\alpha_i)L}-1} = \frac{(e^{(G-\alpha_i)L+1})(e^{(G-\alpha_i)L-1})}{e^{(G-\alpha_i)L}-1} = e^{(G-\alpha_i)L} + 1 \quad (3.22)$$

$$G - \alpha_i = \frac{1}{L} \ln \left[ \frac{I(S1S2)}{I(S1)} - 1 \right] \quad (3.23)$$

The absorption spectrum is calculated from considering the pumped lengths  $S1$  and  $S2$ , the collected intensities are given in equations 3.24 and 3.25 respectively.

$$I(S1) = CI_{spon} [e^{(-A-\alpha_i)L}] \quad (3.24)$$

$$I(S2) = CI_{spon} [e^{(-A-\alpha_i)2L}] \quad (3.25)$$

where  $A$  is the absorption coefficient. The ratio of these equations allows the absorption spectrum to be calculated. The absorption and gain spectra should agree on the value of the internal optical mode loss, if they do not this may indicate poor alignment in the optical collection apparatus.

$$\frac{I(S1)}{I(S2)} = e^{-(-A-\alpha_i)L} = e^{(A+\alpha_i)L} \quad (3.26)$$

$$A + \alpha_i = \frac{1}{L} \ln \left[ \frac{I(S1)}{I(S2)} \right] \quad (3.27)$$

The experimental set-up was similar to that used for the shifting excitation spot experiment, but with a number of differences. The 720 nm emitting devices were pumped using a 532 nm frequency doubled Ti-sapphire Verdi laser. Optics and filters were used to match the required wavelengths, and an additional optical arm was used for beam shaping. The 532 nm pump beam exhibited a Gaussian like intensity profile. In order to evenly pump a stripe of semiconductor material the beam was passed through shaping optics and an adjustable slit aperture, a schema of the set-up can be seen in figure 3.21.

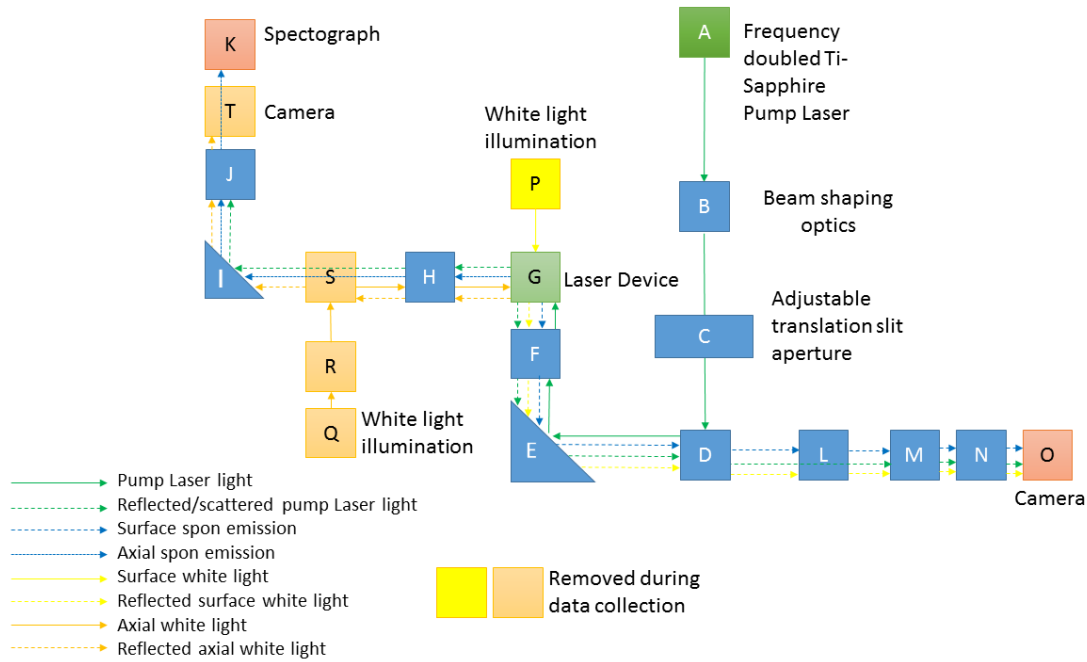


**Figure 3.21: Schema of stripe length measurement optical set-up. Details of all components can be found in the appendix.**

### 3.5. Summary

The chapter has outlined the growth and characterisation techniques for the GaAs oxide and AlGaAs oxide, including methods to determine the barrier height of an oxide and the specific contact resistivity of metal contacts. The device characterisation techniques have been outlined, including EPVS, SES and VSL measurements.

### Chapter References

Choquette, K.D.; Geib, K.M.; Ashby, C.I.; Twesten, R.D.; Blum, O.; Hou.H.Q.; Follstaedt, D.M.; Hammons, B.E.; Mathes, D.; Hull, R. (1997). "Advances in selective wet oxidation of AlGaAs alloys." *Journal of Selected Topics in Quantum electronics*, 3 (3).

Choquette, K.D. Lear, K.L. Schneider, R.P. Geib, K.M (1995). "Cavity characteristics of selectively oxidised vertical cavity lasers." *Appl.Phys.Lett.* 66 (25).

Dallessasse, J.M. Holonyak, N. Sugg, A.R. Richard, T.A. El-Zein, N. (1990). "Hydrolyzation oxidation of  $\text{Al}_x\text{Ga}_{1-x}\text{As-AlAs-GaAs}$  quantum well heterostructures and superlattices." *Appl.Phys.Lett* 57 (26).

- Elliott, S.N. (2010). "High power semiconductor lasers." Optoelectronic Group, Cardiff University, PhD Thesis.
- Grove, M.J. Hudson, D.A. Zory, P.S. Dalby, R.J. Harding, C.M. Rosenberg, A. (1994). "Pulsed anodic oxides for III-V semiconductor device fabrication." J.Appl.Phys. 76 (1).
- Hakki, B.W. Paoli, T.L. (1975). "Gain spectra in GaAs double-heterostructure injection lasers." Journal of applied physics, 46: 1299-1306
- Hasegawa, H. Forward, K.E. Hartnagel, H.L (1975). "New anodic native oxide of GaAs with improved dielectric and interface properties." Applied physics letters, 26 (10).
- Hasegawa, H. (1976). "Anodic native oxidation of GaAs by AGW process", Bulletin of the faculty of engineering, Hokkaido university, 79: 79-88
- Henry, C.H. Logan, R.A. Merritt, F.R. (1980). " Measurement of gain and absorption spectra in AlGaAs buried heterostructure lasers." Journal of applied physics, 51: 3042
- Howland, R. Benatar, L (1998). "A practical guide to scanning probe microscopy." Thermomicroscopes publication.
- Kas, J.A. (2015). <http://www.uni-leipzig.de/~pwm/web/?section=introduction&page=sfm>, University of Leipzig, Soft matter physics division.
- Mexis, M. (2009). "Optoelectronic properties of InAs/GaAs columnar quantum dot laser diodes.", Optoelectronic Group, Cardiff University, PhD Thesis.
- Michell, G.J. (2010). "Characterisation and advanced applications of the steam oxidation of AlGaAs." PhD Thesis 2010, Cardiff University.
- Mogensen, P. (1997). ""Strain limits in  $(\text{Al}_y\text{Ga}_{1-y})_x\text{In}_{1-x}\text{P}$  Quantum Well laser diodes." Optoelectronics Group, Cardiff University, PhD Thesis.
- Oster, A. Erbert, G. Wenzel, H. (1997). "Gain spectra measurements by a variable stripe length method with current injection." Electronic Letters, 33 (10): 864-866
- Schroder, D.K. (2006). "Semiconductor material and device characterisation, third edition." IEEE press, Wiley-Interscience.

Tataroglu, A. Pur, F.Z. (2013). "The Richardson constant and barrier inhomogeneity at Au/Si<sub>3</sub>N<sub>4</sub>/n-Si (MIS) Schottky diodes." Phys. Scr. 88, 015801

Thomas, R. Smowton, P.M. Blood, P. (2015). "Radiative recombination rate measurement by the optically pumped variable stripe length method." Optics Express, 23 (3): 3308-3315

Thomson, J.D. Summers, H.D. Hulyer, P.J. Smowton, P.M. Blood, P. (1999). "Determination of single-pass optical gain and internal loss using a multisection device." Applied physics letters, 75 (17): 2527

Veeco, (1996). "Manual, MultiMode SPM Instruction. Veeco, NanoScope Software Version 5, 004-210-000, 004-210-100".

Woollam, J.A. (2015). [http://www.jawoollam.com/tutorial\\_1.html](http://www.jawoollam.com/tutorial_1.html), J.A. Woollam company ellipsometry solutions tutorial.

# Chapter 4. Hybrid Plasmonic Device

## 4.1. Introduction

This chapter contains the design and fabrication results for the hybrid-plasmonic device. A “nanosquare” plasmonic device was initially fabricated in order to evaluate and explore nanofabrication techniques, followed by a more detailed study of various components of the device which are crucial to its operation. Details of the required dielectric gap fabrication via the anodisation of GaAs, and the semiconductor slab thickness via the steam oxidation of AlGaAs are included.

## 4.2. Device Design

This section describes the design of a hybrid-plasmonic device. The device design explores the use of a semiconductor gain material to compensate the loss associated with plasmonic propagation at the interface between a metal and dielectric. The hybrid mode of the device is the optical mode of the semiconductor which becomes bound to the spatial region of the metal waveguide, resulting in plasmonic oscillations.

The nanosquare structure used a metal-dielectric-semiconductor configuration, in which the gain was provided by a single red emitting quantum well within the semiconductor. The in-plane dimensions of the plasmonic cavity were defined by the area overlap of the metal and dielectric stripes, as shown in the schema of figure 4.1, forming approximately a 1  $\mu\text{m}$  in-plane square. The dielectric and metal stripes were designed to cross over each other at right angles to lessen the need for precise alignment of one layer to the other. An oxide of GaAs was used as the dielectric layer, whilst silver was used as the plasmonic metal.

Full details and fabrication of the nanosquare device can be found in section 4.3. Although the dimensions of the preliminary device were subject to the additional constraints of a “standard” semiconductor wafer design, it acted as an informant to a realistic device design in terms of what can be achieved using current and developed fabrication techniques. The device design included nearby electrical injection contact pads to attempt to achieve carrier recombination directly underneath the nanosquare.

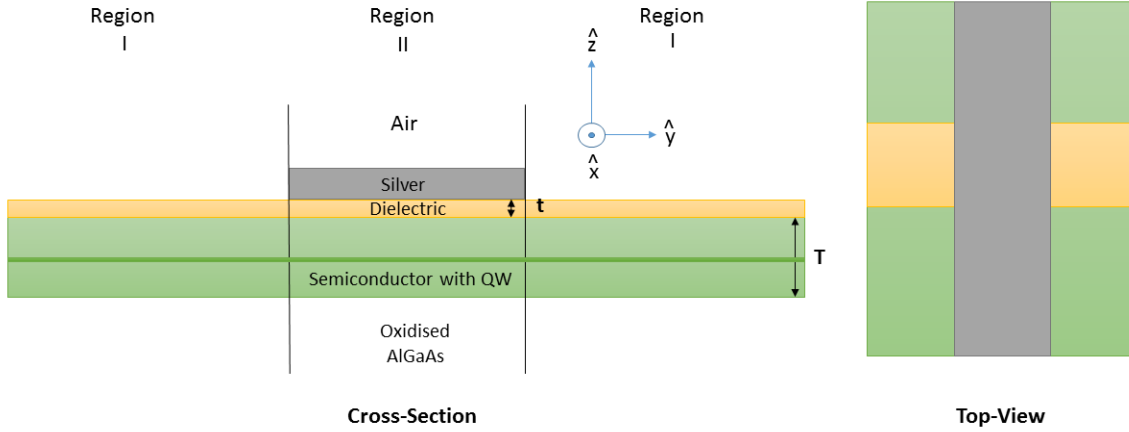


**Figure 4.1: Schema of hybrid-plasmonic device.**

#### 4.2.1. Wafer Design

A wafer was designed to investigate the fabrication of a hybrid-plasmonic device. The wafer provided a platform to investigate the fabrication of components of the structure which are the focus of this work.

The free space optical wavelength of the semiconductor gain material was designed to be 633 nm. Many studies into plasmonic propagation have considered the 633 nm free space wavelength (Burke. 1986) (Berini. 2000), the wavelength was chosen in order to reduce optical losses associated with plasmonic propagation, and to ensure a small effective mode volume.

The propagation length of surface plasmon polaritons (SPPs) on a metal surface is inversely proportional to the imaginary component of the SPP's propagation constant. This depends on the imaginary component of the refractive index of the metal, responsible for Ohmic damping of the surface electron oscillations. This is wavelength dependent. Further than considering the imaginary refractive index of the metal in question, surface roughness plays a big part in realistic systems. For a rough gold surface at 633 nm SPPs have been found to propagate for 3-4  $\mu\text{m}$  before becoming completely attenuated (Kolomenski 2009). The slightly smaller imaginary component of refractive index for silver at this wavelength suggests that SPPs would propagate for a marginally greater distance without any gain assistance. Although larger excitation wavelengths can produce larger propagation lengths



there is a clear compromise regarding the effective mode volume when considering a hybrid-plasmonic architecture. To this effect, 633 nm was chosen as a suitable wavelength to further investigate the feasibility of a hybrid-plasmonic device.

The requirement for TM polarised optical excitation in the given device architecture is supported by the theory of plasmonic excitation discussed in section 2.3.3. The use of strained quantum wells is also useful to allow for lower current thresholds. In addition it gives the ability to access specific wavelengths of operation whilst retaining flexibility in quantum well thickness.

A TM polarised quantum well emitting at 633nm was designed. One wafer was designed without a GaAs layer (layer 4) that would have inhibited the ability to measure the TM mode using edge photo-voltage spectroscopy (EPVS), as described in section 3.4.1. The wafer design can be seen in figure 4.2.

Layer no.	Material	x	Thickness (nm)	Dopant type	Dopant concentration
1	GaAs		50	P	1e18
2	GaInP		10	P	5e17
3	Al(x)GaInP	0.70	1000	P	3e17
4	GaAs		5	P	3e17
5	Al(x)GaInP	0.50	100	Ud	
6	GaIn(x)P	0.40	13	Ud	
7	Al(x)GaInP	0.50	100	Ud	
8	GaInP		5	Ud	
9	Al(x)GaAs	0.98	40	N	1e18
10	Al(x)GaAs	0.80	1000	N	1e18
11	GaAs		100	N	1e18

**Figure 4.2: Wafer design for hybrid-plasmonic device, wafer substrate 10 deg to 111 crystallographic plane.**

The top GaAs layer is a highly doped metal contact layer for the fabrication of Ohmic contacts for electrical injection. As a compromise this layer was made thin to allow for easy photolithography/e-beam lithography steps near the step edge of wet etched trenches. The 70% aluminium AlGaInP layer is an electrical cladding layer to reduce carrier leakage into optical region of the device. The GaAs layer of layer 4 is used for anodisation to produce the dielectric spacer between the plasmonic metal and gain material. This also acts as a wet etch stop layer. Layer 4 is doped to aid in the process of anodisation. The 50% AlGaInP

layers are used for electronic and optical confinement of the mode. The GaInP layer (layer 6) is a single tensile strained 633 nm emitting QW. The lower GaInP layer (layer 8) is required as an intermediary between AlGaInP and AlGaAs due to poor growth interfaces between AlGaInP and AlGaAs. This GaInP layer is absorbing within the structure, however, oxidation of the AlGaAs layer shifts the absorbing wavelength away from the GaInP layer due to an increase in the AlGaAs energy barrier height. The AlGaAs of layers 9 and 10 are used for steam oxidation and vertical confinement of the optical mode, whilst also reducing carrier leakage.

The emission wavelength of the semiconductor active region is controlled by the quantum well width, well composition, and the strain. The strain of the  $\text{Ga}_y\text{In}_{1-y}\text{P}$  quantum well is controlled by varying the Ga composition,  $y$ , which changes the lattice constant with respect to the surrounding material. The surrounding material is lattice matched to the GaAs substrate. A change in the composition causes a change in the bandgap of the material. Furthermore, the strain itself causes a change in the bandgap enhancing the splitting of valence sub-bands and changing the valence band in-plane effective masses. Energy levels in a strained QW are determined using an envelope function calculation where the depth of the well takes into account the strain and composition. The model solid approach of Van de Walle (Van de Walle, 1989) can be used to calculate the strain dependent shifts in valence and conduction band energies and their offset ratios.

The equilibrium lattice constant of  $\text{Ga}_y\text{In}_{1-y}\text{P}$  depends on composition according to  $a = 5.869 - 0.418y$ , which is a linear interpolation between the values of the binaries InP and GaP from Vegard's law. From this equation,  $\text{Ga}_y\text{In}_{1-y}\text{P}$  is lattice matched to GaAs when  $y = 0.516$  (so that  $a = 5.653$  angstroms, the lattice constant of GaAs in the growth plane). The energy gap from an interpolation experimental fit for GaInP is  $E_g(y) = 1.35 + 0.76y + 0.63y^2$  at 300k (P.M.Smowton 1997).

Strain effects the energy bands in two ways, with hydrostatic and shear contributions. Model solid theory calculates the hydrostatic energy shifts of the conduction and valence bands independently, which allows the calculation of the change in conduction and valence band offsets as a function of applied strain. The hydrostatic component of the strain leads to the shift in the average valence and conduction band energy, characterised by band

deformation potentials. The shear strain contribution couples to the spin-orbit interaction and leads to an additional splitting of the valence band energies. The heavy hole, light hole and conduction band positions are given in equations 4.1, 4.2 and 4.3 respectively.

$$E_{hh} = E_{v,av} + \Delta_o/3 + \Delta E_{v,av}^{hy} + \Delta E_{hh}^{sh} \quad (4.1)$$

$$E_{lh} = E_{v,av} + \Delta_o/3 + \Delta E_{v,av}^{hy} + \Delta E_{lh}^{sh} \quad (4.2)$$

$$E_c = E_{v,av} + \Delta_o/3 + \Delta E_c^{hy} + E_g \quad (4.3)$$

Where  $E_{v,av}$  is the average valence band energy,  $\Delta E_{v,av}^{hy}$  is the shift in the average valence band energy due to the hydrostatic component of the strain,  $\Delta E_c^{hy}$  is the shift in the conduction band energy due to the hydrostatic component of the strain,  $\Delta E_{hh}^{sh}$  is the shift in the heavy hole valence band energy as a result of band splitting due to spin-orbit interactions from the shear strain contribution,  $\Delta E_{lh}^{sh}$  is the equivalent for the light hole valence band,  $\Delta_o$  is the spin orbit splitting, and  $E_g$  is the energy band gap.

The values used for the calculation of the band positions are taken from literature (P.M.Smowton 1997) (Krijn 1991). The unstrained state  $\left| \frac{3}{2}, \pm \frac{3}{2} \right\rangle$  is the heavy-hole band position, the unstrained state  $\left| \frac{3}{2}, \pm \frac{1}{2} \right\rangle$  is the light-hole band position. The effective band gap of strained GaInP for heavy holes is given as  $E_c - E_{hh}$ . The effective bandgap of strained GaInP, for light holes is given as  $E_c - E_{lh}$ . Under compressive strain the  $E_{hh}$  band gap is smallest and most significant in operation, in tensile strain the  $E_{lh}$  bandgap is smallest and most significant in operation. A desired 633 nm (1.95780 eV) on the  $e$ - $lh$  transition relates to  $y = 0.6$ . This value of tensile strain also relates to a minimum in the threshold current of similar fabricated devices (Valster, van der Poel et al. 1992). A calculated plot showing the dependence of the energy gap of GaInP with Ga composition can be seen in figure 4.3.

The emission wavelength depends on the energy states within the quantum well, which is dependent on the quantum well width and barrier material. In tensile strained wells the band gap increases with increasing Ga concentration, a higher tensile strain requires a thinner well to avoid misfit dislocations, which causes an increase in quantum confinement. Both of these factors (higher tensile strain and thinner well) shift the transition to a higher energy and therefore a smaller wavelength of operation.

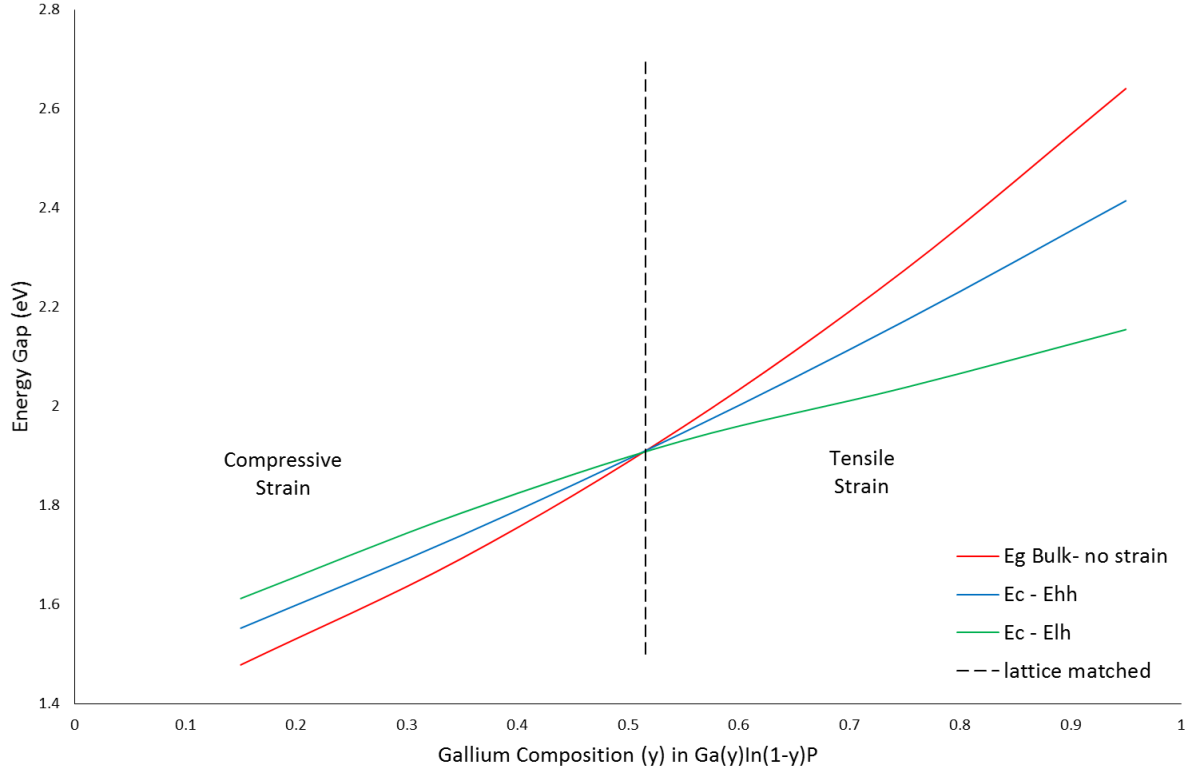


**Figure 4.3:** Energy bandgap for a given Gallium composition ( $y$ ) for bulk  $\text{Ga(In}_{1-y}\text{)P}$  on GaAs, calculated using model solid theory.

To obtain operation at a given wavelength one can use various combinations of well width, and well composition. However, each of these parameters influences the laser threshold current, so an optimised combination must be chosen. In-house software was used to choose the quantum well thickness for the chosen emission wavelength of 633nm.

A separate confinement heterostructure is required for separate optical and electrical confinement, the main components of a typical single quantum well separate confinement heterostructure are shown in the schema of figure 4.4.

For carrier confinement one requires a large difference between the transition energy in the quantum well to the energy bandgap of the optical waveguide layer and also the cladding layer. For optical guiding one requires a large refractive index step between the optical waveguide layer and the cladding layer.

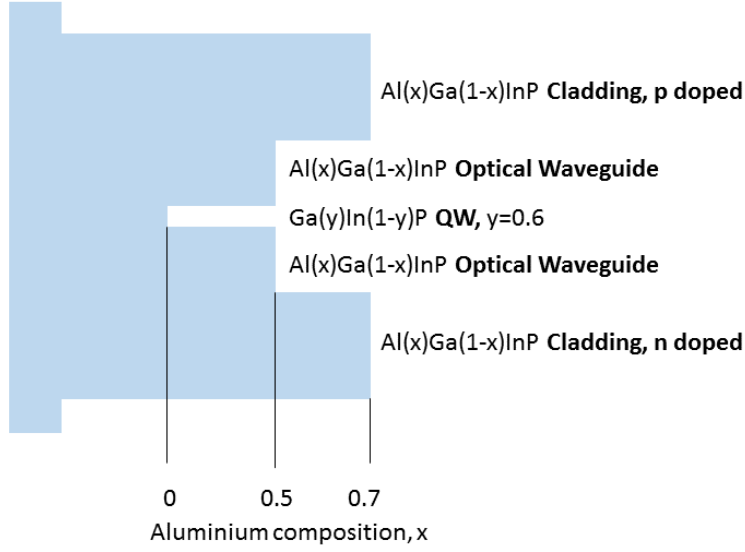


**Figure 4.4: Aluminium composition profile of separate confinement heterostructure, lower aluminium compositions of  $\text{Al}_x\text{Ga}_{(1-x)}\text{InP}$  exhibit a higher refractive index. The structure enables separate confinement of the optical mode, whilst charge carriers are injected in p and n doped regions.**

In this material system the optical waveguide and the cladding layers can be designed to consist of  $\text{AlGaInP}$  of different aluminium compositions. This enables separate optical waveguiding and confinement of charge carriers (for electrical injection). In the designed wafer the lower  $\text{Al}_x\text{Ga}_{(1-x)}\text{InP}$   $x=0.7$  layer shown in figure 4.4 is substituted by  $\text{Al}_x\text{Ga}_{(1-x)}\text{As}$   $x=0.98$  and  $x=0.8$  layers. These layers have a larger energy gap compared to  $\text{Al}_x\text{Ga}_{(1-x)}\text{InP}$   $x=0.7$ . This reduces carrier leakage effects that are often associated with the phosphide system due to the lower energy band gap and refractive index differences available in the  $\text{AlGaInP}$  system at different aluminium compositions compared to the  $\text{AlGaAs}$  system. The optical confinement, which is a factor that determines the threshold gain within the round-trip gain equation, as described in section 2.2.2, is dependent upon the refractive indices of the waveguide and cladding layers.

The edge photovoltage spectrum of the material was measured, as described in section 3.4.1. The spectrum can be seen in figure 4.5, it can be seen that under tensile strain the light hole and heavy hole sub-bands cross. The electron to light hole transition, determined using TM polarisation, is at a lower energy than the electron to heavy hole transition, resulting in TM emission at 633 nm. The additional small peak features observable in figure 4.5 are higher lying transitions in the wide quantum well (Smowton, P.M. Blood, P. et al 1996), whilst the larger absorption at high energy is due to the optical waveguide layers, the

bandgap of which is marked at 557nm. This set of experimental data validates the design and growth of the material.

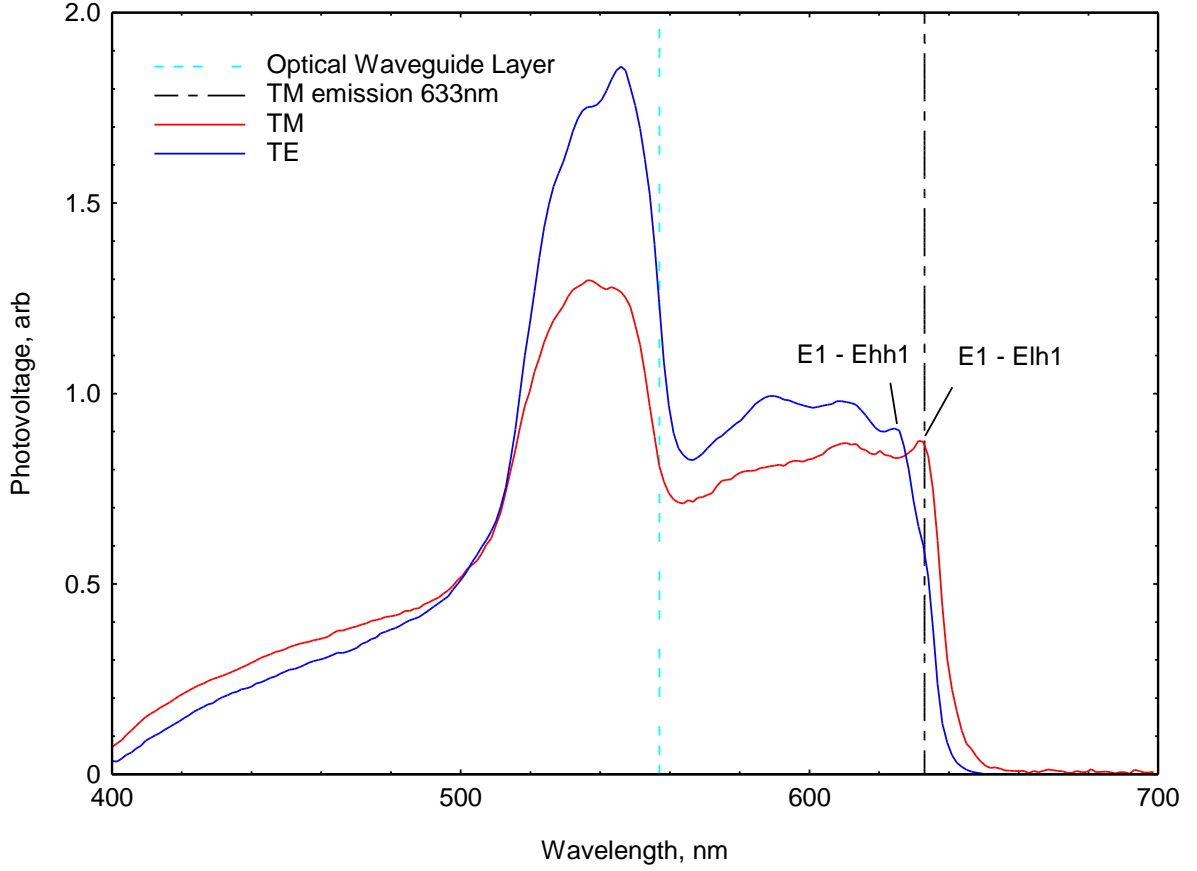
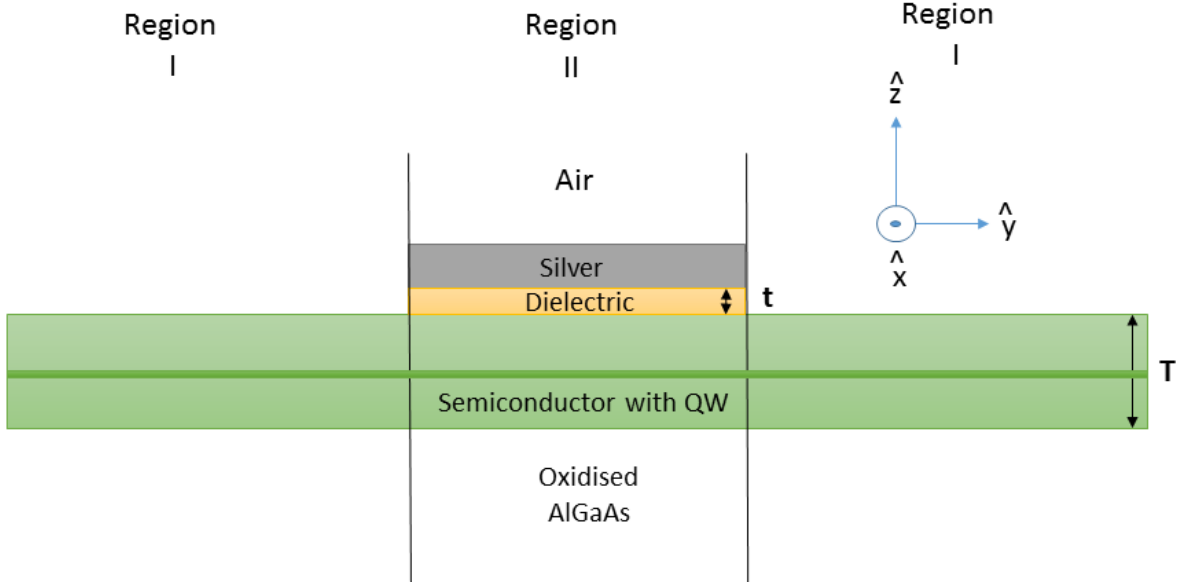


Figure 4.5. EPVS spectrum of designed wafer showing TM emission at 633 nm, performed at room temperature.

#### 4.2.2. Dielectric gap and semiconductor material requirements and constraints

This section describes the constraints on the dielectric gap and semiconductor slab thickness for plasmonic operation. All modelling was done using PhotonD FIMMWAVE and FIMMPROP software. The software is able to find modes, effective refractive indices and model mode propagation in 2D and 3D using a choice of finite element (FEM), finite difference (FDM) and film mode matching (FMM) numerical and semi-analytical solvers. The formulation of this section follows that previously produced for a bulk GaAs metal strip surface plasmon nano-laser (Lafone, Sidiropoulos et al. 2014). This work however utilises a different material structure and operating wavelength. The use of a dielectric gap and gain medium partly helps to address the high loss associated with plasmonics. A schematic of the

cross-section of the designed structure can be seen in figure 4.6, where  $t$  is the dielectric thickness, in this case an oxide of GaAs, and  $T$  is the semiconductor slab thickness, which includes a 633 nm emitting TM quantum well. Refractive index values for the semiconductor and silver were obtained through calculation and the use of the PhotonD database respectively. Values used for the refractive index of the oxide of GaAs and the oxidised AlGaAs were 1.8 and 1.6 respectively.



**Figure 4.6: Schematic cross-section of hybrid-plasmonic device.**

An optical mode bound to region II in figure 4.6 can be engineered to be a hybrid mode of the metallic strip and the semiconductor gain region. This relies on the coupling of light from the optical mode to the collective electron oscillations at the surface of the metal, which results in a reduced cavity size and enhanced spontaneous emission. The pure surface plasmon mode propagates as a bound mode in 1D ( $x$ ), as does the hybrid mode. The unbound optical mode on the other hand propagates in 2D ( $x, y$ ). This guiding is analogous to a traditional ridge waveguide type structure, the mode sees a higher effective refractive index in region II as opposed to region I, so is guided as a 1D mode ( $x$ ).

It has been stated that a TM excitation of surface plasmons is preferential, where the electric field vector of the exciting optical mode is in the  $z$  direction. The formation of a guided TM mode requires the difference in the effective refractive index of the TM mode

between regions I and II to be large, an order of difference in refractive index of 1 will allow strong guiding.

A bound TM mode in region II can be supported as long as it does not couple with the 2D TE mode of region I. The effective index of TE waves in region I therefore represent the minimum effective refractive index for any 1D TM like modes bound to the metal (else they will couple to the 2D TE modes of the semiconductor) (Berini 2000) (Lafone, Sidiropoulos et al. 2014). The amount to which the effective index of the TM mode in region II is raised (coupling strength) depends on the dielectric thickness and semiconductor slab thickness, whilst the metal dimensions also affect loss.

The effective index of the TM mode in regions I and II and the TE mode in region I can be seen in figure 4.7 as a function of semiconductor slab thickness,  $T$ . It is evident that the effective index of the TM modes in region II are also highly dependent on the dielectric gap thickness,  $t$ .

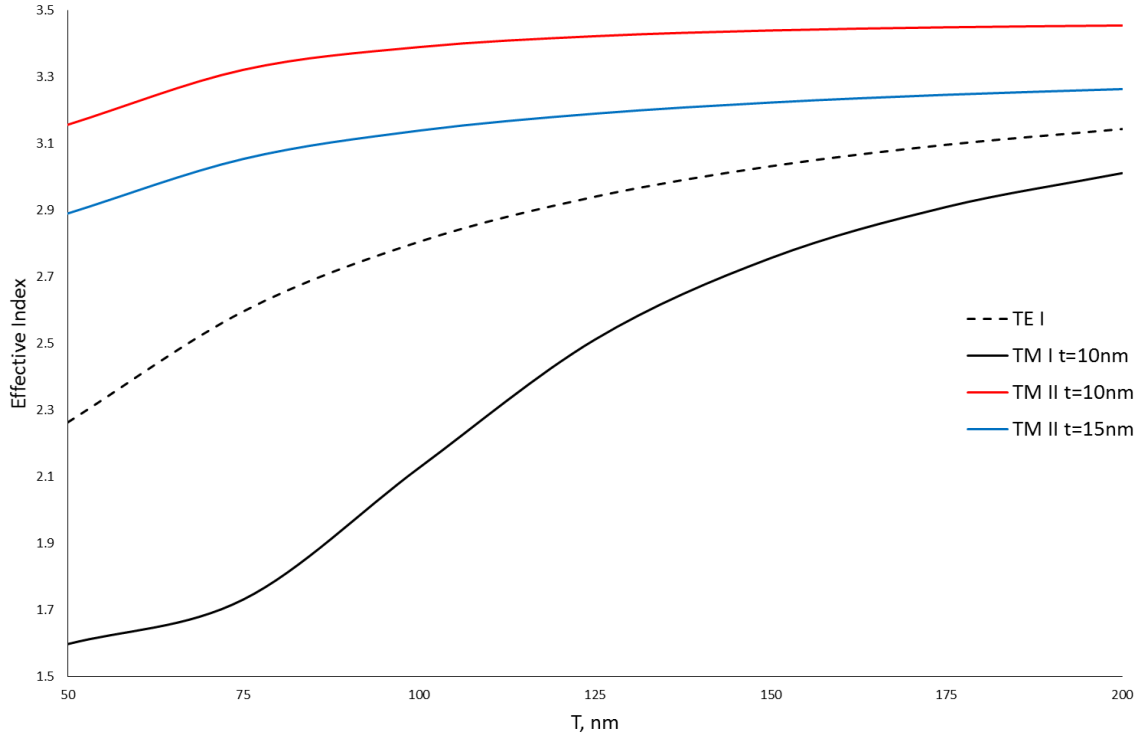


**Figure 4.7:** Effective index as a function of semiconductor slab thickness  $T$ . Included are the TE mode in region I, TM mode in region I at dielectric separation  $t=10\text{nm}$ , TM mode in region II with  $t=10\text{nm}$  and  $t=15\text{nm}$ .



It is evident that there is a large effective refractive index difference between the TM modes of region I and II, plotted for clarity in figure 4.8, allowing the propagation of a 1D TM mode in the  $x$  direction. The figure shows that a larger difference in refractive index is obtained for a smaller value of dielectric gap thickness,  $t$ , resulting in the need to use a very thin dielectric layer for strong lateral confinement.

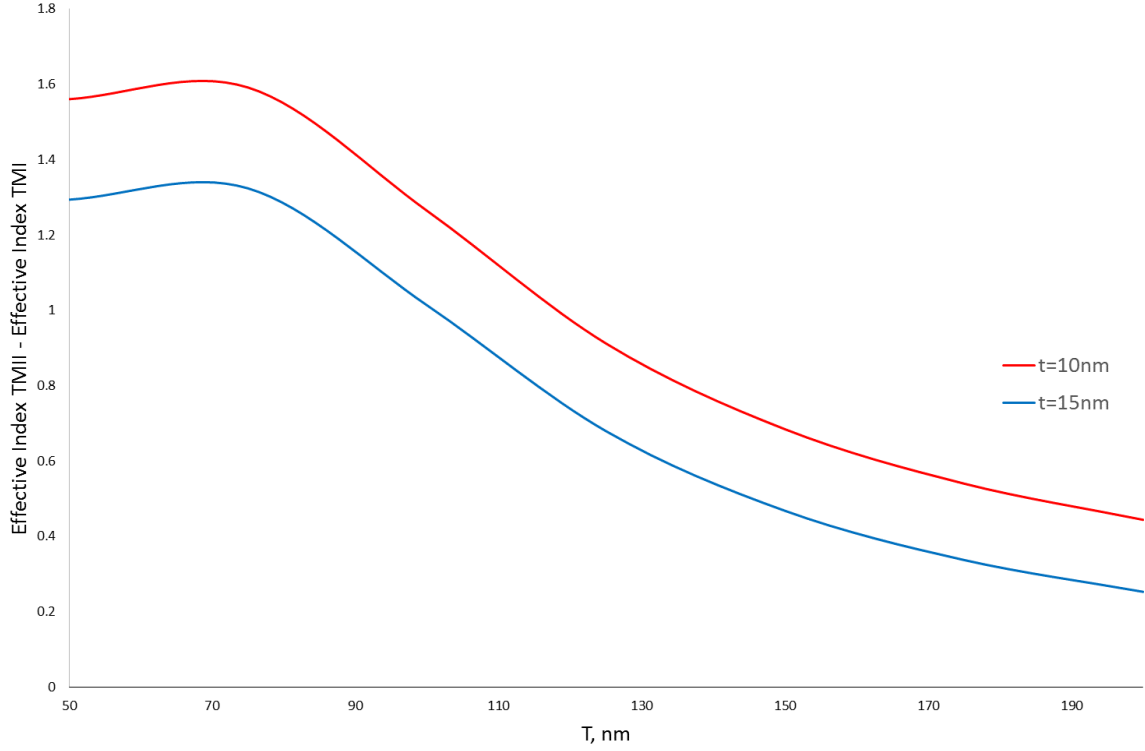


**Figure 4.8:** Effective index difference as a function of slab thickness  $T$  for TM mode in region I and II at different dielectric thicknesses,  $t$ .

The bound hybrid modes were modelled using a metal strip width of 150 nm. The mode cut-off, which is the point at which the hybrid mode couples to the TE component of region I and propagates as a 2D wave, can be seen by the discontinuity of the curves of figure 4.9. Most prominently just a single nanometer change in the dielectric gap thickness can alter the mode cut-off by a semiconductor slab thickness of up to 100 nm at small gap thicknesses. This sensitivity is consistent with the results of Lafone et al. This high sensitivity on dielectric gap thickness necessitates the need for the very precise growth or deposition of a dielectric layer for plasmonic devices.

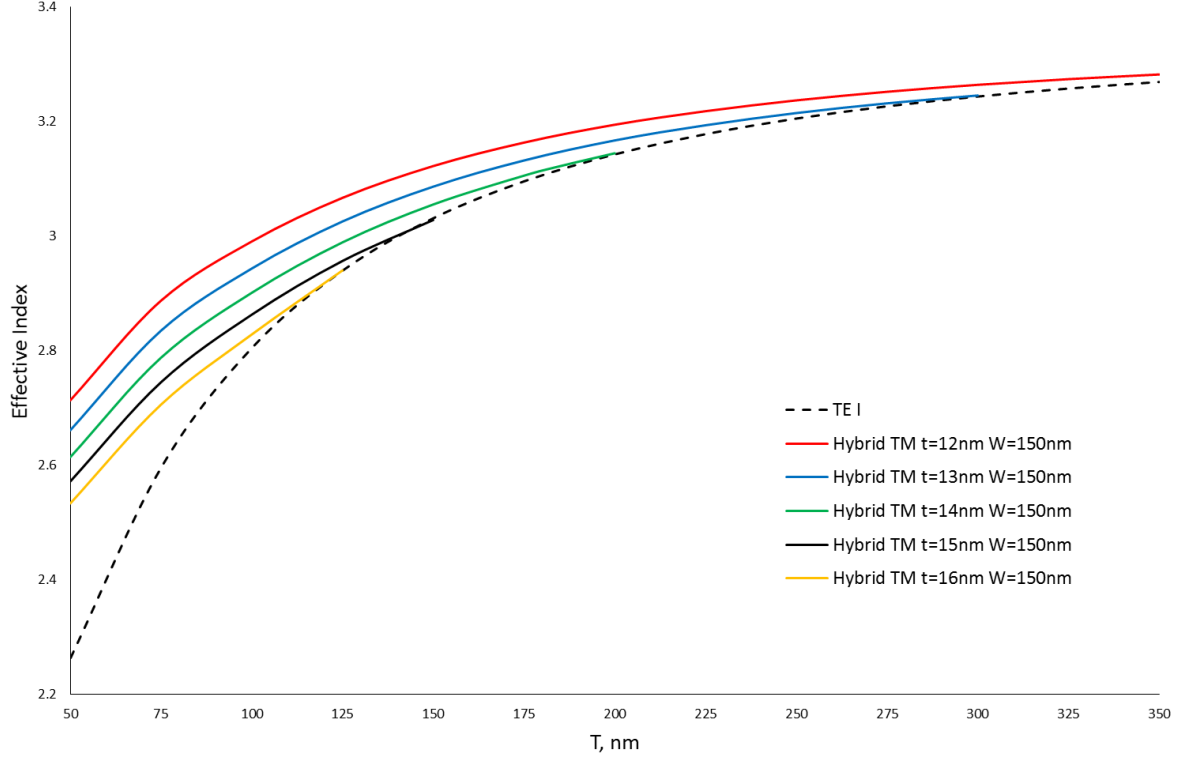


**Figure 4.9: Mode cut-off for 1D propagating hybrid TM waves as a function of semiconductor slab thickness  $T$ , and dielectric gap thickness  $t$ . The intersection of the TM curves with the TE curve of region I represents the point at which the modes propagate in 2D, therefore reducing lateral confinement of the mode.**

A smaller dielectric gap thickness,  $t$ , results in higher mode losses due to increased Ohmic interaction with the metal. However, figure 4.10 shows that the increased losses due to reduced dielectric gap thickness can be compensated for by an increased semiconductor slab thickness. Indeed, figure 4.9 also shows that a reduced dielectric gap thickness does allow for an increased semiconductor slab thickness before reaching mode cut-off.

The mode was modelled for a 200 nm semiconductor slab thickness with a gap dielectric thickness of 12 nm, seen in figure 4.11. It is evident by the large absolute energy density in the dielectric layer shown by the vertical cross section profile of figure 4.11 that there is a mode enhancement within the dielectric layer. This is also represented by the red colour scale which is the highest energy density region. The horizontal cross section profile shows that the mode is highly confined laterally to the metal region.

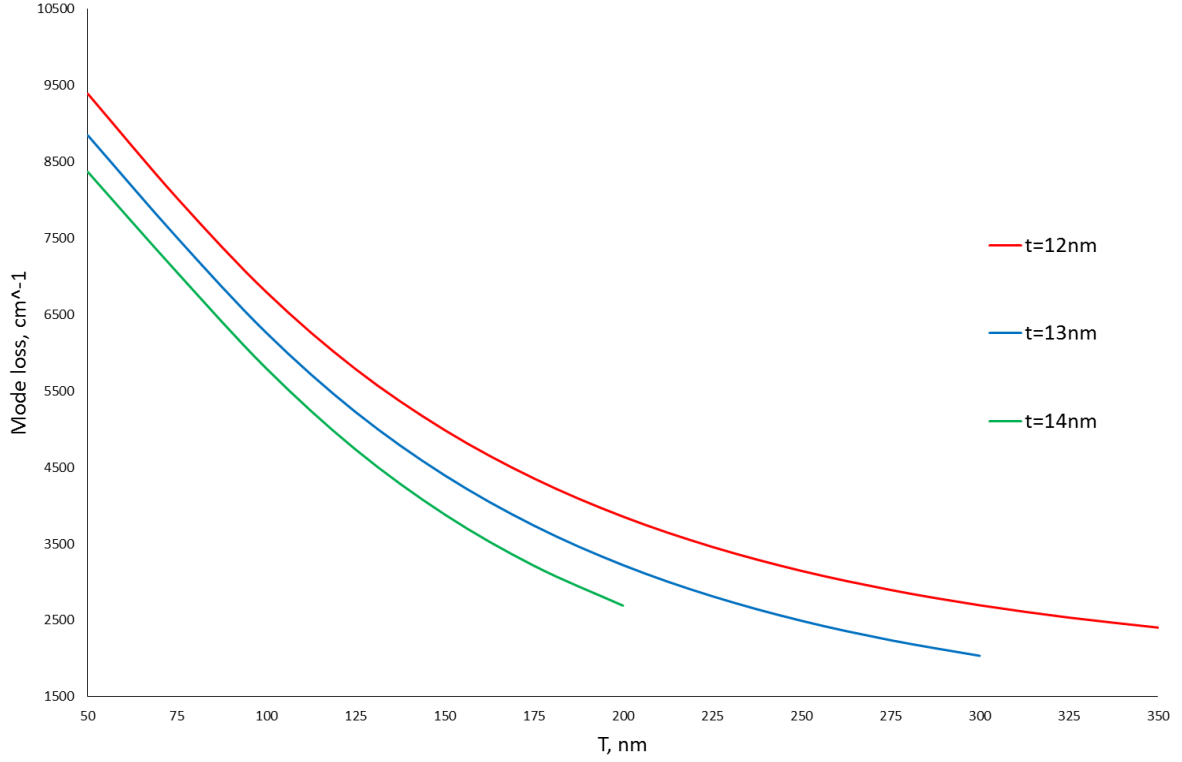


**Figure 4.10: Mode loss of hybrid TM mode as a function of semiconductor slab thickness and dielectric gap thickness. It is evident that increased losses due to decreased gap thickness,  $t$ , necessary for increased lateral confinement, can be compensated for by increased semiconductor slab thickness.**

The mode losses are very high even with compensation by an increased semiconductor slab thickness, which shifts the mode away from the absorbing metal region. A high modal gain is required to match absorption losses (to reach a positive net modal gain). For maximum modal gain a high material gain and a high confinement factor is required. The confinement factor is defined as the fraction of the power within the gain creating region. The confinement factor is proportional to the width of the gain creating region (or well width), whilst the density of states (gain) is inversely proportional to the width of the gain creating region. However, at large well widths or in bulk material there may be many extra energy states that contribute to the gain.

A confinement factor of 0.92 was calculated for a bulk semiconductor gain material (in the plasmonic configuration) with a semiconductor slab width of 300 nm, and dielectric gap thickness of 12 nm. The material gain required to enable the modal gain to match the absorption losses at the given confinement factor is approximately  $2900 \text{ cm}^{-1}$ . An increase in dielectric gap thickness of 1 nm decreases this material gain requirement by over  $700 \text{ cm}^{-1}$ .

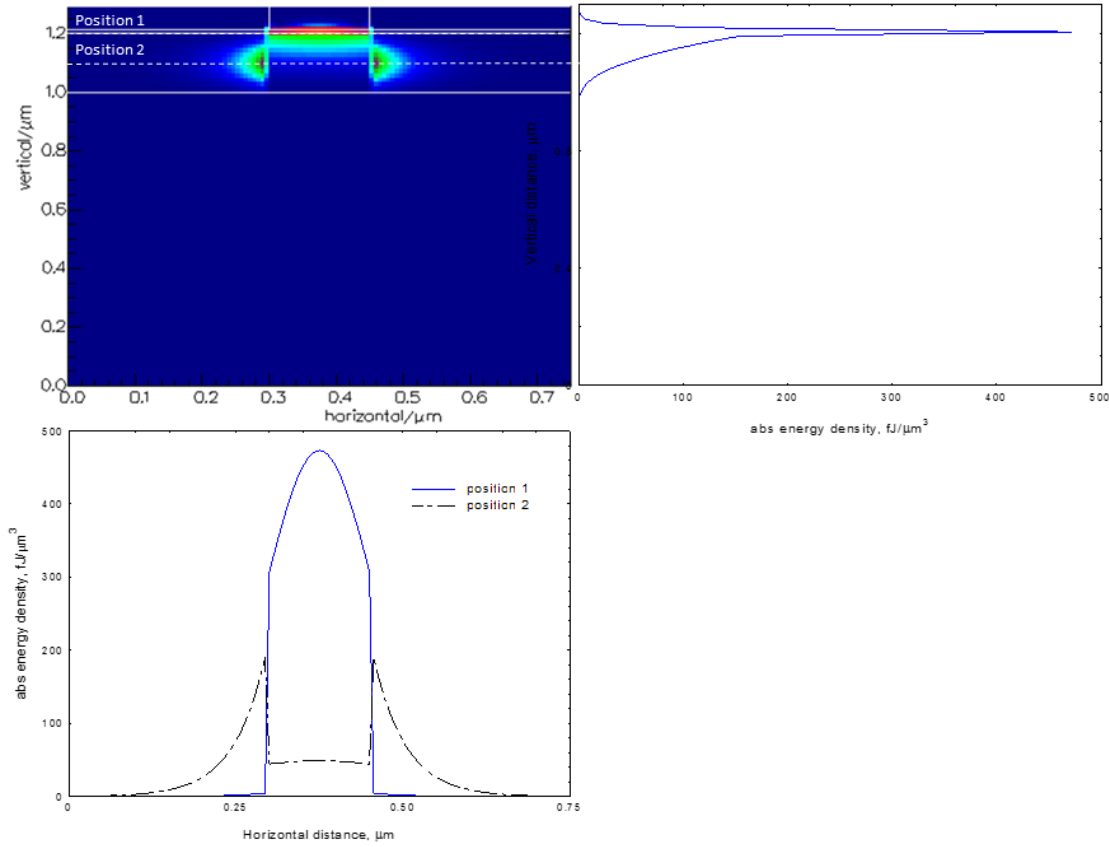


**Figure 4.11: Modelled mode for 200 nm semiconductor slab thickness, 12 nm gap dielectric thickness, 150 nm metal width. A 12 nm dielectric thickness was found to be most suitable through modelling, however, the 5nm grown GaAs layer did not reach this thickness upon oxidation to GaAs-Oxide. The x-axis on the vertical cross section profile, and the y axis of the horizontal cross section profile shows the absolute energy density with position. The colour grade of the graph, blue-red, indicates an increasing absolute energy density. The central rectangle above position 1 is the silver metal cavity. The region appearing red is the dielectric layer (GaAs-Oxide). The Quantum well sits at position 2.**

The confinement factor of the quantum well was calculated to be 0.05, the majority of the power resides closer to the metal layer (figure 4.11). The material gain requirement is approximately  $53000 \text{ cm}^{-1}$ , with a decrease of almost  $16000 \text{ cm}^{-1}$  with a 1 nm increase in gap thickness. The material gain that can be provided by the designed epitaxial structure was calculated from a fit to experimental data of a similar epitaxial structure (Smowton, P.M. Lewis, G.M. Chow, W.W. Jones, G. 2003), plotted in figure 4.12. It is noted that this is plotted to a high current density,  $J$ . The modal gain is plotted for the plasmonic structure in figure 4.13.

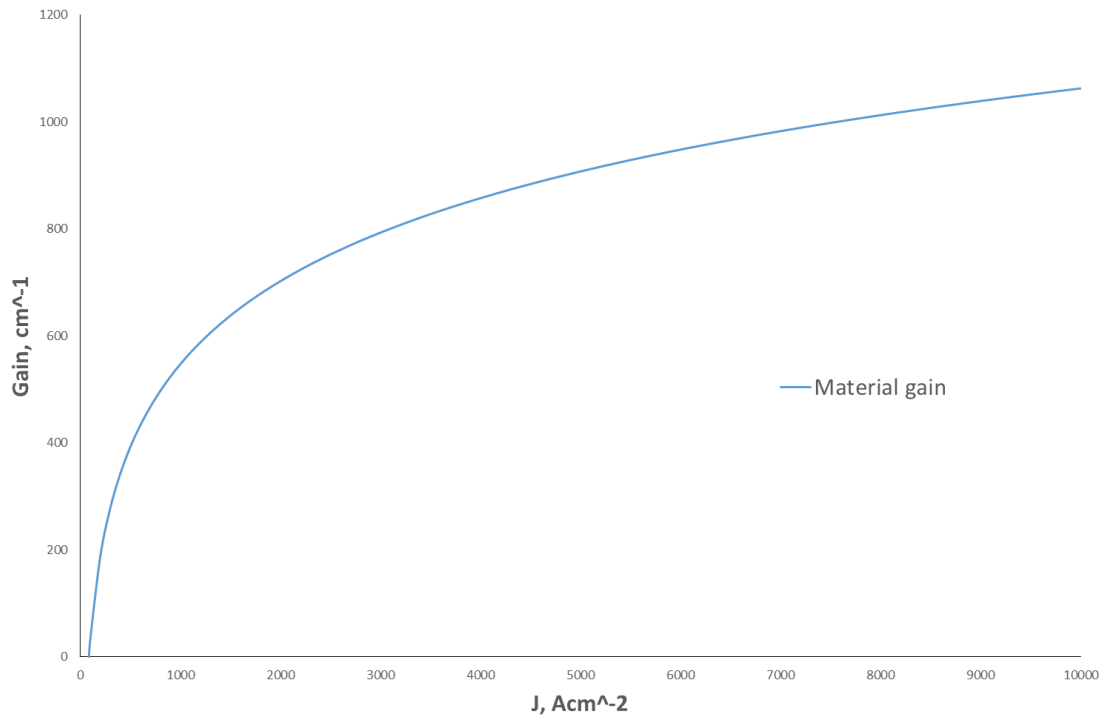


Figure 4.12: Material gain of similar epitaxial structure, extracted from literature (Smowton, P.M. Lewis, G.M. Chow, W.W. Jones, G. 2003). A fit to the experimental data of the modal gain of a  $50\mu\text{m}$  oxide isolated stripe test structure, and its calculated confinement factor, allowed the material gain to be determined.

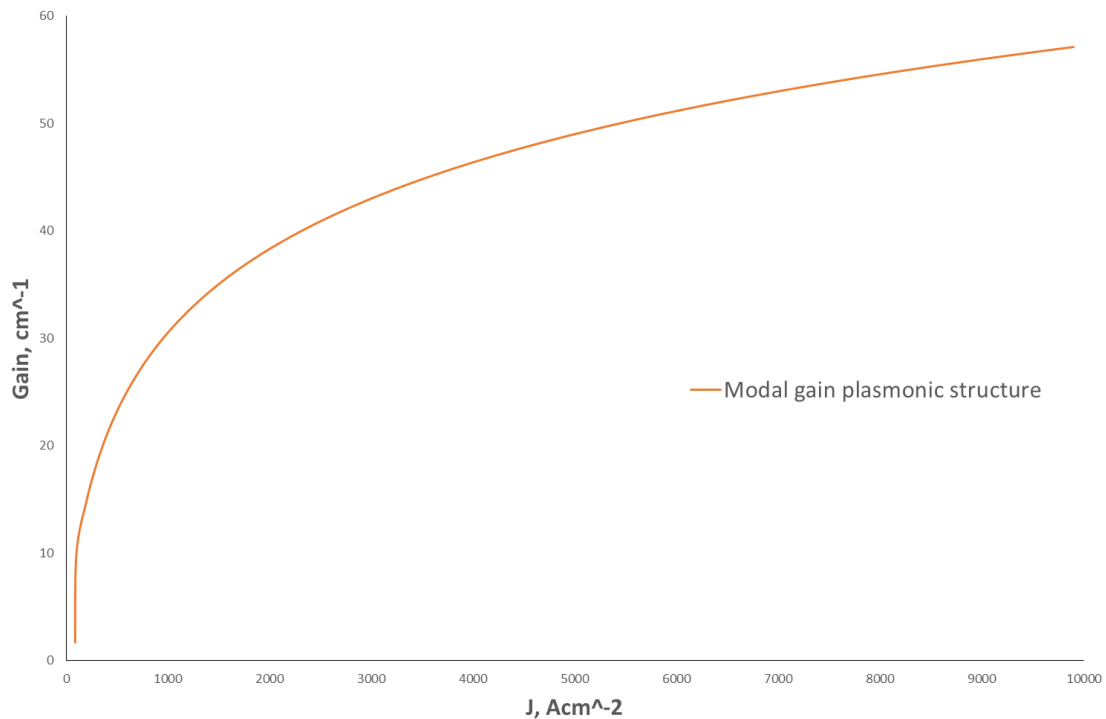


Figure 4.13: Modal gain for the plasmonic structure was plotted using the calculated confinement factor and material gain derived from literature.

The calculations do not predict a positive net modal gain for the plasmonic structure with a single quantum well, however, a recent theoretical study (Ambati, Genov et al. 2008) using a silver layer sandwiched between multiple tensile strained quantum well heterostructures has shown potential for lasing, indicating that the use of multiple quantum wells in a different configuration is a viable route to producing a hybrid-plasmonic nanolaser.

The gain requirement analysis carried out does not take into account the enhancements associated with the nanolaser design. In particular it does not include the enhanced spontaneous emission rate of the quantum well due to the change in the local density of states associated with the surface plasmons. This enhanced spontaneous emission rate affects the photon rate equation. The modification of the spontaneous emission rate compared to its free space spontaneous emission rate is quantified by the Purcell Factor as described in section 2.3.2. In addition few modes exist within a small modal volume, the enhanced emission is channelled into the few existing modes reducing the apparent threshold of the device. Furthermore, a reduced energy velocity at the metal interface has been theorised to exist near the surface plasmon-polariton resonance, resulting in a modal gain that is larger than the material gain. It is theorised that such a structure is able to produce a “giant modal gain” that is 1000 times larger than the material gain in the semiconductor (Li and Ning 2009).

Whether or not laser action can be achieved with the designed configuration, it is clear that a practical device requires precise control over the dielectric gap and semiconductor slab thickness. This work approaches the experimental realisation of the growth of a dielectric gap with high precision, with the definition of a semiconductor slab thickness via the hydrolisation of AlGaAs at elevated temperatures.

## 4.3 Device Fabrication

### 4.3.1. Nanosquare electrical injection

The nanosquare structure is described in section 4.2, a schema of the device can be found in figure 4.14. The device provided a platform to investigate the development and limitations of suitable nanoscale fabrication techniques. The nanosquare device incorporated nearby electrical injection pads to allow carrier recombination to occur within the quantum well beneath the nanosquare. The configuration of the pads relative to the nanosquare are shown in figure 4.14. The material was etched to reach the lower contact, resulting in a vertical injection scheme.

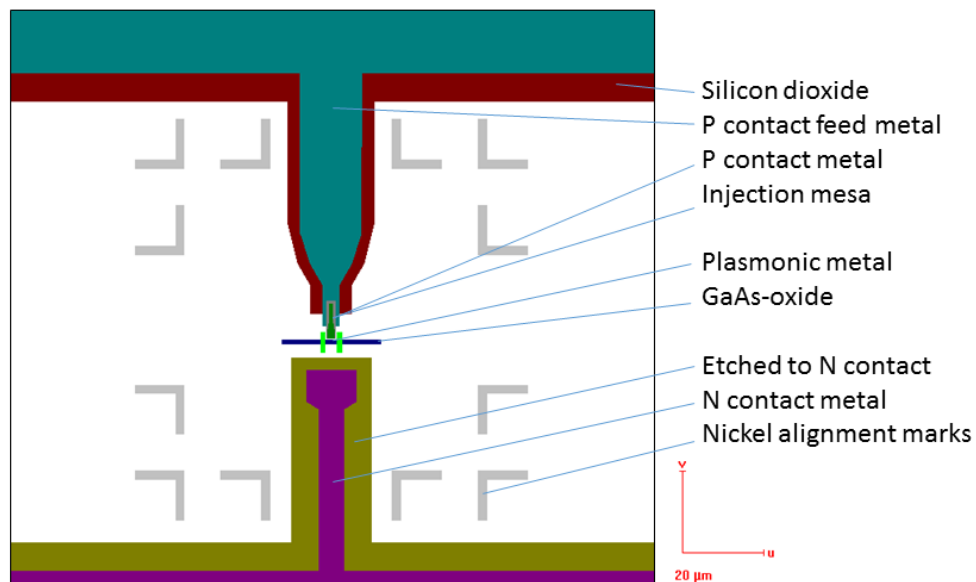


**Figure 4.14:** GDSII image created using e-line Raith software showing the nanosquare structure with electrical injection components. P and N refer to the doping of the contact layers. Plan view.

A “standard” red emitting quantum well wafer was used to investigate the prospect of electrical injection using this configuration. Most notably there are a large number of fabrication steps involved in producing a device of this configuration, many of which require a high amount of precision.

The complex process flow had 21 major steps, utilising a wide combination of fabrication techniques. The steps included photolithography and lift-off, electron beam lithography (using positive and negative tone resists), wet chemical etching, ICP and RIE etching, e-beam evaporation, thermal evaporation, anodic oxidation and rapid thermal annealing. A number

of techniques and wet etches were developed specifically for this wafer structure. Certain aspects of the device required spatial precision, achieved by using local alignment marks when performing e-beam lithography.

An image of the fully constructed device including an anodic oxide can be seen in figure 4.15. Two parallel plasmonic nanosquares are located in the centre of the image, highlighted by the white arrow. Their in-plane cavity dimensions are defined by the cross-over of the silver stripes visible in the image with the underlying oxide stripe. These nanosquares sit in-front of and either side of the shallow injection mesa, and are approximately  $1\mu\text{m}$  square.

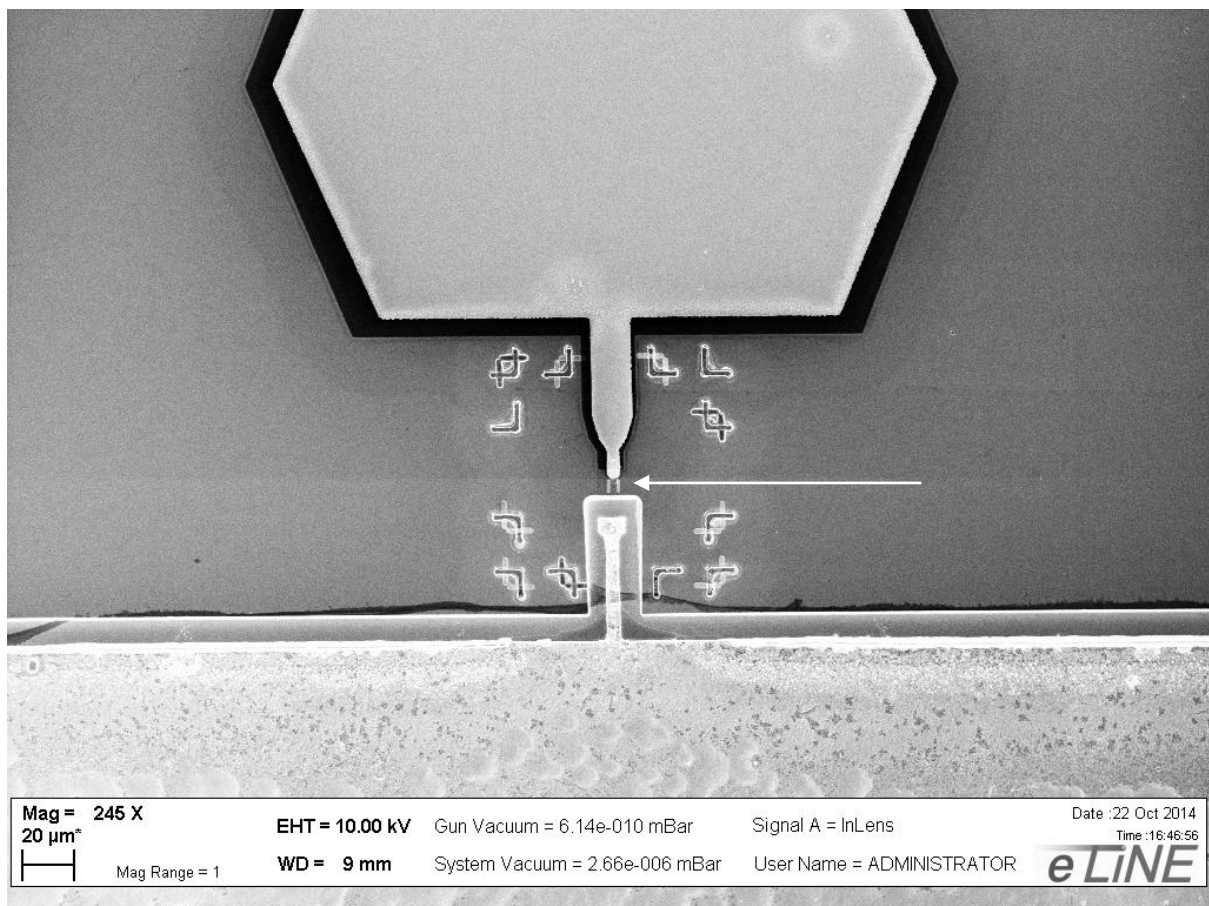


**Figure 4.15: Fully fabricated nanosquare device with electrical injection, devices are indicated by arrow.**

Rather than producing an exhaustive process flow for the fabrication of the device, two primary lessons that relate to nanofabrication and device configuration are presented. These factors are the important issue of alignment when producing small nanostructures within the context of a larger architecture, and the feasibility of the electrical injection



scheme presented. Additional important factors in nanofabrication include precision e-beam definition and clean edge definition when performing metal lift-off procedures. However, these factors have previously been investigated (Ding and Ning 2013), and implementation of similar optimised procedures within this work have not been found to be highly problematic.

#### 4.3.2. Alignment Procedures

Alignment marks are structures initially placed on the sample at the start of the fabrication procedure, to which other patterns can be aligned. During photolithographic alignment procedures new alignment marks can be created during the exposure of the mask. The quality of alignment marks are essentially the most important part of the process flow.

The designed pattern contains a number of features used for alignment, shown in figure 4.16. These alignment marks are placed in a specific order within the process flow, and are not all placed at the start of the process.

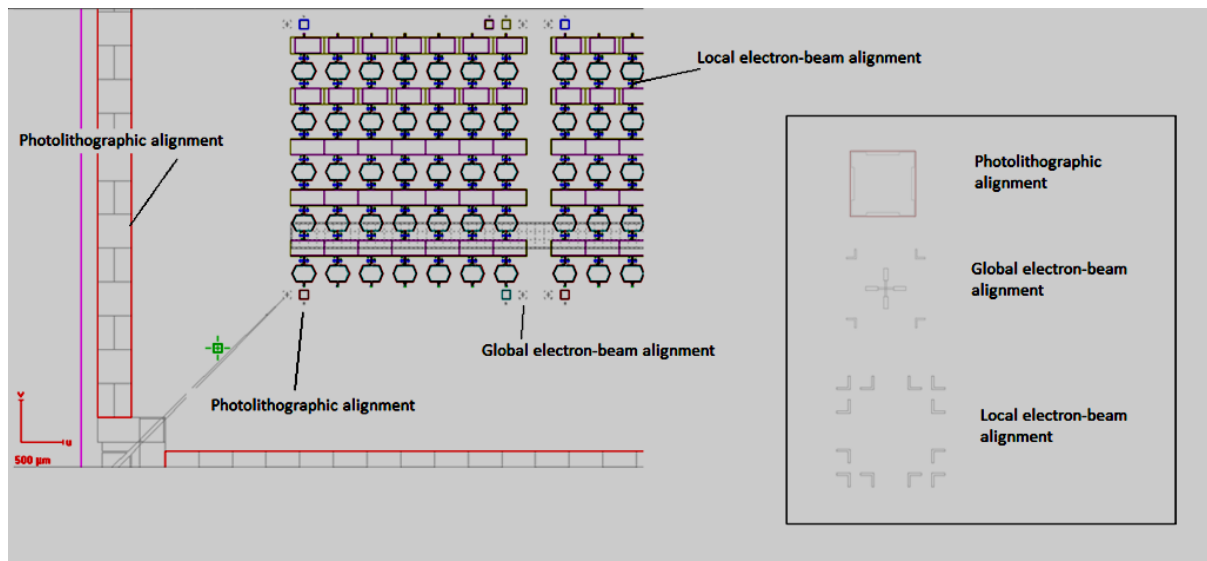


**Figure 4.16: Alignment marks used, shown in GDSII design pattern.**

The initial set of alignment marks were fabricated using photolithography and Ni deposition. Photolithographic marks were set within 100μm squares with mark sizes in the order of a few μm. The design of the first stage of alignment marks can be seen in figure 4.17. The field shown holds 63 devices.

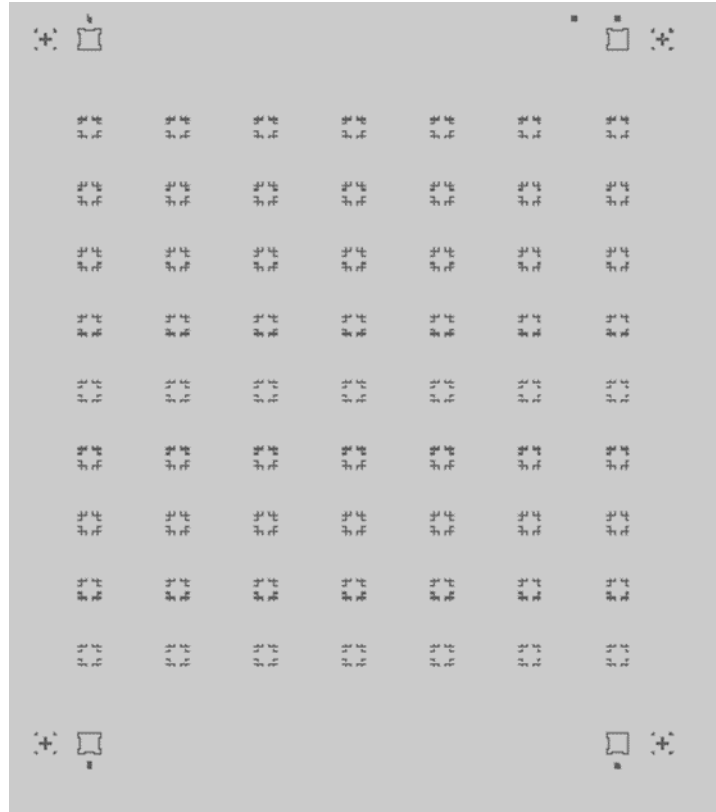


**Figure 4.17: First stage alignment marks for e-beam and photolithographic alignment steps.**

The photo-lithographically defined alignment marks were placed using a bi-layer photoresist consisting of a PMGI polymer and a S18 resist. A schema of the bi-layer metal lift-off process, compared to a single resist lift-off process, can be seen in figure 4.18. To ensure good feature resolution the resist edge-bead that forms at the edge of the sample after spinning of the resist was removed using photolithography. This can otherwise affect the size and position of patterned features.

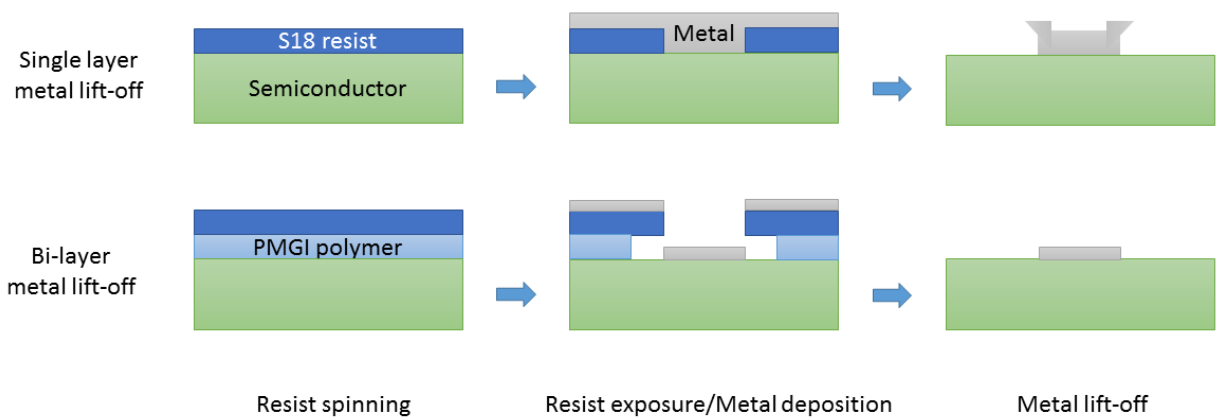


**Figure 4.18: Single and bi-layer metal lift-off technique comparison.**

It can be seen that the resultant metal structure for a single resist lift off-technique has uneven and broken edges. This is particularly evident when metal thicker than the resist is deposited. A bilayer technique utilises PMGI as the lower polymer layer which, when developed using MF319, produces an undercut profile that stops the formation of a continuous metal layer and hence prevents the tearing of metal during the lift-off procedure. The lift-off is performed using acetone and 1165 microdeposit remover in succession.

The device process flow, showing only the alignment steps rather than the whole process flow for simplicity, can be seen in figure 4.19. Included are four photolithographic alignment steps and four local e-beam alignment steps. Alignment steps 2 to 3 were used for the shallow electrical injection mesa and mesa contact metal. Alignment steps 4 to 6 were used for the bottom n contact etch, metal deposition, and definition for the anodic oxide. Alignment step 7 to 9 were used for the plasmonic metal, the top insulator pad, and the top feed metal.

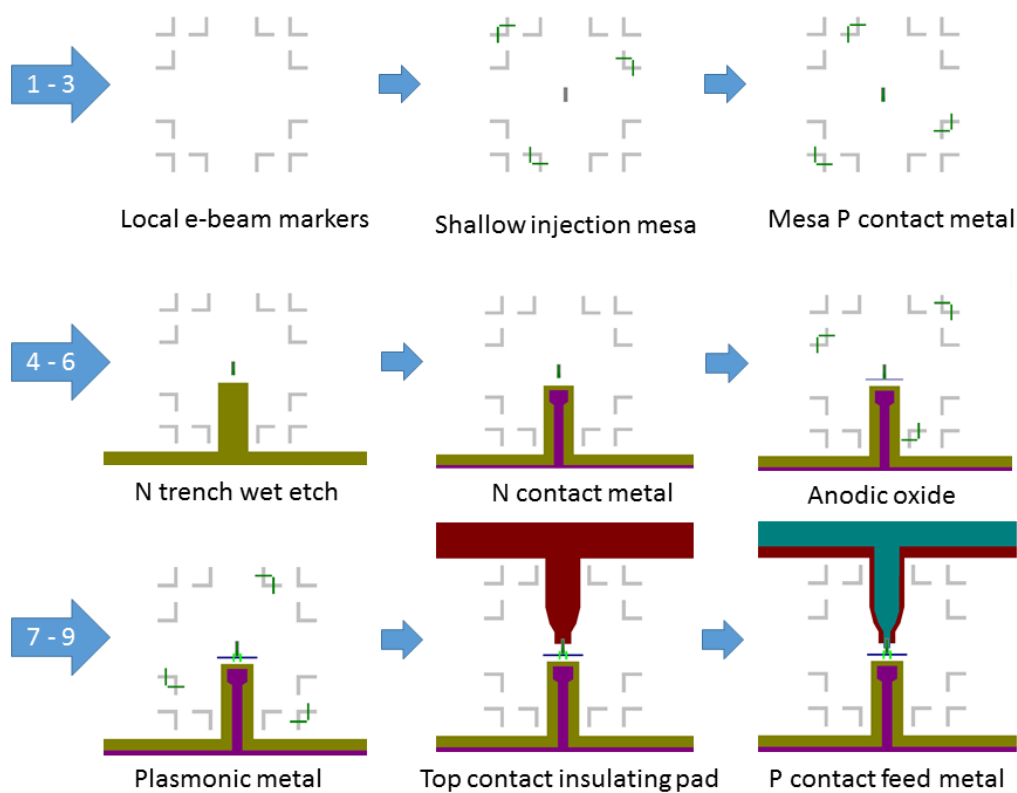


**Figure 4.19: Photolithographic and e-beam alignment steps, shown using GDSII design pattern. Green lines on local e-beam alignment marks are scanned marks for written layer. Steps 6 and 7 were performed after steps 8 and 9 on various samples.**

Each e-beam local alignment step used three e-beam marks, utilising an inbuilt scan algorithm to determine the locally adjusted position to pattern the structure. The photolithographic alignment steps were performed by aligning to structures patterned on the surface, as shown in figure 4.20.

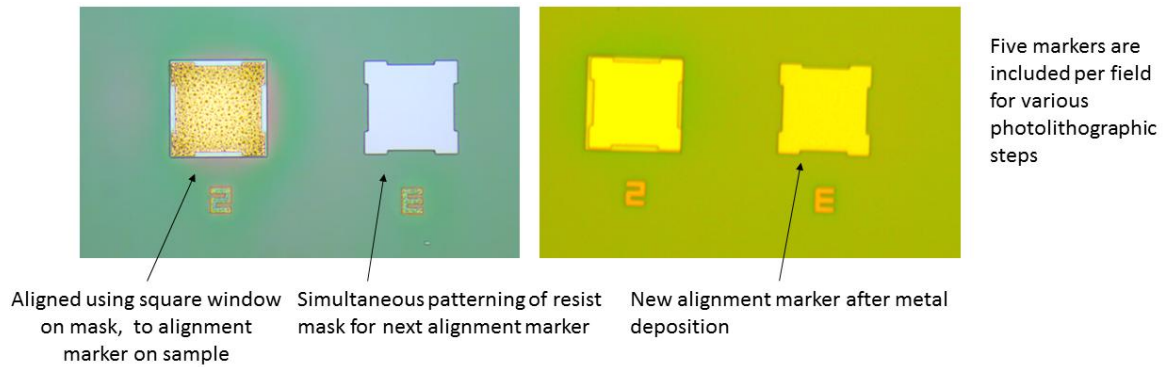


**Figure 4.20: Photolithographic alignment procedure.**

The yield of devices that can be successfully fabricated using a process flow that requires the precision use of local e-beam alignment was examined. The alignment of the top metal contact to the shallow etched injection pad was used for this investigation. The shallow injection mesa and the top injection pad were aligned using local e-beam alignment procedures on different local e-beam markers.

A negative tone e-beam resist Ma-N2401 was used as a mask for the shallow electrical injection mesa, an adhesion promoter HMDS was also used. The area of the shallow injection mesa was defined using e-beam global and local alignment mark protocols. This was then etched using an ICP with a  $\text{Cl}_2/\text{Ar}$  plasma, the resultant structure can be seen in figure 4.21.

The positive tone e-beam resist, PMMA, was then used to define the metal contact on top of the shallow injection mesa. Dose tests were used to select a dose that gave sharp features. A Zn/Au contact was deposited and annealed. An example of the structure with the first two sets of local e-beam alignment marks scanned can be seen in figure 4.22.

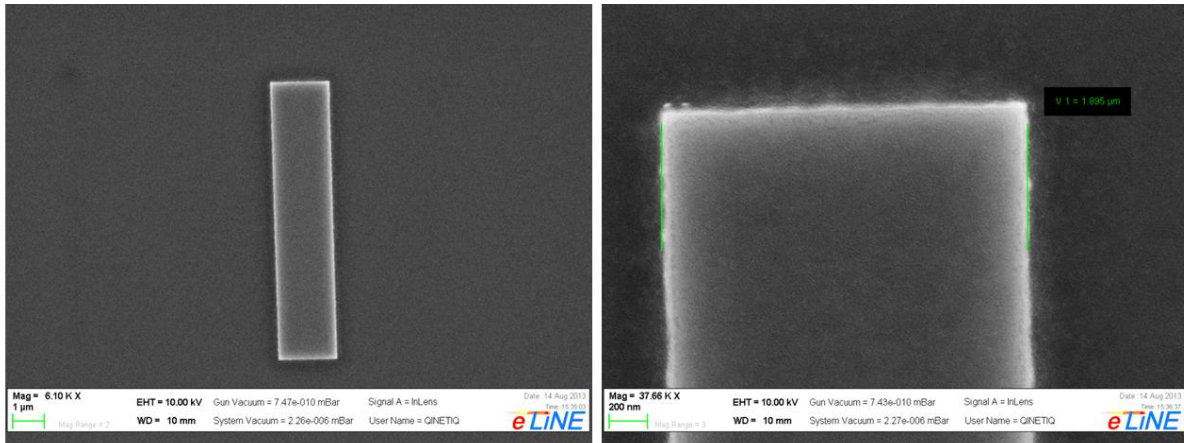


**Figure 4.21: ICP etched shallow injection mesa defined using negative tone e-beam resist**

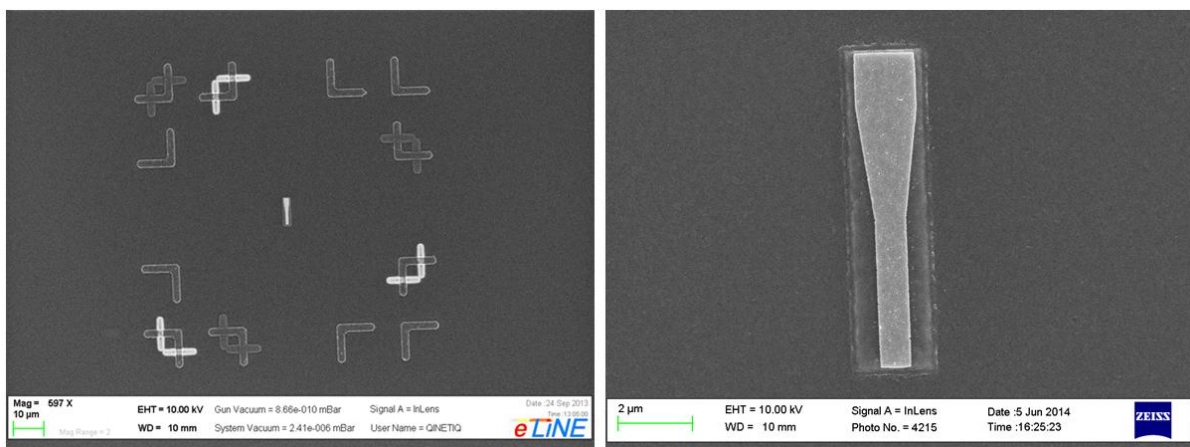


**Figure 4.22: Aligned and annealed metal contact on shallow mesa.**

Automatic e-beam alignment procedures were found to have a high precision, but also a high failure rate. The positional errors of features that fell outside of the acceptable bounds of the required alignment were consistent with the positional errors of procedures in which no local alignment was applied. Approximately only 50% of devices successfully applied both sets of local e-beam alignment for this part of the structure. The devices that sat outside of the bounds of required alignment were clustered together on the sample, indicating that either the initial photolithographic steps were imperfect due to a variation in resist thickness or mask contact, or that a varying focus/brightness/contrast existed across the sample when applying the automatic scan algorithm, resulting in the alignment procedure to be completely aborted. Further alignment procedures for the oxide and plasmonic metal definition, and the ability to closely align the wet etched N contact to these devices, are shown in figure 4.23.

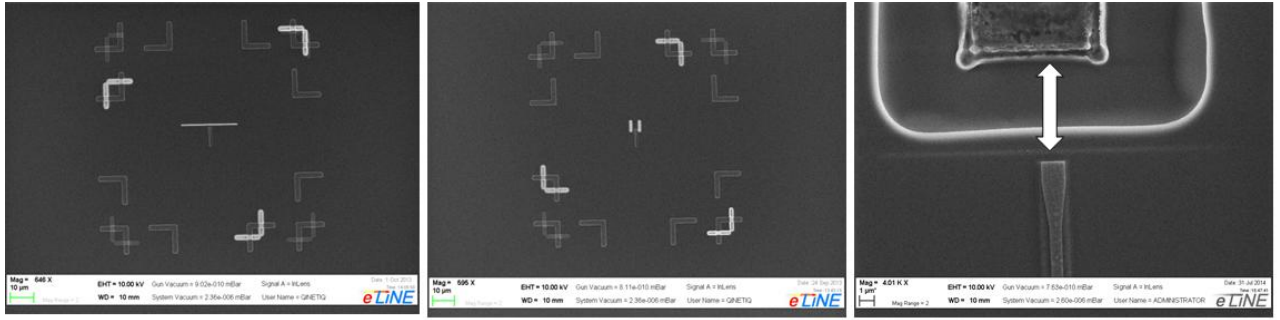


**Figure 4.23: E-beam and photolithographic alignment of structures.**

Although the techniques used in fabrication of this device were not intended to be directly scalable for production, it is fairly evident that the complexity and precision required for this device configuration is inhibitive. It can be concluded that any plasmonic nanodevice should contain more self-aligned steps due to the challenges of nanofabrication. The perpendicular crossing of the oxide and plasmonic metal in this design achieves self-alignment, however, precise alignment for an electrical injection scheme is impractical. A possible solution utilises the steam oxidation of AlGaAs to produce a current aperture placed to encourage recombination beneath the nanosquare. This relies on the precision oxidation of AlGaAs which has been explored in this work.

#### 4.3.3. Current-voltage measurements and contact metallisation

It has been stated that a “standard” wafer design was used for this device, resulting in the use of non-ideal low doped layers for the metal contact layers. The quality of the annealed contacts was investigated prior to current-voltage measurements. The specific contact resistivity of the contacts was determined using transmission line measurements (TLM) as described in section 3.2.4.

Suitable P type contacts for AlInP include Zn/Au whilst suitable N type contacts for AlInP include AuGe/Ni/Au (Baca, Ren et al. 1997). The results for the p-contact TLM measurements can be seen in figure 4.24.

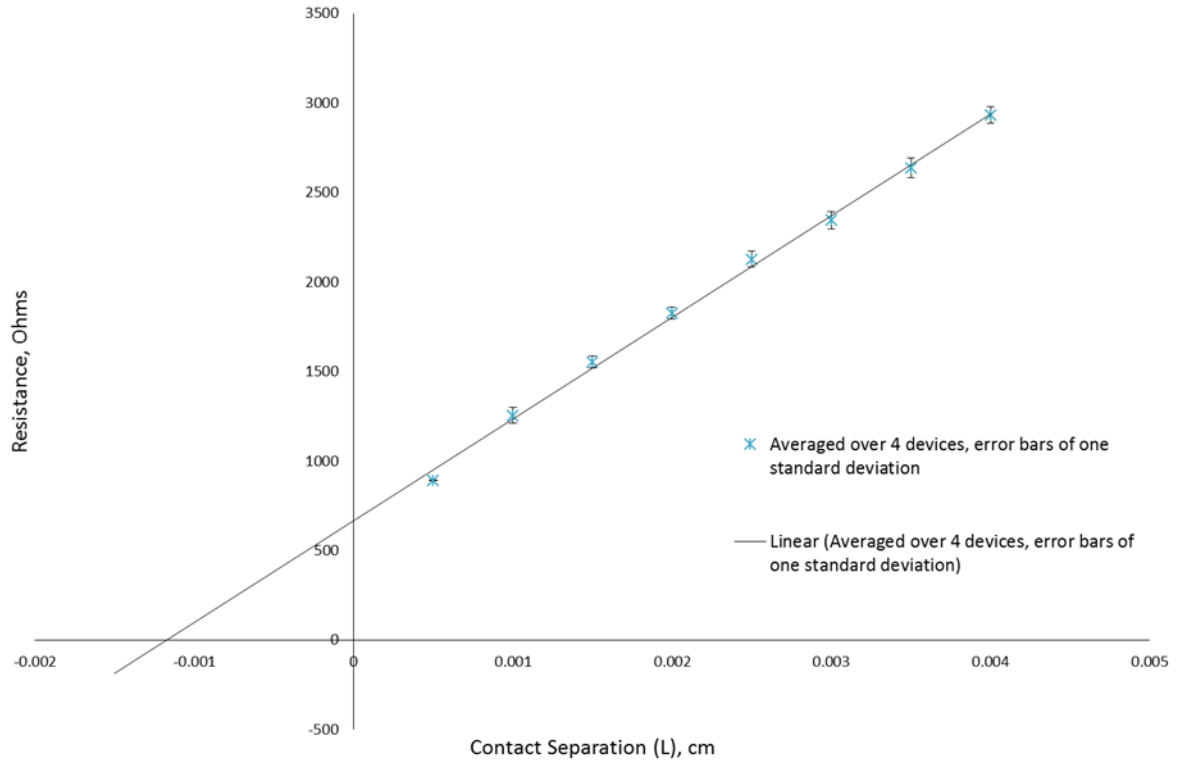


**Figure 4.24: Zn/Au contacts on low doped p AlInP annealed at 530°C, on an ICP etched surface.**

Initially the contact was annealed at 360°C as this has been reported to produce an Ohmic contact (Oparaku, Dargan et al. 1990) on low doped p-InP, however, the contact required annealing at 530°C to produce a good Ohmic contact. A specific contact resistivity of  $3 \times 10^{-3}$  ohms.cm<sup>2</sup> was achieved, which is an order of magnitude smaller than the lowest value obtained by Oparaku et al, which occurred at an anneal temperature of 450°C. Oparaku et al found that low contact resistance was associated with the Au-In phase, whereby the atomic percentage of In increases with temperature whilst the Au percentage decreases. The Zn phase appears at higher temperature. This explains the silvery rough appearance of the contacts in this work, a result of the in-out-diffusion of atoms in which empty lattice sites become occupied by Zinc, lowering the contact resistance.

The deviation from the linear line of best fit at 5µm in figure 4.24 is an indication of deep metal diffusion. For small contact separation lengths,  $L$ , the lateral diffusion of the metal due to a high anneal temperature is a larger percentage of the contact separation, which can be substantiated by the fact that the transfer length was calculated to be 5.8µm.

The specific contact resistivity is high in comparison to other contacts due to the low doping of the AlInP material, but also due to the metallisation used. Zn has a low sticking coefficient to InP, the reactivity and adhesion to InP can be improved using a Au/Zn/Cr/Au metallisation, where the lower Au layer aids adhesion, and the Cr layer prevents out diffusion of dopant atoms. However, this metallisation could not be performed in-house. In addition the low specific contact resistivity is symptomatic of the metallisation achievable in-house. Zn/Au contacts measured on highly p-doped GaAs processed in the same way gave a value in the same order of  $2 \times 10^{-3} \text{ ohms.cm}^2$ , which is 1000 times larger than expected.

In general P-type contacts to InP are difficult to create due to the large barrier height of most metals to p-InP, and a large hole effective mass that limits hole transport (Baca, Ren et al. 1997). For more highly doped p type InP ( $10^{18} \text{ cm}^{-3}$ ) a specific contact resistivity in the region of  $3.7 \times 10^{-5} \text{ ohm.cm}^2$  would be expected.

The results for the AuGe/Ni/Au contact to n-doped AlInP, with graded AlGaInP layers, annealed at  $430^\circ\text{C}$ , can be seen in figure 4.25. The surface was wet etched using a previous wet etch recipe that resulted in more severe surface height undulations, resulting in some variation in TLM results. Data was taken from a region that was more uniform in height. A specific contact resistivity of  $4 \times 10^{-6} \text{ ohms.cm}^2$  was obtained at  $430^\circ\text{C}$ , the anneal temperature was high due to the AlGaInP graded layers. The specific contact resistivity obtained is a magnitude lower than that reported for a AuGe/Ni/Au contact on n type GaP containing material, which had a value of  $6.8 \times 10^{-5} \text{ ohms.cm}^2$  when annealed at  $530^\circ\text{C}$  (L. Peternai 2003).



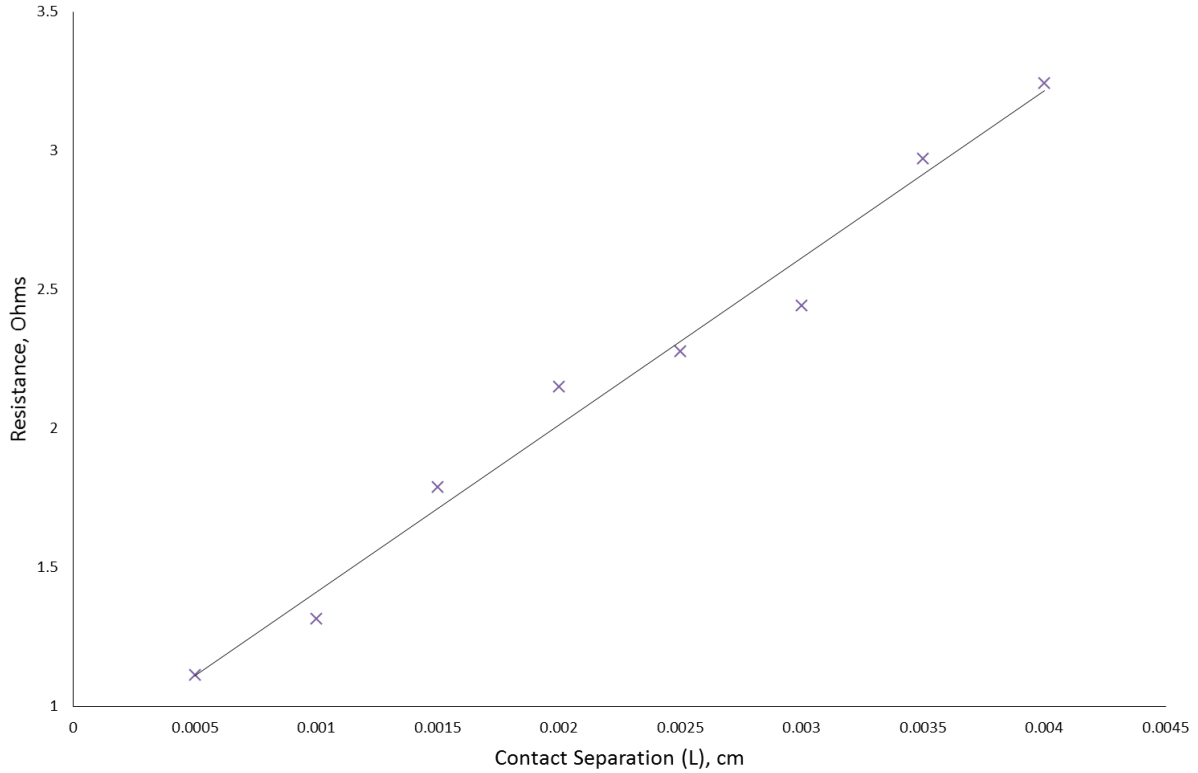


**Figure 4.25: AuGe/Ni/Au contacts to low doped n AlInP/graded AlGaInP, annealed at 430°C, on a wet etched surface.**

The current-voltage (IV) characteristics of the fully fabricated nanosquare devices were investigated by using probes connected to a Keithley current source, and also with gold wires bonded to the contact pads using silver epoxy. The results can be seen in figure 4.26. The probe tests were performed sequentially, with an upper current limit set. It is apparent that there were gradual break-through events indicating continual annealing of the contacts. The results tended to an IV characteristic with a threshold above the bandgap of the semiconductor, necessary for population inversion. However, repeated testing resulted in the p contact delaminating, potentially as a result of heating within the small injection mesa, and the high p contacts specific contact resistivity due to low doping.

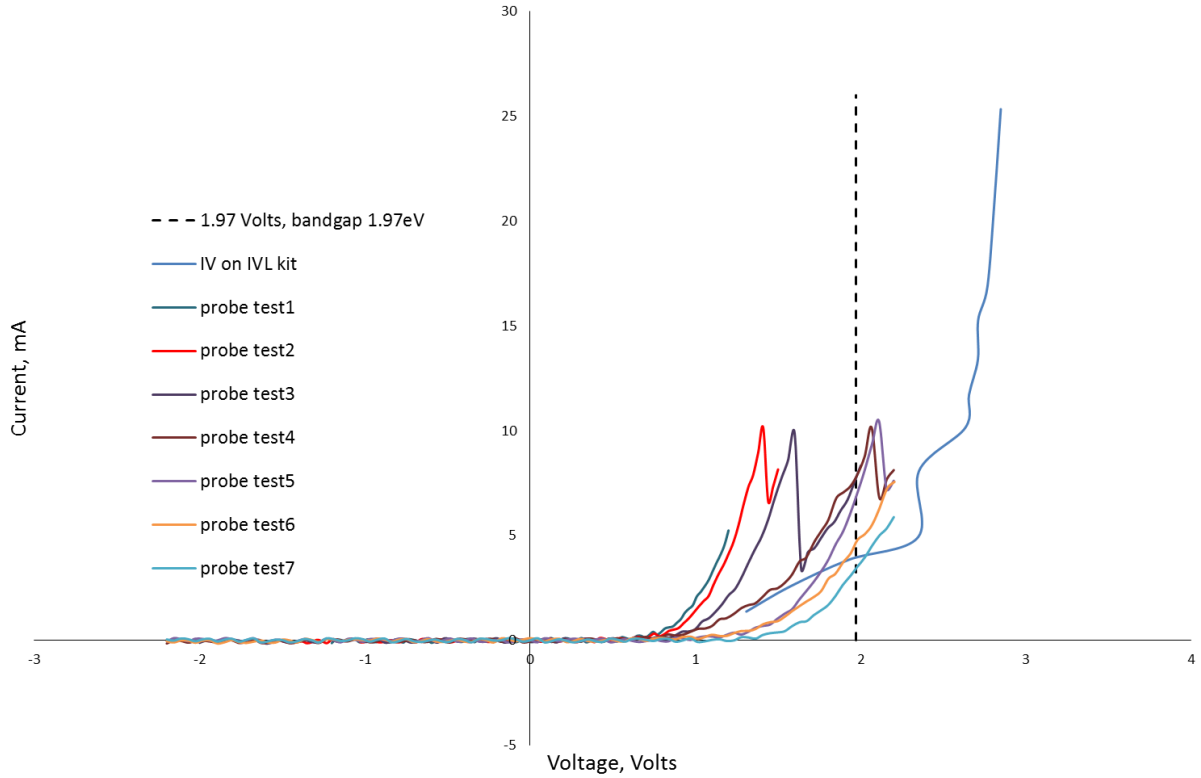


**Figure 4.26: IV characteristics of nanosquare device. The probe tests were performed sequentially with an upper current limit, showing gradual break-through events. The IV test on the IVL kit was performed after connecting gold wires using silver epoxy.**

In conclusion, the complexity and precision required for this vertical electrical injection scheme makes it impractical and inhibitive to employ, even with the use of highly sophisticated electron beam local alignment procedures. The heating effects associated with injection of a small mesa, although exacerbated here due to low doping, puts doubt on the feasibility of this electrical injection scheme. There is a potential for an increased contact resistivity for small area contacts due to charge screening effects, the reduction of the junction cross-section and increased depletion width. In addition the current density required to match losses within the device are very high due to the increased recombination rates due to the Purcell effect. Throughout the development of this work it has become clear within the plasmonic community that the prospect of electrically injecting a plasmonic nanolaser (particularly with sub-wavelength dimensions in all three directions) is at best uncertain (Khurgin and Sun 2012, Khurgin 2015) (Khurgin 2015). This work confirms the difficulties in the practicality of electrically injecting a plasmonic nanolaser using this type of electrical injection scheme.

#### 4.3.4. Current apertures

To further explore the potential of fabricating a plasmonic device with electrical injection a device was designed that incorporated a current aperture through the oxidation of AlGaAs, a large area metal contact to reduce heating, and reduced optical confinement in one direction (x) to reduce the required current densities for operation. A schema of the device can be seen in figure 4.27.

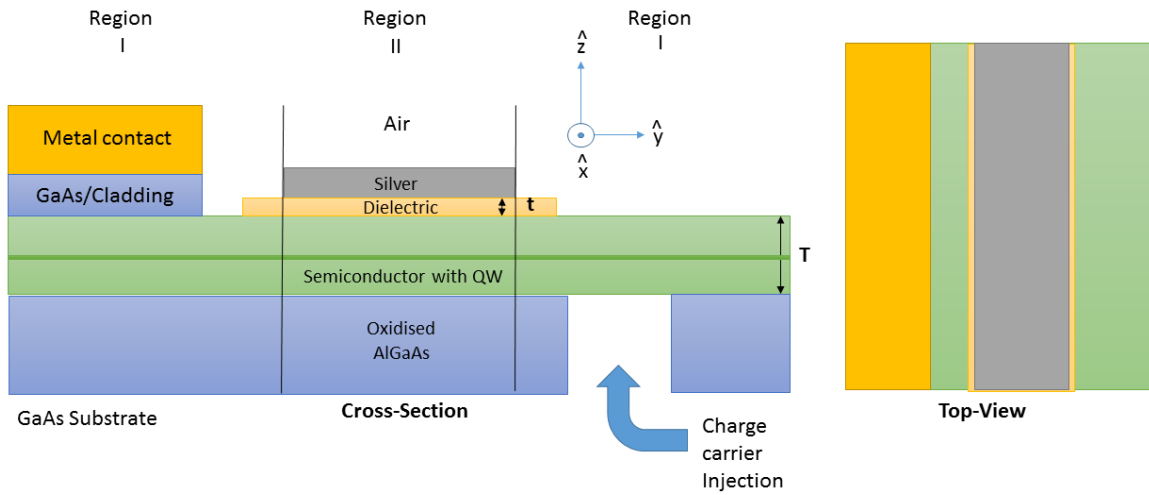


**Figure 4.27:** Schema of hybrid-plasmonic device with a current aperture for electrical injection and reduced optical confinement in the x direction compared to the nanosquare design.

Figure 4.28 shows SEM images of the cleaved tilted cross-section of fabricated devices.

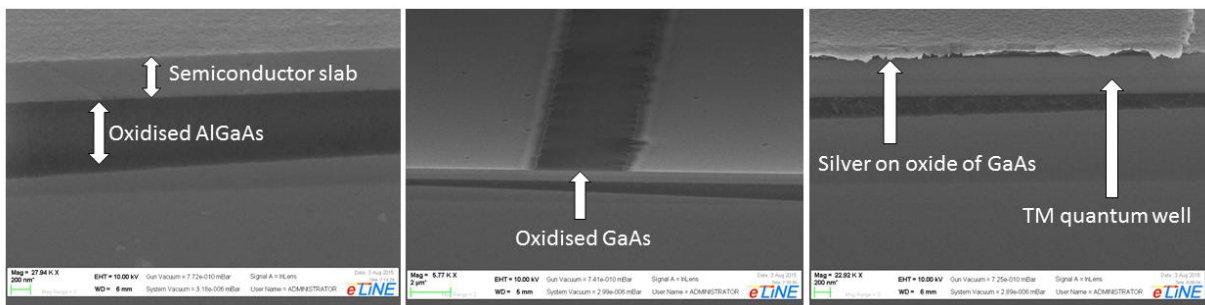


**Figure 4.28:** Cleaved cross-sections of hybrid plasmonic device with current apertures.

The lower AlGaAs was oxidised by first etching trenches and oxidising from the edge of the structures as described in section 3.3.2. The cleaved edge of the plasmonic metal is rough, however, this device is cleaved for imaging purposes only. The anodic oxidation and silver deposition was performed using a single photolithographic mask, simplifying the process

without the need for alignment. Although a fully operational device with contacts was not fabricated, two aspects of the fabrication were explored in more detail, these are the anodisation of GaAs and the steam oxidation of AlGaAs, as described in the following sections.

[This space intentionally left blank]

## 4.4. Dielectric gap via anodisation of GaAs

This section describes the anodisation of GaAs for the fabrication of a dielectric gap as part of the hybrid-plasmonic device design. The dimensions of the dielectric gap are crucial for mitigating Ohmic losses, as described in section 4.2.

### 4.4.1. Thickness control and composition

Control of the thickness of the grown oxide is crucial for the hybrid-plasmonic device, as described in section 4.2. The method of anodisation of GaAs is described in section 3.2. Figure 4.29 shows a linear increase of oxide thickness with oxide growth time, plotted in terms of the drop in measured current density (as described in chapter 3). Oxide thickness was measured using height profilometry, spectroscopic ellipsometry and in some cases atomic force microscopy. The linearity of the collected data suggests a fair experimental control of grown oxide thickness, even for thin films. However, at very low thicknesses there is a delay in increased growth, the thickness remains at 3nm for some time until a higher current drop density is reached for further growth. The time delay due to a low starting anodisation current is advantageous, as described in chapter 2, because it indicates a precursor or higher resistive  $\text{Ga}_2\text{O}_3$  layer formation that is required for high density oxides.

It is possible to elucidate the composition of the oxide by determining its density. A good quality oxide of GaAs has a higher ratio of  $\text{Ga}_2\text{O}_3$  to  $\text{As}_2\text{O}_3$ , and under these conditions has a density closer to that of the original GaAs. The consumption of GaAs and formation of oxide with a thickness ratio of approximately 3:4 (Hasegawa, Forward et al. 1975) is known to possess good electrical characteristics and increased uniformity, where the  $\text{Ga}_2\text{O}_3$  compound likely dominates over the  $\text{As}_2\text{O}_3$  compound.

A compositional analysis has been done using Faraday's law of electrolysis, which is described in section 2.4. Due to only very small decreases in current (from the constant starting current) during growth the analysis uses a constant current model, resulting in a good fit, as shown in figure 4.30. Included in the figure are model results for an oxide with a density equivalent to that of the original GaAs. The experimental results exhibit a density that is 5/8 of this amount, only fractionally less than the 3/4 expected from literature, which is a good result. This indicates that a higher proportion of  $\text{As}_2\text{O}_3$  may remain than is

achievable using this growth method. The excess of  $\text{As}_2\text{O}_3$  may be due to insufficient dissolution, which can be improved by adjustments to the duty cycle of the pulsed voltage. The model fit to the experimental results has a constant offset, which can be attributed to the experimental delay in time for the onset of growth as described above.

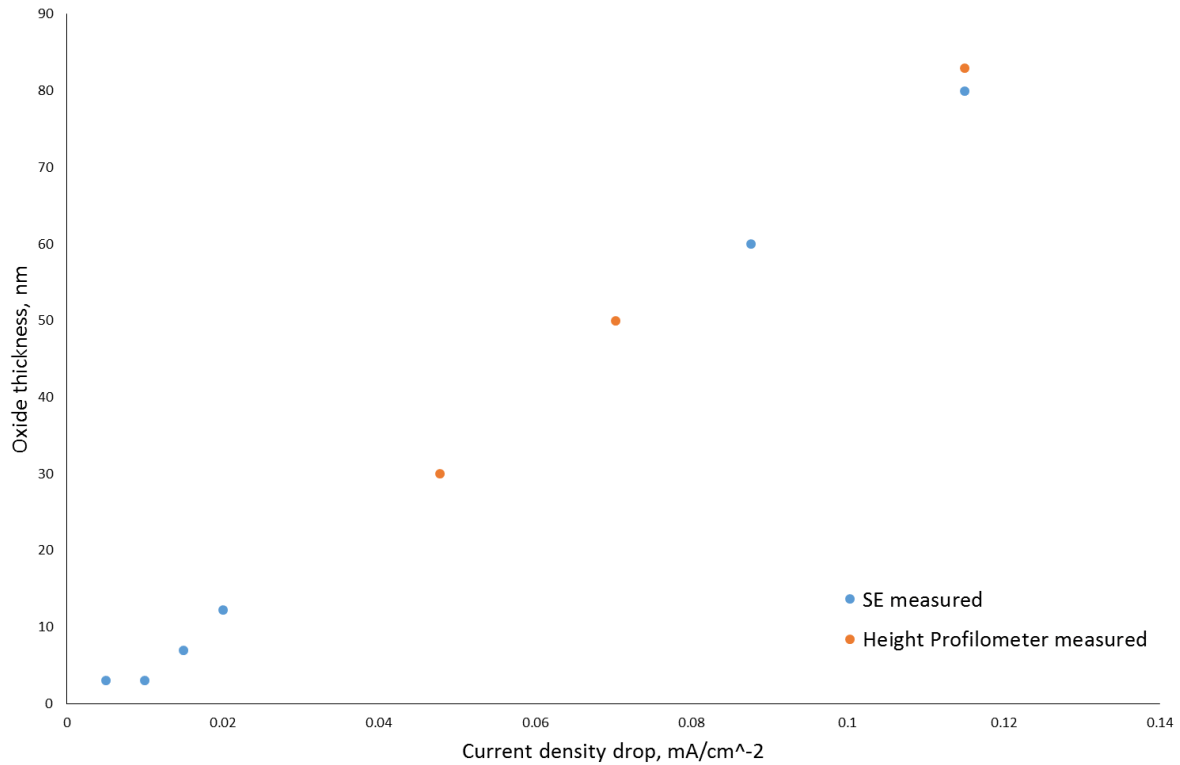


**Figure 4.29: Oxide thickness plotted against current density drop. The current drop relates to the decrease in the monitor current pulse as described in chapter 3. Results in orange were measured using a height profilometer, results in blue were measured more accurately using a spectroscopic ellipsometer (SE), showing good agreement.**

The oxide growth technique has a fair thickness control, however, uncertainties due to the delay of the onset of oxidation and the small amount of time it takes to grow thin oxides, in particular for small area oxides, necessitates the need for further controls. A pre-set measure is to grow a GaAs layer to the required thickness for the application (whilst taking into consideration the change in density and thickness of the layer after oxidation). The density of the oxide of GaAs obtained is close to a value (Hasegawa, H.; Forward, K.E.; Hartnagel, H., 1975) that has been shown to have good electrical and structural characteristics, with an ability to withstand thermal evaporation of metals. A further reduction of  $\text{As}_2\text{O}_3$  compounds may be possible with an altered duty cycle.

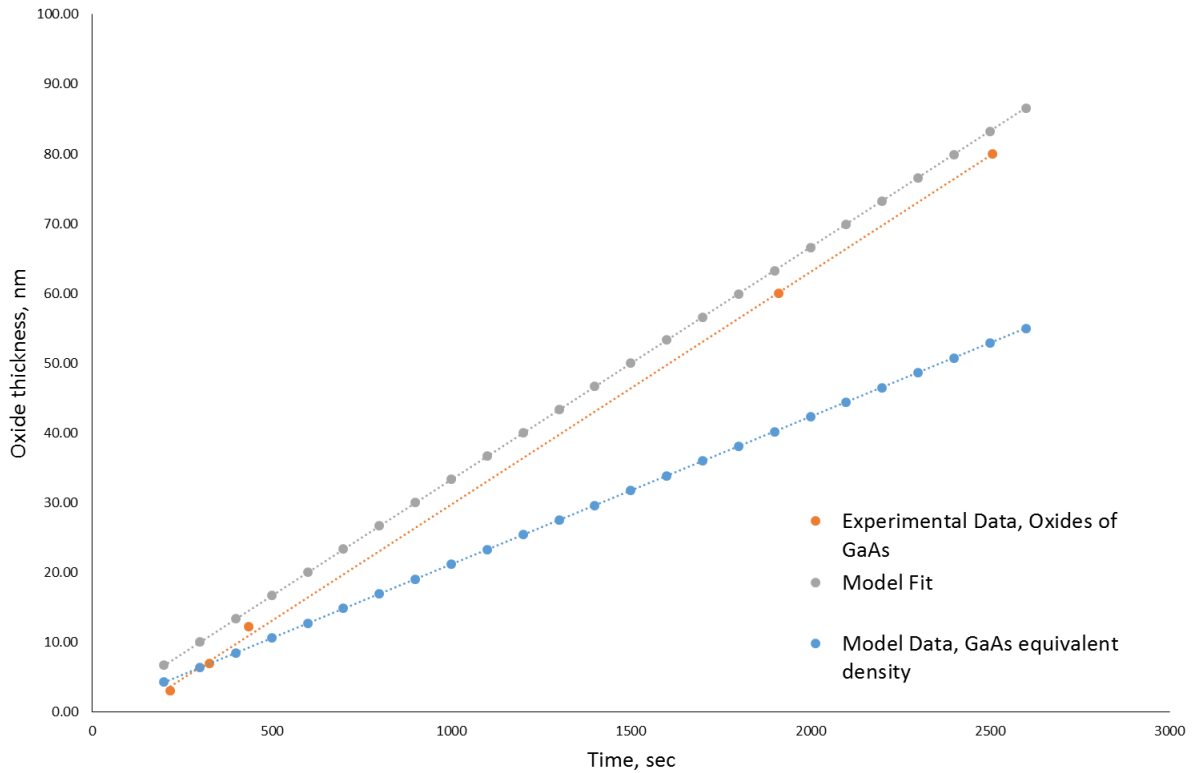


**Figure 4.30: Fit of Faraday’s law of electrolysis to experimental results to determine the comparative density of the grown oxide, which gives indications of the composition.**

#### 4.4.2. Roughness and topography

The roughness and topography of the oxide is important for application in hybrid-plasmonic devices. Slight variations in thickness can alter the losses experienced by an optical mode along the length of the device, whilst metal roughness can cause light scattering and also reduce propagation lengths. The roughness and topography were measured using atomic force microscopy as described in section 3.2.2.

The root mean square (RMS) roughness showed a dependency with the starting anodisation current. Figure 4.31 shows a variation of roughness with starting current. Samples were oxidised for the same drop in current density. A higher anodisation current can affect the roughness and mode of growth of the oxide as described in section 2.4. For further growths a starting current of 0.06 mA was chosen to avoid a high surface roughness whilst being a large enough value to avoid early onset localised dissolution, which has the potential to cause pitting.

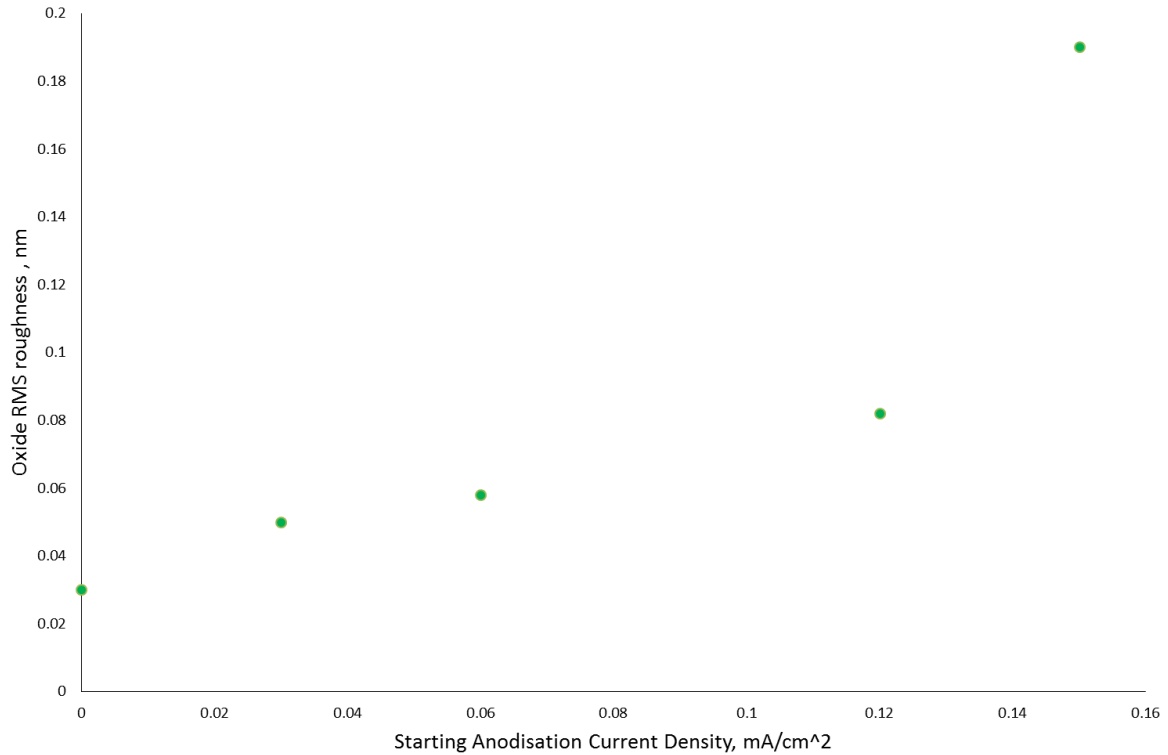


**Figure 4.31: Roughness, measured by atomic force microscopy, as a function of starting anodisation current density, for a constant drop in current density.**

Roughness did not change considerably with time at a fixed starting current, as can be seen in figure 4.32, but showed a variation of approximately 0.03 nm about a value of 0.06 nm. For comparison the roughness of the non-oxidised GaAs was measured to be 0.03 nm.

The peak-to-trough (PT) topography increases with an increasing growth time, measured in terms of current density drop, as can be seen in figure 4.33. This is largely due to height non-uniformities (and non-uniformities in doping distribution) in the underlying topography of the GaAs surface, which are enhanced by the anodic process. The oxide does not grow at a spatially even rate because the growth depends on the spatially dependent local charge conditions. As one part of the oxide becomes thicker there is a locally reduced anodisation current at that point. This results in a lower ion flux, and a higher interface ion concentration, promoting a denser oxide growth in the area. This further promotes field controlled growth in the already thickened region, increasing peak height. In the regions that start off with slower oxide growth it is likely that there will be more competition from the diffusion growth mechanism due to a higher ion flux. This not only results in a growth that is controlled less strongly by the applied potential, but results in the formation of a less



stable less dense oxide that is more susceptible to dissolution. This has the effect of increasing trough depth. In this way, it is possible to see that with an increasing film thickness the peak-to-trough topography can become more pronounced.

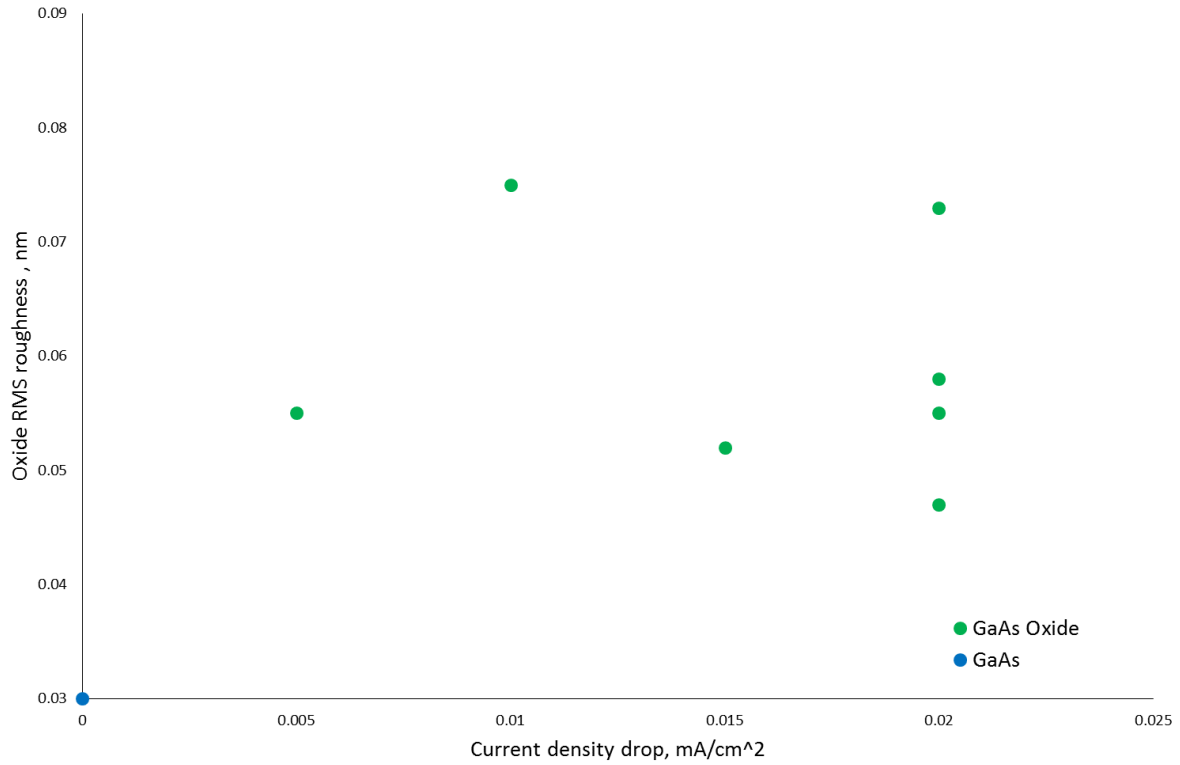


**Figure 4.32: Roughness, measured using AFM, as a function of current density drop, for a constant starting current.**

The growth of thin oxides requires a small drop in current density, this results in only a very small deviation from the PT of the underlying surface. If required a smoothing effect may be obtained by adjusting the duty cycle to allow for a longer off-pulse for increased dissolution, although it is not necessary for the oxide thicknesses required for the hybrid-plasmonic application.

It is evident that under the correct pulsed growth conditions, and by choosing a low enough starting anodisation current, an oxide surface roughness of 0.06 nm is achievable, which is fractionally larger than the roughness of the underlying GaAs. A change in PT of 0.7 nm compared to the underlying surface for thin oxides is achievable. Large surface undulations and roughness would otherwise disrupt the propagation of the hybrid-plasmonic mode at the metal-oxide interface due to increased Ohmic losses and light scattering.

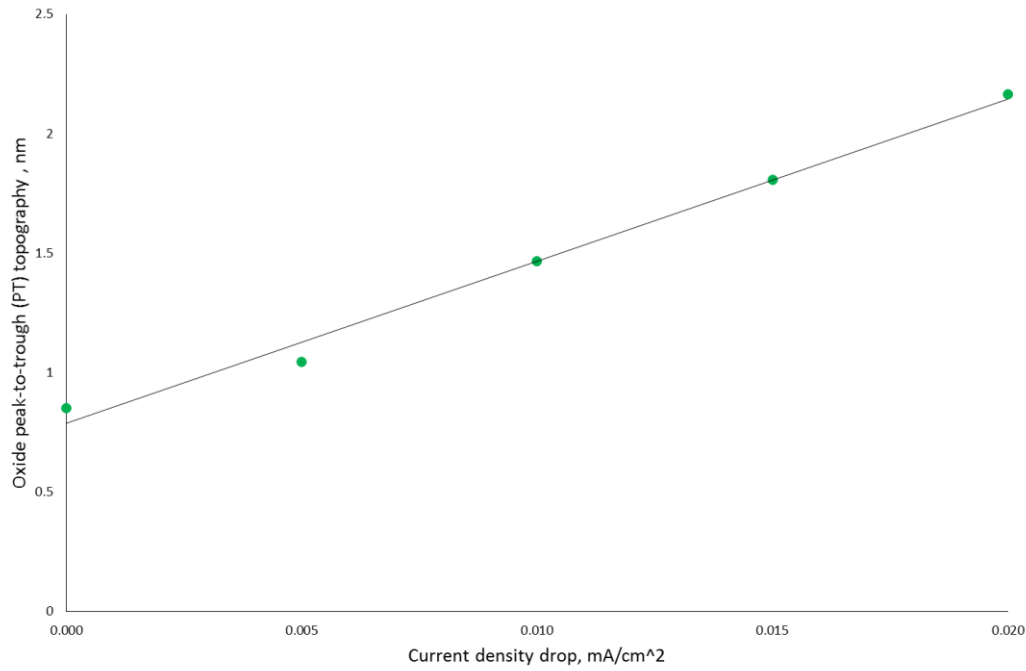
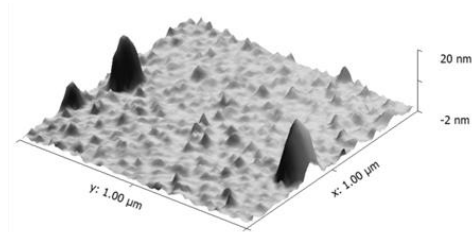
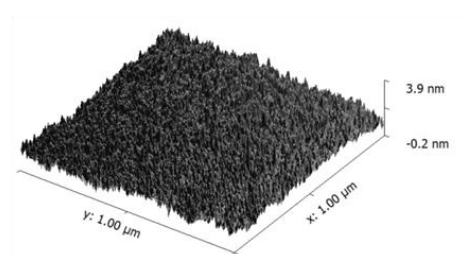


**Figure 4.33: Oxide peak-to-trough topography, measured using an AFM, as a function of current density drop for a fixed starting anodisation current.**

To compare to other available deposition methods a sample was prepared of silicon dioxide evaporated by electron-Beam. It was found that evaporated silicon dioxide (thickness  $t = 100$  nm) has a similar RMS roughness to the grown anodic oxide ( $0.06$  nm), but (within a  $200$  nm scan area) has a higher peak-to-trough topography (of  $4$  nm). This excludes the larger grain sizes that appear in electron-Beam evaporation as can be seen in figure 4.34. For thinner evaporated films this PT depth would result in a poorer coverage than attainable using anodic oxide. Importantly, thin uniform films with controllable thicknesses can not be easily produced by E-Beam evaporation.



**E-Beam Evaporated Silicon Dioxide**  
 **$t = 100\text{nm}$**



**Anodic GaAs-Oxide**  
 **$t = 3\text{nm}$**

**Figure 4.34: Tilted images generated from AFM tapping mode measurements, processed using Gwyddion software. Silicon dioxide presented as a comparison sample to GaAs-Oxide.**

#### 4.4.3. Selective area growth/patterning and chemical resistance

The anodic oxide was patterned post growth using photolithographic techniques and alternatively grown to the desired in-plane dimensions using a resist growth mask. Post-patterning resulted in poor edge definition due to undercutting of the photolithographic mask. Selective growth produced patterns with good edge definition that could be precisely aligned to other structures, particularly when using a PMMA mask coupled with automatic e-beam lithographic alignment protocols. For larger features photoresist was used as a growth mask. An example of an oxide grown using a selective area photoresist growth mask can be seen in figure 4.35.

The chemical resistance of the oxide depends on its stoichiometry, density and surface morphology, which depend on the growth parameters. Chemical resistance is an important factor when considering the fabrication steps necessary for the hybrid-plasmonic device, and for the environment in which the device can operate without degradation. It is also a good indication of the quality of the grown oxide.

Some authors have suggested that oxides of GaAs are stable in deionised (DI) water, trichloroethylene (TCE), acetone, isopropanol (IPA) and methanol, although others have reported high solubility in methanol (Schmuki, P. et al 1996). A two layer oxide structure, shown in figure 4.35, was fabricated by oxidising a sample in two successive steps, with and without a resist mask. This was done in order to produce an oxide step edge from which a thickness change (due to dissolution from chemical exposure) could be measured using a height profilometer. The use of a sample with two oxide thicknesses can also be used to compare the colour changes of the oxides with thickness change, giving an indication of the refractive index by comparison to literature.

The oxide was exposed to various chemicals using exposure times that were larger or comparable to those used for standard operating procedures. Anodic oxide samples showed no detectable ( $\pm 5$  nm) dissolution when exposed to DI water, acetone or IPA after 10 minutes exposure. The oxide showed no detectable dissolution in Isobutyl Methyl Ketone (IBMK) after a 2 minute exposure, the developer used for the e-beam resist Polymethyl methacrylate (PMMA). The oxides were unstable when exposed to metal-ion-free photoresist developer Microposit MF319. Microposit MF319 developer contains 2.45%

Tetramethyl ammonium hydroxide (TMAH) to 97-98% water. Dissolution in TMAH is inconvenient but unsurprising, it is used as an etchant for a number of materials, a solution of 10-40% TMAH to water produces an etch rate of 500-1500nm/min for silicon when heated to 90°C, it etches silicon dioxide and silicon nitride at a rate of approximately 0.05 to 0.25 nm/min (Kovacs, G.T.A. et al 1998). At room temperature MF319 with 2.45% TMAH is used to etch various semiconductor materials, including GaSb, AlGaSb, AlSb, with etch rates of a number of nm/min (Gatzke, C. et al 1997).

The images of the oxide before and after exposure to MF319 can be seen in figure 4.35. The left image shows oxide of two thicknesses (exhibiting light green and light blue colours due to interference) grown in successive oxidation steps, resulting in the pattern shown. The green oxide measured 160 nm +/- 5 nm, the light blue oxide measured 130nm +/- 5nm. The right image shows non-uniform dissolution (and associated colour/thickness change) due to a 30 second exposure to undiluted photoresist developer MF319. The colour change that occurred with thickness fits well to the interference colours recorded for  $\text{Ga}_2\text{O}_3$  of a refractive index of 1.8 (Hasegawa, H.; Hideki.; 1976). The oxide etch rate was recorded to be 1 nm/sec.

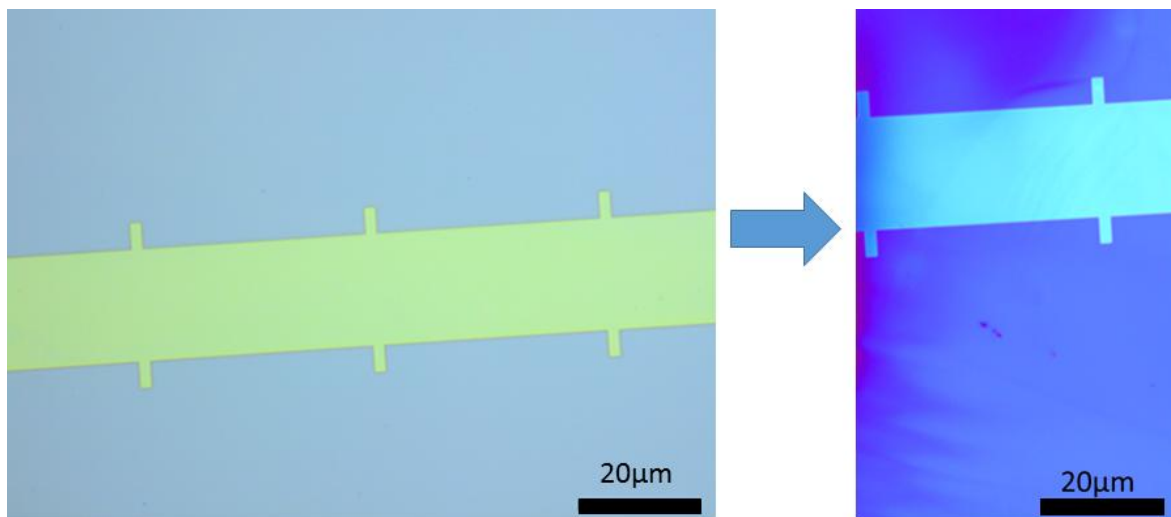


**Figure 4.35: Optical microscope images. Oxide of GaAs before (left) and after (right) exposure to photoresist developer MF319.**

#### 4.4.4. Diode electrical characteristics

Metal-insulator-semiconductor diodes were fabricated on p-type GaAs using the grown oxide of GaAs as the insulator. This was done in order to determine the barrier height of the oxide as an indirect indication of its pinhole density.

Current-voltage-temperature (IVT) measurements were taken using the experimental set-up and analysis method described in section 3.2.5. IVT measurements are useful in determining the conduction mechanisms taking place across the oxide, and the barrier height. The fabrication of the MIS structures are also detailed in section 3.2.5.

A four point IV measurement to the terminal box of the set-up, as described in section 3.2.5, removed resistance associated with the external leads and connectors. Other resistances are the “probe” resistances (bonded wires)  $R_p$ , wire to metal resistance  $R_{p-m}$ , metal to oxide and oxide to semiconductor resistances  $R_{m-o}$ ,  $R_{o-s}$ , and semiconductor resistance  $R_{semi}$ , as shown in figure 4.36 and 4.37. All of these are sources of potential voltage drop.

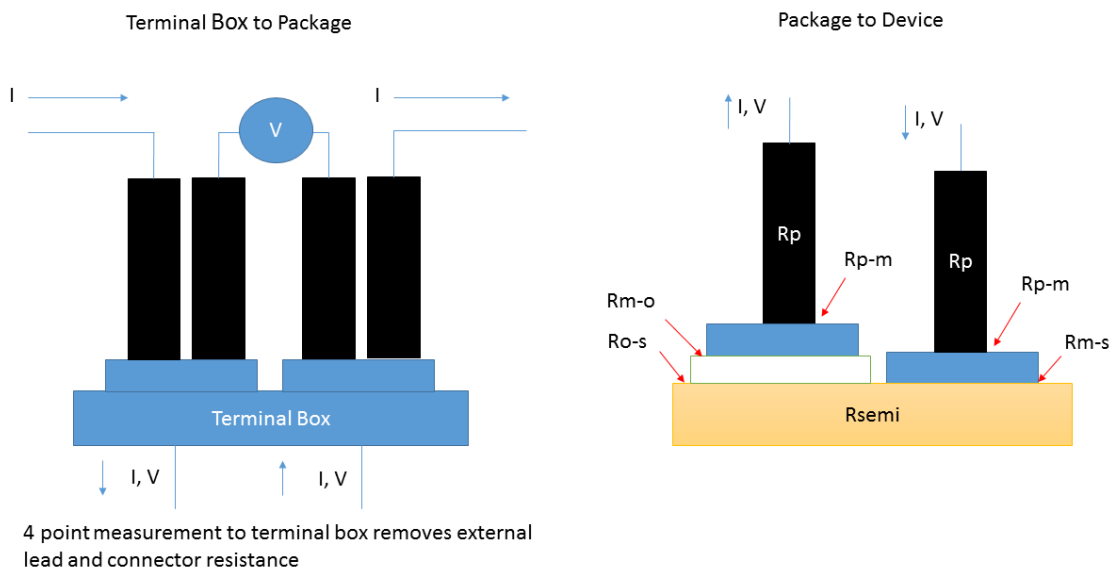


**Figure 4.36: Schema showing sources of resistances associated with the MIS structures.**

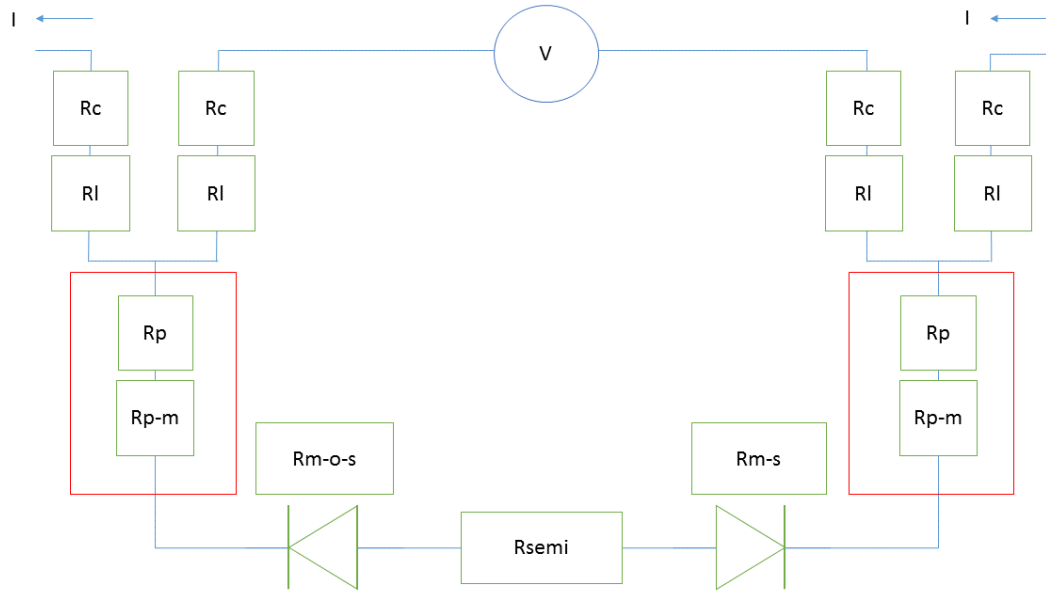


**Figure 4.37: Schema of resistances associated with MIS structure**

The MIS structure under test consisted of a  $120\ \mu\text{m}$  square pad, with an oxide (of GaAs) thickness of approximately 3 nm. The oxide thickness was measured using atomic force microscopy, the scan profile can be seen plotted in figure 4.38. This scan was done across a line of oxide, the high points are wings formed at the edges of the resist layer, and are thought to be composed of redistributed  $\text{As}_2\text{O}_3$  compounds, although this has not been confirmed.

The annealed Ohmic p-type contact consisted of Zn/Au, whilst the top metal for the MIS Schottky was Au. The annealed metal-semiconductor contact is represented as a diode in figure 4.37 for explanatory purposes, although it was indeed an Ohmic contact. The MIS structure was driven under forward bias. IV curves as a function of temperature can be seen in figure 4.39. It can be seen that all of the curves have a common intersection point at a given bias voltage where the current through the junction appears to be temperature independent, which has previously been observed (Tekeli, Z. A. et al 2007) at a similar bias voltage, and has appeared in simulations of IV curves for Schottky contacts. The intersection point is thought to be related to the series resistance of the device and contacts as a function of temperature. It is also evident that above the intersection point the IV curves are metal-like, where the resistance increases with increasing temperature, whilst below the

intersection point the IV curves are semiconductor-like, where the resistance decreases with increasing temperature.

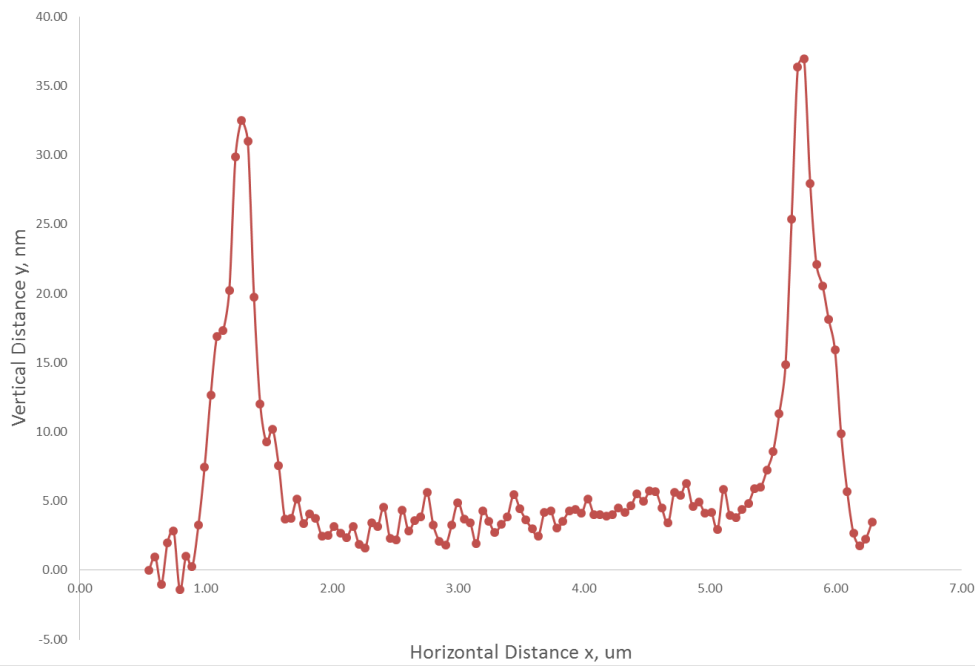


Figure 4.38: AFM scan profile across a line of anodically grown oxide using a resist mask.

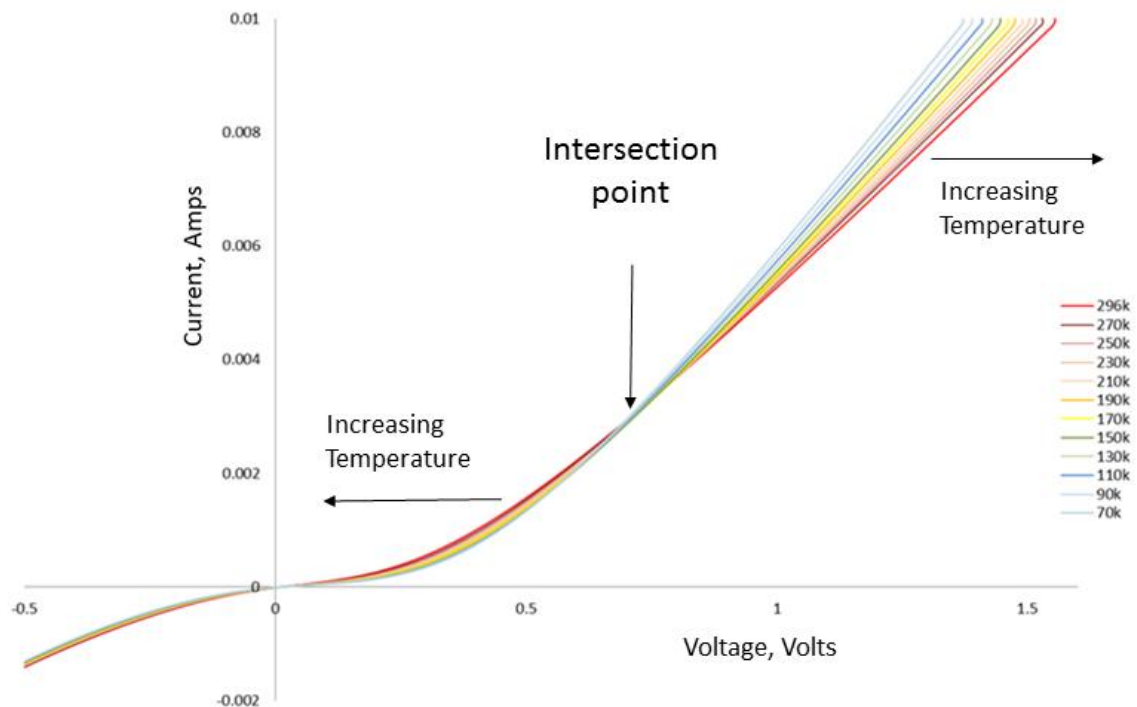
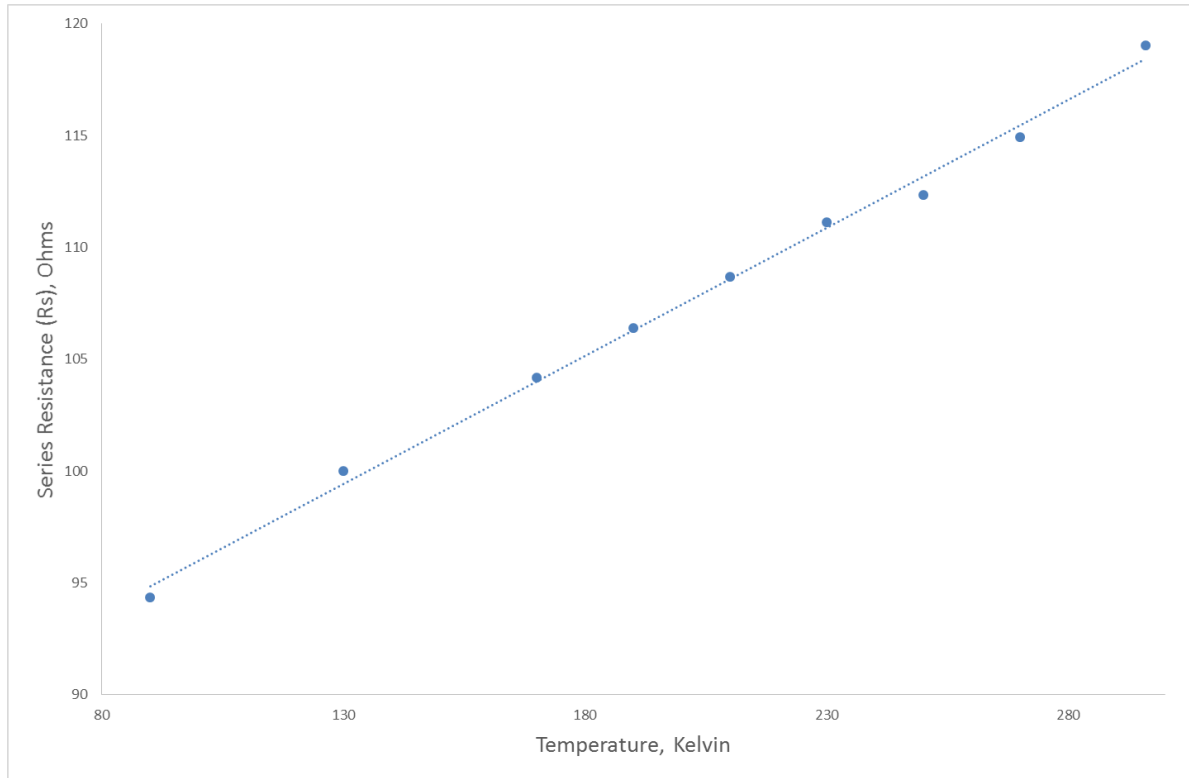


Figure 4.39: Graph of current against voltage for MIS diodes at various temperatures.

It is possible to extract the probe ( $R_p$ ) and probe-metal ( $R_{p-m}$ ) resistance from the higher voltage linear part of the slope, above the intersection point, where this resistance dominates. This series resistance increases linearly with increasing temperature, as shown in figure 4.40.



**Figure 4.40: Series resistance increasing with temperature**

The IV curves were adjusted in order to eliminate this series resistance, an example of the adjustment can be seen in figure 4.41. The data, after removal of series resistance, can be seen in figure 4.42. It can be noted that these structures have a high reverse leakage current.

The annealed Ohmic contact has a small voltage drop across it. However, if this contact shows Schottky behaviour it can be detrimental to the analysis. When the MIS structure is forward biased the apparent Ohmic contact, acting as a Schottky contact, is reverse biased. Under these conditions the voltage drop across the reverse biased Schottky contact dominates at low bias voltages, preventing an accurate measurement of the voltage drop across the MIS structure in this region (Elhadidy, H. et al 2012). In this analysis the annealed contact was treated as an Ohmic contact, from prior experimental determination, and the



other as a Schottky contact. This allows the barrier height of the MIS structure to be determined using Thermionic Emission theory (TE), where the MIS is treated as a Schottky contact with an inhomogeneous insulating layer, for reasons that are apparent below. Further details on the method and theory can be found in chapter 3. The dark current and the ideality factors of each IV curve, needed for the analysis, were found from the plot of the logarithm of the current against the bias voltage using equation 3.9. This graph is shown in figure 4.43. The ideality factor,  $n$ , measures deviation from ideal TE theory, where  $n=1$  represents ideal TE theory.

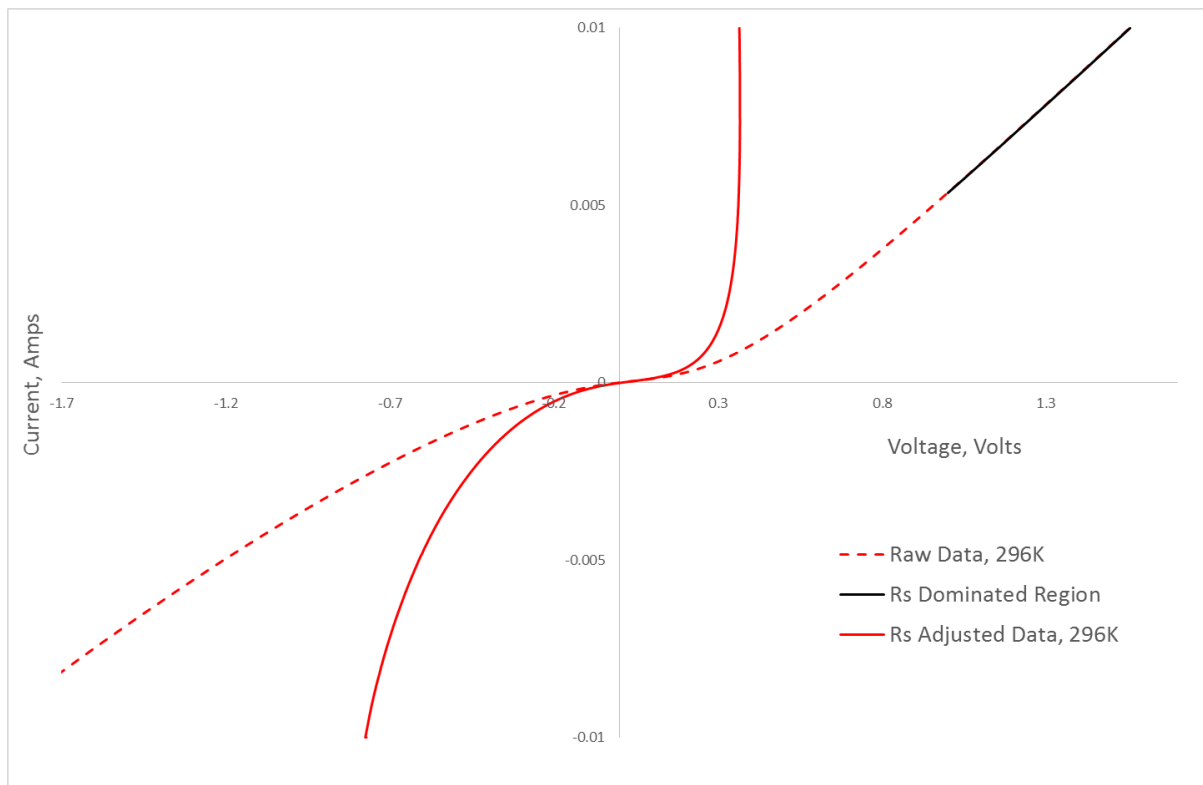


**Figure 4.41: Extraction of series resistance and adjustment of IV curves**

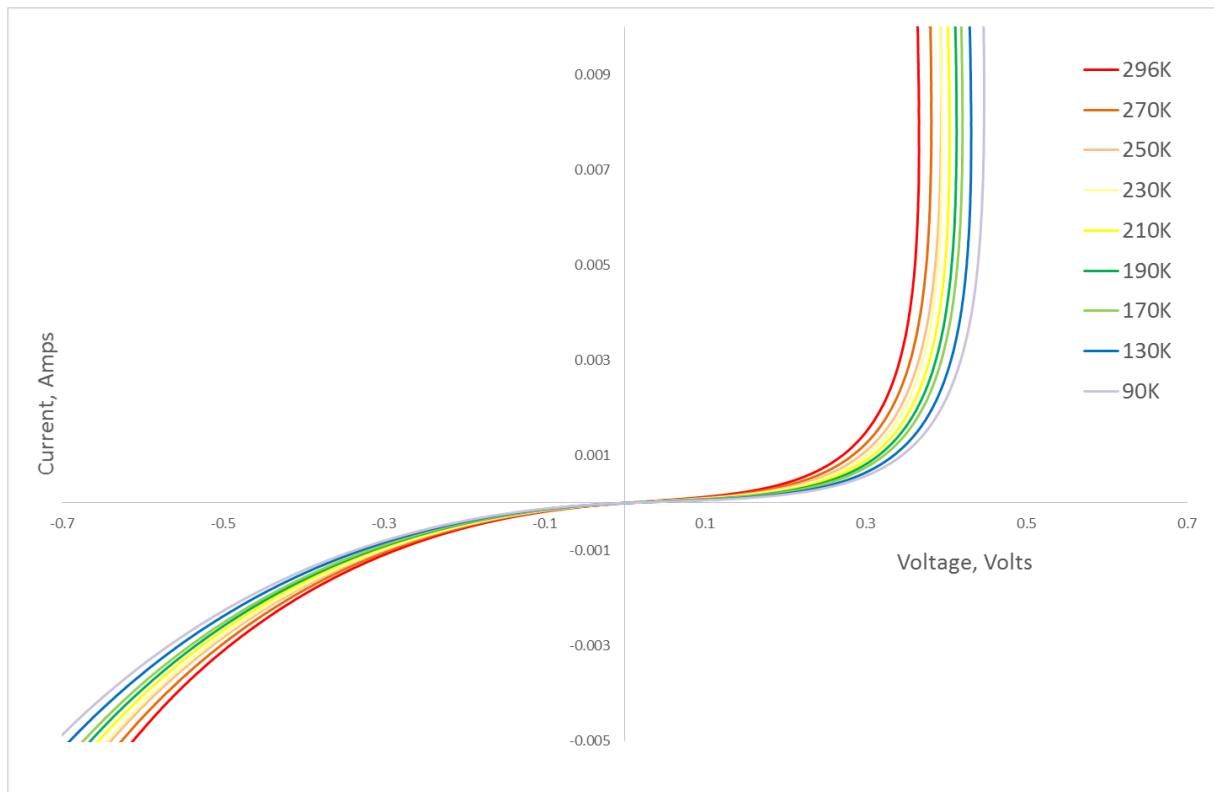


**Figure 4.42: Current-voltage curves at various temperatures for MIS diodes with an oxide thickness of 3nm.**

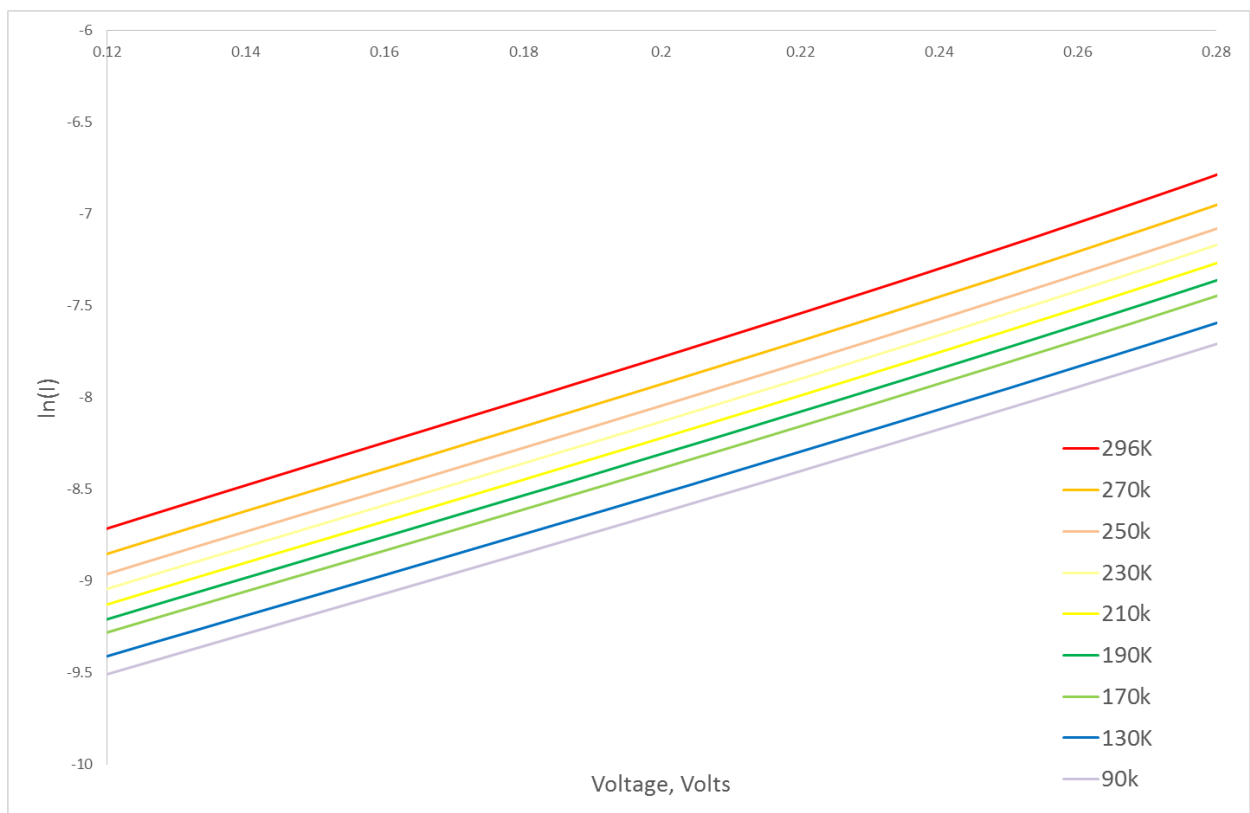


**Figure 4.43: The dark current was determined from the y-intercept, whilst the ideality factor was found from the inverse gradient.**

It was found that the ideality factor decreased with increasing temperature. The high values of the ideality factor, particularly at low temperatures, represent an apparent deviation from TE theory, which may be due to a number of different factors, including other conduction mechanisms.

The apparent barrier height, calculated from experimental data as described in section 3.2.5, increased with increasing temperature. This can be seen in figure 4.44. The behaviour of the barrier height with temperature, although unusual considering the negative temperature coefficient associated with a semiconductor bandgap, is commonly observed (Khanna, S. et al 2011) (Paradzah, A.T. 2014) (Tekeli, Z. A. et al 2007) in Schottky contacts with spatial inhomogeneities. This temperature dependence with barrier height suggests a distribution of Schottley Barrier Diodes (SBD) at the interface. Spatial inhomogeneities at the metal-semiconductor interface is a commonly applied explanation for the observed behaviour, which may be a result of various factors including a spatial variation in doping distribution, or surface damage from metal deposition on the oxide. In future work the possibility of surface damage could be explored by performing deep level transient spectroscopy, as its existence is problematic for the operation of the hybrid plasmonic device.

A modified Richardson plot using a Gaussian distribution of apparent barrier heights was used in order to determine the conduction mechanism and barrier height of the MIS structure. The Richardson constant can't be accurately determined using this method (Schmuki, P et al 1996). The modified model considers patches of low and high barrier material. Current transport across a barrier is a temperature activated process, at low temperatures electrons can only overcome low barriers, so the current is dominated by paths through patches of lower barrier with a larger ideality factor, the dominant barrier height in use increases with increasing temperature.

The standard deviation for the Gaussian distribution of barrier heights was found from figure 4.45 using equation 3.16, where low temperatures were not included due to the very high value of ideality factors being attributed to other conduction mechanisms.

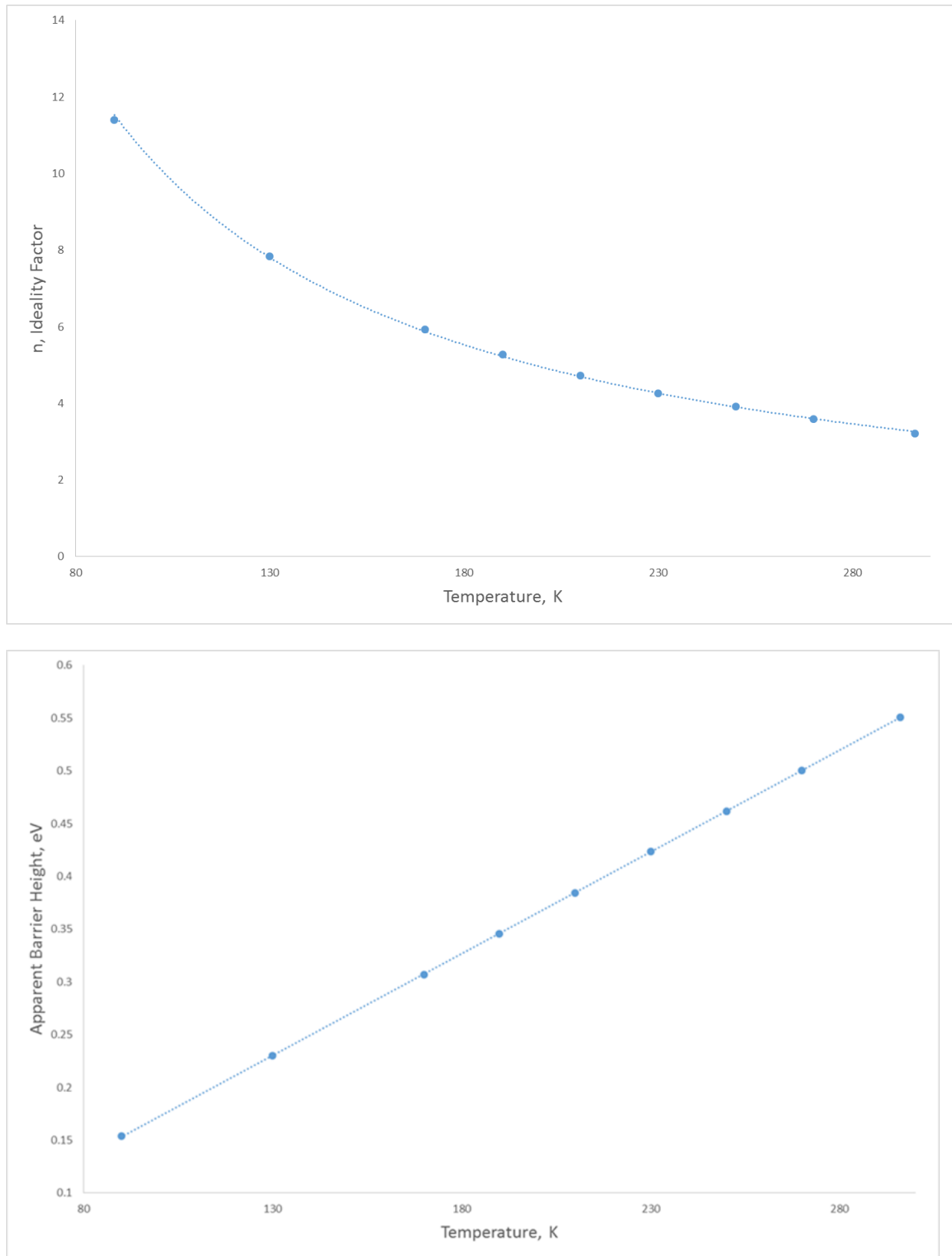
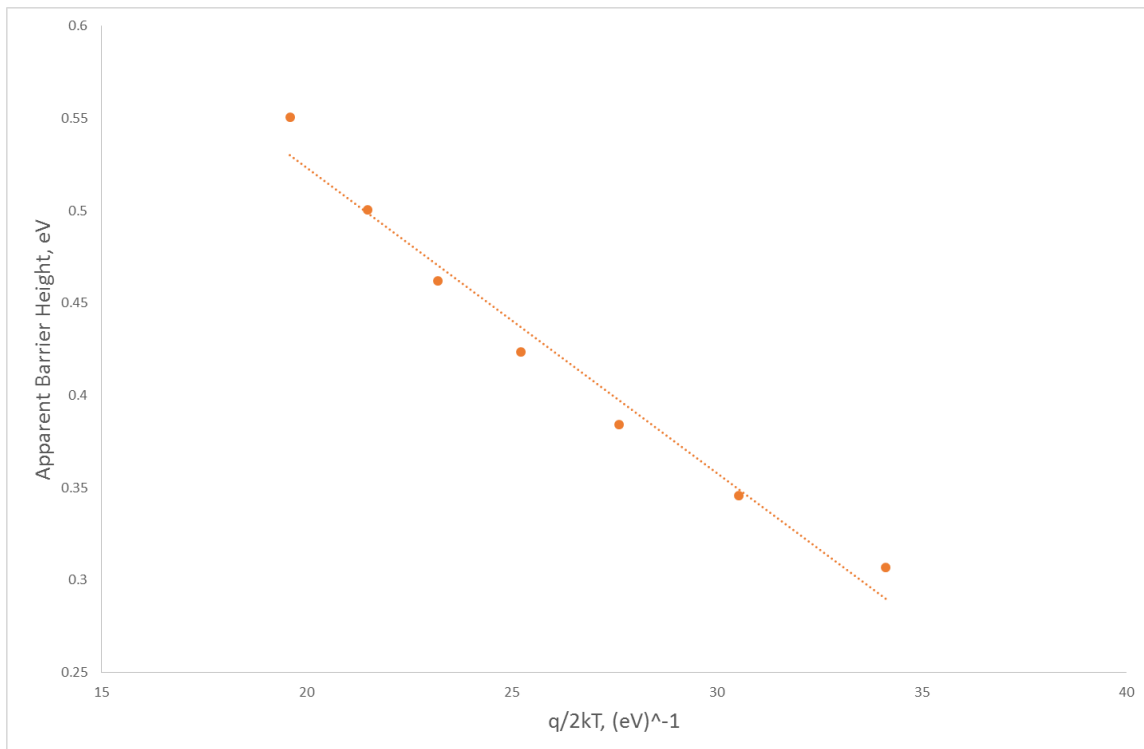
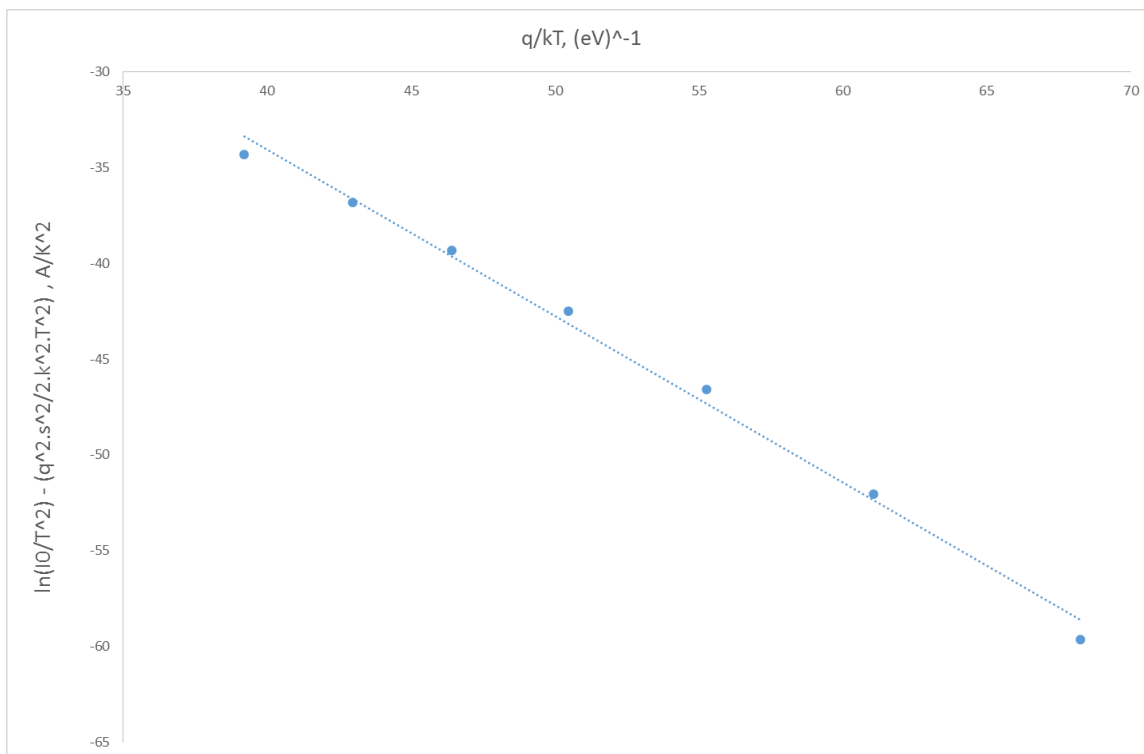


Figure 4.44: Ideality factor and apparent barrier height variation with temperature.



**Figure 4.45: Graph used to find standard deviation of barrier heights for Gaussian distribution.**

The modified analysis was performed on the new temperature range to find the barrier height, as can be seen in figure 4.46.



**Figure 4.46: Modified Richardson plot to determine barrier height.**

The barrier height was found to be 0.87eV with a standard deviation of 0.13 eV, similar to that of a Au/GaAs contact (Missous, M.; Rhoderick, E.H. et al 1992). The new modified Richardson constant, which can't accurately be determined using the modified plot, proved to be higher than expected, but this appears to be due to the poor linearity of the fit as a result of added conduction mechanisms still apparent in the lower temperature measurements. Neglecting further high non-ideality measurements gives a slightly reduced barrier height of 0.69eV with a modified Richardson constant of  $4.9 \times 10^4 \text{ Am}^{-2} \text{ K}^{-2}$ , which is a Richardson constant in the order of that reported for Au-GaAs contacts (Missous, M.; Rhoderick, E.H. et al 1992).

The barrier height can be compared to that of a pure oxide of Ga,  $\text{Ga}_2\text{O}_3$ , which is in the order of 2 eV for a thickness of approximately 1.6nm (Li, Z.; Groot, C.; Moodera, J.H.; 2000). The grown 3 nm  $\text{Ga}_2\text{O}_3/\text{As}_2\text{O}_3$  compound, which has a density of approximately  $5/8^{\text{th}}$  of the original GaAs material, and in the order of  $1/3^{\text{rd}}$  the density of  $\text{Ga}_2\text{O}_3$ , therefore could have a consistent barrier height with the literature, but is indistinguishable from the barrier height of the Au/GaAs contact due to the extent of the inhomogeneity of the interface.

TE theory with a modified Richardson plot due to spatial inhomogeneities at the interface describes the conduction mechanism well at higher temperatures, but at lower temperatures the ideality factor is too high indicating that another conduction mechanism is dominant, most likely tunnelling. The fit required the use of the modified Richardson plot suggesting a variable oxide thickness that may be due to metal partly penetrating the oxide, either due to the metal deposition of the top contact or as a result of connecting bond wires to the device.

## **4.5. Semiconductor slab thickness via AlGaAs steam oxidation**

This section presents the experimental results for the wet steam oxidation of buried AlGaAs layers. This is both for the purpose of defining the semiconductor slab thickness for the hybrid plasmonic device and also to explore the possibility of fabricating current apertures for electrical injection. The calibration of the built equipment is presented and the mode of oxidation was determined. The ability to laterally oxidise to a controllable horizontal length

is presented as evidence for the viability of the fabrication of current apertures in the fabricated wet etched structures.

Wet etched mesas, with the same dimensions of the hybrid-plasmonic device, were fabricated. The wafer design is outlined in section 4.2. Figure 4.47 shows experimental results, measured as discussed in section 3.3.2, of the oxidation rate, averaged over multiple ridges on each sample, against temperature. The oxidation extent was measured using the  $x=0.98$ , 40nm  $\text{Al}_x\text{Ga}_{1-x}\text{As}$  layer. The oxidation time for each sample was 10 minutes. The results fit an exponential curve as expected, for reasons described in section 2.5.

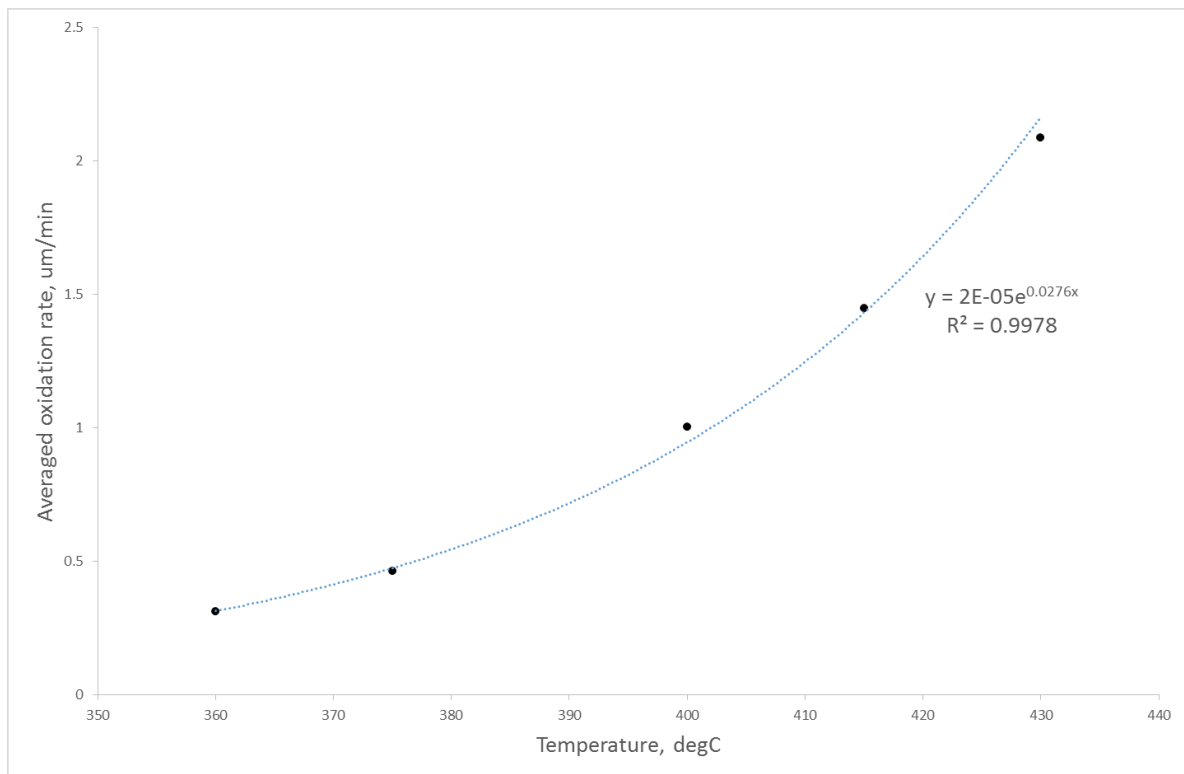


**Figure 4.47:** Averaged oxidation rate against temperature for wet etched mesas containing 40nm  $\text{Al}_x\text{Ga}_{1-x}\text{As}$  layer  $x=0.98$  next to a 1000nm  $\text{Al}_x\text{Ga}_{1-x}\text{As}$  layer  $x=0.8$ . Oxidation extent was measured using the  $x=0.98$  layer.

To determine whether the oxidation was reaction or diffusion limited, and to achieve the best control over the oxidation depth, further tests were performed at 360°C. Figure 4.48 shows the oxide extent as a function of time at 360°C. The raw data in blue has a linear fit, it is evident that there is a y-intercept offset of approximately 2.4  $\mu\text{m}$ , which can be attributed to the under etch of the oxide during the wet etch of the mesas, which is also indicated by scanning electron microscope (SEM) images. The data in grey has been shifted by this constant offset.

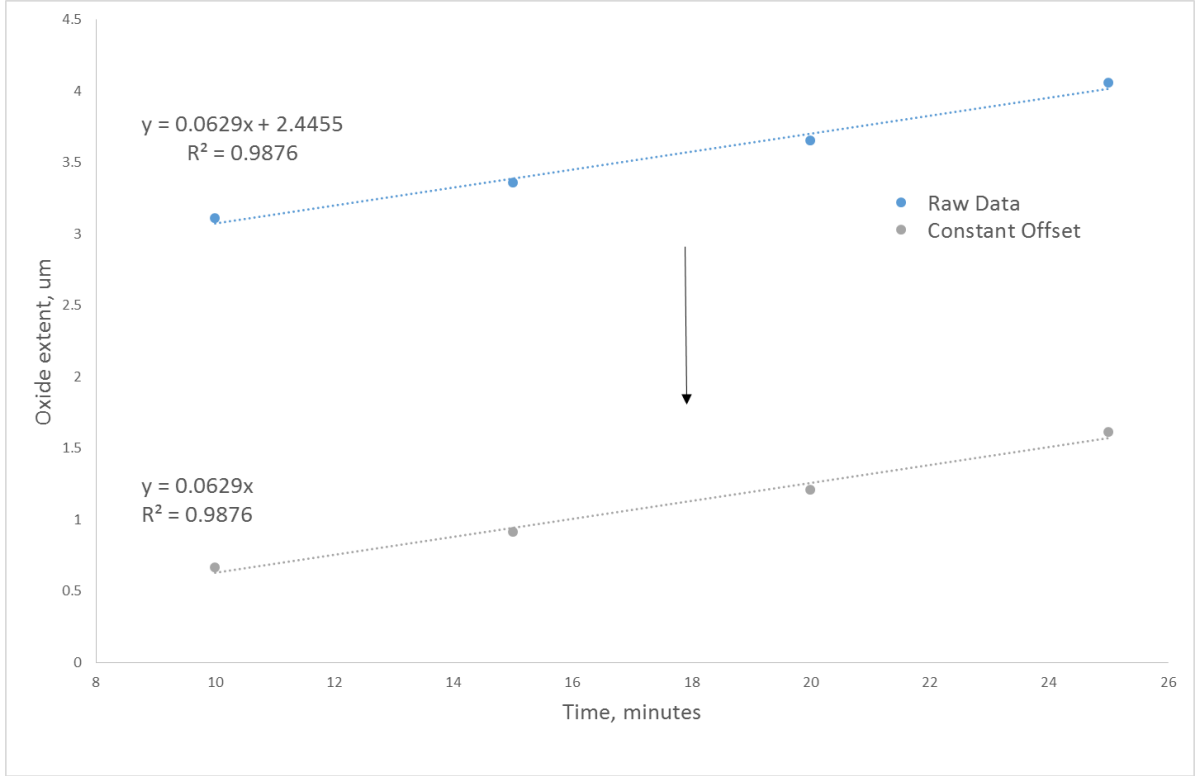


**Figure 4.48: Oxide extent as a function of time at 360°C for a 40nm Al<sub>x</sub>Ga<sub>1-x</sub>As layer x=0.98. A constant offset due to the under-etch of the wet etched mesas is included.**

Through plotting the oxidation rate as a function of time, and including this constant offset due to the under-etch of the wet-etched mesas, it can be seen that the oxidation rate with depth does not change with time. The grey data of figure 4.49 shows no change in the etch rate with depth. This indicates that it is a reaction rate controlled process, allowing a high controllability of oxide extent. This validates the conditions of the experiment and construction of the experimental apparatus, and validates the set-up for the precise and repeatable fabrication of current apertures for the hybrid-plasmonic device. A controlled oxidation rate of approximately 0.06 μm/min at 360°C is achievable using this wet etched structure, set-up and oxidation conditions. This is sufficient for the fabrication of current apertures.

To further validate these results the activation energy of oxidation for the x=0.98 aluminium containing layer has been extracted by using an Arrhenius equation, given in equation 4.4.

$$R = R_0 e^{\frac{-E_a}{k_b T}} \quad (4.4)$$



where  $R$  is the oxidation rate,  $R_0$  is a pre-exponential factor related to the reaction rate,  $E_a$  is the activation energy of oxidation,  $T$  is temperature in units of Kelvin, and  $k_b$  is Boltzmann's constant in units of  $\text{eV K}^{-1}$ .

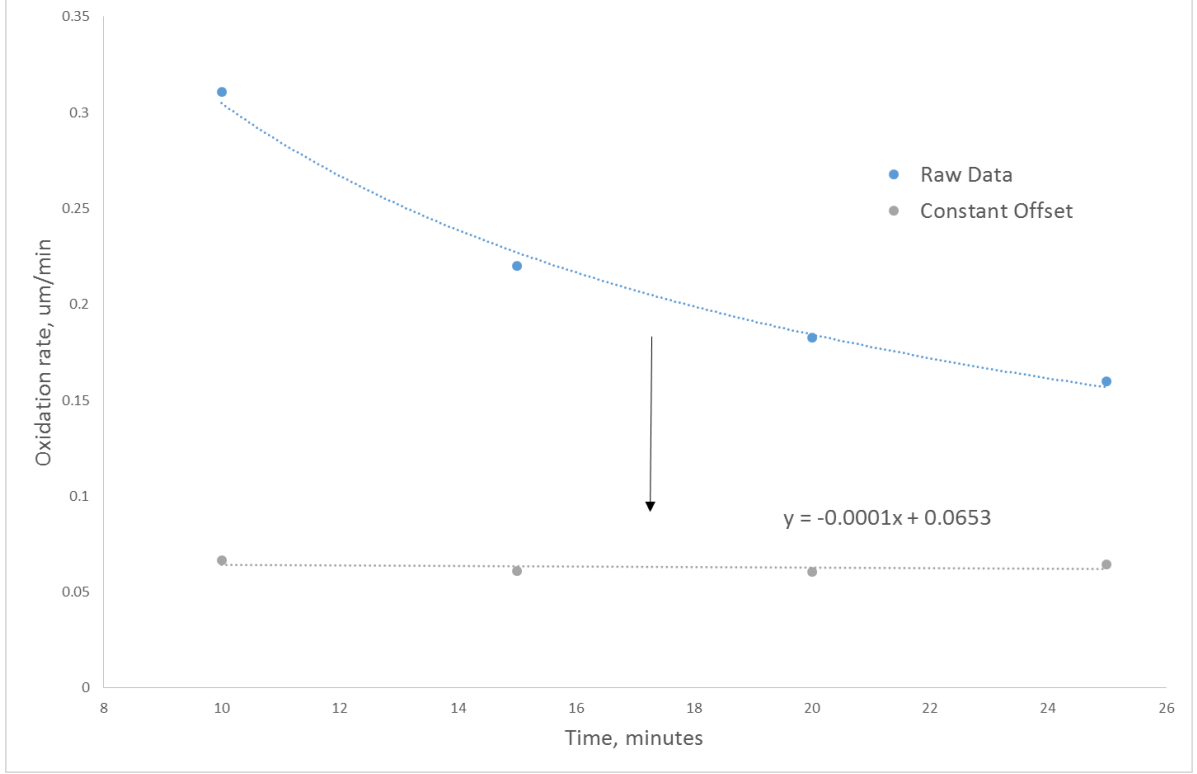


**Figure 4.49: Oxidation rate as a function of time at 360°C for a 40nm  $\text{Al}_x\text{Ga}_{1-x}\text{As}$  layer  $x=0.98$ . A constant offset due to the under-etch of the wet etched mesas is included.**

The activation energy of the 40nm  $\text{Al}_x\text{Ga}_{1-x}\text{As}$  layer  $x=0.98$  can be found from the gradient of figure 4.50. The raw data gives a value of 1.06eV, which is lower than what would be expected for an  $x=1.00$  aluminium containing layer (Choquette, K.D.; Geib, K.M.; Ashby, C.I.; et al 1997). The data processed with the constant offset gives a value of 1.79eV, which is close to the value of 1.75eV that was measured for a  $x=0.98$  84nm thick layer (Choquette, K.D.; Geib, K.M.; Ashby, C.I.; et al 1997). The discrepancy in the values may be due to the fit of the Arrhenius plot, or due to the differences in the layer thicknesses. Thinner layers exhibit higher activation energies due to the increased curvature of the oxidation front, as described in section 2.5. The results validate the built steam oxidation experiment, and confirm the ability to produce current apertures for the hybrid-plasmonic device.

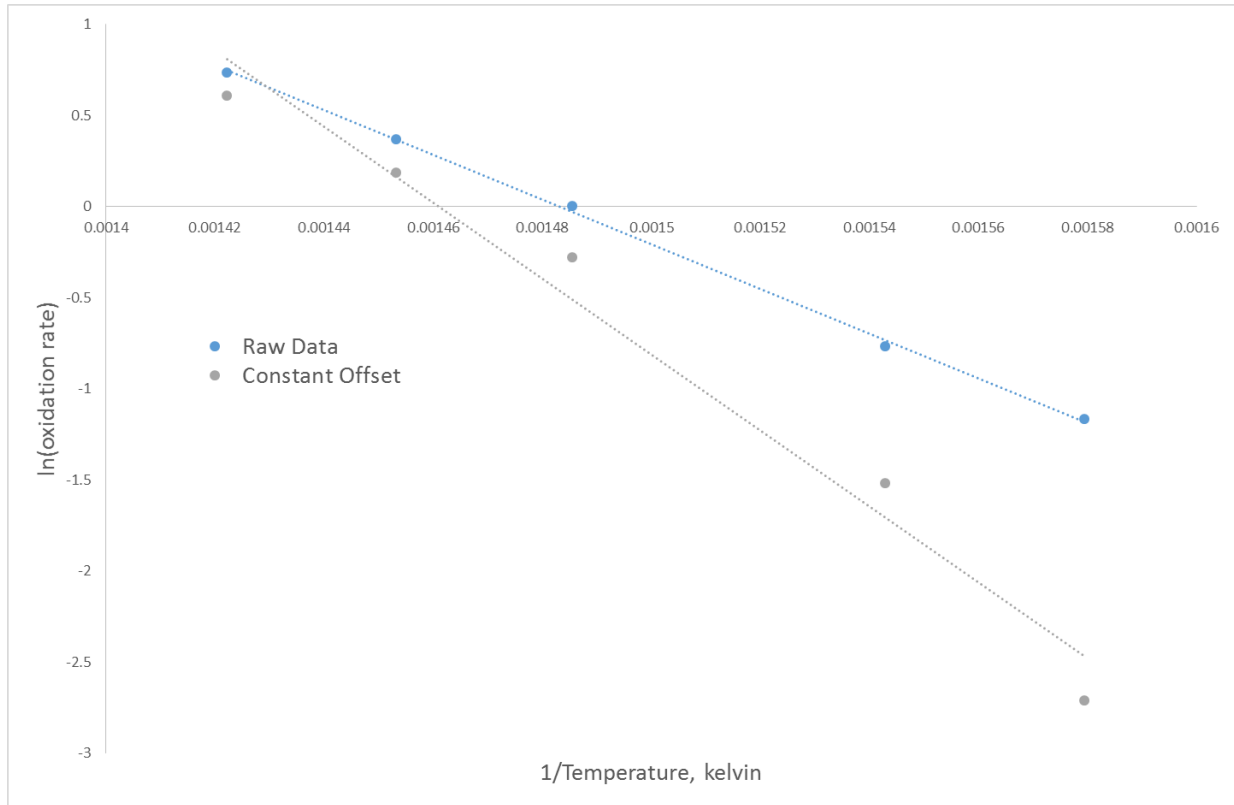


**Figure 4.50: Arrhenius plot to determine activation energy of 40nm Al<sub>x</sub>Ga<sub>1-x</sub>As layer  $x=0.98$ , with and without the constant offset. A value of 1.79eV for the offset data coincides with the expected value for the layer thickness and aluminium concentration.**

## 4.6. Summary

The design of a hybrid-plasmonic device was explored in which a semiconductor gain material is used to attempt to compensate metal losses. A TM emitting 633 nm laser structure was designed to provide gain, the characteristics of the grown wafer were confirmed using edge photovoltage spectroscopy, showing that the electron to light hole transition was at a lower energy than the electron to heavy hole transition, and existed at a wavelength of 633 nm. A strong dependence of loss with the semiconductor slab thickness and dielectric gap thickness was calculated. A single nanometer change in the dielectric gap thickness can alter the mode cut-off by a semiconductor slab thickness of up to 100 nm, and can change the mode loss up to  $600 \text{ cm}^{-1}$ . In addition, the mode is pulled towards the metal/dielectric region, resulting in a small optical confinement factor in the central quantum well region, and a low modal gain that can not compensate losses. A high energy density was modelled within the dielectric layer, and the mode was found to be bound to the metal region, which may be useful for some applications. Fabrication of a nanosquare

device with electrical injection was investigated, the importance of alignment procedures was noted and metallisation was explored. The specific contact resistivity of the contacts was found to be in the order of or better than similar fabricated contacts, found to be  $3 \times 10^{-3} \text{ ohms.cm}^2$  and  $4 \times 10^{-6} \text{ ohms.cm}^2$  for the p and n type contacts respectively. However, the small injection mesa suffered from heating and resulted in contact metal delamination. An alternative injection method using current apertures was presented, and fabrication of aspects of the design was explored.

The fabrication of the semiconductor slab thickness and dielectric gap thickness was further investigated. The dielectric layer was fabricated through the anodisation of GaAs. Growth over large area samples showed a good thickness control, of the order of 1 nm per 0.0018 mA cm<sup>-2</sup>. The Ga-Oxide to As-Oxide ratio was found to be close to 3:4, which has been shown to have good electrical and thermal stability. Growth conditions were optimised in order to obtain a conformal oxide with low roughness and peak to trough topography. At a selected starting current a low roughness in the order of 0.06 nm, close to the roughness of the unoxidised GaAs surface, was obtained. A change in peak to trough topography from the GaAs surface of 0.7 nm was obtained for thin oxides. The ability to selectively oxidise small features using a resist mask, aligned to larger structures, was highlighted. The barrier height of a 3nm layer of the oxide was determined to be in the order of 0.87 eV. The semiconductor slab thickness and current aperture was determined through the steam oxidation of AlGaAs. Calibration of the constructed apparatus showed the ability to repeatedly fabricate small current apertures, and determined that the oxidation was a reaction rate rather than a diffusion rate limited process. A controlled oxidation rate of approximately 0.06  $\mu\text{m}/\text{min}$  at 360°C is achievable. The activation energy of the oxidation process was found to be 1.79 eV.

## Chapter References

- Ambati, M. (2008). "Active plasmonics: surface plasmon interaction with optical emitters." *Selected topics in Quantum Electronics, IEEE Journal* 14 (6): 1395-1403
- Baca, A. G.. (1997). "A survey of ohmic contacts to III-V compound semiconductors." *Thin Solid Films* 308–309: 599-606.
- Berini, P. (2000). "Plasmon-polariton waves guided by thin lossy metal films of finite width: bound modes of symmetric structures." *Physical Review B* 61 (15): 10484-10503
- Burke, J.J., et al (1986). "Surface-polariton-like waves guided by thin lossy metal films." *Physical Review B* 33 (8): 5186-5201
- Choquette, K.D.; Geib, K.M.; Ashby, C.I.; Twesten, R.D.; Blum, O.; Hou.H.Q.; Follstaedt, D.M.; Hammons, B.E.; Mathes, D.; Hull, R. (1997). "Advances in selective wet oxidation of AlGaAs alloys." *Journal of Selected Topics in Quantum electronics*, 3 (3)
- Ding, K. and C. Z. Ning (2013). "Fabrication challenges of electrical injection metallic cavity semiconductor nanolasers." *Semiconductor Science and Technology* 28(12): 124002.
- Elhadidy, H.; Sikula, J.; Franc, J.; (2012). "Symmetrical current-voltage characteristic of a metal-semiconductor-metal structure of Schottky contacts and parameter retrieval of a CdTe structure.", *Semicond Sci Technol* 27: 015006
- Gatzke, C.; Webb, S.J.; Fobelets, K.; Stradling, R.A., (1997). "In-situ monitoring of the selective etching of antimonides in GaSb/AlSb/InAs heterostructures using Raman spectroscopy." *Compound Semiconductors, IEEE International Symposium 1997*: 337-340
- Hasegawa, H.; Forward, K.E.; Hartnagel, H., (1975). "Improved method of anodic oxidation of GaAs," *Electronics Letters* , 11 (3): 53-54
- Hasegawa, H.; Hideki.; (1976). "Anodic Native Oxidation of GaAs by AGW process," *Bulletin of the faculty of engineering, Hokkaido University* (79): 79-88.
- Khanna, S.; Neeleshwar, S.; Noor, A.; (2011). "Current-voltage-temperature characteristics of CR/4H-SiC Schottky diodes." *Journal of Electron Devices*, 9: 382-389

Khurgin, J. B. (2015). "How to deal with the loss in plasmonics and metamaterials." *Nat Nano* 10(1): 2-6.

Khurgin, J. B. and G. Sun (2012). "Practicality of compensating the loss in the plasmonic waveguides using semiconductor gain medium." *Applied Physics Letters* 100(1): 011105.

Kolomenski, A., et al (2009). "Propagation length of surface plasmons in a metal film with roughness." *Applied Optics* 48 (30): 5683-5691

Kovacs, G.T.A.; Maluf, Nadim I.; Petersen, K.E., (1998). "Bulk micromachining of silicon," *Proceedings of the IEEE* , 86 (8): 1536-1551

Krijn, M.P.C.M. (1991). "Heterojunction band offsets and effective masses in III-V quaternary alloys." *Semiconductor Science and Technology* 6(1): 27

Lafone, L., et al (2014). "Feasibility of GaAs-based metal strip surface plasmon nano-lasers." *Optoelectronics, IET* 8 (2): 122-128

Li, D.; ning, C.Z. (2009). "Giant modal gain in a metal-semiconductor waveguide." *Conference on Lasers and Electro-Optics/International Quantum Electronics Conference*, Baltimore, Maryland, Optical Society of America

Li, Z.; Groot, C.; Moodera, J.H.; (2000). "Gallium oxide as an insulating barrier for spin-dependent tunnelling junctions." *Applied Physics Letters*, 77 (22): 3630-3632

L. Peternai, J. J., M.Michalka (2003). "Ohmic contacts to n and p type GaP." *APCOM 2003*, 9th international workshop on applied physics of condensed matter.

Missous, M.; Rhoderick, E.H.; Woolf, D.A.; Wilkes, S.P.; (1992). "On the Richardson constant of intimate metal-GaAs Schottky barriers." *Semicond Sci Technol* 7: 218-221

Oparaku, O., et al. (1990). "Characterization of Zn/Au back contact to low-doped p-InP." *Semiconductor Science and Technology* 5(1): 65.

Paradzah, A.T.; (2014). "Electrical charaterisation of particle irradiated 4H-SiC", University of Pretoria, dissertation MSc.

Schmuki, P.; Buchanan, M.; Mason, B. F.; Sproule, G. I.; Graham, M. J. (1996). "Thickness measurements of thin anodic oxides on GaAs using atomic force microscopy, profilometry, and secondary ion mass spectrometry." *Applied Physics Letters*, 68: 2675-2677

Smowton, P.M.; Blood, P. (1997). "Visible emitting AlGaInP Laser diodes." *Optoelectronic properties of semiconductors and superlattices 4, strained-layer quantum wells and their applications*, M.O. Manasreh, Gordon and Breach Scientific Publishers

Smowton, P.M. Blood, P. Mogensen P.C. and Bour, D.P (1996). "Role of sublinear gain-current relationship in compressive and tensile strained 630nm GaInP lasers." *International journal of optoelectronics*, 10 (5): 383-391.

Smowton, P.M. Lewis, G.M. Chow, W.W. Jones, G. (2003). "Optimisation of 635nm tensile strained GaInP laser diodes." *IEEE journal of selected topics in quantum electronics*, 9 (5).

Tekeli, Z. A.; Altindal, S.; Cakmak, M.; Ozcelik, S.; (2007). "The behaviour of the IVT characteristics of inhomogeneous (Ni/Au)-Al<sub>0.3</sub>Ga<sub>0.7</sub>N heterostructures at high temperature." *Journal of Applied Physics* 102: 054510

Valster, A., et al (1992). "Effect of strain on the threshold current of GaInP/AlGaInP quantum well lasers emitting at 633nm." *Semiconductor Laser conference, 1992, Conference Digest 13<sup>th</sup> IEEE International*.

Van de Walle, C.G. (1989). "Band lineups and deformation potentials in the model-solid theory." *Physical Review B* 39 (3): 1871-1883

# Chapter 5. InP Pillar Device

## 5.1. Introduction

This section details the design, fabrication and characterisation of a composite InP nanopillar-polymer device. The novel design utilises a polymer to create an optical waveguide for light emission from an array of nanopillars. Potential applications include sensing with possible design benefits for silicon integration.

## 5.2. Device Design

A novel 720 nm emitting composite nanopillar-polymer laser device was designed for a variety of potential applications. A laser structure with a central active region consisting of five layers of InP quantum dots in GaInP quantum wells were grown by metalorganic vapour phase epitaxy (MOVPE) at the National Centre for III-V Technologies in Sheffield. The fabricated laser structure consisted of an array of nanopillars terminated at both ends by Distributed Bragg Reflectors (DBRs), designed with a reflectivity of approximately 0.99. A schema showing one end of the device can be seen in figure 5.1. The semiconductor architecture is shown embedded in a three layer polymer waveguide for optical guiding throughout the composite structure. An attempt was made to fabricate a three layer polymer using a low index polymer (MY-133) and a higher index polymer core (Benzocyclobutene, BCB) but the final design utilises the more elegant approach of using a lower air gap to sidestep the incompatibility of the particular low index polymer with the process flow.

The device design is motivated by a number of factors. The use of a composite nanopillar-polymer architecture allows the in-plane waveguiding of the emitted light, which has received little attention in nanolaser development. The use of nanopillars may also lead to a reduction of strain induced defects or dislocations when growing III-V material on silicon substrates, necessary for full integration with silicon microelectronics. The structure is additionally designed as an array of pillars due to its potential application as a sensor. The distributed gain material in the form of nanopillars gives potential for the inclusion of cavities which can be exposed to liquids or gases that will alter the optical output of the device. The use of quantum dot material is advantageous when considering the frequency

tuning of the DBR, the reflectivity of which is designed for a particular emission wavelength. The inhomogeneous size distribution of quantum dots gives access to an inhomogeneously broadened emission wavelength allowing the peak emission wavelength of the dots to be matched to the DBR peak reflectivity by tuning of the drive current.

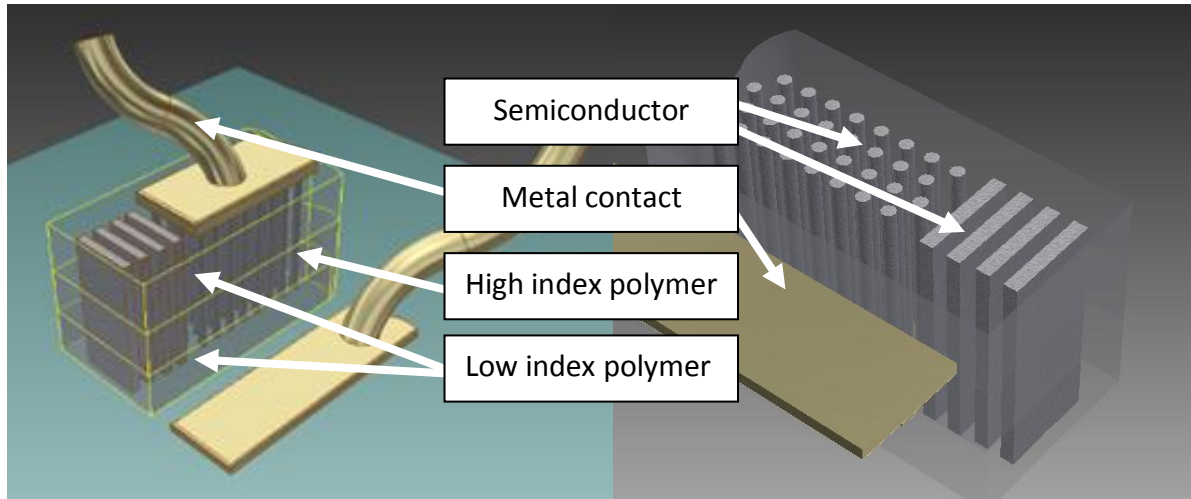


**Figure 5.1:** Schema of one end of the InP device, consisting of an array of nanopyllars terminated at both ends by a DBR, embedded in a three layer polymer waveguide. A potential electrical injection scheme is also shown.

The nanopyllar architecture may be advantageous when considering the dependence of the emission wavelength with temperature. The temperature dependence of the quantum dot emission wavelength is controlled by the carrier distribution and state distribution (density of states) within the material. The electron state distribution could potentially be altered using this pyllar architecture. Within a nanopyllar of a small enough width only a few dot sizes may exist. This sharper size distribution of dots implies a narrower (less inhomogeneously broadened) state distribution per pyllar (compared to a large cavity quantum dot laser). This results in a sharper gain spectrum. Narrowing the energy width of the state distribution compared to the thermal broadening of the carrier Fermi function makes the total number of occupied states less temperature dependent.

### 5.2.1. Epitaxial structure

The designed InP quantum dot laser structure contained an active region consisting of five layers of InP quantum dots (for a large maximum gain) in GaInP quantum wells. An illustration of the layer structure can be seen in figure 5.2.



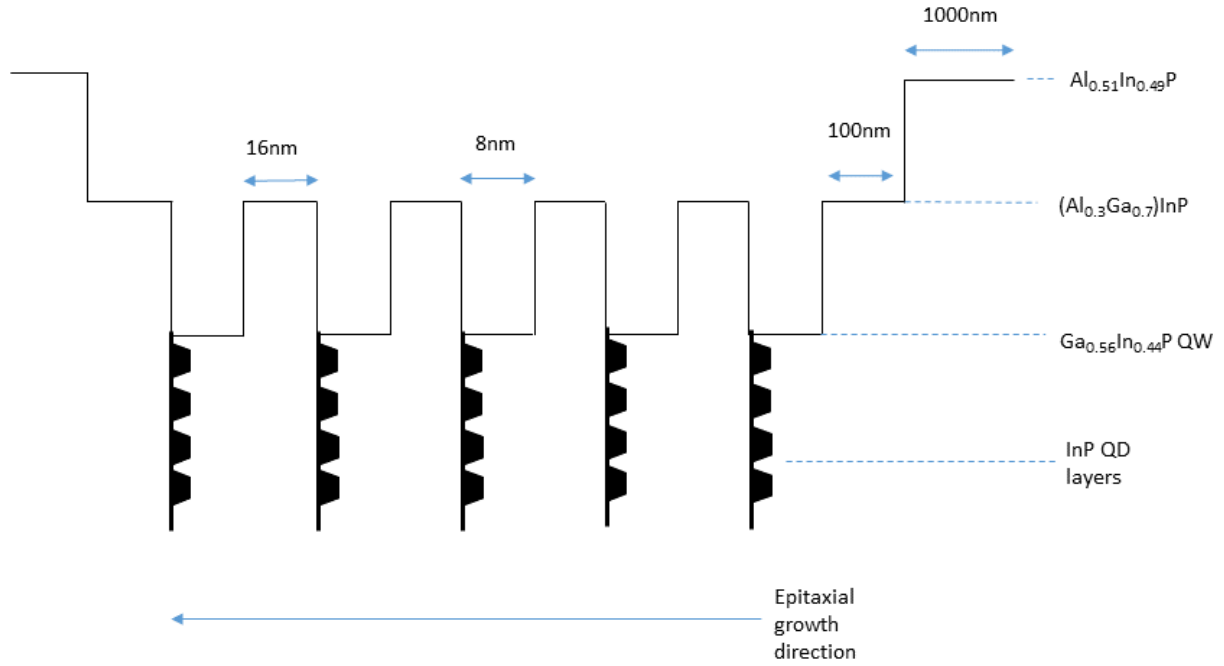
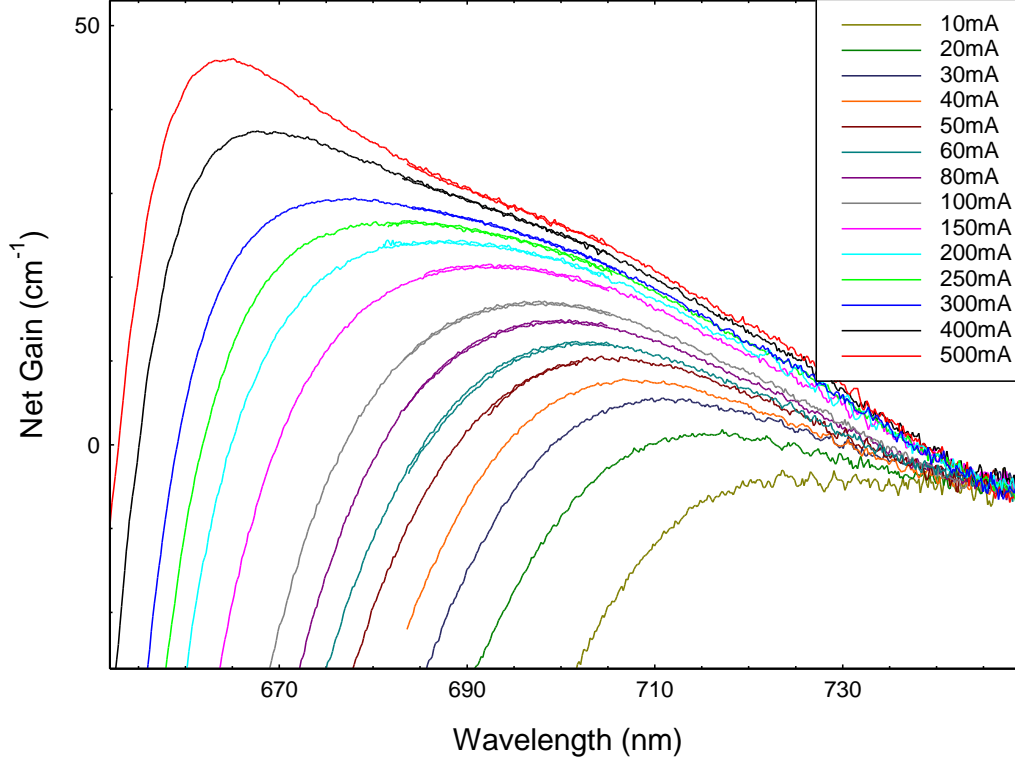


Figure 5.2: Illustration of epitaxial layer structure, showing a representation of the energy band.

### 5.2.2. Wavelength tuning

An ensemble of quantum dots has a broadened gain spectrum due to the size distribution of dots present. The peak of the gain spectrum defines the wavelength of the laser, providing that a cavity mode exists at that wavelength. Increasing the injection current of the device shifts the peak of the gain spectrum to shorter wavelengths due to state filling, this effect is shown in figure 5.3. The range of wavelengths obtainable is much larger for quantum dot ensembles compared to quantum wells due to the range of energy states available in an inhomogeneous dot distribution. This tuning effect is useful to match the emission wavelength to the reflectivity of the DBR structure. At a higher injection current it is also possible to encounter bandgap narrowing, where the wavelength redshifts to longer wavelengths due to a reduction in the bandgap as a result of the screening of the periodic potential of the crystal lattice by carriers (many body Coulomb effect) (Blood, P. 2015). However, bandgap narrowing is not observed in the data presented in figure 5.3 at the current densities used. The data within figure 5.3 was obtained courtesy of Samuel Shutts, Cardiff University, and was measured using semiconductor material with a similar structure (Shutts 2012) to the structure described in section 5.2.1. This data was used for preliminary material values to design the InP pillar device.



**Figure 5.3:** Measured gain spectra for 50 $\mu$ m oxide isolated stripe lasers at various drive currents, containing five layers of InP quantum dots. Measured data courtesy of Sam Shutts.

### 5.2.3. Waveguide design

Various polymer waveguides have been modelled using in-house and commercially available software (FIMMWAVE). Figure 5.4 shows that guiding in the composite structure with a three polymer waveguide is comparable to the guiding that would be obtained in the conventional undiluted gain medium. The term “undiluted gain medium” refers to material in which nanopillars have not been etched. A waveguide consisting of BCB polymer and a lower air gap also allows guiding of the optical mode. Although the optical confinement factor of the BCB-air-gap waveguide is smaller than that of the three polymer waveguide, less of the mode leaks into the GaAs substrate due to the lower refractive index of the air gap, leading to a reduction in absorption losses. The confinement factors for the undiluted medium, three polymer waveguide, BCB-air waveguide, and BCB waveguide are 0.047, 0.038, 0.020 and 0.015 respectively.

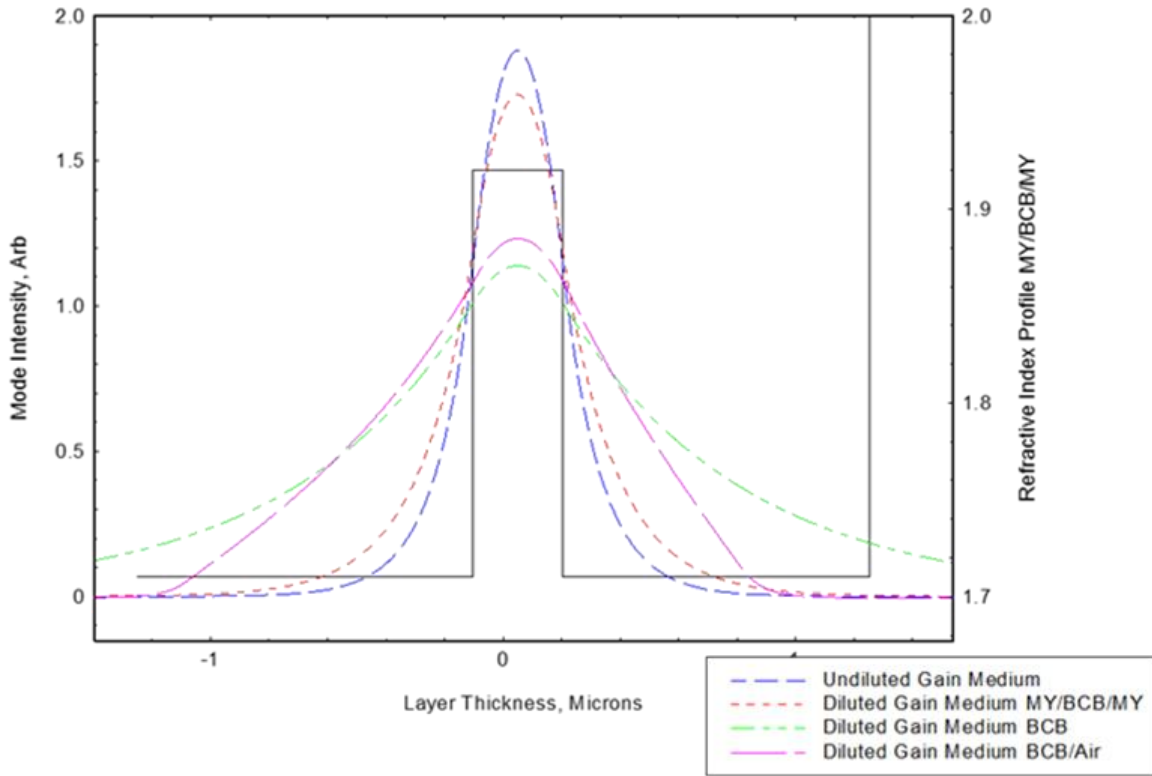


**Figure 5.4: Optical mode of various polymer waveguides modelled for the diluted gain medium, with a comparison to the undiluted gain medium.**

The spatial overlap of the optical mode with the GaAs substrate is used as a measure of optical guiding, a large overlap indicates that the mode would be absorbed into the GaAs substrate and would not be guided. The overlap for the MY/BCB/MY waveguide is 0.069%. A pure BCB waveguide sees an overlap of 7.148% which would inhibit operation, compared to only 0.001% when an air gap of 300 nm is used between the substrate and BCB waveguide. The overlap for the undiluted gain medium is 0.005%.

Photon Design software FIMMWAVE was used to obtain a value for the fraction of optical power within the waveguide core for the fundamental TE mode of the three polymer waveguide. The “core confinement factor” is used as an indication of the optical waveguiding achievable within the guiding core layer. An average refractive index was used to account for the hexagonal array of nanopillars at a specific fill factor within different polymer sections. Calculating an average refractive index in this way relies on a close-packed array where the optical wavelength within the material is comparable to or more than the spacing of the pillars. All simulations were performed at a wavelength of 720 nm to correspond to the InP quantum dot emission in these structures. Figure 5.5 shows the

refractive index profile of the composite nanopillar-polymer waveguide using MY-133/BCB/MY133. The first three TE modes are shown, the core confinement factor of the fundamental TE mode within the guiding layer is 0.9816967 at 720 nm. It is evident that a pillar-polymer architecture can provide strong optical guiding in the absence of a continuous semiconductor waveguide.

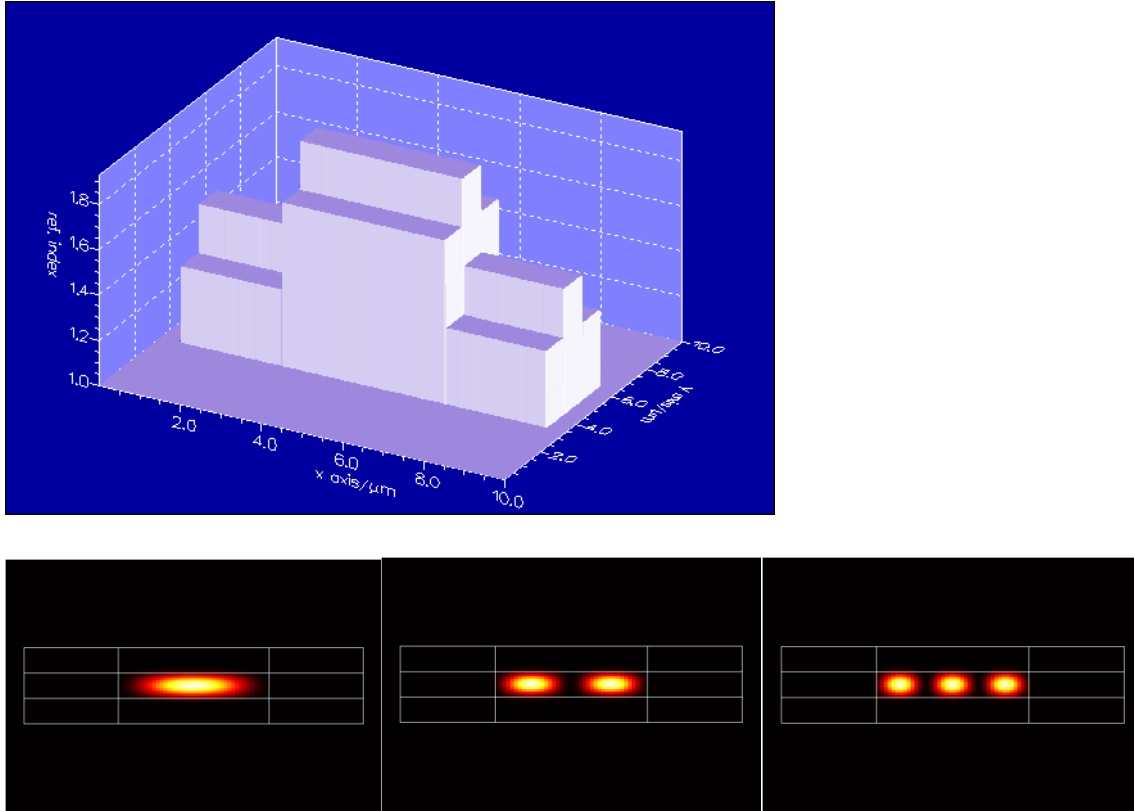
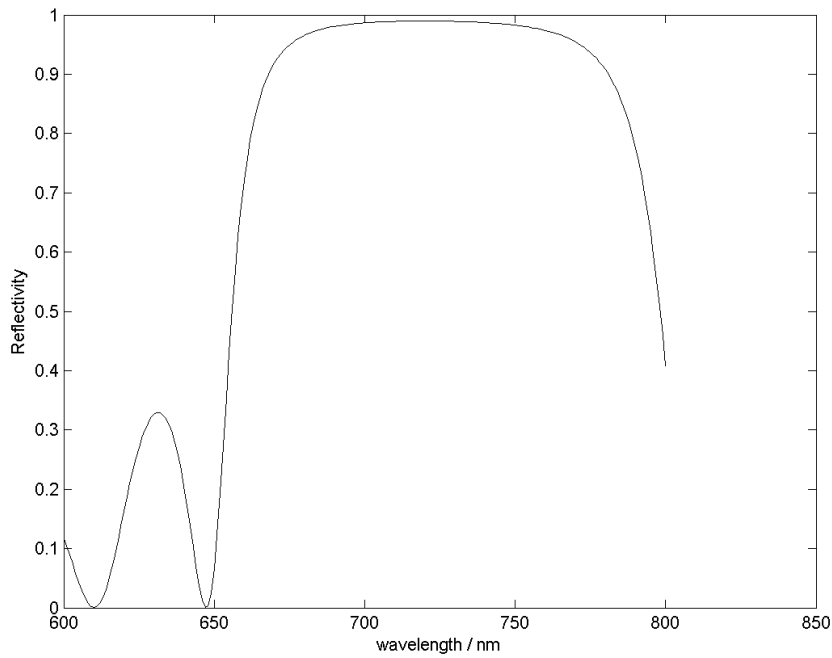


Figure 5.5: Top: Refractive index profile of MY / BCB / MY polymer waveguide, Bottom: First three TE modes of waveguide.

#### 5.2.4. Distributed Bragg reflectors

Due to the dilution of the gain medium highly reflective mirrors in the form of etched distributed Bragg reflectors (DBRs) are required to allow laser action. The DBR was modelled using the field transfer matrix method using in-house software. The calculation uses the quarter wave Bragg condition and solves Fresnel reflectivity equations at the interfaces in one dimension (West and Helmy 2006). A four period, third order DBR, formed from the semiconductor material and BCB polymer, was designed. Figure 5.6 shows the calculated reflectivity spectrum, with a reflectivity of 0.99 at the peak emission wavelength. Fabrication imperfections are likely to reduce this value due to surface roughness.



**Figure 5.6: Reflectivity spectrum for semiconductor-BCB polymer DBR at a 720 nm operating wavelength.**

### 5.2.5. Nanopillar array

A hexagonal array of nanopillars was designed. The pitch, or lattice constant  $a$ , was partly chosen to allow reproducible fabrication of the pillars. The fill factor of the pillars determines the average refractive index of the composite nanopillar-polymer waveguide. The InP pillar arrays have a fill-factor in the order of 20%. For 300 nm diameter nanopillars at this fill factor the reflectivity spectrum is shifted away from the stopband of the DBRs, allowing transmission within the cavity. The reflectivity spectrum can be seen in figure 5.7 (calculated in one dimension). With the width of the stopband of figure 5.6 and the width of the gain spectra of figure 5.3, the minima of the reflectivity spectrum of figure 5.7 should determine the lasing wavelength with operation at a low reflectivity wavelength. A random distribution of pillars may be preferred, however, an ordered structure was used to aid fabrication, allowing for consistent pillar dimensions throughout the structure, and to maintain an equal amount of gain material per unit distance, necessary for the characterisation techniques employed.

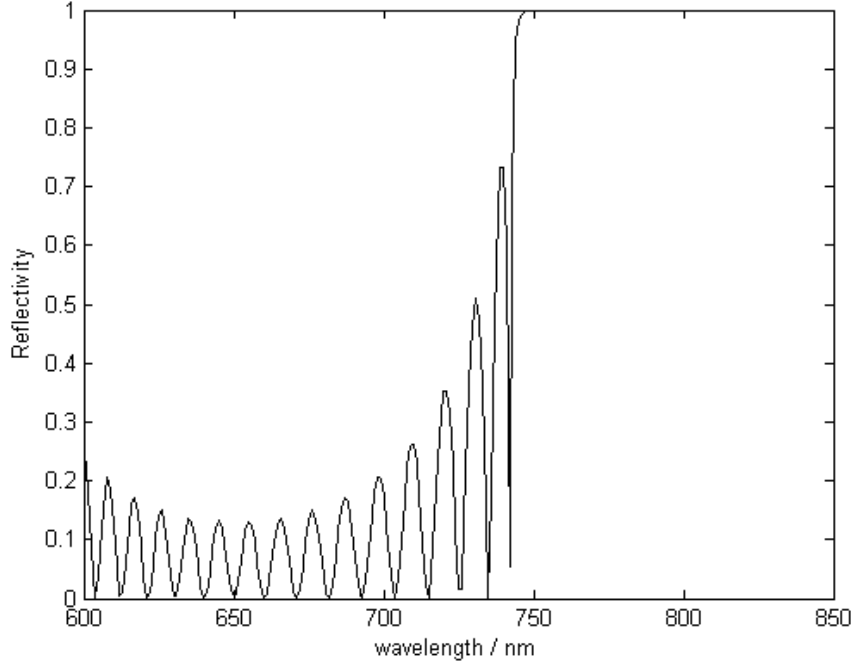


**Figure 5.7: One dimensional reflectivity spectrum of pillar array**

### 5.2.6. Device length

The device length required for laser action was calculated using the round-trip gain condition, equation 2.16. Figure 5.8 contains further experimental data, courtesy of Sam Shutts, Cardiff University, of the preliminary material used for design. It can be seen that for a 50  $\mu\text{m}$  oxide isolated stripe laser a high peak net modal gain in the order of  $26\text{ cm}^{-1}$  for the ground excited state ( $12\text{ cm}^{-1}$  at the knee of the curve) is achievable at room temperature under electrical injection. Due to the smaller confinement factor for the BCB air-gap pillar-polymer configuration the net modal gain obtainable is reduced to approximately  $11.3\text{ cm}^{-1}$  (at the peak of the ground excited state). Using the round-trip gain condition for a pillar fill factor of 20%, with a calculated DBR reflectivity of 0.99 at four periods, reduced to a value of 0.5 due to surface roughness (based on the etched-cleaved facet reflectivity efficiency value found in literature (Thomas, R. 2014), a device of length 3 mm will allow laser action when operating at room temperature at the peak of the gain-current curve for this material.

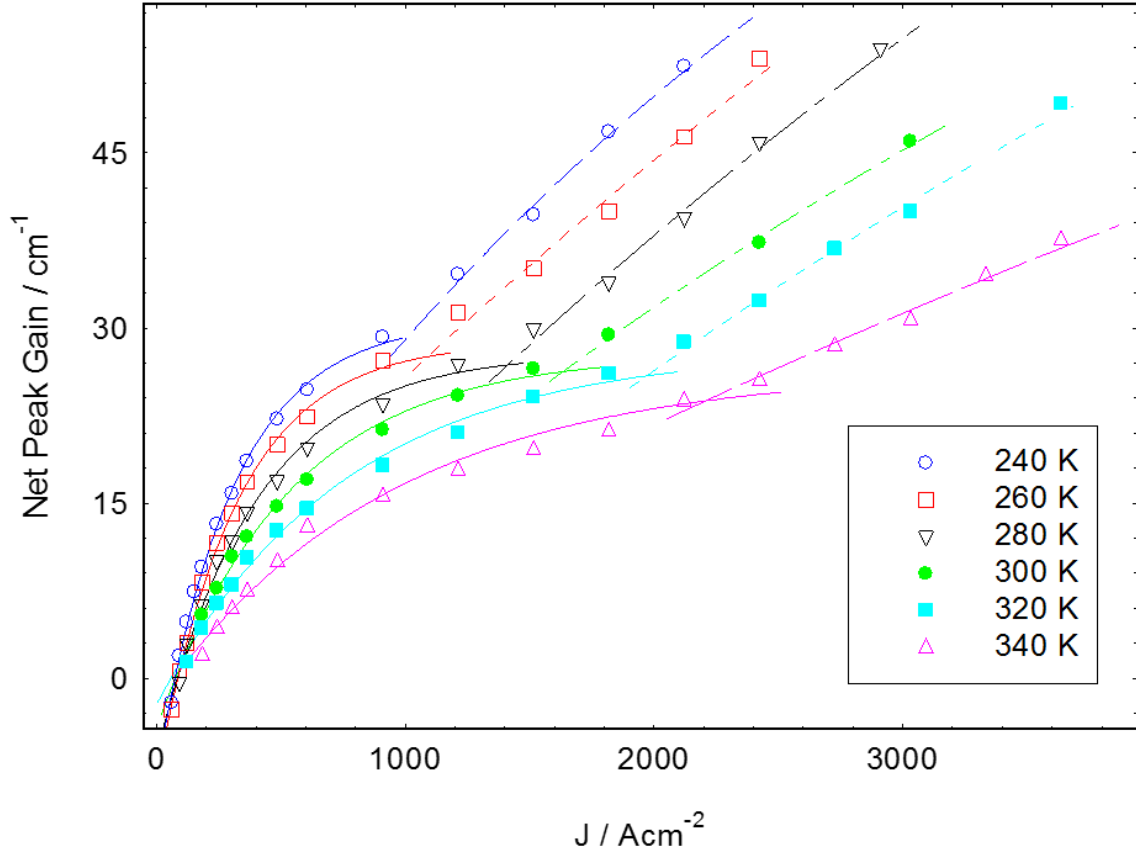


Figure 5.8: Measured net modal gain against current density at various temperatures, 50 $\mu$ m oxide isolated stripe lasers, five layers of InP quantum dots. Data courtesy of Sam Shutts.

### 5.3. Device Fabrication

This section describes the fabrication of the InP nanopillar devices. InP pillar etching was developed in order to fabricate devices within this material system, and a novel polymer waveguide was fabricated.

#### 5.3.1. Electron beam lithography

The fabricated devices consisted of an array of pillars in a polymer waveguide terminated at both ends by distributed Bragg reflectors (DBRs), as described in section 5.2. Note that structures intended for optical pumping were subject to a GaAs wet etch prior to patterning in order to remove the absorbing GaAs cap (electrical contact layer). The ICP etch mask for the pillars and DBRs were defined simultaneously using e-beam lithography. Positive tone e-beam resist PMMA was patterned followed by Nickel (Ni) deposition (60 nm) and lift-off. Nickel forms a good ICP etch mask as it does not tend to sputter, which would cause micro-masking across the sample. Ni also has a high selectivity (which is the ratio of the etch rate

between the mask and the semiconductor) in the order of 1:100. A high selectivity allows the use of a thin etch mask which is important for good mask edge definition to avoid faceting (erosion of etch mask at edges), and to reduce the effects of aspect ratio dependent etching (further described below).

The e-beam exposure dose and pattern type was determined experimentally. Figure 5.9 shows the Ni mask, where the image on the left was produced by using a dot pattern for exposure, and the image on the right was produced using an area dose, with curved element exposure. It is clear that a dot exposure produces less circular features with jagged edges, and is subject more highly to the proximity effect, where the dots on the edges of the array are smaller as they receive a lower exposure dose due to being more isolated from other features. The area exposure, with curved elements, uses a small step size at the edge, resulting in a well defined circle.

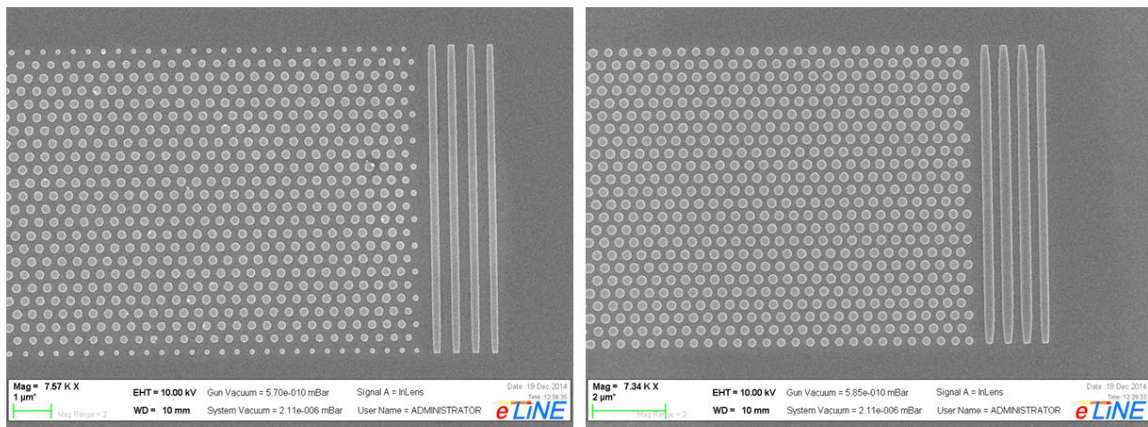


**Figure 5.9: SEM images of Ni etch masks for pillar and DBR structures. The left image used a dot electron-beam exposure, showing high sensitivity to the proximity effect and poor circularity of features. The right image shows area and curved element exposure, showing good circularity.**

Subsequent dose tests showed improvements to the dimensions of the required patterned shapes. The required dimensions were achieved through an iterative process, whereby information from the final etched structures were fed back to the original GDSII files used by the RAITH software. The drawn dimensions were altered when necessary, as were the exposure doses. Further examples of the Ni mask, and examples of a variation in pillar size can be seen in figure 5.10.



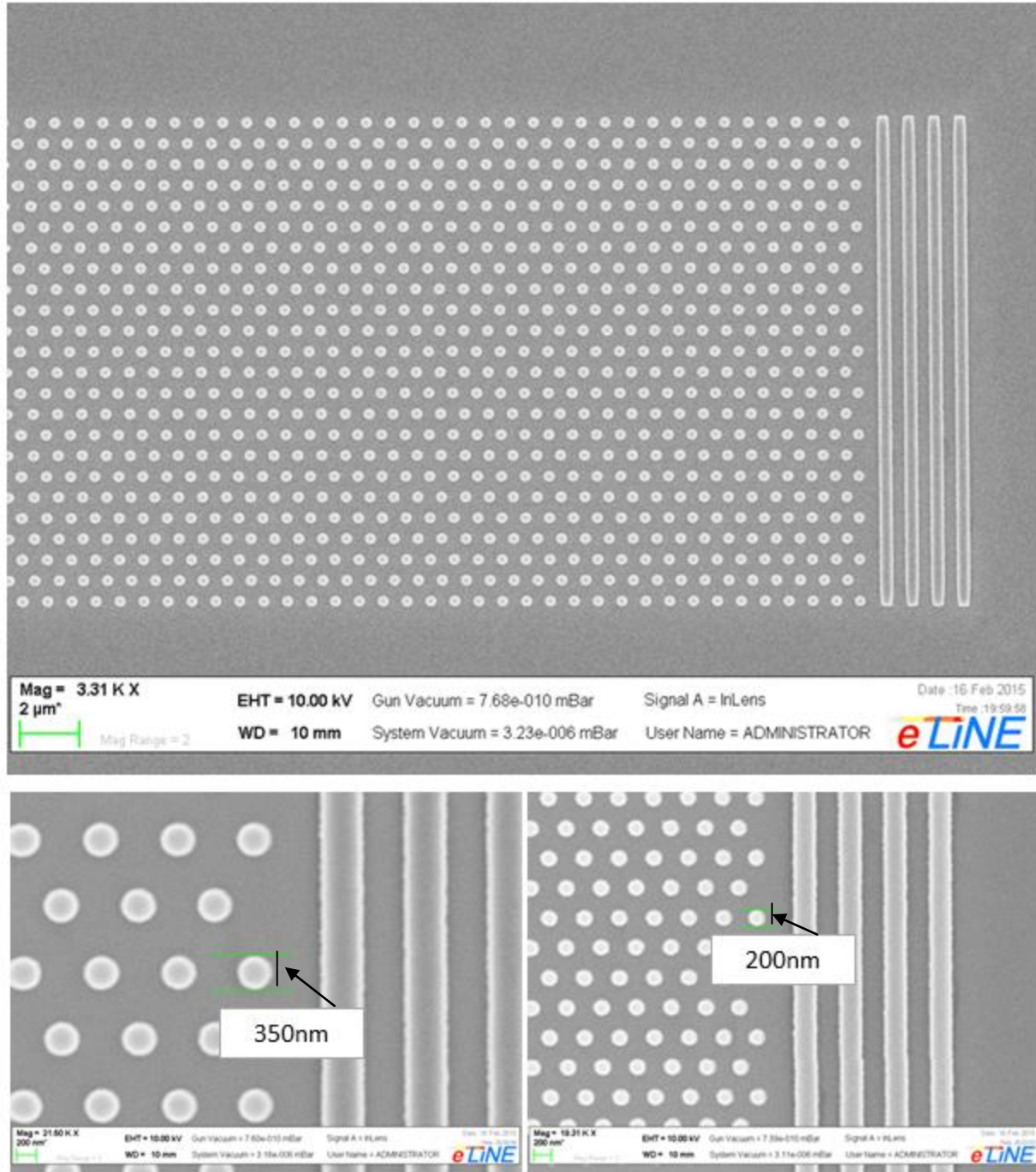


Figure 5.10: Ni masks used for etching of structures. Various mask dimensions for the pillars are shown.

### 5.3.2. ICP etching

An inductively coupled plasma was used to etch the pillar and DBR structures in order to obtain a highly anisotropic etch with a high aspect ratio. Previous work has been carried out on the dry etching of InP/AlGaInP (Shutts, S. 2012), however, the etching of closely packed

arrays of structures requires further work due to the altered local conditions in which etching occurs. Chiefly this regards aspect-ratio-dependent etching, which is an effect where the etch rate reduces with the width of the gap being etched, and is reduced further with the depth of the etch. This is primarily due to the difficulty in removing etch products in a confined space. In addition chemical etching components of the plasma interact more strongly with the semiconductor in a confined space, reducing anisotropy of the etch.

Alternative methods of etching could include purely chemical wet etching, purely physical etching (sputtering) or reactive ion chemical etching. A purely chemical process, such as wet etching, is unsuitable because it often produces an isotropic etch, with an etch rate that is limited by chemical reactions, reducing the aspect ratio achievable. Wet chemical etching can also show high selectivity to the composition of each layer. A purely physical process, such as sputtering, is unsuitable because it has a low etch rate and has a poor etch mask selectivity which limits the aspect ratio achievable. Purely physical etching can also cause damage to the semiconductor material. A combination of chemical and physical etching in the form of reactive ion etching (RIE) is advantageous. In RIE etching the sample is placed under vacuum between two parallel plate electrodes, across which a potential can be applied. Reactive ion species in the chamber are subject to the applied potential, controlling the kinetic energy of the ions striking the sample surface, therefore affecting the etch rate. The system is under vacuum to ensure that removed material escapes the surface and does not redeposit locally. The ions strike the sample perpendicular to the surface of the sample, resulting in a high vertical etch rate, and, depending on the gas chemistry, can also react chemically with the material being etched. Under the correct chemical conditions the reactive ion species are adsorbed onto the surface, a chemical reaction occurs, and the etch product is desorbed and removed. The desorption is dependent upon the volatility (vapour pressure) of the etch product and is often the limiting factor of an etch (Shutts, S. 2012). The physical bombardment of ions on the surface helps to remove etch product that would otherwise remain in a purely chemical process, and also ensures verticality as the horizontal etch rate is not kinetically assisted. The chemical aspect of the etch helps to ensure a higher etch rate and a higher mask selectivity than would otherwise be achievable for a purely physical process. It is important to note that in general terms any undesired horizontal etching using this method of dry etching is a result of too much chemical etching,

which can cause a matchsticking effect on pillars, where the top of the pillars appear wider or undercut.

An inductively coupled plasma (ICP) was chosen as it has further control compared to a reactive ion etch. The energy and the flux of the ions can be controlled independently. In an ICP the RIE part of the reactor controls the ion energy hitting the sample surface, as described above, whilst the flux (ion density) is controlled by the RF power across the walls of the chamber, perpendicular to the sample stage/RIE electrode (which is capacitively coupled to the plasma). A high flux is required for a high etch rate, although a high ion energy can cause damage to the surface.

The main parameters that can be altered when etching using an ICP are gas chemistry, temperature, ICP power, RIE power, gas flow and chamber pressure. The gas chemistry was chosen to chemically interact with the material being etched (Chlorine), and an inert gas was chosen for physical bombardment (Argon). Altering the temperature primarily affects the rate of removal of etch products which can otherwise limit the etch rate. Altering the RIE power primarily controls the ion energy, whilst altering the ICP power controls the ion flux

An Oxford Instruments Plasmalab 100 system with an ICP380 chamber design was used. Prior to etching the chamber was conditioned to ensure it was free of contaminants. This ensures repeatability of the etch. Contaminants were removed by conditioning the chamber with an oxygen plasma, followed by an inert gas, followed by the intended chemistry. The sample to be etched was placed on a three inch silicon carrier wafer. Parameters were user set and the etch was monitored using a camera/laser interferometer system. The laser light incident on the sample during the etch was partially reflected at each semiconductor interface as a function of the refractive index step between each semiconductor layer. The intensity of the reflected light was detected and monitored as the etch progressed. As the layer thickness decreased during the etch the reflected light intensity oscillated sinusoidally between constructive and destructive interference, producing an interferogram, an example of which can be seen in figure 5.11. This enabled the etch rate to be determined by observing when the desired epitaxial structure was completely etched.

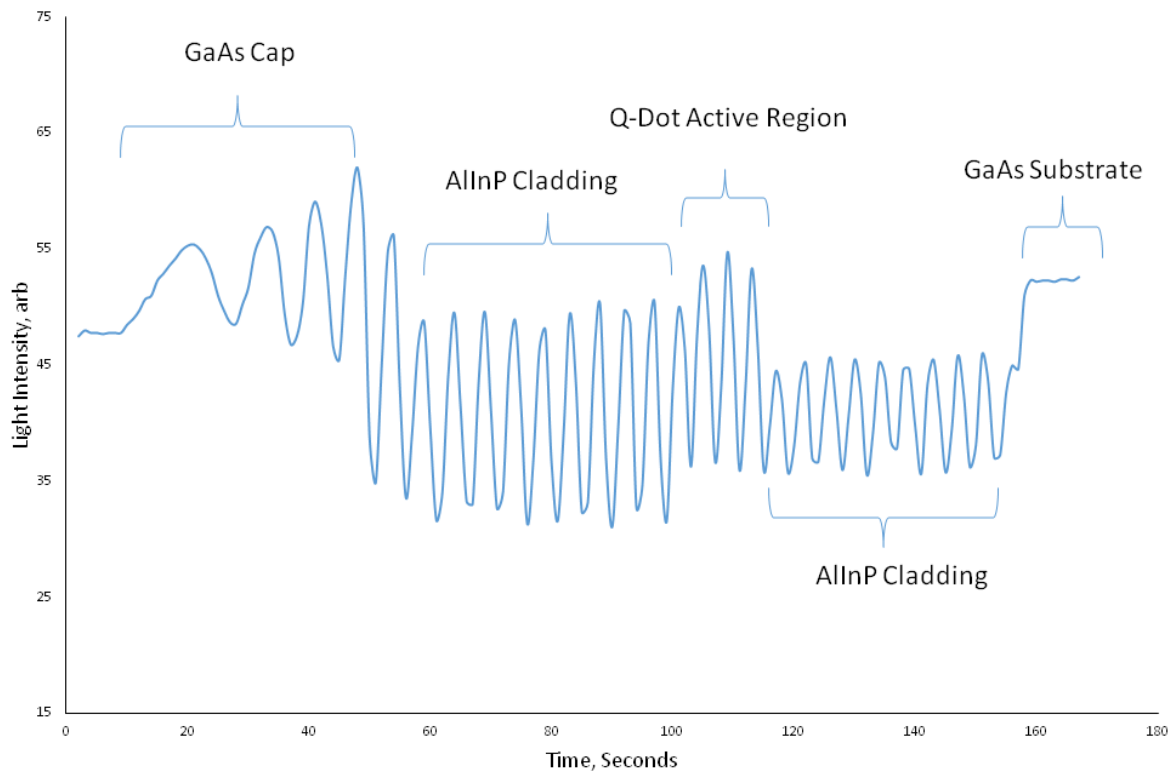


**Figure 5.11: Interferogram of etch for InP pillar/DBR structures**

A number of tests were performed to find the etch parameters suitable for the material and structures. Initially the  $\text{Ar}/\text{Cl}_2$  ratio was changed, whilst keeping the overall flow rate constant. The ICP power was set to 500W, with the RIE power set to 200W, at a temperature of  $180^\circ\text{C}$ . The  $\text{Cl}_2$  amount was decreased, moving from an  $\text{Ar}/\text{Cl}_2$  ratio of 35/5 to 38/2. The etch rate as a function of chlorine flow in standard cubic centimetres per minute (sccm) can be seen in figure 5.12.

The etched structures associated with the etch rates of figure 5.12 can be seen in figure 5.13. It is evident that at a  $\text{Ar}/\text{Cl}_2$  ratio of 35/5 there was too much chlorine present, causing a chemical undercutting, resulting in the curling of the DBR structures and the cut-off of the pillar structures as they thinned in their centre. At a ratio of 36/4 the undercutting decreased, with a further decrease at a ratio of 37/3. At a ratio of 37/3 the pillars are approaching a uniform width, although they are lower in height than the DBR structures. This may be due to the length of the etch and associated faceting of the Ni mask, resulting in the premature depletion of the mask and etching of the semiconductor material. Increasing the temperature of the etch can reduce the time and therefore also improve the uniformity of the width of the pillars because horizontal etching has less time to progress. The DBRs

also show signs of matchsticking, where the top of the structures have indentations, this can either be improved by a reduction of chlorine or a reduction of etch time by varying other parameters. At a further decreased chlorine content of 38/2, the structures etched have no real definition, chemical etching has effectively stopped. The etching in this case was dominated by the physicality of the argon atoms. The ratio 37/3 for Ar/Cl<sub>2</sub> was chosen for further parameter changes.

The etch rate as a function of temperature, for the Ar/Cl<sub>2</sub> chemistry of 37/3, can be seen in figure 5.14. The Temperature was varied, whilst the Ar/Cl<sub>2</sub> ratio was kept at 37/3, ICP power at 500W and RIE power at 200W. The temperature was varied between 180°C and 240°C.

As the temperature increases the plasma surrounding the heated sample becomes more energetic, the rate of desorption of the etch product InCl<sub>3</sub> increases, increasing the etch rate. At a certain temperature the etch rate falls, this may be a result of the conditions becoming more unfavourable for the adsorption of species for continued chemical etching.

Figure 5.15 shows structures etched at 180°C and 200°C. There is a definite reduction in matchsticking and increase in height of the pillars from 180°C to 200°C. Etches performed at 210°C and 220°C exhibited a marginally improved width uniformity. However, at these higher temperatures the Ni tended to sputter, anneal and inter-diffuse with the semiconductor material, so the compromise of 200°C was chosen.

To try to further improve the etch the ICP power, which controls the ion flux, was adjusted, whilst keeping the Ar/Cl<sub>2</sub> ratio at 37/3 and temperature at 200°C. For a close packed structure it is conceivable that the flux of ions can be a sensitive parameter due to the balance required between adsorption and desorption in a confined space. An ion flux that is slightly too high may cause increased sputter damage if etch product is produced in a high concentration before being removed, whilst a flux that is slightly too low will not sufficiently remove etch product slowing down the etch, meaning chemical horizontal etching has more time to progress. Figure 5.16 shows the etch rate as a function of ICP power. The etch rate does not change significantly between 500W and 600W, but does fall off sharply at 400W.

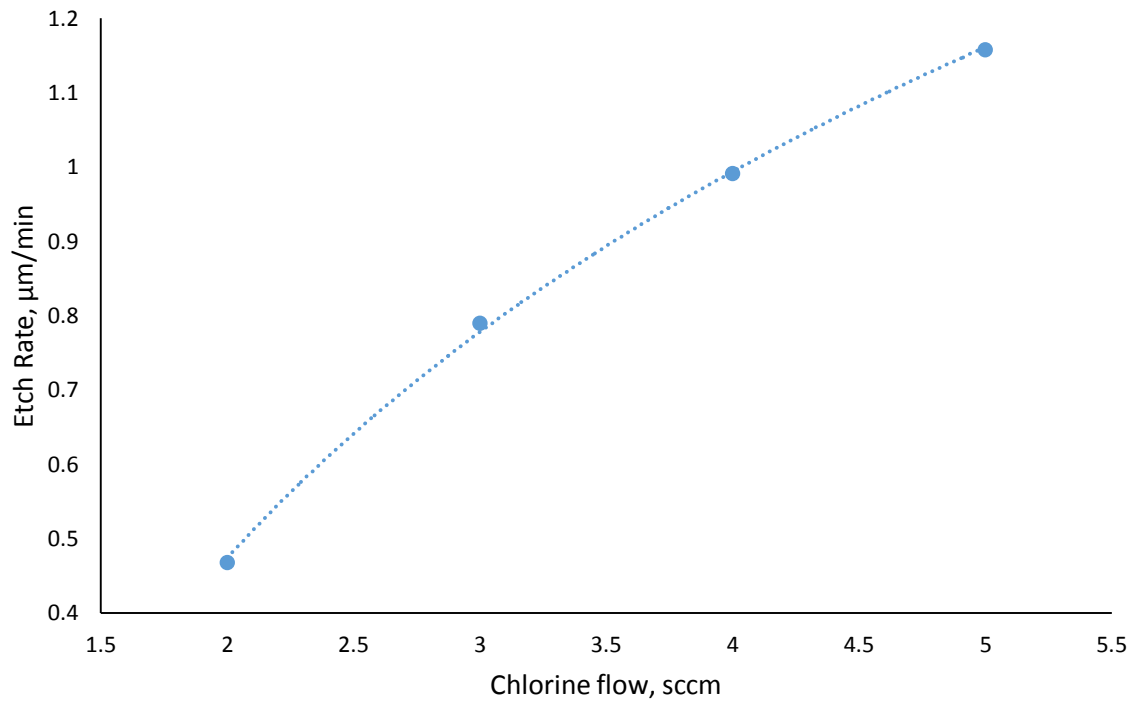


Figure 5.12: Etch rate as a function of chlorine flow, with an Ar/Cl<sub>2</sub> ratio in the range of 35/5 to 38/2.

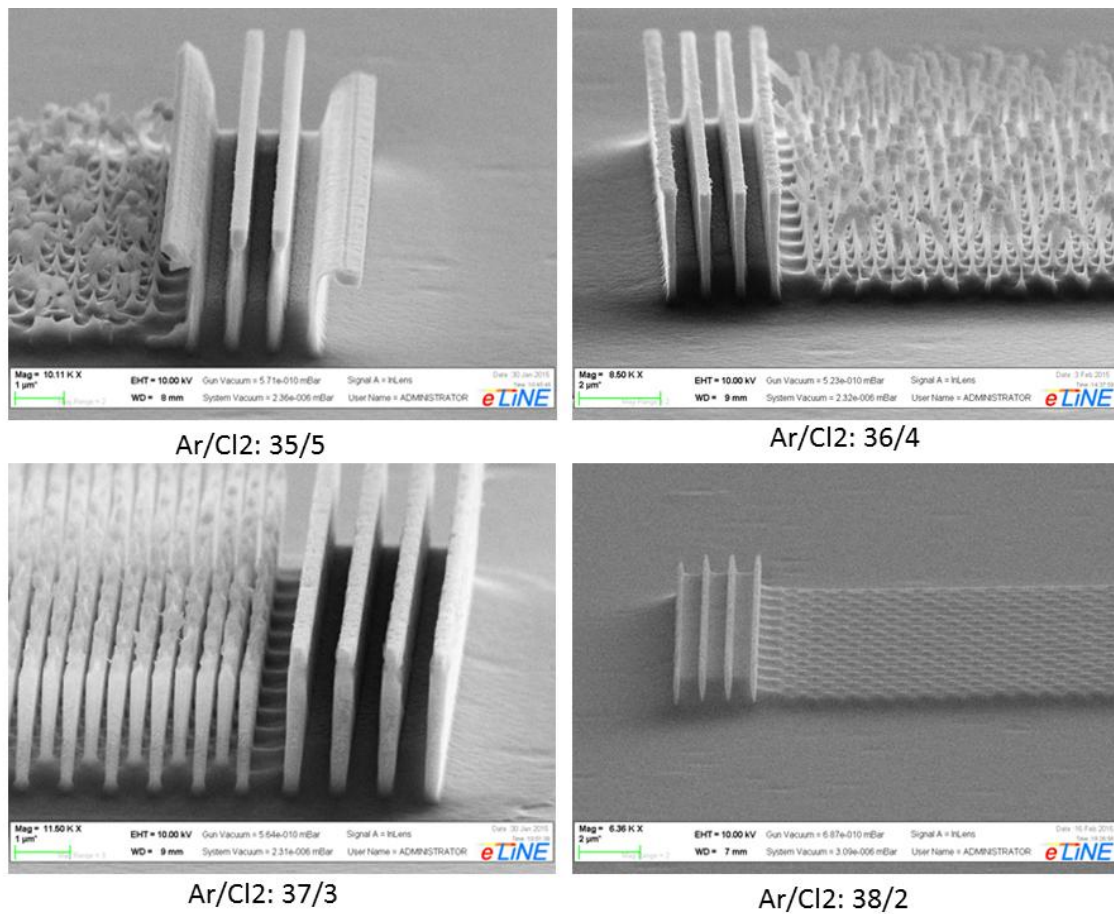


Figure 5.13: Decreasing the Chlorine gas content whilst keeping the Ar/Cl<sub>2</sub> ratio constant.

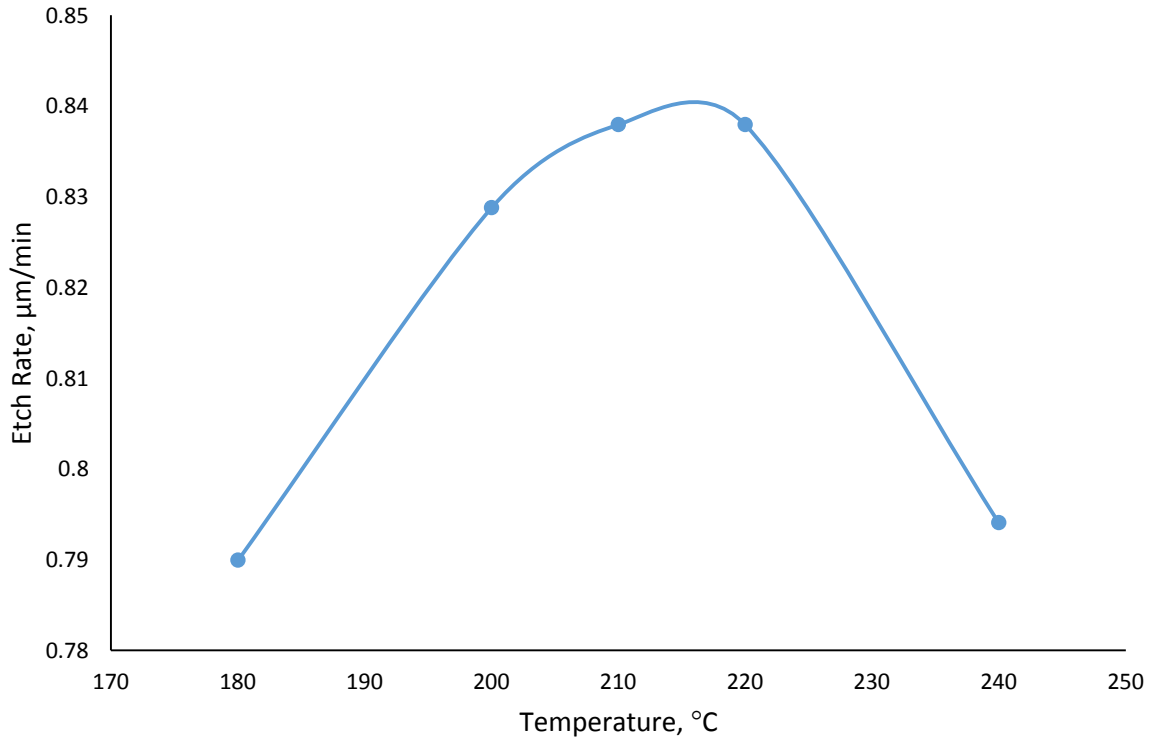


Figure 5.14: Etch rate as a function of temperature for a gas chemistry ratio of  $\text{Ar}/\text{Cl}_2$  37/3.

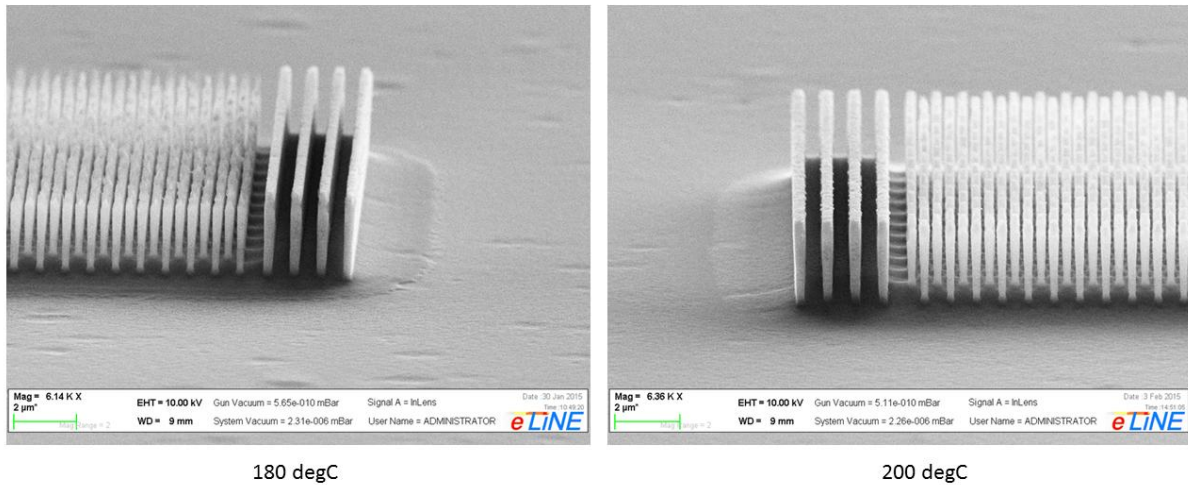


Figure 5.15: Structures etched at 180°C and 200°C at an  $\text{Ar}/\text{Cl}_2$  chemistry of 37/3.

Figure 5.17 shows structures etched at various ICP powers. An ICP power of 600W resulted in pillars that were smaller in height than expected, with increased damage to the Ni mask. The etch rate of the 500W and 600W etches were similar, although the 500W etch resulted in improved structures. This indicates that, in this parameter space, the etch rate may be more dominated by the RIE power, which was not changed between these samples, and the local interaction within the close-packed array is dependent more highly on the ion flux. An



ICP power of 400W had a smaller etch rate, and as a result suffered from increased horizontal chemical etching. Within this work a full study in the change of RIE power was not done, only small changes in RIE power were implemented (50W change). Further work could see a further increase in RIE power at an ICP power of 500W to further improve the anisotropy of the etch. However, for the purpose of this work the structures produced were adequate.

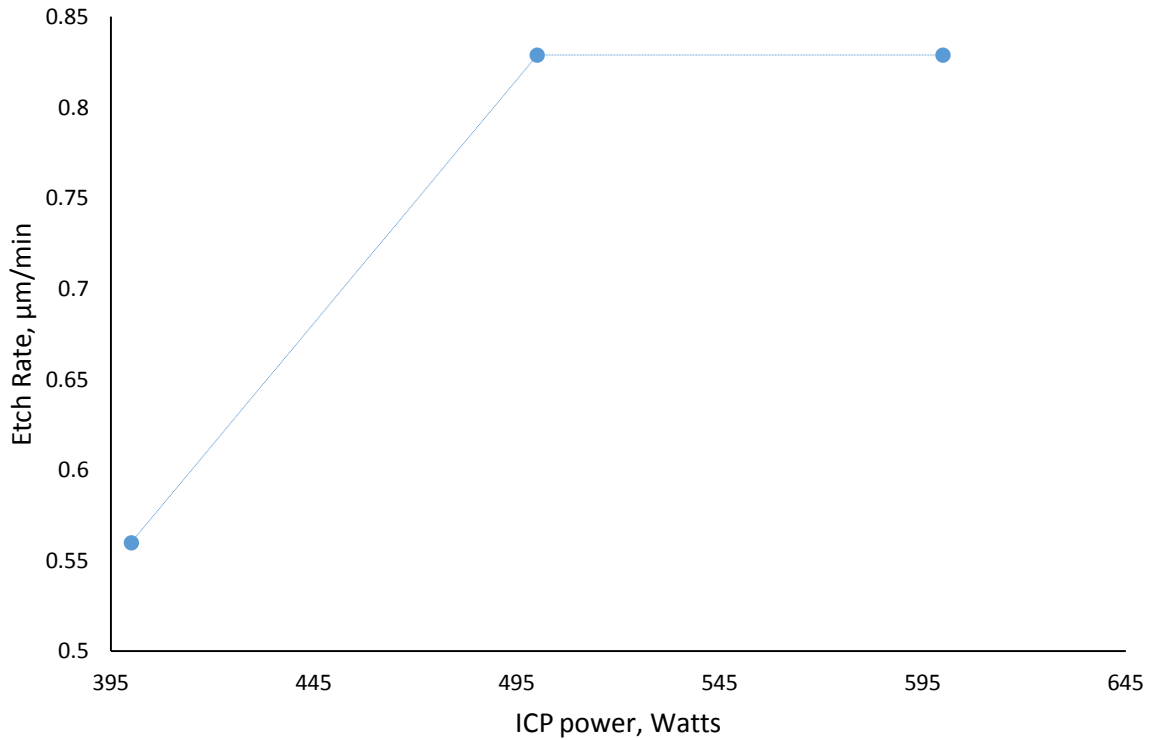


Figure 5.16: Etch rate as a function of ICP power.

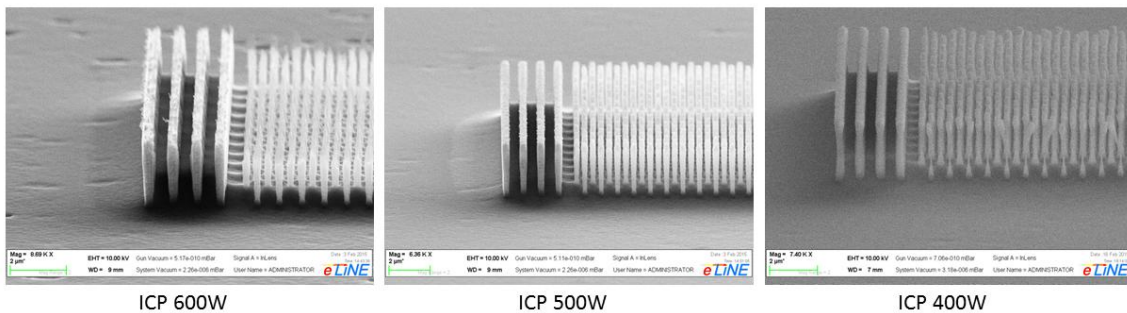
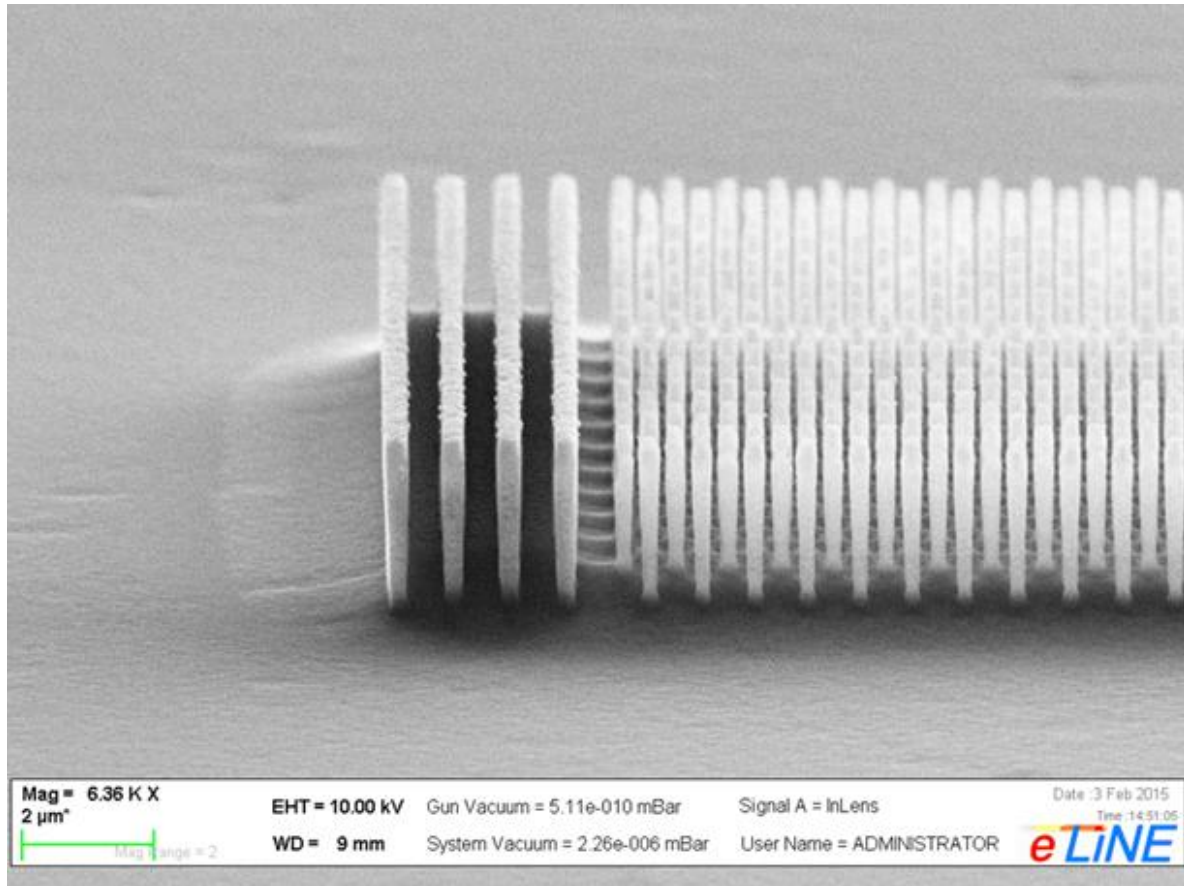


Figure 5.17: Etched structures as a function of ICP power.



An example of the final etched structure can be seen in figure 5.18. Immediately after ICP etching the structures were subject to a chemical wet etch in an attempt to remove any remaining nickel etch mask.



**Figure 5.18:** Etched structure, using ICP power 500W, RIE power 200W, Temperature 200°C, Ar flow 37sccm, Cl<sub>2</sub> flow 3sccm, Chamber pressure 10mTorr.

### 5.3.3. Polymer waveguide fabrication

In order to test the conformity of the central polymer, BCB, to the pillar structures, pillars were coated in BCB and baked. An example of this can be seen in figure 5.19. The cleaved cross-section shows a degree of aspect ratio dependent etching, as described above, where the material inbetween the pillars did not etch as deeply as the material away from the pillars. The image shows good conformity of the polymer around the nanopillars.

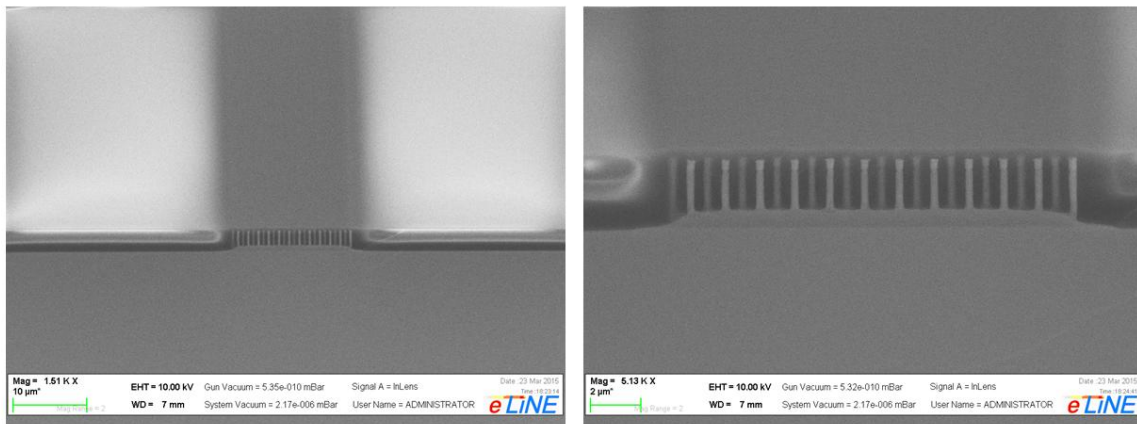


**Figure 5.19: Cleaved cross-section of early tests of etched InP pillars coated in polymer, imaged at an angle using SEM. Conformal coverage of pillars with BCB polymer is shown. Enhanced view (right) shows aspect-ratio-dependent etching and matchsticking of early etch tests.**

Although a three polymer waveguide using polymers MY133/BCB/MY133 was experimentally tested, intermixing of these polymers, and in particular the evaporation of the MY133 polymer during baking as a result of its temperature sensitivity, made fabrication of this waveguide using these materials impossible. However, the BCB waveguide with a lower air gap was further explored.

The waveguide was fabricated using Benzocyclobutene (BCB) polymer with an air gap at the base of the pillars, formed via the use of a sacrificial polymer layer, which consisted of Polydimethylglutarimide (PMGI). This is a novel and new use of the polymer. PMGI is a photosensitive polymer, however, even when unexposed it has a high development rate, and does not intermix with resists once baked. It has a glass transition temperature of 185°C and a reflow temperature between 200-300°C, stable up to 325°C, making it compatible with BCB baking steps.

PMGI SF6 was spun onto the sample at a rate of 5000 rpm at an acceleration of 1000 rpm/sec for 20 secs, obtaining a PMGI layer thickness in the order of 360 nm. The PMGI was baked at a high temperature to ensure the reflow of the polymer for conformal coverage. The temperature was also chosen to ensure compatibility with the whole process flow, where thermal expansion and contraction throughout the various steps was considered. The PMGI was baked for 10 minutes at 100°C for an initial softbake, and slowly increased to 210°C by 10°C per minute to reduce thermal stress. The PMGI was then then baked at 210°C

for a further 10 minutes to ensure reflow above the glass transition temperature. The unexposed development time of PMGI was found to vary with bake temperature. Photoresist developer MF319 was used to remove the PMGI in a number of test developments. The PMGI was patterned into 50  $\mu\text{m}$  stripes using a S1813 resist mask in order to form a step-edge for height profilometer measurements. It was found that removal of PMGI after a 210°C bake took twice as long as that of a 100°C bake. The end height of the polymer is also dependent on the bake conditions. Baking at 210°C reduced the height of the polymer from 360 nm (obtained from a 100°C bake) to 320 nm.

The BCB layer was spun on top of the PMGI layer. An adhesion promoter AP300 was used in order to aid adhesion of the BCB to the semiconductor pillars, but also to provide a small barrier between the polymers. BCB was spun on using a two step process to ensure that the top surface was planar, rather than conforming too strongly to the underlying topography of the pillars, which can cause undulations in height. However, small undulations of 20 nm still persisted even after high temperature annealing of the BCB. ICP etching of the BCB can be used to reduce the final thickness of the top BCB layer, and to allow metallisation. The BCB was baked at 100°C for 2 minutes to drive out solvents, and further baked in a nitrogen atmosphere to harden, where the temperature was slowly increased to 210°C, and baked for 40 minutes.

The samples were cleaved to expose the cross-section of PMGI/BCB, and submerged in MF319 to remove the PMGI layer. The PMGI used in this process flow was chosen to exceed the manufacturers predicted dissolution rate. The increased rate was obtained by purposefully using out of date PMGI (6 months out of date). It was found that the whole PMGI layer is removed within 15-30 seconds. An additional advantage to using PMGI is that it is derived from the e-beam resist Polymethyl methacrylate (PMMA). It can be exposed using deep UV wavelengths but can also be exposed using e-beam, requiring a dose 3 to 5 times smaller than that one would use for PMMA for a similar feature. In this mode of use PMGI which is not out of date would be used, resulting in a development time on these structure of 4.5 minutes if the PMGI is attacked from all sides, which would require patterning of the top BCB layer. These attributes make PMGI particularly suitable as a sacrificial layer for small waveguides, as it can be patterned using these methods when required.

The fast and complete removal of the lower PMGI layer leaves a floating BCB layer where there are no structures to anchor it in place. Figure 5.20 shows a sample where the BCB layer has lifted and, upon meeting the pillar array, has torn off. This could be advantageous, however, in practice the floating BCB has also been seen to pull away from the pillar array, often breaking the pillars away from the semiconductor which remain embedded in the polymer. Although this may also have useful applications, it is not intended for this structure.

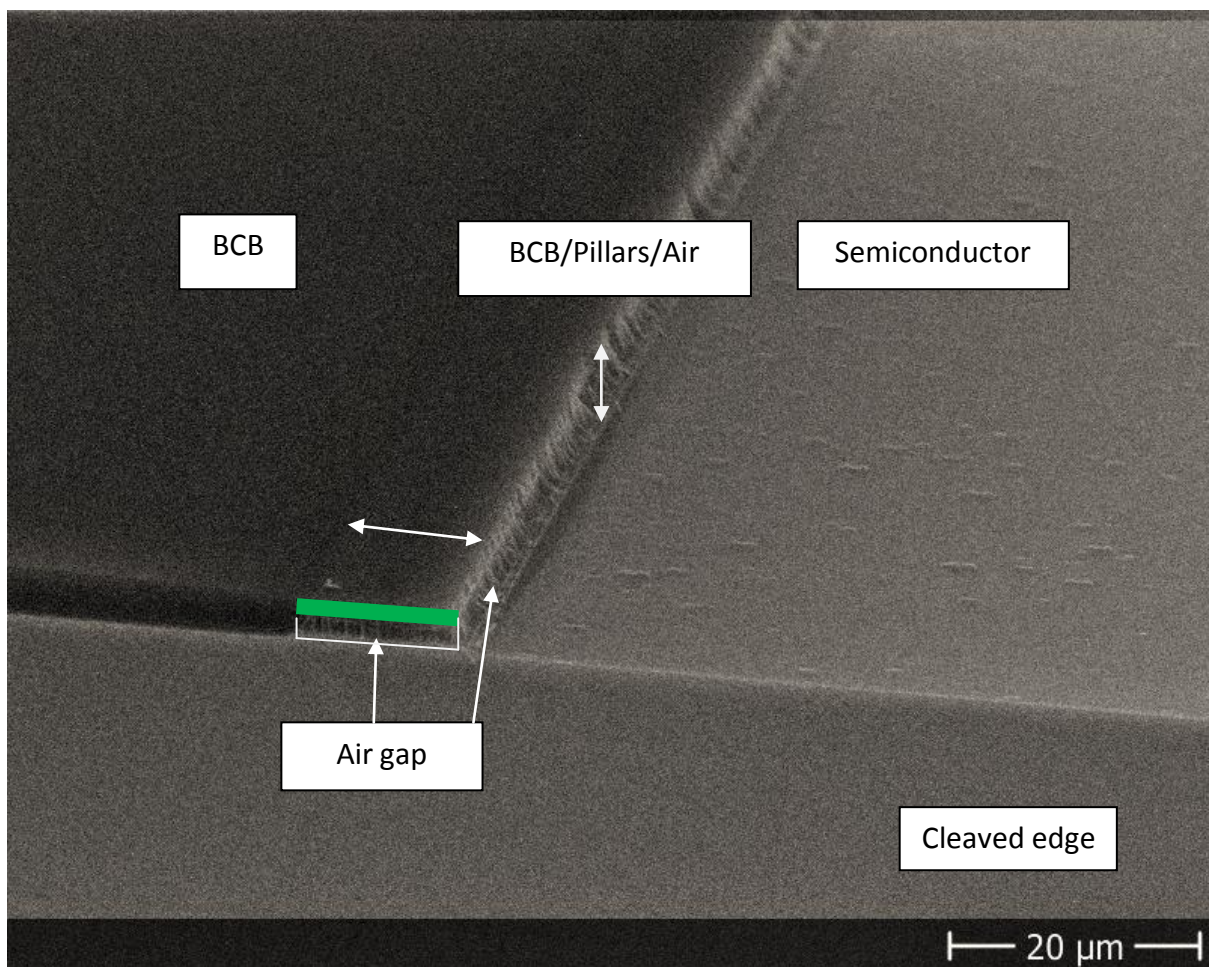


**Figure 5.20:** SEM image showing an array of pillars in a BCB-air gap waveguide. The right hand side of the image shows an area where the floating BCB has torn away along the edge of the pillar array, due to a lack of structural anchors. The air gap at the cleaved edge has been highlighted using white indicator lines, the cross-section of the BCB polymer on the pillar array is highlighted in green.

Figure 5.21 shows a sample on the left where the PMGI has not been removed evenly, leaving a bimodal type waveguide, whilst the example on the right shows a structure where all of the PMGI was removed in the pillar region, although with evidence of an uneven air



gap height due to BCB sheet tearing forces. These effects appear to be dependent on development time, and the existence of surrounding structures to control the BCB sheet tearing.

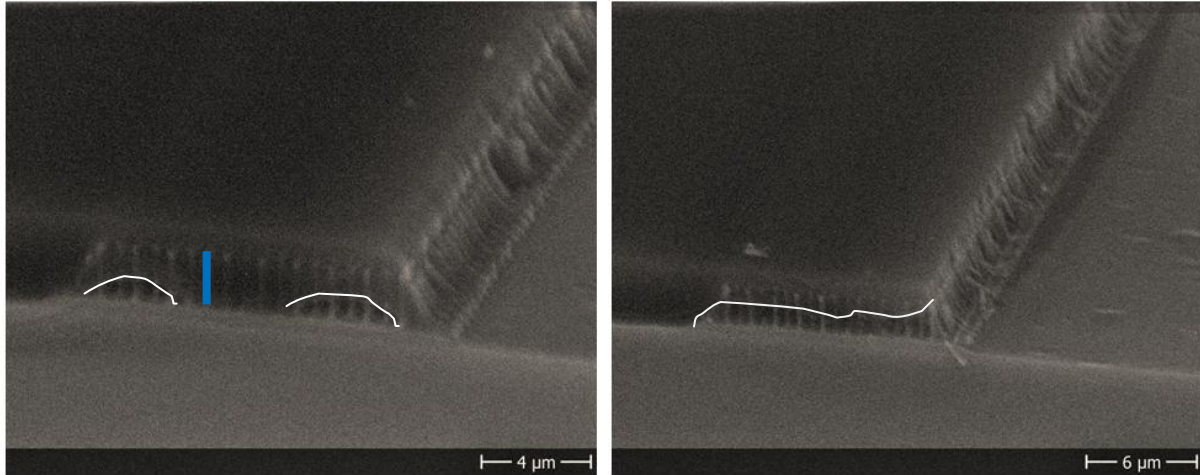


**Figure 5.21:** Examples of BCB-air gap waveguides in which development time was too small (left) and too large (right). The air gap has been outlined in white for clarity, and single pillar has been highlighted in blue.

In order to prevent the BCB sheet from lifting around the pillar arrays, anchor structures in the form of ridges were included on the sample, which were also included for material characterisation purposes. The inclusion of these structures allowed for the use of a development time that removed all of the PMGI without leading to full BCB lift-off. Using this method samples with even air gaps were fabricated, as shown in figure 5.22. The sample image on the right also shows a phenomenon in which edge pillars on some devices were bent. This is most likely as a result of cleaving.

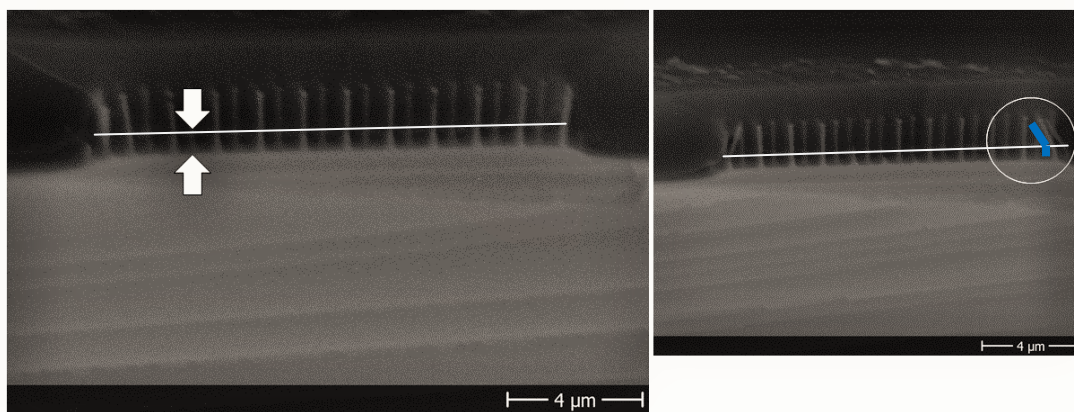


**Figure 5.22:** BCB-air gap waveguides with even air gaps, indicated by arrows and a white line. The image on the right shows bent edge pillars, circled and highlighted in blue, as a result of cleaving.

## 5.4 Results

### 5.4.1. Gain and absorption measurements

The optical stripe length measurement for gain and absorption, described in section 3.4.3, was used to characterise the fabricated devices. An equivalent electrical injection method of measuring gain and absorption, the segmented contact method, was also performed on the material for comparison. Electrical measurements were performed by Ivan Karomi, Cardiff University.

The characterisation technique requires single-pass propagation of light, therefore DBR structures were not included in the characterisation device structures to avoid optical feedback. Light emission was not detected from the nanopillar-polymer composite arrays. To explore the potential reasons for this, 10  $\mu\text{m}$  wide ridges in polymer were fabricated and characterised. It is important to note that these ridges were made in the same process and at the same time as the nanopillar structures, both were subject to the same fabrication conditions. The reason for the lack of light emission was determined from this analysis, whilst also determining the internal optical loss of the material. A change in absorption with optical pump power was also observed.

As described and illustrated in section 3.4.4, the stripe length absorption measurement requires the optical pumping of sections S1 and then section S2, whilst the gain measurement requires pumping of section S1S2 and then section S1. The light intensity spectra of these sections at a pump laser power of 5 watts are shown in figure 5.23 for a ridge structure.

Absorption of the material was measured using the optically pumped variable stripe length method, the absorption spectrum can be seen in figure 5.24. The optically pumped absorption measurements were taken on a 10  $\mu\text{m}$  wide ridge in BCB. The states within the material can be determined from the shape of the absorption curve. The gain mirrors the absorption if all available states achieve population inversion. The absorption edge of the quantum well is not shown as this exists at a lower wavelength, as indicated by the arrow. In this material system a bimodal distribution of dot sizes has previously been observed, in

which lower energy states are produced by larger dots, whilst higher energy states are produced by smaller dots. The dot ground state is labelled.

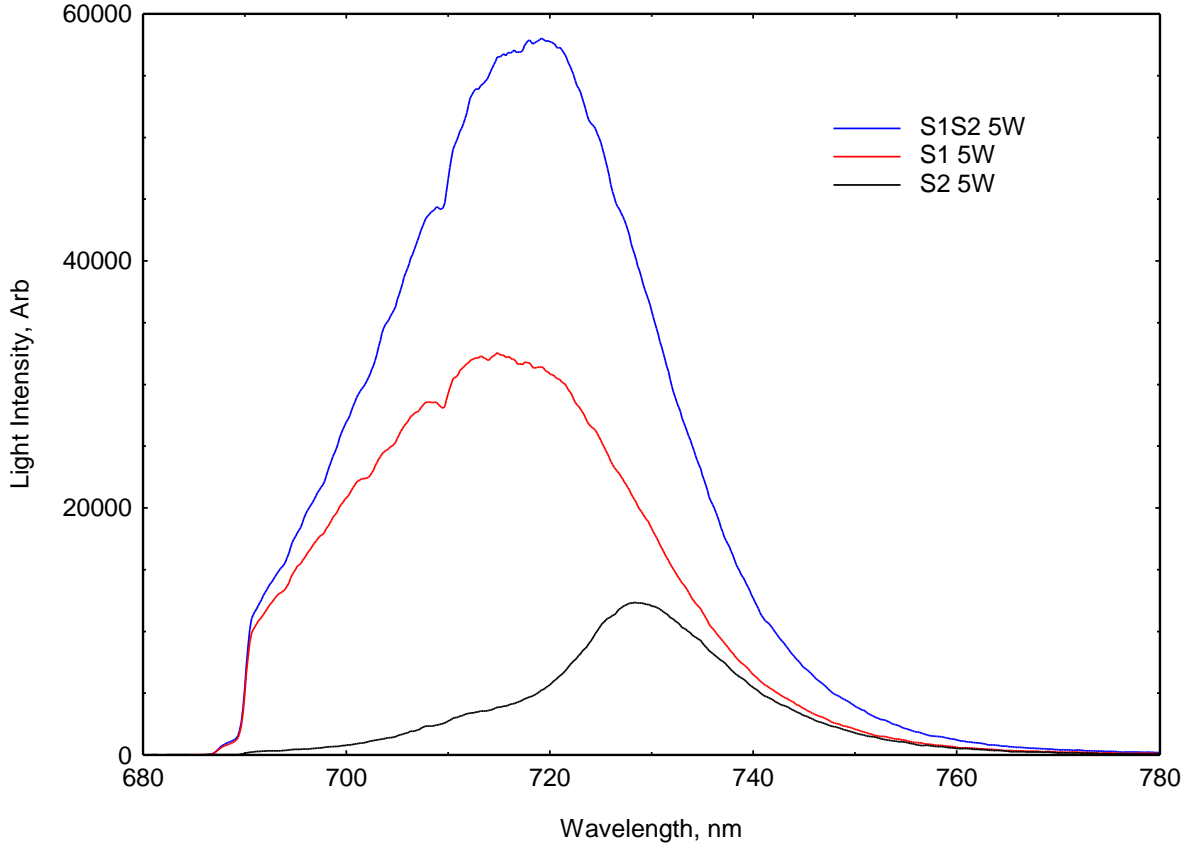


**Figure 5.23:** Light intensity in arbitrary units measured as a function of wavelength for optical pumping of stripe length sections, for sections S1S2, section S1 and section S2, at a pump laser power of 5 watts. For a 10  $\mu\text{m}$  ridge in polymer structure.

Below the band edge (long wavelengths), where there are no states, the absorption value tends to the value of internal optical loss,  $\alpha_i$ . Figure 5.24 shows additional absorption data (at the high wavelength end of the spectrum) obtained from a 50  $\mu\text{m}$  oxide isolated stripe laser using the electrically injected segmented contact method. The measurements on this larger structure (with higher light intensity output) show significantly less noise in the longer wavelength region, allowing a more precise determination of the internal optical loss. For the electrically injected measurement the internal optical loss tends to  $3.5\text{cm}^{-1}$  (for the 50  $\mu\text{m}$  oxide isolated stripe structure), for the optically pumped measurement the signal-to-noise ratio is poor, although a value of  $5.5\text{cm}^{-1}$  can be indicated from extrapolation (for the 10  $\mu\text{m}$  ridge structure).

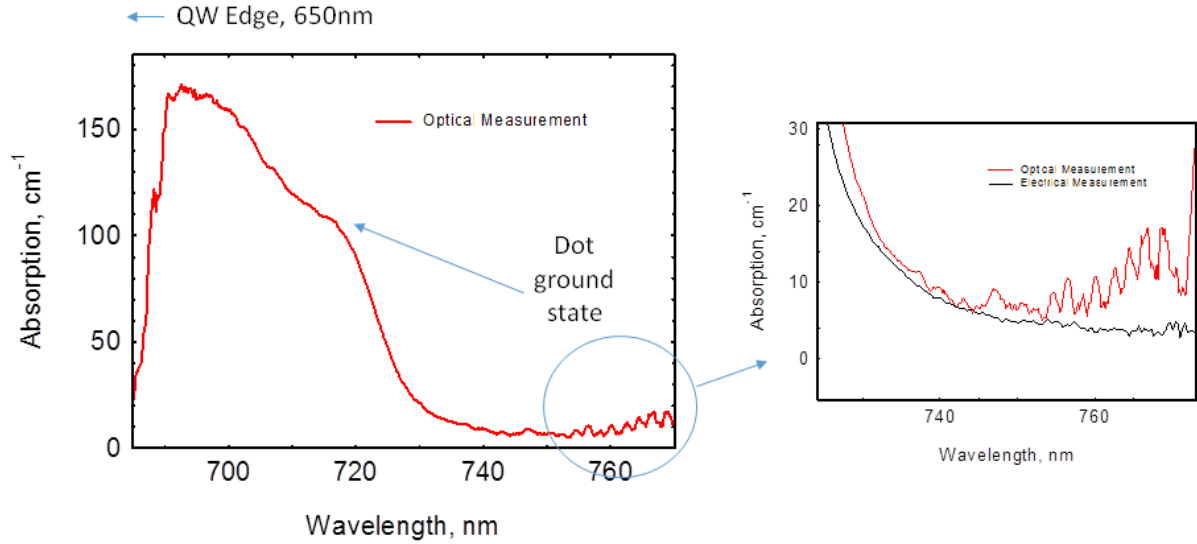


**Figure 5.24: Left: Absorption spectra measured using optical pumping, showing the available states within the material. Right: Comparison of the absorption curves in the higher wavelength region obtained through electrical and optical pumping methods. Optical measurements were taken on a 10 $\mu$ m ridge, electrical measurements on a 50 $\mu$ m oxide isolated stripe laser.**

A decrease in absorption with increasing optical pump power was observed, and has previously been noted (Thomas, R. 2014). This can be seen in figure 5.25. This is a consequence of the fact that the optically pumped material is electrically floating. As light is absorbed from the guided optical mode electron-hole pairs are generated, but do not have a current path in which to escape. This results in the occupation of dot states by these trapped carriers, reducing the number of empty states available for absorption. Therefore with an increasing carrier injection (pump power) the absorption decreases due to an increased number of states occupied by carriers that are unavailable for absorption. From this data the internal optical mode loss for the 10 $\mu$ m ridge structure is further estimated as  $7.5 \pm 2.5 \text{ cm}^{-1}$ .

The gain and absorption curves for the 10 $\mu$ m ridge obtained through optical pumping can be seen in figure 5.26. It is evident that an increase in pump power leads to an increase in gain. With an increasing pump power more carriers are supplied, resulting in an increased population inversion and a higher gain. However, at a pump laser power of 6 Watts the gain stops increasing. The point at which increased carriers no longer result in an increased gain can be an indication of gain saturation. The carriers start to populate higher lying states which do not contribute to the peak gain. An inhomogeneous size distribution of dots has a wide distribution of electronic states and is therefore susceptible to gain spectrum



broadening as the peak gain saturates. The low gain values obtained however indicate that the lack of increasing gain with increasing pump laser power is more likely due to the increasing spot size of the pump laser at high powers (as a function of the response of the optics). This can be confirmed because the absorption curves also do not change at these increasing pump powers.

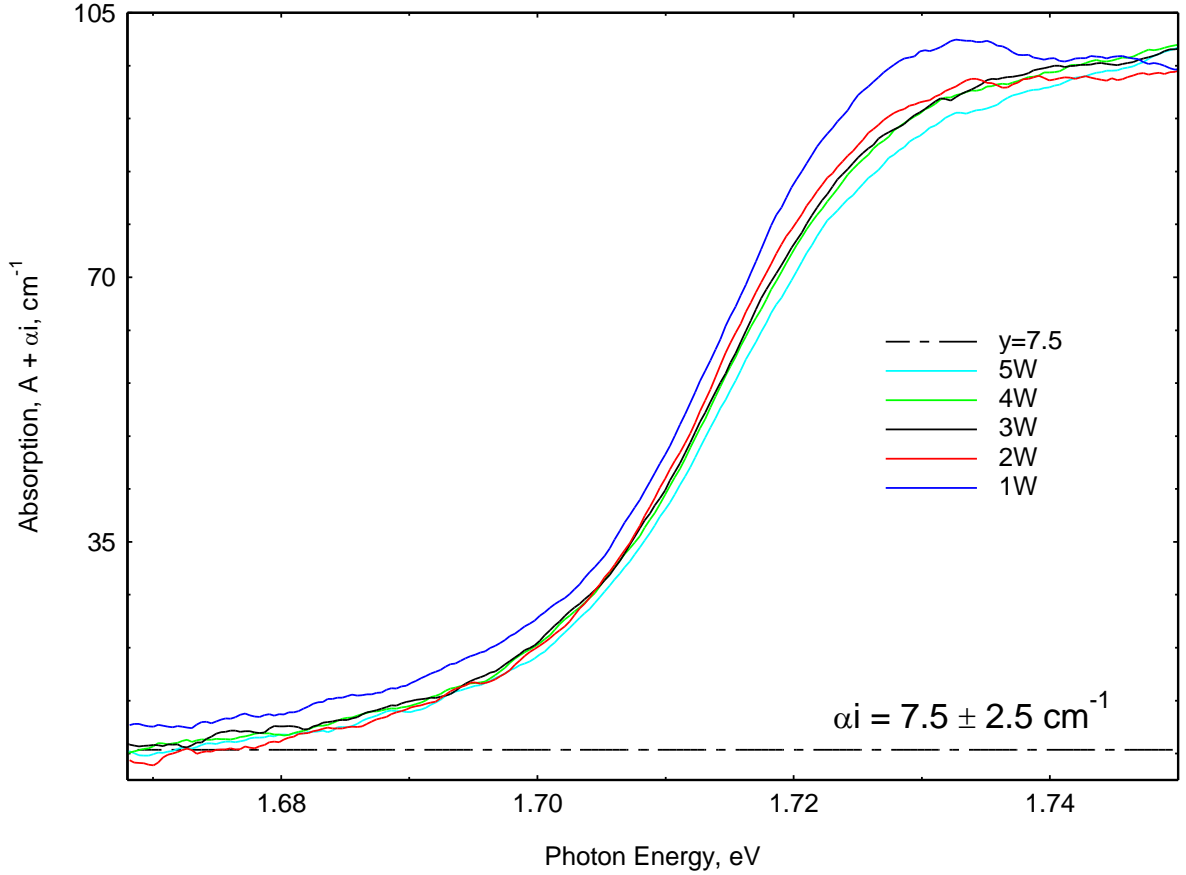


**Figure 5.25: Absorption decrease observed with an increasing optical pump power. Also given is an estimate of the value of internal optical mode loss for the 10 $\mu$ m ridge structure at  $7.5 \pm 2.5 \text{ cm}^{-1}$**

A comparison of the gain curves of figure 5.26 (which do not reach the transparency point), and the values obtained in figure 5.27 (for the 50  $\mu$ m oxide isolated stripe laser) is informative. The transparency point at different current injections (and levels of gain) are indicated in figure 5.27, the transparency point is dependent upon the Fermi level separation so increases in energy with increasing carrier injection. It is evident that a much larger gain is available than is being observed from the 10  $\mu$ m ridge.

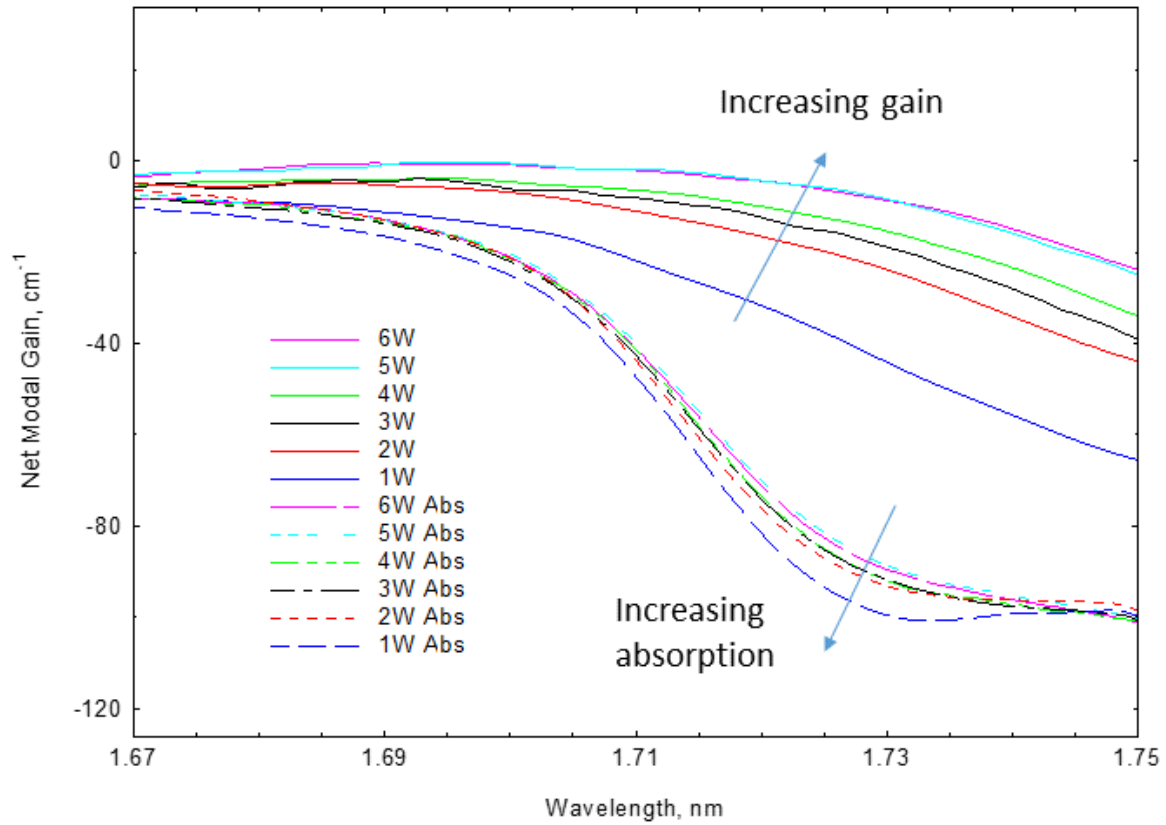


Figure 5.26: Net modal gain and absorption (plotted as negative gain) for 10 $\mu$ m ridge, using the optically pumped variable stripe length method.

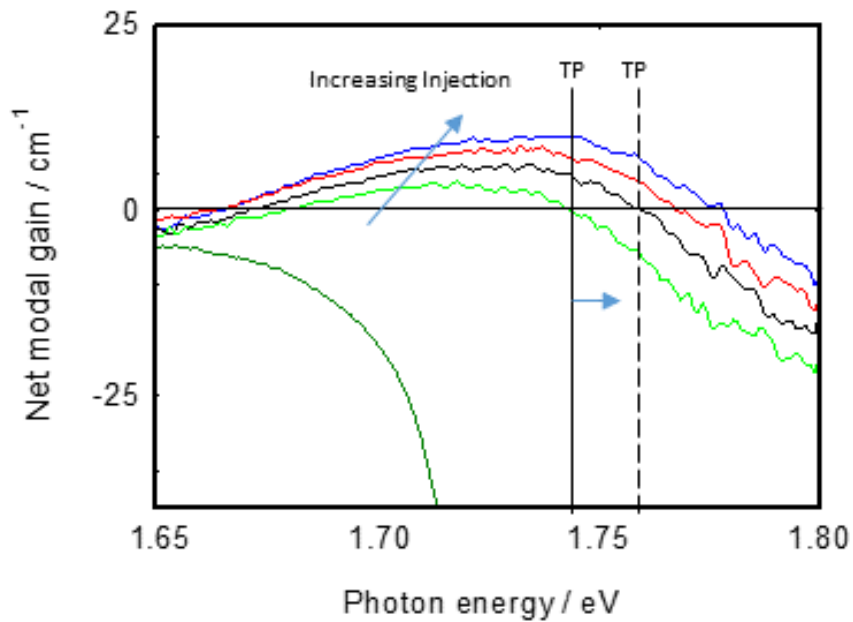


Figure 5.27: Shows the gain available under increased levels of electrical injection on a 50 $\mu$ m oxide isolated stripe laser, and the shift in transparency point. Included is an absorption curve as an indication of the injection level.

The highest gain curve for the 10  $\mu\text{m}$  ridge has been included in figure 5.28 aside two gain curves under electrical injection for the oxide stripe laser. The absorption curves for both devices are included because the degree of population inversion can be determined from the difference in the absorption edge and the transparency point. The absorption curves are similar for both devices although there is a discrepancy. It is evident that even at the highest optical pump power used, the Fermi level separation (gain) does not reach the value obtained by an electrical carrier injection of  $70 \text{ A cm}^{-2}$ . This is a strong indication that optical pump light is not reaching the active region of the device. The most likely reason for this is the high temperature annealing of the nickel ICP mask during the high temperature etch procedure. It is possible that the subsequent wet etch is unable to remove the nickel from the top of the ridge or the top of the pillars (which may heat more than the ridges during the etch), therefore inhibiting optical pumping of the device. An alternative explanation concerns high surface recombination that may be inhibiting emission. As a result of the etch process, and without any chemical passivation of the surface, a large density of extrinsic states may exist within the forbidden energy gap. This can pin the Fermi level at that position. This can increase the non radiative recombination rate at surface recombination centres. Chemical passivation of the surface may help to tie up dangling bonds, ridding the pillar surface of electronically active sites. This may result in a greatly enhanced photoluminescence and gain.

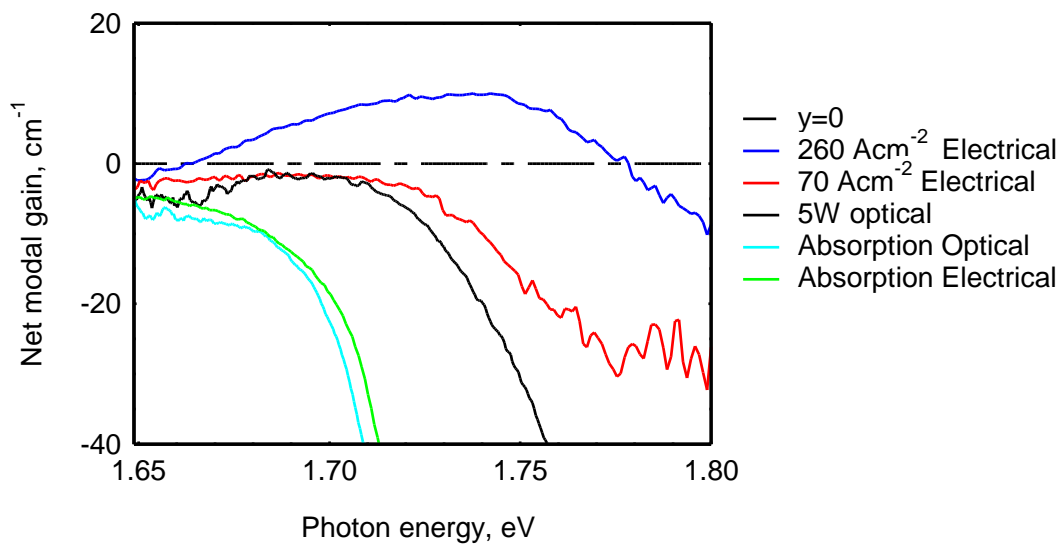


Figure 5.28: The net modal gain ( $G-\alpha_i$ ) for TE polarisation is shown, with net modal absorption curves for comparison shown as negative gain.

## 5.5. Summary

In conclusion I have shown a viable design for a composite pillar-polymer nanolaser, and successfully fabricated the device. This included the development of InP ICP etching and the novel and new use of polymer materials in a waveguide. The absorption and gain of the nanopillar structure were not successfully measured due to a lack of light coupling into the active region when optically pumped. This is likely a result of the unintentional annealing of the nickel etch mask which resists chemical removal, blocking pump light from reaching the active region. However, the absorption and internal optical mode loss of a ridge of an equivalent width was measured, and a dependency of absorption with pump power was noted. To allow characterisation using this optically pumped technique further work must see the development of an ICP etch mask that is able to better preserve the semiconductor surface, such as an oxide-nickel bilayer etch mask.

## Chapter References

Blood, P. (2015). Quantum Confined Laser Devices, Optical gain and recombination in semiconductors, Oxford Master series in atomic, optical, and laser physics, Oxford University Press.

Thomas, R.; Smowton, P.M.; Blood, P. (2014). Radiative recombination rate measured by the optically pumped variable stripe length method. Optics Express 3308 23(3).

Shutts, S. (2012). Monolithic dual-wavelength InP/AlGaInP quantum dot lasers. Condensed Matter and Photonics. ORCA, Cardiff Univerity. PhD.

West, B. R. and A. S. Helmy (2006). Dispersion tailoring of the quarter-wave Bragg reflection waveguide. Optics Express 14(9): 4073-4086.

# Chapter 6. GaN Pillar Device

## 6.1. Introduction

This chapter details the design, fabrication, and characterisation of a GaN composite pillar-polymer device. The shifting excitation spot experiment, as described in section 3.4.2, was used to investigate the absorption and waveguiding properties of the composite structure.

## 6.2. Device Design

A large array of 450 nm emitting GaN pillars containing single InGaN quantum wells were embedded in the BCB-air gap polymer waveguide described in chapter 5. III-Nitride materials are an increasing area of interest for novel light emitters and detectors (Malis 2013). InGaN quantum well nanopillars have recently received increasing attention in the development of nanolaser and LED devices (Yi Ding, Lewins et al. 2013) (Christopher, YiDing et al. 2013) (Ahmed, Chimalgi et al. 2015).

The emission wavelength of the InGaN quantum wells blueshift to increasingly smaller wavelength with a decreasing pillar diameter due to quantum confinement (Yi, Szymon et al. 2013) (Kuokstis, Yang et al. 2002), the wavelength is also known to be strongly dependent upon strain relaxation (Yulong, Zhibiao et al. 2015).

Nanopillar architectures offer strain relaxation and a reduction in threading dislocations that can lead to an increased quantum efficiency. A reduction of strain effects allows increased bandgap engineering of InGaN quantum wells via an increased indium content (which would otherwise cause strain-induced defects), allowing access to a wide range of operating wavelengths, useful for LED devices. InN and GaN typically have a lattice mismatch of 11 percent (Ahmed, Chimalgi et al. 2015).

GaN nanopillar arrays may also prove useful for sensing applications, particularly when combined with an on-chip microfluidic architecture for analyte delivery. The potential for short pulse lasing necessary for sensing and the enhanced light-matter interaction provided by the nanostructure architecture makes this device configuration particularly interesting. Modelling of the composite pillar-polymer waveguide can be found in the results section of this chapter.

### 6.3. Device Fabrication

This section describes the fabrication of Gallium Nitride (GaN) pillar devices within a polymer waveguide. The GaN pillars, seen in figure 6.1, were etched by Bath University. The pillars had a height of  $3.1\mu\text{m}$ , diameter of  $240\text{nm}$  and pitch of  $600\text{nm}$ . The material consisted of a Sapphire substrate, n doped GaN 2D layer, and pillars. The pillars consisted of n doped GaN, single InGaN quantum well (QW) and p doped GaN. After etching the samples were cleaned by Bath University with potassium hydroxide to remove the rough lower surface at the base of the pillars. The pillars covered the whole of the sample surface.

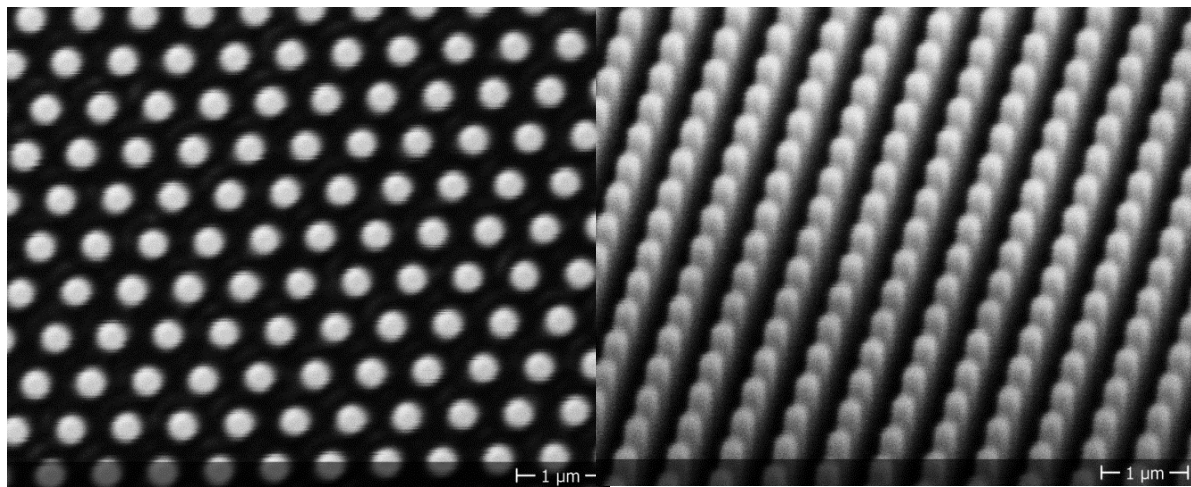


Figure 6.1: SEM image of GaN pillars from above (left) and angled view (right).

The sample was cleaved into approximately  $1\text{cm} \times 1\text{cm}$  sections using a diamond tipped scribe. Cleaving of Sapphire substrates is difficult due to the lack of a suitable cleave plane, the difficulty is dependent on the growth plane and substrate thickness. A cleave line was scribed on the back of the wafer to try to avoid damage to the pillars, and pressure was applied to initiate fracture.

The BCB air-gap waveguide was fabricated using the method described in chapter 5. The sample was cleaved in half to reveal the removal of the lower PMGI polymer throughout the whole sample, resulting in the formation of a lower air-gap. This can be seen in figure 6.2. The foreground of the image is an area where pillars were removed during the cleaving process.

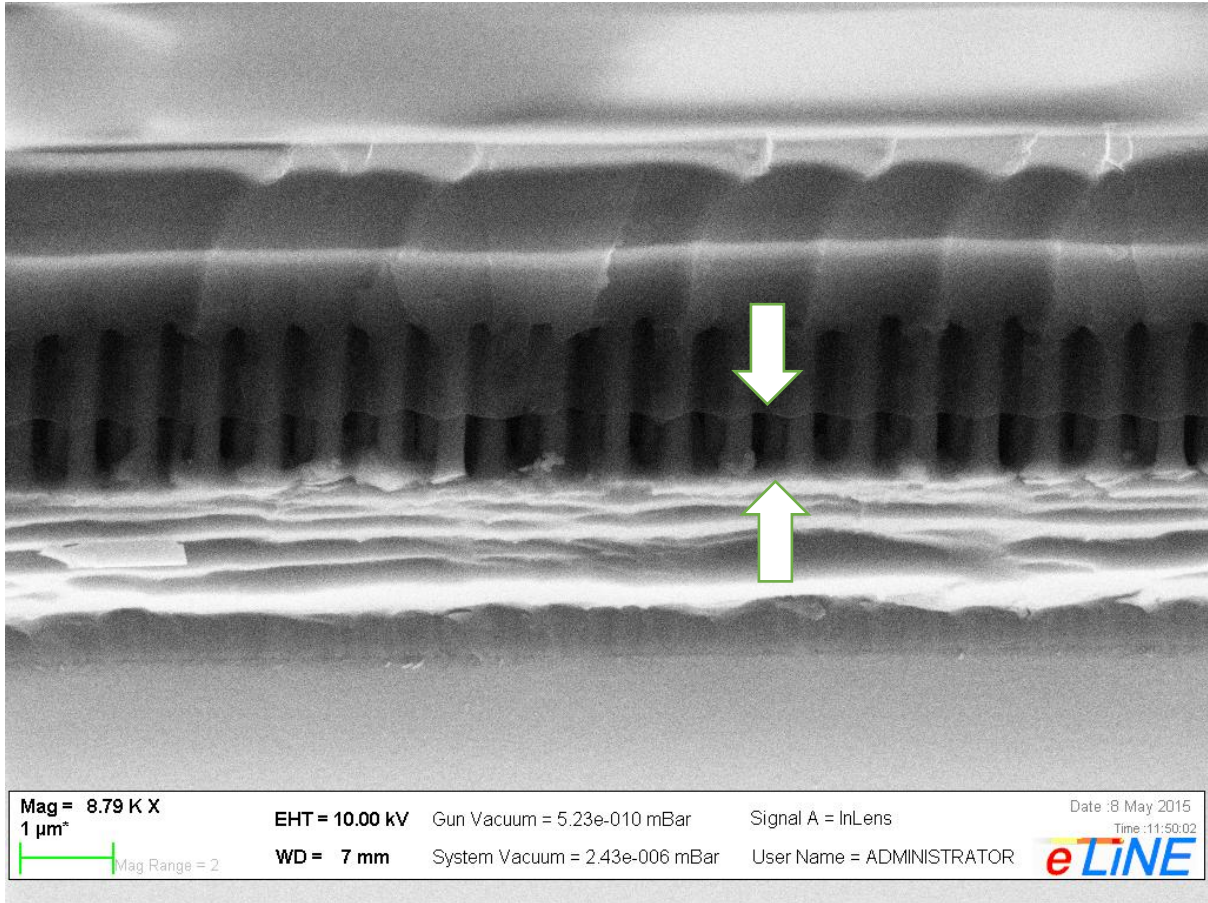


Figure 6.2: SEM image of GaN pillars in BCB polymer with air gap at base of pillars, indicated by arrows.

## 6.4. Results

The device was characterised using the shifting excitation spot experiment as described in section 3.4.2. The light intensity spectra for a GaN pillar array without and with the polymer waveguide can be seen in figures 6.3 and 6.4 respectively. The exciting laser pump spot was moved away from the sample edge, where S1 refers to the spot closest to the sample edge. The pump diode laser was driven with the same current density for both samples, however, the magnitude of the light intensity collected is arbitrary, and dependent upon the alignment and focusing of the collection optics, which may not have been identical for both samples. The experiment only depends upon the difference in light intensity on a given sample with a change in distance moved from the edge. The lower magnitude of the emitted light intensity for the BCB waveguide sample does however give an indication that the sample was not pumped as hard as the sample without the BCB waveguide, this is most likely a result of light scattering rather than absorption. The BCB is not absorbing at the wavelengths used, it has a 99% transmittance (Dow, 2015), and therefore does not possess

any states within this wavelength range. The transmission spectrum can be seen in figure 6.5, reproduced from Dow Company (Dow, 2015), included are the transmission spectra of other polymers for comparison.

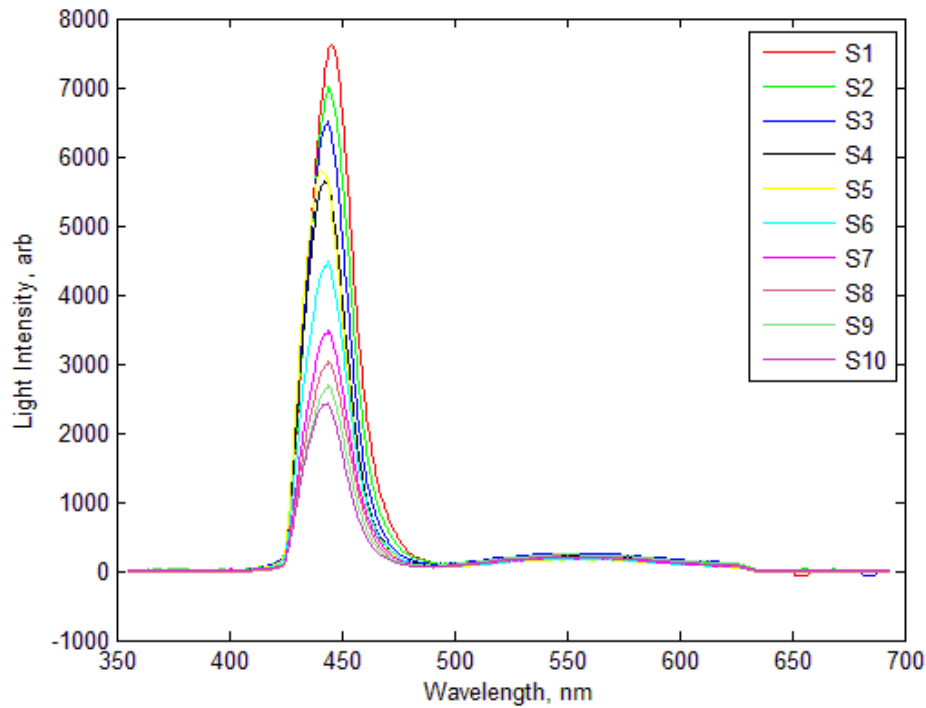


Figure 6.3: Light intensity spectra from the SES experiment for GaN pillars without a polymer waveguide.

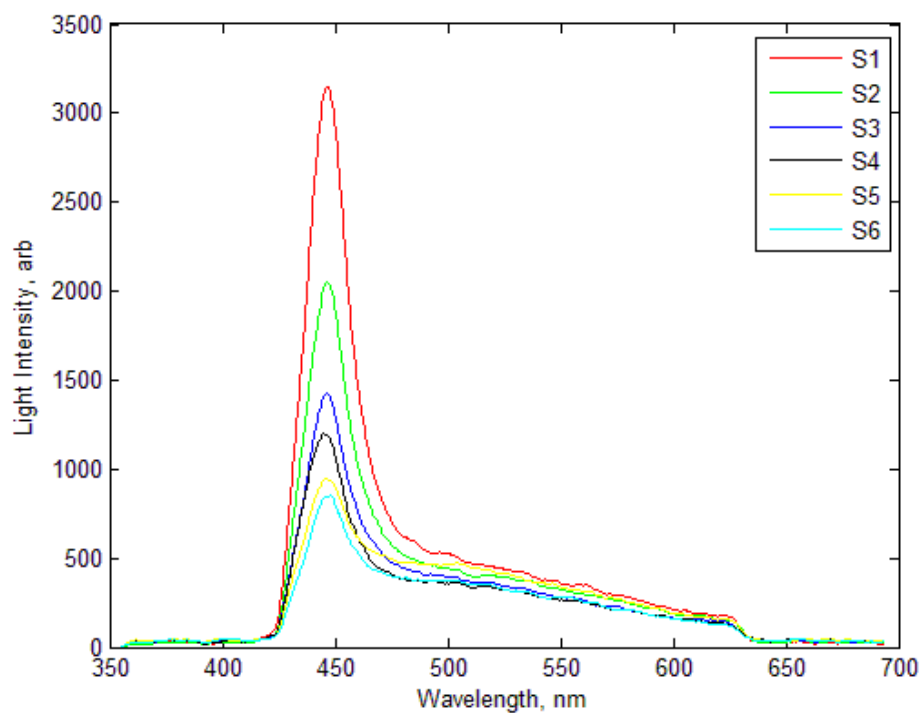
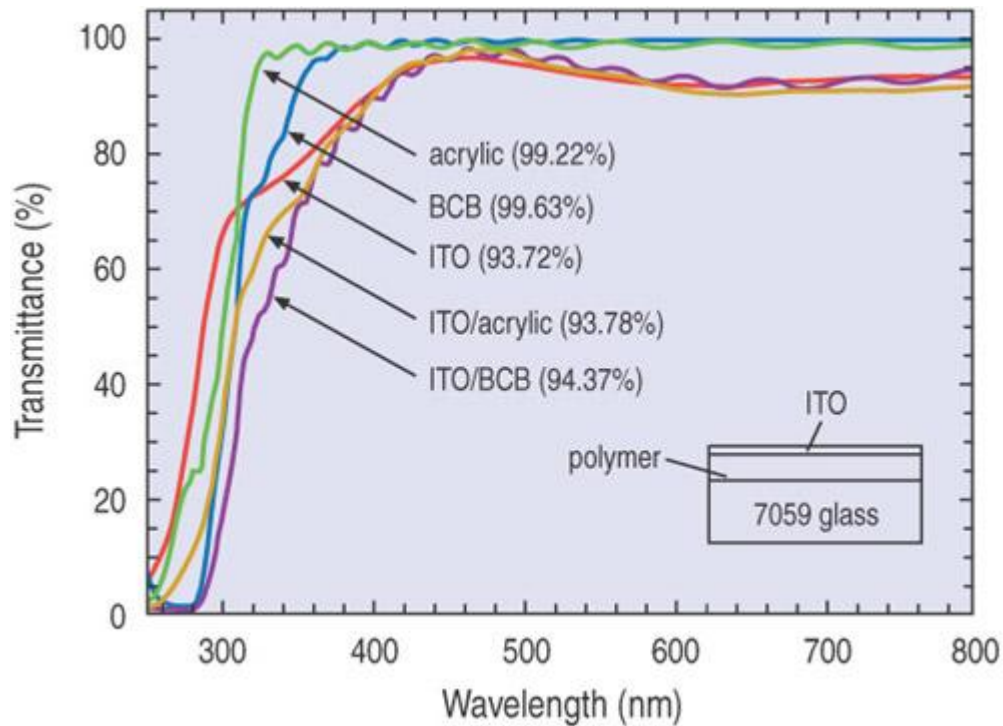


Figure 6.4: Light intensity spectra from the SES experiment for GaN pillars with a polymer waveguide.





**Figure 6.5: Transmission spectrum of BCB between 300nm and 800nm, reproduced from (Dow, 2015)**

The light intensity curves for the nanopillar array with and without the polymer waveguide have been scaled and included in figure 6.6. The peak intensities of the two structures are shifted, exhibiting approximately a 3.3 nm difference in peak wavelength. Decreased quantum confinement in the individual pillars, or a higher strain, will redshift the peak wavelength of emission. The redshift observed of approximately 20 meV for the sample with the polymer can be accounted for by the lower quantum confinement in the individual pillars in this configuration (Kuokstis, Yang et al. 2002). A higher electronic confinement per pillar is expected for the non-polymer sample due the energy gap step between InGaN and air.

It can also be noted that the polymer guided structure shows an enhanced light intensity at longer wavelengths. The origins of this emission are uncertain, however, light emission in this wavelength band may either be due to doping atoms, or the un-etched lower 2D GaN epitaxial layer, and may appear due to the polymer waveguides ability to guide higher order modes that are not guided within the structure without the polymer waveguide. As previously mentioned, the BCB polymer does not have states at this wavelength. Furthermore, in chapter 5 the InP ridge was optically pumped in air and whilst buried in a

BCB layer, both produced identical absorption curves in the higher wavelength range, and no emission was observed when pumping BCB alone in the tested range of 600-750 nm.

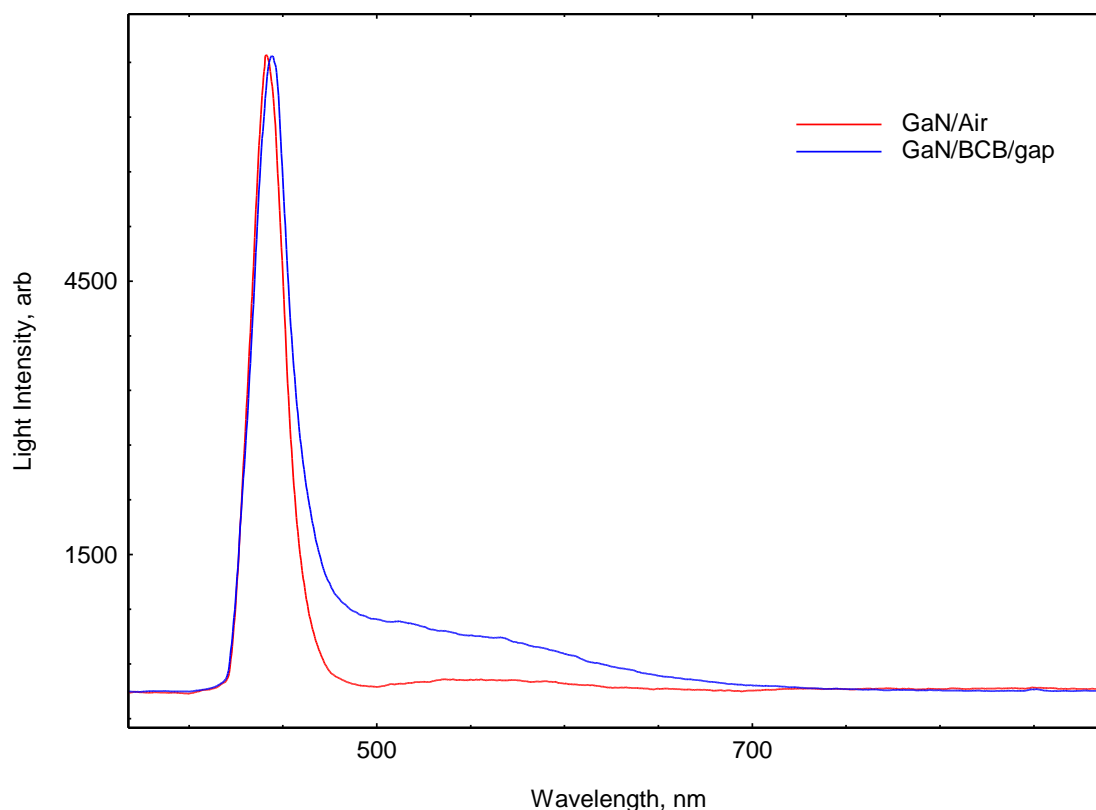


**Figure 6.6: Light intensity curve comparison for GaN nanopillar array with and without polymer waveguide. The curves were obtained by stitching together intensity curves using a number of centre wavelengths on the spectograph in order to obtain reliable data at this extended wavelength range.**

The absorption curves for the GaN samples were calculated using the shifting excitation spot method described in section 3.4.2. Beer-Lambert's law was applied to the data, and the absorption was determined from the gradient of the plot of the natural log of the light intensity against the spot distance from the edge of the sample. An example of a plot can be seen in figure 6.7 for one wavelength position. The use of many spot positions increases the accuracy of the data compared to the gain stripe length method that only uses two pump lengths. A matlab code was written to extract the absorption coefficient at every wavelength.

The quality of the fit was determined by plotting the R squared value of the line of best fit. Absorption curves with R squared values that deviated strongly from unity across the wavelength range were disregarded. An example of an R squared value plot across the wavelength range is shown in figure 6.8. The areas where there is a poor fit is a result of a

low signal and the response of the spectrograph at the set grating and centre wavelength. In addition at the low wavelength edge a wavelength filter was used to block the pump diode laser light. The reliable wavelength range is between approximately 420 nm and 600 nm for the single centre wavelength used on the spectrograph for further measurements.

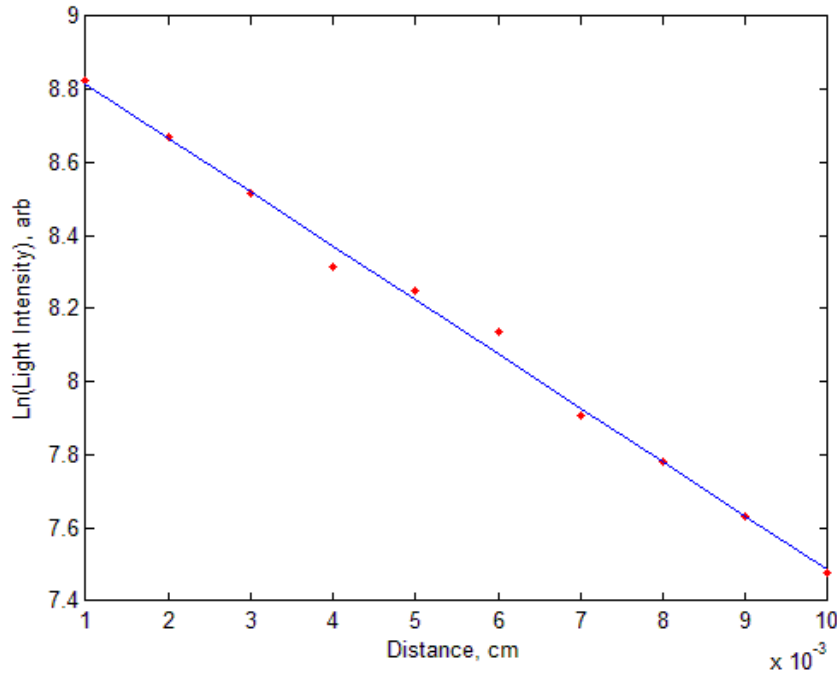


**Figure 6.7:** Plot of the natural log of the light intensity against the spot distance from the edge of the sample, at a wavelength of 480nm. The gradient of the plot is used to find the absorption coefficient.

An example of the absorption spectra output for the polymer and non-polymer GaN nanopillar arrays can be seen in figure 6.9. Although the internal optical mode loss  $\alpha_i$  was not determined for the polymer sample due to emission at longer wavelengths, the value for the pillar array without the polymer waveguide has been determined to be  $4 \pm 4 \text{ cm}^{-1}$ . The large error is a result of the undulations in the absorption spectrum as a result of variations in the fit obtained as a function of wavelength (figure 6.8).

In figure 6.9 it would appear that there are states contributing to the absorption spectrum in the polymer sample that are not contributing to the absorption spectrum in the sample without polymer. If the states exist they do not originate from the BCB, which would indicate that they are present in both structures, but do not interact with the guided mode of the structure without the polymer waveguide (the states therefore do not appear in the absorption spectra), which may be due to spatial separation, with emission that is not optically guided (and therefore does not appear in the intensity spectra of figure 6.6).

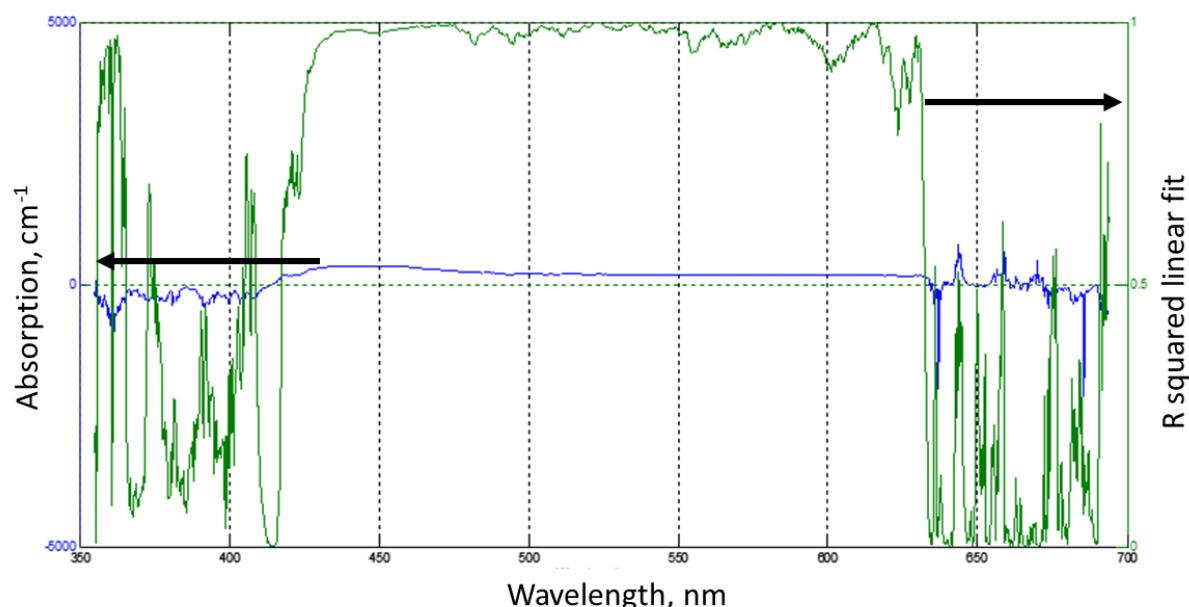


**Figure 6.8:** A plot of the R squared linear fit value, used to determine the reliability of the absorption spectrum across the wavelength range. The arrows indicate the axis for each set of data.

The detection of these states with the polymer waveguide may be due to the polymers ability to guide longer wavelength emission that may be coupled into the waveguide from the lower 2D GaN layer (or doping atoms), which are otherwise spatially separated and not guided. Alternatively the absorption spectra may be anomalous if the polymer waveguide is guiding higher order modes which are not guided by the non-polymer structure.

At a wavelength of 450nm the ratio of the absorption between the sample with and without a polymer waveguide is 1.30, whilst the ratio of the calculated confinement factors of the structures (seen in figure 6.10) for the first order mode is 1.13. If these values were in closer agreement it would suggest that the increased absorption at low wavelengths for the sample with the polymer is due to the increased confinement factor. If a 2<sup>nd</sup> order mode exists within the polymer waveguide but not the non-polymer waveguide the confinement factor ratio becomes 1.34, which is closer to the experimental ratio of absorptions at this wavelength. An example of a higher order mode is shown in figure 6.11 for the polymer and non-polymer sample. It is evident that for the non-polymer samples a large proportion of the mode exists within the absorbing region of the device, prohibiting existence of this higher mode. Higher order modes are therefore more strongly supported by the polymer

waveguide, and at low wavelengths the calculated confinement factor ratio using this model adequately describes the observed enhancement in absorption.

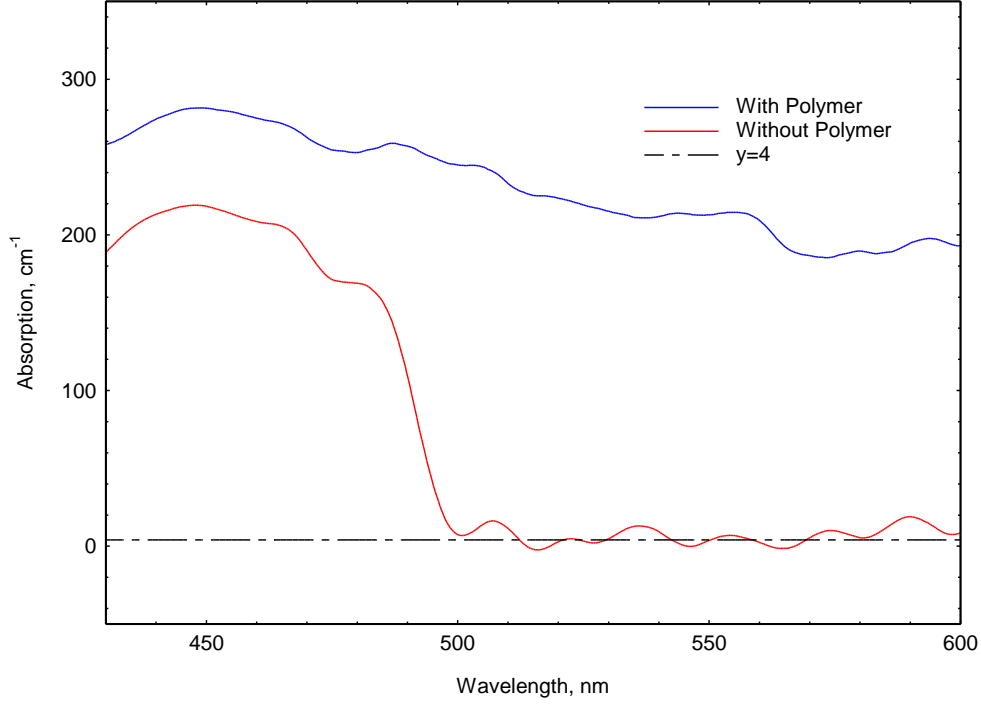


**Figure 6.9: Absorption spectrum of polymer and non-polymer GaN nanopillar arrays. Measurement of internal optical mode loss for sample without polymer,  $\alpha_i = 4 \pm 4 \text{ cm}^{-1}$**

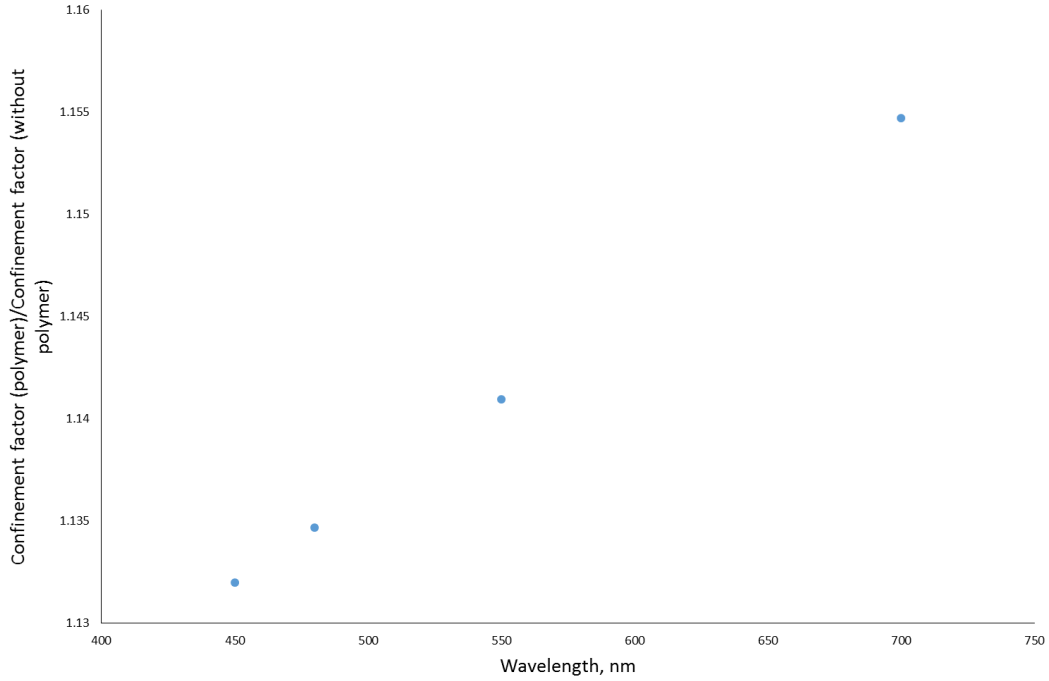


**Figure 6.10: Ratio of calculated confinement factors of polymer and non polymer structures for first order mode.**

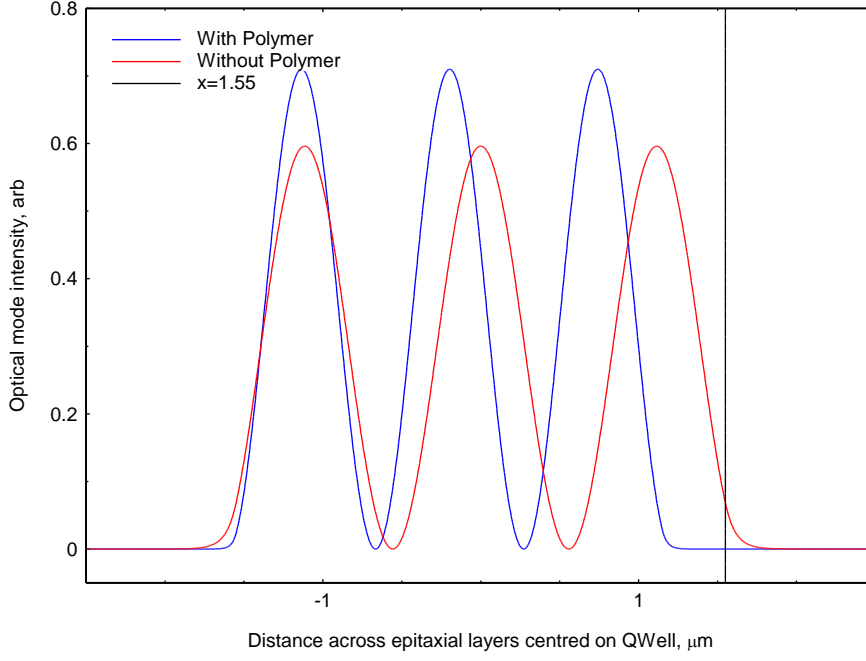


**Figure 6.11: Higher modes for polymer and non-polymer waveguides, where the vertical black line represents the lower absorbing layers.**

Modelling was performed to further explore the longer wavelength guiding in the polymer sample. Figure 6.12 shows the optical mode intensity across the composite pillar-polymer epitaxial layers for the sample with and without polymer, at various wavelengths.

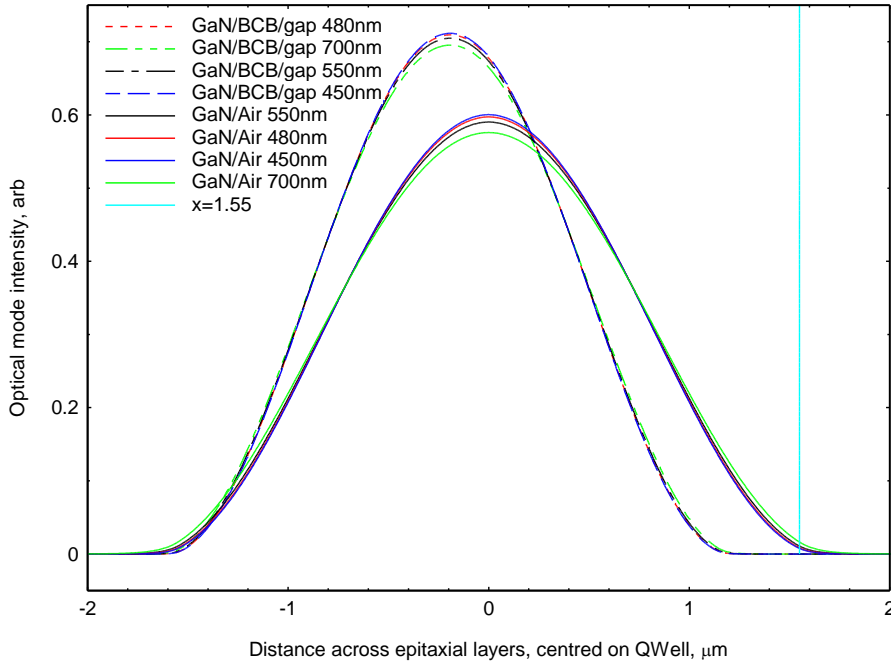


**Figure 6.12: Calculated optical mode intensity across composite pillar-polymer epitaxial layers for samples with and without polymer, at various wavelengths. The line  $x=1.55$  is the base of the pillars.**

The polymer waveguide with a lower air gap shifts the peak of the optical mode further away from the unetched 2D GaN layer at the base of the pillar, allowing for improved optical guiding of the mode. The polymer waveguide is able to guide a broader range of wavelengths to a better degree than the sample without the polymer waveguide. The modelled intensity of the optical mode changes to a smaller degree with a change in wavelength for the polymer waveguide. A value of  $dl/d\lambda$  close to zero in spatial regions where an optical mode is to be guided (and is present) is desirable for broad wavelength guiding.

The polymer waveguide is in particular able to guide longer wavelengths to a better degree than the non-polymer sample. A large positive value of  $dl/d\lambda$  indicates a larger light intensity at long wavelengths, therefore if a large positive value of  $dl/d\lambda$  exists at a position near the lower un-etched layers/substrate, where the light is not supported by the waveguide and are likely to suffer absorption, it indicates that longer wavelengths are more poorly supported.

In figure 6.13 it can be seen that the sample without polymer has a large positive value of  $dl/d\lambda$  coinciding with the absorbing region (vertical black line), indicating that long wavelengths will be strongly absorbed in the lower layers. The polymer structure has a value of  $dl/d\lambda$  that is closer to zero within the InGaN well region, indicating that the range of wavelengths are guided more strongly by the polymer waveguide. In particular the peak of the positive value of  $dl/d\lambda$  does not coincide with the absorbing lower layers, allowing longer wavelengths to be guided within the central core.

If the area integral of the optical mode beyond 1.55  $\mu\text{m}$  is a large percentage of the area integral of the whole optical mode, then the wavelength in question is unlikely to be supported by the waveguide. It is evident from figure 6.14 that due to the percentage of the optical mode at longer wavelengths within the substrate for the non-polymer sample, that this sample would not support longer wavelengths to the same extent as the polymer sample.

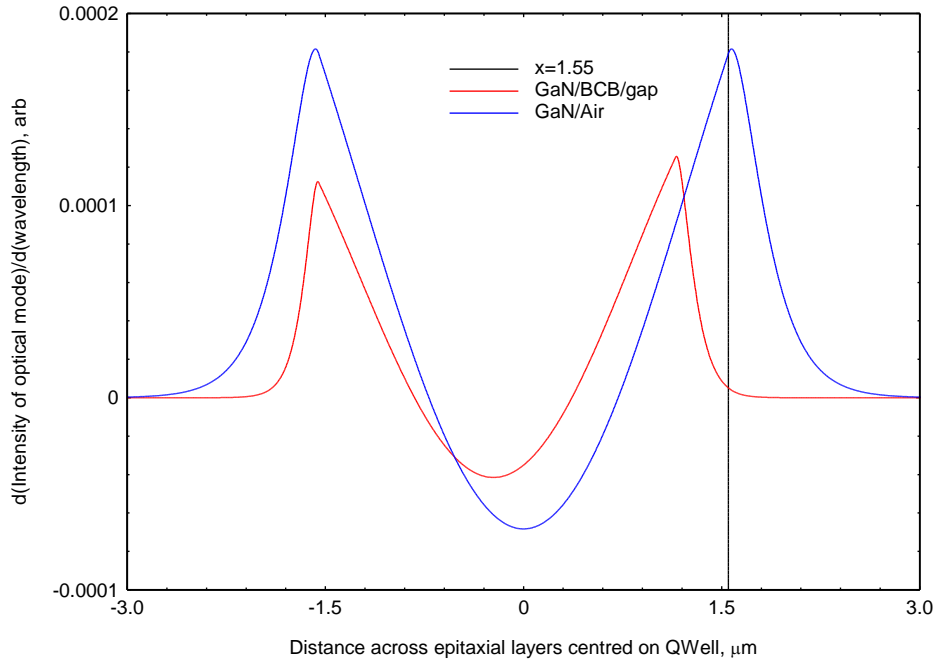


**Figure 6.13: Change in optical mode intensity with wavelength as a function of spatial position.**

Wavelength,nm	GaN/Air %	GaN/BCB/gap %
450	0.62203	0.00022
480	0.71473	0.00038
550	0.94538	0.00129
700	1.50453	0.00725

**Figure 6.14: Table of the percentage of the optical mode within the lower absorbing layers at various wavelengths for the polymer and non-polymer structures.**

## 6.5. Summary

A GaN nanopillar array was embedded in a BCB polymer with a lower air gap to act as an optical waveguide. The internal optical mode loss of the nanopillar array without a polymer waveguide was determined to be  $\alpha_i = 4 \pm 4 \text{ cm}^{-1}$ . A slight redshift in peak wavelength was observed for the polymer sample, attributed to a lower confinement factor of each individual pillar. Additional optical emission at long wavelengths was detected from the composite nanopillar-polymer waveguide which was not detected for the structure without a waveguide, and did not emanate from the polymer itself. The emission may be attributed to emission from doping atoms or the lower unetched 2D GaN layer. These states exist in both structures, but do not form part of the guided mode for the structure without the



polymer, and therefore do not appear in the absorption spectrum on the non-polymer sample. Modelling showed that the polymer waveguide is able to more strongly guide a broader and longer range of wavelengths, whilst the non-polymer structure shows indications that long wavelengths are not guided. The increased absorption at the peak wavelength for the polymer waveguide indicates an increased optical confinement factor across the composite polymer quantum well layer, the magnitude suggests that a 2nd order mode is guided within the polymer waveguide that is not guided with the non-polymer waveguide.

## Chapter References

Ahmed, S. S., et al. (2015). Nanoscale Solid-State Lighting Device Simulator.

Christopher, C. S. C., et al. (2013). "Photoluminescence of Single GaN/InGaN Nanorod Light Emitting Diode Fabricated on a Wafer Scale." Japanese Journal of Applied Physics 52(8S): 08JE20.

Dow, C. (2015) "Cyclotene advanced electronics resins- Optical Transparency." <http://www.dow.com/cyclotene/solution/optical.htm>.

Kuokstis, E., et al. (2002). "Two mechanisms of blueshift of edge emission in InGaN-based epilayers and multiple quantum wells." Applied Physics Letters 80(6): 977-979.

Malis, O. (2013). Quantum Band Engineering in III-nitride Semiconductors.

Yi Ding, Z., et al. (2013). "Fabrication and Characterization of Light-Emitting Diodes Comprising Highly Ordered Arrays of Emissive InGaN/GaN Nanorods." Photonics Technology Letters, IEEE 25(11): 1047-1049.

Yi, D. Z., et al. (2013). "Optical Properties of GaN Nanorods Containing a Single or Multiple InGaN Quantum Wells." Japanese Journal of Applied Physics 52(8S): 08JE11.

Yulong, H., et al. (2015). "Nano-fabrication and related optical properties of InGaN/GaN nanopillars." Nanotechnology 26(7): 075302.

# Conclusions

This work investigated three types of nanodevices, these were a hybrid-plasmonic nanolaser, an InP composite nanopillar-polymer nanolaser and a GaN composite nanopillar-polymer device.

A number of important design concepts have been identified for a hybrid-plasmonic device which informed upon the necessary fabrication development steps. Gain-assisted hybrid plasmonic device configurations are viable providing that the optical mode within the gain material has a large confinement factor, and can provide a large gain to overcome Ohmic losses. Quantum confined gain regions such as quantum wells have a small confinement factor, further to this the confinement factor decreases when the hybrid mode becomes bound to the metal region of the device, where much of the optical power resides in the dielectric layer. This results in a small modal gain which is unlikely to match the device losses. Quantum wells do however have the advantage that their emission can be strain engineered to ensure an electric field vector perpendicular to the metal surface, which is required for the generation of surface plasmon oscillations. For the configuration studied in this work this relates to a TM polarisation. A multiple quantum well epitaxial structure will lead to an increased confinement factor and gain, and could be a viable route to laser action. To mitigate losses the degree of hybridisation is adjusted by using a dielectric gap between the semiconductor gain material and metal, whilst ensuring that the condition of a bound mode to the metal region is not violated. A single nm change in dielectric gap thickness can alter the mode absorption by  $600\text{cm}^{-1}$ , and can change the allowed semiconductor slab thickness (cut-off thickness) by up to 100nm. The gap dielectric and semiconductor slab thickness were therefore identified as important areas requiring the development of optimised fabrication techniques. A study concerning the growth of a dielectric gap utilising an electrolytic process was carried out in which GaAs was oxidised through anodisation. An oxide of GaAs, grown under optimised conditions, was found to exhibit a number of characteristics beneficial for the hybrid-plasmonic application. In particular a smooth and conformal oxide was grown, with a low RMS roughness (0.06nm) and peak-to-trough topography, which is necessary to ensure propagation of the plasmonic mode. The use of an e-beam defined growth mask allowed the accurate alignment of the

oxide to other structures. However, although a high control of the oxide thickness can be obtained over large areas, this proves difficult for decreasing sample areas (and post patterning of large oxide areas does not result in well-defined edges). This necessitates the use of larger oxide growth areas on other parts of the sample when patterning small oxide areas using growth masks. A 3nm oxide of GaAs showed a reasonable barrier height of 0.87eV, although this was obtained with a modified Richardson theory, which indicates a distribution of barrier heights that may have been caused by metal penetration into the oxide, or alternatively it may be due to the altered doping distribution of the material after anodisation. A draw back to the use of an oxide of GaAs is its solubility in photoresist developer, and the need to completely cover any exposed surface-metal to perform the anodisation procedure. These factors are not catastrophic, but it does mean that process flows must be carefully planned to account for this. In conclusion, an oxide of GaAs grown through a process of anodisation is a good candidate for the dielectric gap as long as the process flow of the device is well designed. The semiconductor slab thickness and current aperture (as a possible scheme of electrical injection) was defined through the steam oxidation of AlGaAs. Calibration of the constructed apparatus showed an ability to repeatedly fabricate small current apertures, with a controlled oxidation rate of approximately 0.06 $\mu\text{m}/\text{min}$ .

A viable composite pillar-polymer design was investigated, with potential applications as a sensor, and potential benefits from the reduction of strain dislocations when growing III-V material on silicon substrates. The use of a diluted gain medium however requires the use of highly reflective mirrors to meet the round-trip gain condition at a reasonable device length. For this reason, and for the accurate fabrication of nanopillars, work was carried out on the inductive coupled plasma etching of nanoscale structures. An etch recipe was developed that was able to simultaneously etch a close-packed array of nanopillars and distributed Bragg reflectors, crucial for this design. A polymer waveguide was fabricated via the novel use of materials. A sacrificial polymer was used to form a lower air gap with a BCB guiding layer, anchored by the nanopillars. A modelled three layer polymer suggests that a negligible change in guiding can be achieved between undiluted gain medium and the pillar-three layer polymer structure. Further work on this device should see the fabrication of the designed three layer polymer, with a suitable low index polymer as the cladding polymer. In

addition, the optical characterisation methods employed in this work were unable to characterise the gain or absorption of the pillar arrays. The unintentional high temperature annealing of the nickel etch masks on the pillars during the etch procedure resulted in a low optical coupling from the pump source into the pillars. This difficult to remove nickel layer would also prove problematic for electrical characterisation techniques. Therefore further work should see the development of a dielectric/metal etch mask.

A GaN nanopillar array was embedded in a BCB polymer with a lower air gap to act as an optical waveguide. This interesting study showed a potential additional application for the developed BCB waveguide with lower air gap. The polymer waveguide was found to guide longer and higher order wavelengths to a greater degree than the structure with no waveguide. This may have potential uses in light sources that require a broad wavelength range. To further investigate this a study should be performed using a central BCB waveguide core of various dimensions in order to prevent higher order modes from propagating, allowing a more accurate investigation of the apparent long wavelength guiding within the polymer material. In addition, un-processed GaN material should be obtained to allow optical characterisation of the plain material, which should give extra insight into the origins of the observed emission.

# Appendix

Shifting excitation spot apparatus: Provided are a list of further details for the components of the shifting excitation spot experimental set-up.

A: 405nm diode pump laser, 150mW output power. Operated using a pulse generator with a pulse with of 1 $\mu$ s, frequency 10kHz, at a current of 140mA. The current was measured using a current probe and oscilloscope.

B: Objective lens with x,y,z translation stage for focusing.

C: Cube mounted UV enhanced aluminium mirror with linear translation for spot movement.

D: Dichroic mirror, small transmittance at pump wavelength to image pump spot (10% transmission 380-410nm), large pump wavelength reflectance (90% 380-410nm) for pumping, large spontaneous emission wavelength transmittance (85% 440-770nm) to image surface spontaneous emission spot.

E: Mirror

F: Objective lens

G: GaN device mounted. Adjustments were made to sample position when necessary using a x,y,z,tilt mount.

H: Objective lens

I: Mirror

J: Long pass filter to cut out scattered pump laser light in order to protect the spectrograph.

K: Andor 260i Spectograph, gated with respect to the pulse generator of the pump diode laser through a delay/pulse generator. Spectograph chilled using a peltier cooler with heat extraction using a chiller and water cooling system. The diffraction grating and centre wavelength was selected using Andor computer software. Background light was taken off results using background measurements prior to pumping, using inbuilt routines. The signal was integrated over a user-set count rate. The pixels were calibrated to real wavelength using a mercury lamp with known emission lines.

L: Long pass wavelength filter to cut out reflected pump laser light in order to image surface spontaneous emission spot. This filter was removed when imaging the pump light spot.

M: Neutral density filters to protect camera.

N: Objective lens

O: Camera

P: White light illumination for imaging of surface of sample.

Q: White light illumination for imaging of facet of sample.

R: Lens

S: Partially reflecting mirror to allow illumination of sample facet, and transmission of reflected light to CMOS camera.

T: CMOS camera connected to laptop.